UCLA
UCLA Electronic Theses and Dissertations

Title
Structure and Mixing Characterization of Variable Density Transverse Jet Flows

Permalink
https://escholarship.org/uc/item/13s2n03s

Author
Gevorkyan, Levon

Publication Date
2015

Peer reviewed|Thesis/dissertation

eScholarship.org Powered by the California Digital Library
University of California

University of California
Los Angeles

Structure and Mixing Characterization of Variable Density Transverse Jet Flows

A dissertation submitted in partial satisfaction
of the requirements for the degree
Doctor of Philosophy in Mechanical Engineering

by

Levon Gevorkyan

2015

© Copyright by
Levon Gevorkyan
2015

Abstract of the Dissertation

Structure and Mixing Characterization of Variable Density Transverse Jet Flows

by

Levon Gevorkyan

Doctor of Philosophy in Mechanical Engineering

University of California, Los Angeles, 2015

Professor Ann R. Karagozian, Co-Chair

Professor Owen I. Smith, Co-Chair

This dissertation describes an experimental study of the structural and mixing characteristics of transverse jets, or jets in crossflow (JICF). Hot-wire anemometry, stereo particle image velocimetry (PIV), and acetone planar laser-induced fluorescence (PLIF) measurements were utilized to illuminate and quantify the wind-ward (upstream) jet shear layer instability characteristics and their relationship to the velocity field evolution, as well as the effect of the overall velocity field on the scalar field distribution and resulting mixing characteristics. Transverse jets of various jet-to-crossflow momentum flux ratios in the range $41 \geq J \geq 2$, and jet-to-crossflow density ratios in the range $1.00 \geq S \geq 0.35$, were generated using mixtures of helium and nitrogen in the jet fluid. Jets were injected from one of three different injectors explored: a convergent nozzle with circular geometry which was mounted flush with the wind tunnel floor, another convergent nozzle with circular geometry whose exit plane lies above the crossflow boundary layer, and a flush-mounted straight pipe injector with a circular orifice. Jet Reynolds number was kept constant for the majority of the mixing and structural exploration experiments at $Re_j = 1900$, except when the effect of Reynolds number on cross-sectional jet structure was explored.

Previous hot-wire based measurements at UCLA (Megerian et al., 2007; Davitian et al., 2010a; Getsinger et al., 2012) suggest that the upstream jet shear layer transitions from

convective instability to absolute instability, giving rise to self-excited nonlinear states, as either the momentum flux ratio is lowered below $J \approx 10$, or the density ratio is lowered below $S \approx 0.45$ for the JICF injected from the flush nozzle injector. A similar transition to absolute instability when lowering momentum flux ratio was found in this work for the flush-mounted pipe injector. Cross-sectional PLIF measurements in the present studies suggested clear correspondence between the formation of a symmetric counter-rotating vortex pair (CVP) and the generation of strong upstream shear layer instability. In contrast, weak, convectively unstable upstream shear layers corresponded with asymmetries in the jet cross-sectional shape and/or lack of a CVP structure. While momentum flux ratio J and density ratio S most significantly determined the strength of the instabilities and CVP structures, an additional dependence on jet Reynolds number for CVP formation was found, with significant increases in jet Reynolds number resulting in enhanced symmetry and CVP generation.

The mixing characteristics of $Re_j = 1900$ jets of various J, S, and injector type were explored in detail in the present studies using jet centerplane and cross-sectional PLIF measurements. Various mixing metrics such as the jet fluid centerline concentration decay, Unmixedness, and Probability Density Function (PDF) were applied systematically using a novel method for comparing jets with different mass flux characteristics. It was found that when comparing mixing metrics along the jet trajectory, strengthening the upstream shear layer instability by reducing J, and achieving absolutely unstable conditions, enhanced overall mixing. Reducing density ratio S for larger J values, which under equidensity ($S = 1.00$) conditions would create a convectively unstable shear layer, was also observed to enhance mixing. On the other hand, reducing S for low J conditions, which are known to produce absolutely unstable upstream shear layers even for equidensity cases, was actually observed to reduce mixing, a result attributed to a reduction in crossflow fluid entrainment into shear layer vortex cores as jet density was reduced. Comparing injectors, the flush-mounted pipe was generally the best mixer, whereas the worst mixer was the nozzle that was elevated above the crossflow boundary layer due to upstream shear layer co-flow generated by the elevated nozzle contour; this co-flow was observed here and in prior studies to stabilize the shear layer.

The effect of the evolution of the velocity and vorticity fields on the scalar concentration field was studied in more detail using simultaneous PLIF/PIV measurements of the jet centerplane. General correspondence between regions of high vorticity/strain and high scalar dissipation rate was found. Moreover, proper orthogonal decomposition (POD) analysis of both scalar and velocity fields suggested that transition to absolute instability with J reduction dominated the scalar field evolution near the jet exit, consistent with the mixing results. However, time-varying and/or three-dimensional effects resulted in scalar diffusion layer-normal strain rates extracted from PIV measurements to be consistently higher than that calculated from PLIF-based extraction of scalar dissipation rate data for strained advection-diffusion layers in the scalar field. Nevertheless, trends in PIV-based strain field evolution and PLIF-based scalar dissipation rate evolution along the upstream shear layers were generally consistent with one another, and differences in the magnitudes of wind-ward and lee-side strain rates provided evidence for associated differences in jet wind-ward and lee-side ignition processes in the presence of a reaction.

The dissertation of Levon Gevorkyan is approved.

Luminita A. Vese

Robert T. M'Closkey

Owen I. Smith, Committee Co-Chair

Ann R. Karagozian, Committee Co-Chair

University of California, Los Angeles

2015

To Eduard and Lamara

Table of Contents

1 Background and Motivation 1

1.1 Transverse Jet Structure and Characterization 3

1.1.1 Flow Parameters 3

1.1.2 Classic JICF Characteristics 4

1.1.3 Recent Studies on Strategic JICF Control 14

1.2 Mixing Quantification of Fluid Flows 22

1.3 Velocity Field Strain and Scalar Dissipation 30

1.3.1 Strained Laminar Layer Models for Turbulence 31

1.3.2 Strain, Dissipation, and Reaction 33

1.4 Focus of Current Studies 34

2 Experimental Setup and Diagnostics 36

2.1 The Jet in Crossflow Experimental Setup 36

2.2 Hotwire Measurements 40

2.3 Optical Diagnostics 40

2.3.1 PLIF 42

2.3.2 PIV 51

3 Transverse Jet Structure and Stability 54

3.1 Flowfield Features 54

3.2 Upstream Shear Layer Stability and Vortex Rollup 57

3.3 Transverse Jet Cross-Sectional Characteristics 64

3.3.1 Constant Jet Reynolds Number, Equidensity 64

3.3.2 Variable Jet Reynolds Number, Equidensity 72

3.3.3 Constant Jet Reynolds Number, Low Density 77
3.4 Structure and Mixing 78

4 Transverse Jet Mixing 81
4.1 Scales and Resolution 81
4.2 Differential Diffusion Effects 83
4.3 Jet Trajectory Comparison 84
4.4 Mean Entrainment Measures 90
4.4.1 Maximum Mean Concentration Decay 90
4.4.2 Mean Jet Spread 97
4.5 Turbulent Stirring and Diffusion Measures 103
4.5.1 Cross-sectional Mixing Metrics 103
4.6 Centerplane and Cross-sectional Mixing Metric Comparison 112
4.7 Effect of Resolution on Mixing Results 123
4.8 Mixing and Scalar Dissipation 127

5 Simultaneous Scalar and Velocity Field Characterization 129
5.1 Simultaneous PLIF/PIV Measurements 129
5.2 POD Analysis 134
5.3 Strain and Scalar Dissipation Rates 142
5.3.1 Mixing Layer Determination 142
5.3.2 Maximum Scalar Dissipation Rate and Minimum Principal Strain Rate 145
5.3.3 Maximum Scalar Dissipation Rate and Layer-Normal Strain Rate . . 150
5.3.4 SDRL Model Applied to the JICF 151
5.3.5 PLIF Resolution Effects on SDRL Model Application 156

6 Conclusions and Future Work 162

A Mean Cross-sectional (yz-plane) Scalar Field Data 166

B Centerplane Mean and Instantaneous Data 182

C Additional Instantaneous High Resolution Centerplane Scalar Field Data 203

D Simultaneous PLIF/PIV Data 207

List of Figures

1.1 Schematic of the transverse jet, introduced flush with respect to the injection wall, and relevant vortical structures. Adapted from Fric and Roshko (1994). 4

1.2 Vertical velocity spectra in the equidensity transverse jet at two R conditions, one each above and below the apparent transition in spectral character. Spectra are measured within the jet shear layer at varying distance s/D from the jet exit. Conditions correspond to $Re_j = 2000$. From Megerian et al. (2007). 15

1.3 Comparison of the development along the shear layer of the fundamental and subharmonic modes as (a & b) momentum flux ratio is lowered for an $S = 1.00$ jet and (c & d) density ratio is lowered for a $J = 20$ jet. From Getsinger (2012). 17

1.4 (a) Power spectra (amplitude in dB) as measured at $s/D = 2.0$ in the $(J, S) = (5, 0.55)$ transverse jet shear layer at several normalized forcing amplitudes. The dashed lines represent the spectra of the forced shear layer, and the solid line represents the unforced shear layer spectra. Forcing is applied at $f_f = 2528$ Hz and the fundamental frequency is $f_0 = 2248$ Hz. (b) Forcing amplitude at which lock-in to the forcing frequency is achieved, as a function of forcing frequency f_f, for several values of J at $S = 0.55$. Data from Getsinger et al. (2012). 20

1.5 Comparison of high and low scales of segregation with constant intensity of segregation. Adapted from Kukukova et al. (2009). 23

1.6 The evolution of a mixing layer from (a) large, coherent structures to (b) smaller scales. From Koochesfahani and Dimotakis (1986). 24

1.7 Concentration probability density function of a jet in crossflow with increasing Reynolds number indicating increase in mixing. From Shan and Dimotakis (2006). 28

2.1 Variable density transverse jet wind tunnel, with associated data acquisition and optical diagnostic apparatus. One additional tunnel section, of identical dimensions, was situated downstream of the test section shown. 37

2.2 Alternative jet injectors studied: (a) flush nozzle (b) elevated nozzle (c) straight pipe. 38

2.3 Schematic of the basic excitation and imaging setup for stereo PIV and acetone PLIF measurements in the transverse jet wind tunnel test section. 41

2.4 An example of several steps in the PLIF image correction process: (a) The raw image, (b) Background subtracted (c) Flat-field corrected and warped (d) Laser sheet profile and absorption corrected. Data from Getsinger (2012) . . 50

3.1 Crossflow boundary Layer measurements for (a) $U_\infty = 0.909m/s$ and (b) $U_\infty = 7.48m/s$ at $(x/D, y/D) = (-0.5, 0)$. Solid line is Blasius solution. . . . 56

3.2 For the flush nozzle with $Re_j = 1900$, $S = 1.0$, and varying momentum flux ratios J, (a) Shear layer spectra at various locations s/D, (b) equivalent spectral contour plots with magnitude of instability strength (in dB) for various s/D locations and Strouhal numbers, and (c) scaled instantaneous spanwise vorticity field ω_y measured via PIV. Data for columns (a) and (b) are from Getsinger (2012). 59

3.3 Contour plots of upstream shear layer spectral characteristics with $Re_j = 1900$ and density ratio $S = 1.0$: (a) flush straight pipe injector (b) flush nozzle injector, and (c) elevated nozzle injector. Data are shown for varying momentum flux ratios $J = 41$, 20, 12, 8, and 2. Data for column (b) is from Getsinger (2012). 62

3.4 Centerplane (side) instantaneous acetone concentration fields of the JICF nearfield with $Re_j = 1900$ and density ratio $S = 1.00$: (a) flush straight pipe injector (b) flush nozzle injector, and (c) elevated nozzle injector. Data are shown for varying momentum flux ratios $J = 41$, 20, 12, 8, and 2. . . . 63

3.5 Cross-sectional jet slices at $x/D = 10.5$, visualized via acetone PLIF, with $Re_j = 1900$ and density ratio $S = 1.0$, averaged over 300 images: (a) flush straight pipe injector, (b) flush nozzle injector, and (c) elevated nozzle injector. A linear colormap is used. Data are shown for varying momentum flux ratios $J = 41$, 20, 12, 8, and 2. 66

3.6 Instantaneous cross-sectional jet slices at $x/D = 10.5$, visualized via acetone PLIF, with $Re_j = 1900$ and density ratio $S = 1.0$: (a) flush straight pipe injector, (b) flush nozzle injector, and (c) elevated nozzle injector. A linear colormap is used. Data are shown for varying momentum flux ratios $J = 41$, 20, 12, 8, and 2. 68

3.7 Instantaneous cross-sectional jet slices at $x/D = 10.5$, visualized via acetone PLIF, with $Re_j = 1900$ and density ratio $S = 1.0$, at a separate time distinct from the images in Figure 3.6: (a) flush straight pipe injector, (b) flush nozzle injector, and (c) elevated nozzle injector. A linear colormap is used. Data are shown for varying momentum flux ratios $J = 41$, 20, 12, 8, and 2. 69

3.8 Evolution of cross-sectional jet slices of the flush nozzle-generated JICF, visualized via acetone PLIF, with $Re_j = 1900$ and density ratio $S = 1.0$, averaged over 300 images at different downstream locations: (a) $x/D = 2.5$ (b) $x/D = 5.5$ and (c) $x/D = 10.5$. Data are shown for varying momentum flux ratios $J = 41$, 20, 12, 8, and 2. 71

3.9 Crossflow boundary layer velocity measurements via hotwire: (a) Velocity profile upstream of the jet nozzle, at $x/D = -5.0$ and $y/D = 0.0$; (b) Local streamwise velocity measured at several different locations relative to the tunnel wall ($z/D = 0.5, 1.0, 3.0$) at $x/D = -5.0$ with variable spanwise location y/D. Conditions correspond to crossflow velocity in the freestream $U_\infty = 1$ m/s, with the jet flow turned off. 72

3.10 Cross-sectional jet slices (location $x/D = 10.5$) visualized via acetone PLIF, with fixed $U_\infty = 1.01$ m/s, density ratio $S = 1.0$, averaged over 300 images: (a) flush nozzle injector and (b) elevated nozzle injector. Data are shown for varying momentum flux ratios and jet Reynolds numbers as given. 74

3.11 Cross-sectional jet slices at location $x/D = 10.5$, visualized via acetone PLIF, with fixed $J = 41$ and density ratio $S = 1.0$, averaged over 300 images for the flush nozzle-generated jet. A linear colormap is used. Data are shown for varying jet Reynolds numbers as indicated. 75

3.12 Cross-sectional jet slices at location $x/D = 10.5$, visualized via acetone PLIF, with fixed $J = 41$ and density ratio $S = 1.0$, averaged over 300 images for the elevated nozzle-generated jet. A linear colormap is used. Data are shown for varying jet Reynolds numbers as indicated. 76

3.13 Instantaneous centerplane ($y = 0$) jet slices of the flush nozzle-generated JICF nearfield, visualized via acetone PLIF, with $Re_j = 1900$ and density ratios: (a) $S = 1.00$, (b) $S = 0.55$, and (c) $S = 0.35$. Data are shown for varying momentum flux ratios $J = 41$, 20, 12, 8, and 5. 79

3.14 Cross-sectional jet slices for the flush nozzle-generated JICF at $x/D = 10.5$, visualized via acetone PLIF, with $Re_j = 1900$ and density ratios: (a) $S = 1.00$, (b) $S = 0.55$, and (c) $S = 0.35$. Images averaged over 300 snapshots. A linear colormap is used. Data are shown for varying momentum flux ratios $J = 41$, 20, 12, 8, and 5. 80

4.1 Mean scalar concentration image in the $y = 0$ centerplane, with colorbar values corresponding to local concentration C/C_o, for the $J = 20$, $S = 1.00$ transverse jet. Averaging takes place over 300 images. Green data points on this mean jet image show the loci of scalar maxima, while the blue line shows the power law curve fit, with corresponding normal (n) and trajectory s_c coordinates scaled by diameter D. Data from Getsinger (2012) 85

4.2 Scalar centerline trajectories of flush nozzle-injected transverse jets of various density ratios ($1.00 \geq S \geq 0.35$) and momentum flux ratios ($41 \geq J \geq 5$) as indicated. 87

4.3 Scalar centerline trajectories of $S = 1.00$ transverse jets injected from flush nozzle, elevated nozzle, and flush straight pipe injector configurations. Data shown for momentum flux ratios is the range $41 \geq J \geq 5$ as indicated. 89

4.4 Scalar centerline trajectories of $S = 1.00$ transverse jets for various momentum flux ratios. (a) flush nozzle injector (b) elevated nozzle injector (c) flush straight pipe injector. Data are shown for various physical coordinate scalings (D, JD, and $\sqrt{J}D$). 91

4.5 Maximum mean concentration decay trends along the scalar centerline trajectory coordinate s_c for equidensity transverse jets at various momentum flux ratios. (a) Flush nozzle injector (b) elevated nozzle injector (c) flush straight pipe injector. Data are shown for various physical coordinate scaling (D, JD, and $\sqrt{J}D$). 93

4.6 Maximum mean concentration decay as a function of centerline trajectory coordinate s_c/D for flush nozzle-injected transverse jets of various density ratios ($1.00 \geq S \geq 0.35$) and momentum flux ratios in the range $41 \geq J \geq 5$, as indicated above each plot. 95

4.7 Maximum mean concentration decay as a function of scalar centerline trajectory coordinate s_c/D for equidensity transverse jets injected from the flush nozzle, elevated nozzle, and flush straight pipe injector configurations, with momentum flux ratios in the range $41 \geq J \geq 5$, as indicated above each plot. 97

4.8 Top row: normalized mean jet spread, δ/D, in the jet trajectory normal direction, n, as a function of normalized centerline trajectory coordinate, s_c/D, for flush nozzle-injected, $S = 1.00$ transverse jets. Bottom row: mean jet spread visualization images for various threshold concentrations as indicated in the legend of the plots in the top row. Data shown for momentum flux ratios (a) J=41 (b) J=12 (c) J=5. 98

4.9 Mean spread and flame length visualization of the JICF with $Re_j = 1900$ and density ratio $S = 1.00$, transformed to the $s_c - n$ coordinate system and binarized according to a chosen target threshold concentration. (a) Flush straight pipe injector (b) flush nozzle injector, and (c) elevated nozzle injector. Data are shown for varying momentum flux ratios $J = 41$, 12, 8, and 5. Target threshold concentrations shown are $C/C_o \geq 0.05$ (black), $C/C_o \geq 0.10$ (red), $C/C_o \geq 0.15$ (blue), and $C/C_o \geq 0.20$ (green). 101

4.10 Mean spread and flame length visualization of the JICF with $Re_j = 1900$ injected from the flush nozzle at various density ratios, transformed to the $s_c - n$ coordinate system and binarized according to a chosen target threshold concentration. (a) $S = 1.00$, (b) $S = 0.55$, and (c) $S = 0.35$. Data are shown for varying momentum flux ratios $J = 41$, 12, 8, and 5. Target threshold concentrations shown are $C/C_o \geq 0.05$ (black), $C/C_o \geq 0.10$ (red), $C/C_o \geq 0.15$ (blue), and $C/C_o \geq 0.20$ (green). 102

4.11 $\hat{C}(x)/C_o$ variation with downstream distance x and momentum flux ratio J for the equidensity JICF with $Re_j = 1900$ injected from the three different injectors: (a) Flush Nozzle (b) Elevated Nozzle, and (c) Flush Pipe. $\hat{C}(x)/C_o$, as defined in Equation 4.3, is calculated with $A_{cs} = 18D \times 18D$ for all J and x/D. 104

4.12 Cross-sectional (constant x/D)-based unmixedness, U_{yz}, for equidensity flush nozzle-injected transverse jets, plotted against downstream coordinate x/D. U_{yz} was calculated by matching each instantaneous image's spatial mean to the spatial mean value of the temporal mean image at $x/D = 10.5$ for two different flow conditions: (a) $J = 2$ and (b) $J = 41$. Results are shown for various momentum flux ratios. . 106

4.13 Cross-sectional (constant x/D)-based PDF, for equidensity flush nozzle-injected transverse jets, plotted at various downstream coordinates x/D as indicated. PDF was calculated by matching each instantaneous image's spatial mean to the spatial mean value of the temporal mean image at $x/D = 10.5$ for two different flow conditions: $J = 2$ (top row) and $J = 41$ (bottom row). Results are shown for various momentum flux ratios. 107

4.14 Cross-sectional (constant x/D)-based unmixedness, U_{yz}, for equidensity transverse jets at various momentum flux ratios as indicated, plotted against downstream coordinate x/D. U_{yz} was calculated by matching each instantaneous image's spatial mean to the spatial mean value of the temporal mean image at $x/D = 10.5$ for the flush nozzle-injected, $S = 1.00$, $J = 2$ jet. Results are shown for two different injectors: (a) Elevated Nozzle, and (b) Flush Pipe. 108

4.15 Cross-sectional (constant x/D)-based PDF, for equidensity transverse jets, plotted for various downstream coordinates x/D and momentum flux ratios as indicated. PDF was calculated by matching each instantaneous image's spatial mean to the spatial mean value of the temporal mean image at $x/D = 10.5$ for the flush nozzle-injected, $S = 1.00$, $J = 2$ jet. Results are shown for two different injectors: Elevated Nozzle (top row) and Flush pipe (bottom row). 109

4.16 Cross-sectional (constant x/D)-based unmixedness, U_{yz}, for equidensity transverse jets at various momentum flux ratios as indicated, plotted against jet trajectory coordinate s_c/D. U_{yz} was calculated by matching each instantaneous image's spatial mean to the spatial mean value of the temporal mean image at $x/D = 10.5$ for the flush nozzle-injected, $S = 1.00$, $J = 2$ jet. Results are shown for three different injectors: (a) Flush Nozzle, (b) Elevated Nozzle, and (c) Flush Pipe. 110

4.17 Cross-sectional (constant $x/D = 10.5$)-based metrics: (a-c) spatial probability density function (PDF) and (d) Unmixedness U_{yz} for flush nozzle-injected transverse jets with density ratios $S = 1.00$, $S = 0.55$, and $S = 0.35$. Data are shown for various momentum flux ratios: (a) PDF, $J = 41$, (b) PDF, $J = 12$, (c) PDF, $J = 5$, and (d) U_{yz} vs. S for various J values. 111

4.18 (a) Instantaneous scalar centerline trajectory in the $y = 0$ centerplane of the transverse jet for $J = 20$ and $S = 1.00$. As in Fig. 4.1, the blue line shows the power law curve fit for the corresponding mean jet image. (b) Instantaneous image transformed into the s_c/D, n/D coordinate system with an example of a thin interrogation area slice centered at $s_c/D = 10$, of total width 0.25, used to evaluate centerplane Unmixedness $U_{c,sn}$. 113

4.19 (a) $U_{c,sn}$ and (b) $U_{c,xz}$ trends at various J for $S = 1.00$, flush nozzle-injected jets with two different reference mean values utilized for mean-matching. Reference mean values were extracted from the $J = 5$ (top row) and $J = 41$ (bottom row) data for the flush nozzle-injected, $S = 1.00$ transverse jet. 115

4.20 (a) $U_{c,sn}$ and (b) $U_{c,xz}$ trends at various J for $S = 1.00$ transverse jets. Data shown for the elevated nozzle (top row), and flush pipe injectors (bottom row). Reference mean value was extracted from the $J = 5$ data for the flush nozzle-injected, $S = 1.00$ transverse jet. 116

4.21 $U_{c,sn}$ variation along jet trajectory coordinate s_c/D for the momentum flux ratio range $41 \geq J \geq 5$. Data shown on log-log plots for $S = 1.00$ jets with $Re_j = 1900$ injected from the three different injectors: (a) Flush Nozzle (b) Elevated Nozzle, and (c) Flush Pipe. 118

4.22 Transformed-plane Unmixedness, $U_{c,sn}$, as a function of centerline trajectory coordinate s_c/D for flush nozzle-injected transverse jets at various density ratios S, with $41 \geq J \geq 5$ as indicated. 120

4.23 Instantaneous high-resolution centerplane (side view) acetone PLIF imaging of the $S = 1.00$, flush nozzle-generated JICF with varying momentum flux ratios in the range $41 \geq J \geq 5$ as indicated. 121

4.24 Instantaneous high-resolution centerplane (side view) acetone PLIF imaging of the $S = 0.35$, flush nozzle-generated JICF with varying momentum flux ratios in the range $41 \geq J \geq 5$ as indicated. 122

4.25 Transformed-plane Unmixedness, $U_{c,sn}$, as a function of centerline trajectory coordinate s_c/D for $S = 1.00$ transverse jets injected from flush nozzle, elevated nozzle, and flush pipe injectors, with $41 \geq J \geq 5$ as indicated. 124

4.26 Instantaneous high-resolution centerplane (side view) acetone PLIF imaging of the flush pipe-generated JICF with varying momentum flux ratios in the range $41 \geq J \geq 5$ as indicated. 125

4.27 $U_{c,sn}$ trends for flush nozzle-injected, equidensity transverse jets at various momentum flux ratios as indicated, plotted against jet trajectory coordinate s_c/D. Results are shown for (a) low resolution data used for the mixing study, and (b) high resolution data used for jet near-field visualization. 126

4.28 $U_{c,sn}$ trends for flush nozzle-injected, $S = 0.35$ transverse jets at various momentum flux ratios as indicated, plotted against jet trajectory coordinate s_c/D. Results are shown for (a) low resolution data used for the mixing study, and (b) high resolution data used for jet near-field visualization. 127

5.1 Instantaneous centerplane (side view) simultaneous PLIF/PIV imaging of $S = 1.00$, flush nozzle-generated JICF with varying momentum flux ratios: $J = 41$ (top row), $J = 12$ (middle row), $J = 5$ (bottom row). Data shown for (a) scaled vorticity $\omega_y/(U_j/D)$ and (b) scaled jet fluid concentration gradient magnitude $|\nabla C|^2/(C_o/D)^2$. 131

5.2 Instantaneous centerplane (side view) simultaneous PLIF/PIV imaging of $S = 0.35$, flush nozzle-generated JICF with varying momentum flux ratios: $J = 41$ (top row), $J = 12$ (middle row), $J = 5$ (bottom row). Data shown for (a) scaled vorticity $\omega_y/(U_j/D)$ and (b) scaled jet fluid concentration gradient magnitude $|\nabla C|^2/(C_o/D)^2$. 132

5.3 Instantaneous centerplane (side view) simultaneous PLIF/PIV imaging of $S = 1.00$, flush pipe-generated JICF with varying momentum flux ratios: $J = 41$ (top row), $J = 12$ (middle row), $J = 5$ (bottom row). Data shown for (a) scaled vorticity $\omega_y/(U_j/D)$ and (b) scaled jet fluid concentration gradient magnitude $|\nabla C|^2/(C_o/D)^2$. 133

5.4 PIV POD mode structures extracted from instantaneous centerplane (side view) simultaneous PLIF/PIV imaging of $S = 1.00$, flush nozzle-generated JICF with varying momentum flux ratios: (a) $J = 41$, (b) $J = 12$, (c) $J = 5$. Data shown for Mode 1 (first row), Mode 2 (second row), Mode 3 (third row), Mode 4 (fourth row). Arrows in images indicate in-plane velocity component structure contribution, while colormap indicates out-of-plane velocity component structure contribution. Percent of total kinetic energy (KE) contributed by each mode is indicated below each image. 136

5.5 PLIF POD mode structures extracted from instantaneous centerplane (side view) simultaneous PLIF/PIV imaging of $S = 1.00$, flush nozzle-generated JICF with varying momentum flux ratios: (a) $J = 41$, (b) $J = 12$, (c) $J = 5$. Data shown for Mode 1 (first row), Mode 2 (second row), Mode 3 (third row), Mode 4 (fourth row). Percent of total scalar fluctuation energy (SE) contributed by each mode is indicated below each image. 137

5.6 (a) PIV POD and (b) PLIF POD coefficients for the first two modes plotted against each other. POD analysis extracted from instantaneous centerplane (side view) simultaneous PLIF/PIV imaging of $S = 1.00$, flush nozzle-generated JICF with varying momentum flux ratios: $J = 41$ (top row), $J = 12$ (middle row), $J = 5$ (bottom row). 138

5.7 PIV POD mode structures extracted from instantaneous centerplane (side view) simultaneous PLIF/PIV imaging of $S = 0.35$, flush nozzle-generated JICF with varying momentum flux ratios: (a) $J = 41$, (b) $J = 12$, (c) $J = 5$. Data shown for Mode 1 (first row), Mode 2 (second row), Mode 3 (third row), Mode 4 (fourth row). Arrows in images indicate in-plane velocity component structure contribution, while colormap indicates out-of-plane velocity component structure contribution. Percent of total velocity fluctuation energy (VE) contributed by each mode is indicated below each image. 140

5.8 PLIF POD mode structures extracted from instantaneous centerplane (side view) simultaneous PLIF/PIV imaging of $S = 0.35$, flush nozzle-generated JICF with varying momentum flux ratios: (a) $J = 41$, (b) $J = 12$, (c) $J = 5$. Data shown for Mode 1 (first row), Mode 2 (second row), Mode 3 (third row), Mode 4 (fourth row). Percent of total scalar fluctuation energy (SE) contributed by each mode is indicated below each image. 141

5.9 PIV POD mode structures extracted from instantaneous centerplane (side view) simultaneous PLIF/PIV imaging of $S = 1.00$, flush pipe-generated JICF with varying momentum flux ratios: (a) $J = 41$, (b) $J = 12$, (c) $J = 5$. Data shown for Mode 1 (first row), Mode 2 (second row), Mode 3 (third row), Mode 4 (fourth row). Arrows in images indicate in-plane velocity component structure contribution, while colormap indicates out-of-plane velocity component structure contribution. Percent of total kinetic energy (KE) contributed by each mode is indicated below each image. 143

5.10 PLIF POD mode structures extracted from instantaneous centerplane (side view) simultaneous PLIF/PIV imaging of $S = 1.00$, flush pipe-generated JICF with varying momentum flux ratios: (a) $J = 41$, (b) $J = 12$, (c) $J = 5$. Data shown for Mode 1 (first row), Mode 2 (second row), Mode 3 (third row), Mode 4 (fourth row). Percent of total scalar fluctuation energy (SE) contributed by each mode is indicated below each image. 144

5.11 Example scalar field (C/C_o) image in $x-z$ coordinate system with mean jet trajectory overlapped onto image (a), transformed scalar field image in s_c-n coordinate system (b), and transformed scalar dissipation rate (χ) image used to track mixing layer location with upstream mixing layer overlapped onto image (c). Data shown for flush nozzle-injected, $S = 1.00$, $J = 12$ transverse jet. 145

5.12 Mixing layer average maximum scalar dissipation rate $\overline{\chi}$ and average minimum principal compressive strain rate $\overline{\epsilon}_{min}$ of $S = 1.00$, flush nozzle-injected transverse jets with $J = 41$, $J = 12$, and $J = 5$ as indicated below each plot. Data shown for (a) upstream mixing layer, and (b) downstream mixing layer. 147

5.13 Mixing layer average maximum scalar dissipation rate $\overline{\chi}$ and average minimum principal compressive strain rate $\overline{\epsilon}_{min}$ of $S = 1.00$, flush pipe-injected transverse jets with $J = 41$, $J = 12$, and $J = 5$ as indicated below each plot. Data shown for (a) upstream mixing layer, and (b) downstream mixing layer. 148

5.14 Magnitude of average angle difference, $|\alpha|$, between the minimum principal compressive strain axis, and the maximum scalar gradient vector. Data shown for both the upstream mixing layer (UML) and downstream mixing layer (DML) of flush nozzle-injected, and flush pipe-injected, $S = 1.00$ transverse jets with (a) $J = 41$, (b) $J = 12$, and (c) $J = 5$. 149

5.15 Mixing layer average maximum scalar dissipation rate, $\overline{\chi}$, and average strain rate normal to the scalar gradient direction, $\overline{\epsilon}$, of $S = 1.00$, flush nozzle-injected transverse jets with $J = 41$, $J = 12$, and $J = 5$ as indicated below each plot. Data shown for (a) upstream mixing layer, and (b) downstream mixing layer. Data points with extensive strain in the scalar gradient direction are removed from averaging process. 152

5.16 Mixing layer average maximum scalar dissipation rate, $\overline{\chi}$, and average strain rate normal to the scalar gradient direction, $\overline{\epsilon}$, of $S = 1.00$, flush pipe-injected transverse jets with $J = 41$, $J = 12$, and $J = 5$ as indicated below each plot. Data shown for (a) upstream mixing layer, and (b) downstream mixing layer. Data points with extensive strain in the scalar gradient direction are removed from averaging process. 153

5.17 Example error function fits for flush-nozzle injected, $S = 1.00$, $J = 5$ transverse jets. Data shown for (a) PLIF portion of simultaneous PLIF/PIV, and (b) high-resolution PLIF measurements. 154

5.18 Average strain rate on the mixing layer calculated from scalar measurements using Equation 1.13, and average strain rate extracted from PIV in the direction normal to the scalar gradient direction, of $S = 1.00$, flush nozzle-injected transverse jets with $J = 41$, $J = 12$, and $J = 5$ as indicated below each plot. Data shown for (a) upstream mixing layer, and (b) downstream mixing layer. Data points with extensive strain in the scalar gradient direction are removed from averaging process. 157

5.19 Average strain rate on the mixing layer calculated from scalar measurements using Equation 1.13, and average strain rate extracted from PIV in the direction normal to the scalar gradient direction, of $S = 1.00$, flush pipe-injected transverse jets with $J = 41$, $J = 12$, and $J = 5$ as indicated below each plot. Data shown for (a) upstream mixing layer, and (b) downstream mixing layer. Data points with extensive strain in the scalar gradient direction are removed from averaging process. 158

5.20 Average scalar dissipation rate comparison between high resolution PLIF imaging data, and PLIF portion of simultaneous PLIF/PIV measurements. Data shown for $S = 1.00$, flush nozzle-injected transverse jets with (a) $J = 41$, and (b) $J = 5$. . . 160

5.21 Average strain rate comparison between high resolution PLIF imaging data, and PLIF portion of simultaneous PLIF/PIV measurements. Data shown for $S = 1.00$, flush nozzle-injected transverse jets with (a) $J = 41$, and (b) $J = 5$. 160

5.22 Resolution-corrected strain rates calculated from high-resolution PLIF measurements. Data shown for $S = 1.00$, flush nozzle-injected transverse jets with (a) $J = 41$, and (b) $J = 5$. 161

A.1 Mean cross-sectional scalar field visualization at (a) $x/D = 2.5$, (b) $x/D = 5.5$, and (a) $x/D = 10.5$ for $S = 1.00$, flush nozzle-generated JICF with varying momentum flux ratios: $J = 41$ (top row), $J = 30$ (middle row), $J = 20$ (bottom row). Colormap linearly scaled to maximum value within FOV. Quantitative C/C_o values only given when fluorescence data was scalable to jet fluid concentration. 167

A.2 Mean cross-sectional scalar field visualization at (a) $x/D = 2.5$, (b) $x/D = 5.5$, and (a) $x/D = 10.5$ for $S = 1.00$, flush nozzle-generated JICF with varying momentum flux ratios: $J = 12$ (top row), $J = 10$ (middle row), $J = 8$ (bottom row). Colormap linearly scaled to maximum value within FOV. Quantitative C/C_o values only given when fluorescence data was scalable to jet fluid concentration. 168

A.3 Mean cross-sectional scalar field visualization at (a) $x/D = 2.5$, (b) $x/D = 5.5$, and (a) $x/D = 10.5$ for $S = 1.00$, flush nozzle-generated JICF with varying momentum flux ratios: $J = 5$ (top row), $J = 2$ (bottom row). Colormap linearly scaled to maximum value within FOV. Quantitative C/C_o values only given when fluorescence data was scalable to jet fluid concentration. 169

A.4 Mean cross-sectional scalar field visualization at (a) $x/D = 2.5$, (b) $x/D = 5.5$, and (a) $x/D = 10.5$ for $S = 0.55$, flush nozzle-generated JICF with varying momentum flux ratios: $J = 41$ (top row), $J = 30$ (middle row), $J = 20$ (bottom row). Colormap linearly scaled to maximum value within FOV. Quantitative C/C_o values only given when fluorescence data was scalable to jet fluid concentration. 170

A.5 Mean cross-sectional scalar field visualization at (a) $x/D = 2.5$, (b) $x/D = 5.5$, and (a) $x/D = 10.5$ for $S = 0.55$, flush nozzle-generated JICF with varying momentum flux ratios: $J = 12$ (top row), $J = 10$ (middle row), $J = 8$ (bottom row). Colormap linearly scaled to maximum value within FOV. Quantitative C/C_o values only given when fluorescence data was scalable to jet fluid concentration. 171

A.6 Mean cross-sectional scalar field visualization at (a) $x/D = 2.5$, (b) $x/D = 5.5$, and (a) $x/D = 10.5$ for $S = 0.55$, flush nozzle-generated JICF with varying momentum flux ratios: $J = 5$ (top row), $J = 2$ (bottom row). Colormap linearly scaled to maximum value within FOV. Quantitative C/C_o values only given when fluorescence data was scalable to jet fluid concentration. 172

A.7 Mean cross-sectional scalar field visualization at (a) $x/D = 2.5$, (b) $x/D = 5.5$, and (a) $x/D = 10.5$ for $S = 0.35$, flush nozzle-generated JICF with varying momentum flux ratios: $J = 41$ (top row), $J = 30$ (middle row), $J = 20$ (bottom row). Colormap linearly scaled to maximum value within FOV. Quantitative C/C_o values only given when fluorescence data was scalable to jet fluid concentration. 173

A.8 Mean cross-sectional scalar field visualization at (a) $x/D = 2.5$, (b) $x/D = 5.5$, and (a) $x/D = 10.5$ for $S = 0.35$, flush nozzle-generated JICF with varying momentum flux ratios: $J = 12$ (top row), $J = 10$ (middle row), $J = 8$ (bottom row). Colormap linearly scaled to maximum value within FOV. Quantitative C/C_o values only given when fluorescence data was scalable to jet fluid concentration. 174

A.9 Mean cross-sectional scalar field visualization at (a) $x/D = 2.5$, (b) $x/D = 5.5$, and (a) $x/D = 10.5$ for $S = 0.35$, flush nozzle-generated JICF with $J = 5$. Colormap linearly scaled to maximum value within FOV. Quantitative C/C_o values only given when fluorescence data was scalable to jet fluid concentration. 175

A.10 Mean cross-sectional scalar field visualization at (a) $x/D = 2.5$, (b) $x/D = 5.5$, and (a) $x/D = 10.5$ for $S = 1.00$, elevated nozzle-generated JICF with varying momentum flux ratios: $J = 41$ (top row), $J = 30$ (middle row), $J = 20$ (bottom row). Colormap linearly scaled to maximum value within FOV. Quantitative C/C_o values only given when fluorescence data was scalable to jet fluid concentration. . 176

A.11 Mean cross-sectional scalar field visualization at (a) $x/D = 2.5$, (b) $x/D = 5.5$, and (a) $x/D = 10.5$ for $S = 1.00$, elevated nozzle-generated JICF with varying momentum flux ratios: $J = 12$ (top row), $J = 10$ (middle row), $J = 8$ (bottom row). Colormap linearly scaled to maximum value within FOV. Quantitative C/C_o values only given when fluorescence data was scalable to jet fluid concentration. . 177

A.12 Mean cross-sectional scalar field visualization at (a) $x/D = 2.5$, (b) $x/D = 5.5$, and (a) $x/D = 10.5$ for $S = 1.00$, elevated nozzle-generated JICF with varying momentum flux ratios: $J = 5$ (top row), $J = 2$ (bottom row). Colormap linearly scaled to maximum value within FOV. Quantitative C/C_o values only given when fluorescence data was scalable to jet fluid concentration. 178

A.13 Mean cross-sectional scalar field visualization at (a) $x/D = 2.5$, (b) $x/D = 5.5$, and (a) $x/D = 10.5$ for $S = 1.00$, flush pipe-generated JICF with varying momentum flux ratios: $J = 41$ (top row), $J = 30$ (middle row), $J = 20$ (bottom row). Colormap linearly scaled to maximum value within FOV. Quantitative C/C_o values only given when fluorescence data was scalable to jet fluid concentration. 179

A.14 Mean cross-sectional scalar field visualization at (a) $x/D = 2.5$, (b) $x/D = 5.5$, and (a) $x/D = 10.5$ for $S = 1.00$, flush pipe-generated JICF with varying momentum flux ratios: $J = 12$ (top row), $J = 10$ (middle row), $J = 8$ (bottom row). Colormap linearly scaled to maximum value within FOV. Quantitative C/C_o values only given when fluorescence data was scalable to jet fluid concentration. 180

A.15 Mean cross-sectional scalar field visualization at (a) $x/D = 2.5$, (b) $x/D = 5.5$, and (a) $x/D = 10.5$ for $S = 1.00$, flush pipe-generated JICF with varying momentum flux ratios: $J = 5$ (top row), $J = 2$ (bottom row). Colormap linearly scaled to maximum value within FOV. Quantitative C/C_o values only given when fluorescence data was scalable to jet fluid concentration. 181

B.1 Instantaneous centerplane (side view) acetone PLIF imaging of $S = 1.00$, flush nozzle-generated JICF with varying momentum flux ratios: (a) $J = 41$, (b) $J = 30$, (c) $J = 20$, (d) $J = 12$. Data shown in logarithmic scale. 183

B.2 Instantaneous centerplane (side view) acetone PLIF imaging of $S = 1.00$, flush nozzle-generated JICF with varying momentum flux ratios: (a) $J = 10$, (b) $J = 8$, (c) $J = 5$, (d) $J = 2$. Data shown in logarithmic scale. 184

B.3 Instantaneous centerplane (side view) acetone PLIF imaging of $S = 0.55$, flush nozzle-generated JICF with varying momentum flux ratios: (a) $J = 41$, (b) $J = 30$, (c) $J = 20$, (d) $J = 12$. Data shown in logarithmic scale. 185

B.4 Instantaneous centerplane (side view) acetone PLIF imaging of $S = 0.55$, flush nozzle-generated JICF with varying momentum flux ratios: (a) $J = 10$, (b) $J = 8$, (c) $J = 5$, (d) $J = 2$. Data shown in logarithmic scale. 186

B.5 Instantaneous centerplane (side view) acetone PLIF imaging of $S = 0.35$, flush nozzle-generated JICF with varying momentum flux ratios: (a) $J = 41$, (b) $J = 30$, (c) $J = 20$, (d) $J = 12$. Data shown in logarithmic scale. 187

B.6 Instantaneous centerplane (side view) acetone PLIF imaging of $S = 0.35$, flush nozzle-generated JICF with varying momentum flux ratios: (a) $J = 10$, (b) $J = 8$, (c) $J = 5$. Data shown in logarithmic scale. 188

B.7 Instantaneous centerplane (side view) acetone PLIF imaging of $S = 1.00$, flush pipe-generated JICF with varying momentum flux ratios: (a) $J = 41$, (b) $J = 30$, (c) $J = 20$, (d) $J = 12$. Data shown in logarithmic scale. 189

B.8 Instantaneous centerplane (side view) acetone PLIF imaging of $S = 1.00$, flush pipe-generated JICF with varying momentum flux ratios: (a) $J = 10$, (b) $J = 8$, (c) $J = 5$, (d) $J = 2$. Data shown in logarithmic scale. 190

B.9 Instantaneous centerplane (side view) acetone PLIF imaging of $S = 1.00$, elevated nozzle-generated JICF with varying momentum flux ratios: (a) $J = 41$, (b) $J = 30$, (c) $J = 20$, (d) $J = 12$. Data shown in logarithmic scale. 191

B.10 Instantaneous centerplane (side view) acetone PLIF imaging of $S = 1.00$, elevated nozzle-generated JICF with varying momentum flux ratios: (a) $J = 10$, (b) $J = 8$, (c) $J = 5$, (d) $J = 2$. Data shown in logarithmic scale. 192

B.11 Mean centerplane (side view) acetone PLIF imaging of $S = 1.00$, flush nozzle-generated JICF with varying momentum flux ratios: (a) $J = 41$, (b) $J = 30$, (c) $J = 20$, (d) $J = 12$. Data shown in logarithmic scale. 193

B.12 Mean centerplane (side view) acetone PLIF imaging of $S = 1.00$, flush nozzle-generated JICF with varying momentum flux ratios: (a) $J = 10$, (b) $J = 8$, (c) $J = 5$, (d) $J = 2$. Data shown in logarithmic scale. 194

B.13 Mean centerplane (side view) acetone PLIF imaging of $S = 0.55$, flush nozzle-generated JICF with varying momentum flux ratios: (a) $J = 41$, (b) $J = 30$, (c) $J = 20$, (d) $J = 12$. Data shown in logarithmic scale. 195

B.14 Mean centerplane (side view) acetone PLIF imaging of $S = 0.55$, flush nozzle-generated JICF with varying momentum flux ratios: (a) $J = 10$, (b) $J = 8$, (c) $J = 5$, (d) $J = 2$. Data shown in logarithmic scale. 196

B.15 Mean centerplane (side view) acetone PLIF imaging of $S = 0.35$, flush nozzle-generated JICF with varying momentum flux ratios: (a) $J = 41$, (b) $J = 30$, (c) $J = 20$, (d) $J = 12$. Data shown in logarithmic scale. 197

B.16 Mean centerplane (side view) acetone PLIF imaging of $S = 0.35$, flush nozzle-generated JICF with varying momentum flux ratios: (a) $J = 10$, (b) $J = 8$, (c) $J = 5$. Data shown in logarithmic scale. 198

B.17 Mean centerplane (side view) acetone PLIF imaging of $S = 1.00$, flush pipe-generated JICF with varying momentum flux ratios: (a) $J = 41$, (b) $J = 30$, (c) $J = 20$, (d) $J = 12$. Data shown in logarithmic scale. 199

B.18 Mean centerplane (side view) acetone PLIF imaging of $S = 1.00$, flush pipe-generated JICF with varying momentum flux ratios: (a) $J = 10$, (b) $J = 8$, (c) $J = 5$, (d) $J = 2$. Data shown in logarithmic scale. 200

B.19 Mean centerplane (side view) acetone PLIF imaging of $S = 1.00$, elevated nozzle-generated JICF with varying momentum flux ratios: (a) $J = 41$, (b) $J = 30$, (c) $J = 20$, (d) $J = 12$. Data shown in logarithmic scale. 201

B.20 Mean centerplane (side view) acetone PLIF imaging of $S = 1.00$, elevated nozzle-generated JICF with varying momentum flux ratios: (a) $J = 10$, (b) $J = 8$, (c) $J = 5$, (d) $J = 2$. Data shown in logarithmic scale. 202

C.1 Instantaneous high-resolution centerplane (side view) acetone PLIF imaging of $S = 1.00$, flush nozzle-generated JICF with (a) $J = 30$, (b) $J = 20$, (c) $J = 10$, (d) $J = 2$. 204

C.2 Instantaneous high-resolution centerplane (side view) acetone PLIF imaging of $S = 0.35$, flush nozzle-generated JICF with (a) $J = 30$, (b) $J = 20$, (c) $J = 10$. 205

C.3 Instantaneous high-resolution centerplane (side view) acetone PLIF imaging of $S = 1.00$, flush pipe-generated JICF with varying momentum flux ratios (a) $J = 30$, (b) $J = 20$, (c) $J = 10$, (d) $J = 2$. 206

D.1 Instantaneous centerplane (side view) simultaneous PLIF/PIV imaging of $S = 1.00$, flush nozzle-generated JICF with varying momentum flux ratios: $J = 41$ (top row), $J = 30$ (middle row), $J = 20$ (bottom row). Data shown for (a) scaled vorticity $\omega_y/(U_j/D)$ and (b) scaled jet fluid concentration gradient magnitude $|\nabla C|^2/(C_o/D)^2$. 208

D.2 Instantaneous centerplane (side view) simultaneous PLIF/PIV imaging of $S = 1.00$, flush nozzle-generated JICF with varying momentum flux ratios: $J = 12$ (top row), $J = 10$ (middle row), $J = 8$ (bottom row). Data shown for (a) scaled vorticity $\omega_y/(U_j/D)$ and (b) scaled jet fluid concentration gradient magnitude $|\nabla C|^2/(C_o/D)^2$. 209

D.3 Instantaneous centerplane (side view) simultaneous PLIF/PIV imaging of $S = 1.00$, flush nozzle-generated JICF with varying momentum flux ratios: $J = 5$ (top row), $J = 2$ (bottom row). Data shown for (a) scaled vorticity $\omega_y/(U_j/D)$ and (b) scaled jet fluid concentration gradient magnitude $|\nabla C|^2/(C_o/D)^2$. 210

D.4 Instantaneous centerplane (side view) simultaneous PLIF/PIV imaging of $S = 0.35$, flush nozzle-generated JICF with varying momentum flux ratios: $J = 41$ (top row), $J = 30$ (middle row), $J = 20$ (bottom row). Data shown for (a) scaled vorticity $\omega_y/(U_j/D)$ and (b) scaled jet fluid concentration gradient magnitude $|\nabla C|^2/(C_o/D)^2$. 211

D.5 Instantaneous centerplane (side view) simultaneous PLIF/PIV imaging of $S = 0.35$, flush nozzle-generated JICF with varying momentum flux ratios: $J = 12$ (top row), $J = 10$ (middle row), $J = 8$ (bottom row). Data shown for (a) scaled vorticity $\omega_y/(U_j/D)$ and (b) scaled jet fluid concentration gradient magnitude $|\nabla C|^2/(C_o/D)^2$. 212

D.6 Instantaneous centerplane (side view) simultaneous PLIF/PIV imaging of $S = 0.35$, flush nozzle-generated JICF with $J = 5$. Data shown for (a) scaled vorticity $\omega_y/(U_j/D)$ and (b) scaled jet fluid concentration gradient magnitude $|\nabla C|^2/(C_o/D)^2$. 213

D.7 Instantaneous centerplane (side view) simultaneous PLIF/PIV imaging of $S = 1.00$, flush pipe-generated JICF with varying momentum flux ratios: $J = 41$ (top row), $J = 30$ (middle row), $J = 20$ (bottom row). Data shown for (a) scaled vorticity $\omega_y/(U_j/D)$ and (b) scaled jet fluid concentration gradient magnitude $|\nabla C|^2/(C_o/D)^2$. 214

D.8 Instantaneous centerplane (side view) simultaneous PLIF/PIV imaging of $S = 1.00$, flush pipe-generated JICF with varying momentum flux ratios: $J = 12$ (top row), $J = 10$ (middle row), $J = 8$ (bottom row). Data shown for (a) scaled vorticity $\omega_y/(U_j/D)$ and (b) scaled jet fluid concentration gradient magnitude $|\nabla C|^2/(C_o/D)^2$. 215

D.9 Instantaneous centerplane (side view) simultaneous PLIF/PIV imaging of $S = 1.00$, flush pipe-generated JICF with varying momentum flux ratios: $J = 5$ (top row), $J = 2$ (bottom row). Data shown for (a) scaled vorticity $\omega_y/(U_j/D)$ and (b) scaled jet fluid concentration gradient magnitude $|\nabla C|^2/(C_o/D)^2$. 216

D.10 Instantaneous centerplane velocity field visualization for $S = 1.00$, flush nozzle-generated JICF with varying momentum flux ratios in the range $41 \geq J \geq 12$ as indicated below each image. Data shown for (a) u_x/U_∞, (b) u_y/U_j, and (c) u_z/U_j. Black line corresponds to delineation between positive and negative values. 217

D.11 Instantaneous centerplane velocity field visualization for $S = 1.00$, flush nozzle-generated JICF with varying momentum flux ratios in the range $10 \geq J \geq 2$ as indicated below each image. Data shown for (a) u_x/U_∞, (b) u_y/U_j, and (c) u_z/U_j. Black line corresponds to delineation between positive and negative values. 218

D.12 Instantaneous centerplane velocity field visualization for $S = 1.00$, flush pipe-generated JICF with varying momentum flux ratios in the range $41 \geq J \geq 12$ as indicated below each image. Data shown for (a) u_x/U_∞, (b) u_y/U_j, and (c) u_z/U_j. Black line corresponds to delineation between positive and negative values. 219

D.13 Instantaneous centerplane velocity field visualization for $S = 1.00$, flush pipe-generated JICF with varying momentum flux ratios in the range $10 \geq J \geq 2$ as indicated below each image. Data shown for (a) u_x/U_∞, (b) u_y/U_j, and (c) u_z/U_j. Black line corresponds to delineation between positive and negative values. 220

D.14 Instantaneous centerplane velocity field visualization for $S = 0.35$, flush nozzle-generated JICF with varying momentum flux ratios in the range $41 \geq J \geq 12$ as indicated below each image. Data shown for (a) u_x/U_∞, (b) u_y/U_j, and (c) u_z/U_j. Black line corresponds to delineation between positive and negative values. 221

D.15 Instantaneous centerplane velocity field visualization for $S = 0.35$, flush nozzle-generated JICF with varying momentum flux ratios in the range $10 \geq J \geq 5$ as indicated below each image. Data shown for (a) u_x/U_∞, (b) u_y/U_j, and (c) u_z/U_j. Black line corresponds to delineation between positive and negative values. 222

D.16 Mean centerplane velocity field visualization for $S = 1.00$, flush nozzle-generated JICF with varying momentum flux ratios in the range $41 \geq J \geq 12$ as indicated below each image. Data shown for (a) u_x/U_∞, (b) u_y/U_j, and (c) u_z/U_j. Black line corresponds to delineation between positive and negative values. 223

D.17 Mean centerplane velocity field visualization for $S = 1.00$, flush nozzle-generated JICF with varying momentum flux ratios in the range $10 \geq J \geq 2$ as indicated below each image. Data shown for (a) u_x/U_∞, (b) u_y/U_j, and (c) u_z/U_j. Black line corresponds to delineation between positive and negative values. 224

D.18 Mean centerplane velocity field visualization for $S = 1.00$, flush pipe-generated JICF with varying momentum flux ratios in the range $41 \geq J \geq 12$ as indicated below each image. Data shown for (a) u_x/U_∞, (b) u_y/U_j, and (c) u_z/U_j. Black line corresponds to delineation between positive and negative values. 225

D.19 Mean centerplane velocity field visualization for $S = 1.00$, flush pipe-generated JICF with varying momentum flux ratios in the range $10 \geq J \geq 2$ as indicated below each image. Data shown for (a) u_x/U_∞, (b) u_y/U_j, and (c) u_z/U_j. Black line corresponds to delineation between positive and negative values. 226

D.20 Mean centerplane velocity field visualization for $S = 0.35$, flush nozzle-generated JICF with varying momentum flux ratios in the range $41 \geq J \geq 12$ as indicated below each image. Data shown for (a) u_x/U_∞, (b) u_y/U_j, and (c) u_z/U_j. Black line corresponds to delineation between positive and negative values. 227

D.21 Mean centerplane velocity field visualization for $S = 0.35$, flush nozzle-generated JICF with varying momentum flux ratios in the range $10 \geq J \geq 5$ as indicated below each image. Data shown for (a) u_x/U_∞, (b) u_y/U_j, and (c) u_z/U_j. Black line corresponds to delineation between positive and negative values. 228

List of Tables

3.1 Governing flow parameter ranges explored in this experiment. Here, θ_∞ is the crossflow boundary layer momentum thickness, measured on the centerplane of the jet, 5 diameters upstream of the center of the jet exit at $(x/D, y/D) = (-5, 0)$. 55

Nomenclature

A_{cs}	Cross-sectional area of the control surface containing all of the jet fluid at a downstream location x
A_i	Interrogation area utilized in cross-sectional mixing metric quantification
A_{jet}	Cross-sectional area of the jet
C/C_o	Concentration of jet fluid
$\hat{C}/C_o$	Mean concentration of jet fluid over A_{cs}
$\overline{C}/C_o$	Reference mean jet fluid concentration used for determination of A_i
D	Jet nozzle diameter or molecular mass diffusivity
Da	Damköhler number
DC	Duty cycle of square wave forcing (pulse width/period)
ϵ	Strain rate
f_f	Applied jet forcing frequency
f_h	Horseshoe vortex instability frequency
f_0	Natural (fundamental) frequency of jet shear layer instability
L/D	Non-dimensional stroke ratio related to vortex ring formation, or length to diameter ratio
J	Jet-to-crossflow momentum flux ratio, $\rho_j {U_j}^2/\rho_\infty {U_\infty}^2$
J_{cr}	Critical jet-to-crossflow momentum flux ratio at which bifurcation to a global mode occurs
n	Spatial coordinate normal to the jet fluid concentration centerline trajectory
n_l	Spatial coordinate parallel to the scalar gradient vector direction
$\dot{Q}$	Volumetric flow rate
R	Jet-to-crossflow velocity ratio, U_j/U_∞
Re_j	Jet Reynolds number, based on mean jet velocity and nozzle diameter D
Re_∞	Crossflow Reynolds number, based on freestream crossflow velocity and nozzle diameter D

s	Spatial coordinate along the center of the upstream shear layer
s_c	Spatial coordinate along the jet fluid concentration centerline trajectory
S	Jet-to-crossflow density ratio ρ_j/ρ_∞
Sc	Schmidt number
SMD	Spatial mixing deficiency
St	Strouhal number based on diameter, fD/U_j
T	Period of acoustic forcing, or temperature
U_j	Mean jet velocity
u'_{rms}	Root mean square of the jet velocity perturbation
U_∞	Freestream crossflow velocity
U	Cross-sectional Unmixedness
U_c	Centerplane Unmixedness
x, y, z	Downstream, spanwise, and axial coordinates measured from jet orifice (see Fig. 1.1)
χ	Mole fraction or scalar dissipation rate
λ_D	Scalar diffusion scale
θ	Momentum thickness
τ	Temporal pulse width of applied square wave jet excitation
ζ	Mixture fraction

Acknowledgments

This work would not have been possible had it not been for the support and guidance of several individuals and groups. I would first like to thank my advisor, Professor Ann Karagozian. She is one of the most intelligent, caring, and helpful individuals I have ever met, and the lessons I learned from her have had an invaluable impact on my life. I would also like to thank my co-advisor, Professor Owen Smith, for guiding the experimental work and imparting his wisdom gained from decades of experimental research experience. Thanks are also in order for Professor Robert M'Closkey and Professor Luminita Vese for their helpful and encouraging comments on my work, and for Professor Luca Cortelezzi for his insights as well.

I have had a great experience working in the Energy and Propulsion Research Laboratory, and my labmates have made my time at UCLA both productive and memorable. I would like to thank Dr. Daniel Getsinger for taking the time to show me how to think like an experimental researcher, and for being a sounding board for many of my ideas. Thanks also to Takeshi for his significant assistance with this work, and to Terry, Dario, Andrea, Cory, Aaron, Jennifer, Sarah, Jeff, Cris, Phuoc Hai, Brett, and Andres for their assistance as well.

I would not have had the opportunities I've had in my life if it wasn't for the love and support of my father, Eduard, and my mother, Lamara. I thank them for working so hard to give me a chance to better myself, and I am forever grateful for their many sacrifices. Thank you to my brother as well, and to my extended family for their love and kindness.

This research has been supported by the National Science Foundation under grants CBET-1133015 and CBET-1437014, and by the Air Force Office of Scientific Research under grant FA9550-11-1-0128 and DURIP grant FA9550-10-1-0461.

Vita

2009-2010	Undergraduate Research Assistant, California State University, Northridge, Mechanical Engineering Department. Northridge, CA.
2010	B.S. (Mechanical Engineering), Summa Cum Laude, California State University, Northridge. Northridge, CA
2010-2011	Departmental Graduate Student Fellowship, UCLA Mechanical and Aerospace Engineering Department.
2011	Graduate Teaching Assistant, UCLA. MAE 103 - Elementary Fluid Mechanics.
2011	Graduate Teaching Assistant, UCLA. MAE 150P - Aircraft Propulsion Systems.
2011-2012	Outstanding Teaching Assistant Award, UCLA Mechanical and Aerospace Engineering Department.
2012	M.S. (Mechanical Engineering), UCLA
2013	Graduate Teaching Assistant, UCLA. MAE 150P - Aircraft Propulsion Systems.
2010-2015	Graduate Student Researcher, UCLA Energy and Propulsion Research Laboratory. Los Angeles, CA

Publications and Presentations

L. Gevorkyan, T. Shoji, O. Smith, and A. Karagozian, Transverse jet mixing efficiency characterization, submitted to The Journal of Fluid Mechanics.

D. Getsinger, L. Gevorkyan, O. Smith, and A. Karagozian, Structural and stability characteristics of jets in crossflow, Journal of Fluid Mechanics, 760, pp 342-367, December 2014.

L. Gevorkyan, T. Shoji, W. Y. Peng, D. Getsinger, O. Smith, and A. Karagozian, Mixing characteristics for flush and elevated jets in crossflow, 67th Annual Meeting of the American Physical Society Division of Fluid Dynamics, San Francisco, CA, November, 2014.

L. Gevorkyan, D. Getsinger, W. Y. Peng, T. Shoji, O. Smith, and A. Karagozian, Mixing characteristics of transitional transverse jets, 8th Southern California Symposium on Flow Physics, UCLA, April, 2014.

L. Gevorkyan, D. Getsinger, O. Smith, and A. Karagozian, Structural and stability characteristics of jets in crossflow, Paper AIAA-2014-0230, 52nd AIAA Aerospace Sciences Meeting/SciTech Forum, National Harbor, MD, January, 2014.

L. Gevorkyan, D. Getsinger, W. Y. Peng, O. Smith, and A. Karagozian, Structure, mixing, and stability of flush and elevated jets in crossflow, 66th Annual Meeting of the American Physical Society Division of Fluid Dynamics, Pittsburgh, PA, November 2013.

L. Gevorkyan, D. Getsinger, O. Smith, and A. Karagozian, Structural Symmetry and Asymmetry in Low Reynolds Number Jets In Crossflow, 7th Southern California Symposium on Flow Physics, Caltech, April 13, 2013.

L. Gevorkyan, D. Getsinger, O. Smith, and A. Karagozian, Mixing Characteristics of Convectively and Absolutely Unstable Jets in Crossflow, 65th American Physical Society/Division of Fluid Dynamics Meeting, San Diego, CA, November, 2012.

CHAPTER 1

Background and Motivation

The transverse jet or jet in crossflow (JICF) typically involves a jet of fluid issuing perpendicularly into a crossflow of another fluid. Many variations of this basic flowfield exist, including gas injection into gas, liquid injection into liquid or gas, reactive flows, flush or elevated jet fluid injection with respect to a wall, circular or rectangular jets of various aspect ratios, multiple impinging jets, and compressible flows with shock-wave effects on jet behavior. Some early studies of this flowfield were intended to shed light on the dynamics of pollutants issuing from chimneys and smokestacks, and their mixing and dispersal rates (Margason, 1993). More recent studies have focused on characterizing quantities such as mixing efficiency and trajectories of the jet for applications such as dilution air injection and fuel/air mixing in combustion systems as well as turbine blade film cooling and fluidic thrust vectoring.

Transversely injected dilution air jets have been used in gas turbine combustors for decades. Dilution air jets are introduced after the combustion zones of a gas turbine engine to decrease the peak temperature of the gases entering the turbine (Vermeulen et al., 1992; Karagozian, 2010). Reduction in peak turbine inlet temperatures results in weakened maximum thermal stresses on solid surfaces, allowing an increase in the average turbine inlet temperature and a subsequent increase in power extraction from the gas by the turbine. Forcing of these dilution air jets can result in further reductions of the peak temperatures in the exhaust gas stream entering the turbine (Vermeulen et al., 1992).

Transverse jets are a practical and efficient means of mixture ratio control in low-speed reactive flowfields such as those present in the primary combustion zone of gas turbine engines. The ratio of fuel to oxidizer/diluent is one of the main governing parameters that determines

the formation of undesirable by-products of combustion such as NO_x and CO, so being able to tune this parameter in real-time is desirable for active control of emissions. Jets in crossflow are also used as primary fuel injectors for ramjet and scramjet applications. This is because high-speed engines require rapid molecular mixing to feed a stable combustion process, and because the upstream recirculation region of a transverse jet can provide flame-holding characteristics to stabilize the ignition process (Ben-Yakar et al., 1998). Moreover, transverse jet injection behind a rearward-facing step or cavity provides superior flame-holding for supersonic crossflows, resulting in a more efficient combustion process (Karagozian et al., 1996; Gruber et al., 2004).

Another widely-accepted application for the jet in crossflow is control of real-time thrust vectors during the high-speed flight of missiles and rockets, and the takeoff/landing transition of V/STOL aircraft. One of the main factors governing V/STOL aircraft performance in transition from hover to winged flight is the surface pressure distribution. Various studies have been aimed at quantifying this distribution during different flow regimes using single circular and rectangular jets as well as dual jet configurations (Oh and Schetz, 1990). Moreover, fluidic nozzle throat skewing techniques for thrust vectoring applications have shown potential for significant decreases in weight and complexity of nozzle design (Miller et al., 1999; Yagle et al., 2001).

Not all applications of the transverse jet require increased penetration and mixing. Turbine blade film cooling is an application example where these parameters would be minimized in an optimal configuration. Film cooling creates a barrier layer of fluid between the turbine blade and the expanding hot gases. This barrier fluid would ideally have low thermal diffusivity so as to decrease the diffusion of heat from the exhaust gas stream to the solid turbine blade, and it would penetrate very little into the crossflow so as to ensure this film layer acts as a thermal barrier for the turbine blade for most (if not all) of its chord length. Excitation of these film cooling jets with square-wave forcing has been shown to provide potential increases in cooling rates (Ekkad et al., 2006).

1.1 Transverse Jet Structure and Characterization

1.1.1 Flow Parameters

As shown in Fig. 1.1, the seemingly simple setup of the jet in crossflow results in a complex interaction among numerous vortical structures. The appearance and relative strength as well as the direction of vorticity of these structures is governed by the pertinent flow parameters that have been shown to characterize this flowfield. These parameters include the jet-to-crossflow velocity ratio, R, the jet-to-crossflow density ratio, S, and the jet-to-crossflow momentum flux ratio, J, as defined in Equation 1.1.

$$R = U_j/U_\infty \qquad S = \rho_j/\rho_\infty \qquad J = SR^2 \tag{1.1}$$

Other governing parameters include the momentum thickness of the jet, θ_j, the momentum thickness of the crossflow's wall boundary layer, θ_∞, the Reynolds number of the jet, $Re_j = U_j D/\nu_j$, and the Reynolds number of the crossflow, $Re_\infty = U_\infty D/\nu_\infty$. The Schmidt number of the jet, $Sc_j = \nu_j/D_{j\to\infty}$, where $D_{j\to\infty}$ is the mass diffusivity between the jet fluid and the crossflow fluid, can also play a role in differences between liquid and gas experiments due to the significant difference in length scales associated with momentum and mass diffusion for liquids as compared to gases. The effects of Schmidt number for diffusion of mass and Prandtl number for diffusion of heat are more important for relatively low Reynolds number jets since scalar transport is dominated by turbulent mixing in the high Reynolds number regime (Dowling and Dimotakis, 1990). However, it should be noted that in reactive jets in crossflow, the relationship between chemical reaction scales and the other scales associated with this flowfield also needs to be characterized. This is usually accomplished by calculating the Damköhler number, Da, which is a ratio between the limiting chemical reaction rate and the convective mass transport rate. Depending on the Damköhler number, the reaction in a gaseous flowfield ($Sc \approx 1$) may take place at momentum and mass diffusion scales ($Da \approx O(1)$), but typically the reaction occurs at much shorter timescales than both mass and momentum diffusion ($Da \gg 1$).

For elevated injection, the jet injection orifice typically extends above the wall boundary

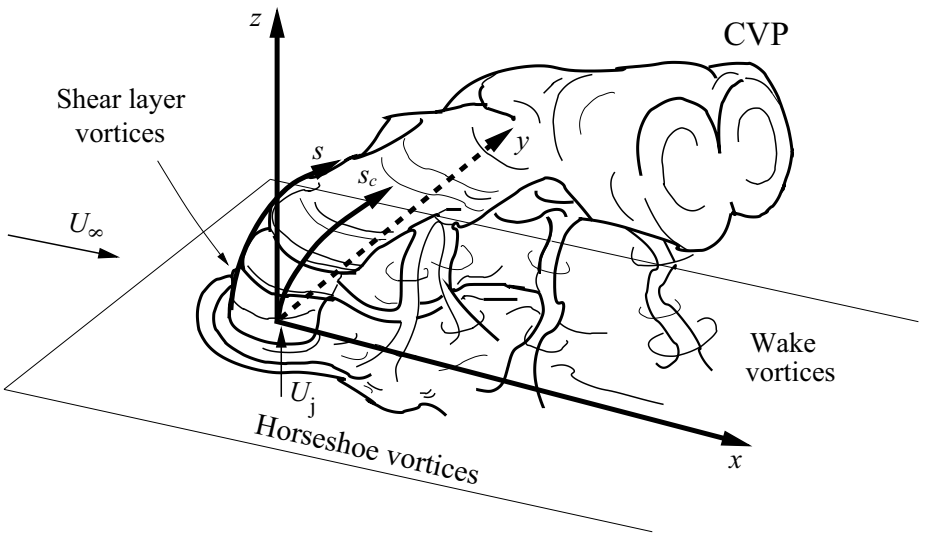


Figure 1.1: Schematic of the transverse jet, introduced flush with respect to the injection wall, and relevant vortical structures. Adapted from Fric and Roshko (1994).

layer created by the crossflow so that θ_∞ is no longer a significant parameter. For compressible flows, the Mach number of the jet, M_j, the crossflow mach number, M_∞, and the total enthalpy of both the jet and the crossflow also become important. Reactive flow characterization must also take into account the reaction rates associated with the combustion process, the energy release associated with the reaction, and the coupling between the reactive process and the fluid density/velocity fields.

1.1.2 Classic JICF Characteristics

1.1.2.1 JICF Vortical Structures

Near the injection plane of the jet, the interaction between the jet and crossflow creates two primary vortical structures: the horseshoe vortex system and the shear layer vortices. The horseshoe vortices wrap around the jet column and persist downstream. The character of the horseshoe vortices and the resulting Strouhal numbers, $St = \frac{f_h D}{U_j}$, associated with their oscillations at frequency f_h can be similar to the set of vortices generated by the interaction between a crossflow and a wall-mounted circular cylinder, as evidenced by Kelso and Smits (1995). Kelso and Smits (1995) show that the horseshoe vortex system can be persistent,

oscillating, or coalescing depending on the jet Reynolds number, Re_j, and jet-to-crossflow velocity ratio, R. The Strouhal number of oscillation in the non-steady horseshoe vortex regime is the same as or double that of the Strouhal number in the wake of the transverse jet, suggesting interaction between the horseshoe vortices and the wake vortices. Similarity between the oscillation frequency of the horseshoe vortices and the wake vortices is also found for rectangular jets in crossflow by Krothapalli et al. (1990). The horseshoe vortices near the upstream edge of the jet can have a significant impact on the velocity profile of the flowfield near the injection plane of the jet as evidenced by Andreopoulos (1985), which can result in an alteration of the frequency and energy content of the shear layer vortices. The shear layer vortices were previously thought to be produced by a Kelvin-Helmholtz instability in the shear layer between the jet and crossflow near the jet exit (Fric and Roshko, 1994; Kelso et al., 1996). However, more recent explorations of the transverse jet shear layer instabilities and the associated vortex rollup have shown that the nature of this instability is more complex than that of a simple planar shear layer. Previous work on the jet in crossflow at UCLA has focused on characterizing the nature of this shear layer instability throughout the entire parameter space of this flowfield and development of control methods to alter the instability in useful ways (Megerian et al., 2007; Davitian et al., 2010a,b; Getsinger, 2012). A comprehensive look at the findings of these studies will be presented in Section 1.1.3.1.

There are two dominant vortical structures present further downstream in the transverse jet: the wake vortices and the counter-rotating vortex pair (CVP). The wake vortices were examined thoroughly by Fric and Roshko (1994) by smoke seeding of the jet and wall boundary layer. These vortices are transient in character and similar to the von Kármán vortex street behind a solid cylinder (Schlatter et al., 2011). However, according to Fric and Roshko (1994), the mechanism for their formation is very different. As opposed to the vortex street formation mechanism of an absolute instability giving rise to a global mode (Huerre and Monkewitz, 1990), the wake vortices in the jet in crossflow were found to be linked to separation events in the wall boundary layer resulting in boundary layer fluid being drawn into the jet and contributing circulation to the CVP. Smith and Mungal (1998) suggest that an extension of this phenomenon is responsible for the presence of jet fluid in the wake

structures, which is also apparent in the work of Fric and Roshko (1994).

Although the wake vortices dominate the section of the flowfield between the jet and the tunnel wall further downstream of jet fluid injection, the jet itself is dominated by the CVP. There is some disagreement about the formation mechanism of the CVP, but the general consensus seems to be that the CVP is near-field generated, with links to the evolution of the shear layer as well as the pressure differences between the upstream and downstream edges of the jet (Kelso et al., 1996; Smith and Mungal, 1998; Cortelezzi and Karagozian, 2001; Muppidi and Mahesh, 2007). There is also a contribution to the CVP circulation by the channel wall boundary layer as evidenced by the water tunnel experiments of Kelso et al. (1996), and CVP formation seems to occur much closer to the jet exit when wall boundary layer separation events are taken into account in the numerical simulations of Schlegel et al. (2011). Moreover, the work of Peterson and Plesniak (2004) suggests that vortex structures within the pipe leading up to the jet injection plane can interfere with the CVP, further enhancing the strength of the contention that the CVP is a near-field generated phenomenon that evolves downstream to eventually dominate the jet cross-section. The evolution and eventual breakdown of the CVP has been linked to the mixing enhancement of certain regimes of the JICF as compared to the free jet (Kamotani and Greber, 1972; Moussa et al., 1977; Karagozian, 1986; Margason, 1993).

1.1.2.2 Symmetry of the JICF

Theoretically, the round jet in crossflow should be symmetric about the centerplane of the jet when averaged over time. If the velocity profile of the jet and crossflow are symmetric, there is no immediately apparent reason for the swirl-free jet to prefer one orientation about the centerplane over another. This is evidenced by the lack of numerical simulations of this flowfield with symmetric boundary conditions that resulted in a time-averaged asymmetric jet in crossflow. However, some experimental researchers have found asymmetric characteristics during their exploration of the transverse jet. For relatively high velocity ratios ($R = 10$ & $R = 20$), Smith and Mungal (1998) show concentrations of jet fluid to be unequal about

the centerplane of the jet, with increasing asymmetry as either velocity ratio or distance downstream are increased. Kuzo (1995) explored the asymmetry phenomenon using particle image velocimetry (PIV) measurements of the jet cross-section and found that asymmetry was most apparent below a cutoff jet Reynolds number, Re_{cr}, that increases with increasing jet-to-crossflow velocity ratio, R. Kuzo's velocity measurements showed tertiary vortices below the familiar counter-rotating vortex pair that skew the orientation of the entire jet cross-section; a similar finding using scalar measurement in the present experiments will be shown in Chapter 3. Shan and Dimotakis (2006) also found a similar trend with asymmetry in the jet and appearance of tertiary vortices as jet Reynolds number is decreased. Kamotani and Greber (1972) and Narayanan et al. (2003) also observed jet concentration profiles that are not symmetric about the centerplane. It should be noted that all the experiments mentioned here, with the exception of the work of Narayanan et al. (2003), used a nozzle for jet injection. Narayanan et al. (2003) used a straight pipe for jet fluid injection in their experiments.

The asymmetry in transverse jet cross-sections at relatively high velocity or momentum flux ratios and relatively low jet Reynolds number can be explained theoretically. The inviscid linear stability analysis of Alves et al. (2007) for transverse jets found unequal growth rates of helical jet modes of opposite sign when $R \gtrsim 10$, suggesting that flows in this regime might be more susceptible to asymmetry if helical modes are triggered. The extension to jets in crossflow with a continuous base flow in Alves et al. (2008) found comparable growth rates between the axisymmetric (m=0) and first helical (m=1) modes for $R \gtrsim 10$, which suggests that in certain regimes, the jet in crossflow could exhibit mode competition characteristics, potentially resulting in an asymmetric jet cross-section due to flow asymmetries that could trigger helical modes.

There are relatively few computational studies that exhibit clear cross-sectional flowfield asymmetries in the mean for the jet in crossflow configuration. While there are Direct Numerical Simulation (DNS) (Muppidi and Mahesh, 2007) and Large Eddy Simulation (LES) (Yuan et al., 1999) studies of the JICF that produce temporally evolving asymmetries, most produce flows that are symmetric in the mean. In fact, this author is only aware of one

numerical simulation that produces severe transverse jet cross-sectional asymmetry in the mean, with evidence of tertiary vortices: the DNS simulations of pulsed jets in crossflow at $(Re_j, R) = (5000, 6)$ by Muldoon and Acharya (2010). Muldoon and Acharya (2010) used a turbulent pipe flow model as the jet exit velocity profile and a turbulent boundary layer model as the crossflow profile. However, neither the jet or the crossflow boundary conditions were allowed to change in time, resulting in essentially laminar inlet conditions similar to the current experiments in our lab. The crossflow boundary layer thickness for this simulation was also relatively large ($\delta/D = 16$). For comparison, the crossflow boundary layer thickness for our experimental setup for a $(S, J) = (1, 41)$ jet is $\delta/D \lesssim 2$. Since the boundary conditions for the simulations of Muldoon and Acharya (2010) were temporally stationary and symmetric to within numerical accuracy about the centerplane of the jet, to analyze the effect of asymmetric perturbation these researchers introduced a velocity deficit in a small spherical region in the crossflow upstream of the jet as an initial condition. Their simulations show a time-averaged asymmetric jet cross-sectional fluid distribution with evidence of tertiary vortices similar to the experimental results of Kuzo (1995), Shan and Dimotakis (2006), and the results from the present experiments shown in Chapter 3. Moreover, these researchers found that flipping the asymmetric perturbation location about the transverse jet centerplane results in an asymmetric jet cross-section that flips its orientation about the centerplane as well. These researchers also forced the jet at different Strouhal numbers and found that some forcing conditions resulted in a symmetric jet cross-section while others did not. The results from this simulation seem to suggest that high R jet in crossflow configurations with laminar inflow conditions, a thin jet shear layer thickness, a relatively thick crossflow boundary layer thickness, and an asymmetric perturbation imposed on the flow result in high degrees of asymmetry in both the time-averaged and instantaneous scalar distributions.

The extent of research and discussion in the literature concerning the asymmetry of the jet in crossflow is minimal, possibly resulting from early experiments suggesting that the flowfield should be symmetric. Since then it has become common for researchers to only model half the flow domain in computational studies, or only acquire half the jet flow structure

data in experimental studies. Yet due to experimental tolerances, slight asymmetries in the geometrical setup of all experimental work could possibly result in flowfield imperfections, as noted by Smith and Mungal (1998). Improper flow conditioning could also create asymmetric mean velocity and concentration distributions. A more in-depth exploration of transverse jet asymmetry in the present experiments is described in Chapter 3.

1.1.2.3 Scaling and Trajectories of the JICF

Comparing jets of different momentum flux ratios, J, in physical space can be a bit misleading. For example, at an equivalent downstream position (x in Figure 1.1), a high J transverse jet has been interacting with the crossflow over a longer distance than a low J jet, possibly leading to more evolved structures. Hence comparing the mixing properties of transverse jets for applications such as combustion and other processes that require rapid molecular mixing can lead to erroneous conclusions about which transverse jets mix more effectively. This is why considerable effort has gone into finding a scaling parameter for the jet in crossflow that scales physical space to enable accurate comparisons between different transverse jets and also to explore possible transverse jet self-similarity for predictive purposes.

Numerous studies have focused on determining relevant length scales for the jet in crossflow. Special attention has been given to producing scaling laws capable of collapsing jet trajectories (Broadwell and Breidenthal, 1984; Hasselbrink and Mungal, 2001; Muppidi and Mahesh, 2005; Forliti et al., 2015). It should be noted that the definition of the trajectory of the jet plays a role in its scaling, so care should be taken when comparing trajectory data that have different definitions. For example, Smith and Mungal (1998) define the trajectory as a least-squares power-law fit to the loci of maximum scalar concentration values on the centerplane of the jet, whereas Kamotani and Greber (1972) fit a power-law to the maximum velocity values on the same plane. Kamotani and Greber (1972) find that trajectories based on maximum velocity fits penetrate 5-10% deeper into the crossflow than those based on concentration.

Another trajectory definition used extensively in computational studies is the center

streamline of the jet. Keffer and Baines (1963) were among the first to propose a scaling of the jet with a global flow parameter ($R^2 = J$). Their scaling correlation is shown in Equation 1.2 (A_1 and B_1 are constants in this equation).

$$\frac{z}{JD} = A_1 \left(\frac{x}{JD}\right)^{B_1} \tag{1.2}$$

Yet this correlation does not collapse data for the lower R or J cases, a discrepancy they attributed to effects associated with jet proximity to the tunnel wall. The work of Broadwell and Breidenthal (1984) suggests that after using a similarity theory to treat the jet as a point source of momentum, the RD length scale reveals itself to be the pertinent large length scale capable of collapsing JICF trajectory data using Equation 1.3, in which A_1 is a constant and $B_2 \sim 1/3$.

$$\frac{z}{RD} = A_2 \left(\frac{x}{RD}\right)^{B_2} \tag{1.3}$$

This result is corroborated by the work of Smith and Mungal (1998) who found better data collapse when scaling concentration-based trajectories by RD as opposed to D or R^2D. Using a similar analysis but also incorporating some intermediate asymptotic theory, Hasselbrink and Mungal (2001) found trajectories of concentration maxima to best scale with RD, but with near-field and far-field trajectory fits that differ from one another, each with its own entrainment coefficient to take into account differences in entrainment of fluid in the near-field and far-field. However, these trajectory fits are only valid for relatively high R values. In fact, trajectories for $R = 5$ tend to differ from those for $R \gtrsim 10$ (Smith and Mungal, 1998).

There is a growing body of evidence that suggests the complicated interaction between the jet and the crossflow cannot be completely characterized by a momentum flux or velocity ratio. The computational studies of Muppidi and Mahesh (2005) show that transverse jets of equivalent R but different crossflow and jet velocity profiles have different trajectories. These researchers find that jets with thinner boundary layers tend to penetrate less, a result they attribute to increased crossflow fluid entrainment rates. They also show a decrease in penetration when the crossflow boundary layer thickness is decreased, consistent with studies of transverse jets injected behind a rearward facing step (Karagozian, 2010). None

of these factors are taken into account when only scaling jet trajectory by RD, which is why Muppidi and Mahesh (2005) suggested another length scale for trajectory data scaling. This length scale, h, is defined theoretically as the position in the z direction (see Figure 1.1 for coordinate system) where the cumulative effect of the pressure gradient on the jet developed by the transverse momentum of the crossflow becomes equal to the vertical momentum of the jet. The h length scale is used in the power law scaling function shown in Equation 1.4, which is similar to the RD scaling power-law function but with an added multiplicative factor that is dependent on h. A_3 and B_3 are constants in this equation.

$$\frac{z}{RD} = A_3 \left(\frac{x}{RD}\right)^{B_3} \left(\frac{h}{D}\right)^{0.15} \tag{1.4}$$

However, New et al. (2006) show that even this scaling does not collapse all the available pipe and nozzle injection trajectory data. Another interesting finding is displayed in the work of Niederhaus et al. (1997). Their water-tunnel experiments showed that asymmetries in the jet cross-section resulting from swirl of the incoming jet can affect the trajectory differently depending on the velocity ratio regime of the jet in crossflow. High R jets seem to penetrate more into the crossflow for relatively low swirl, whereas low R jets seem to penetrate less with the introduction of swirl. To date there is no definitive scaling capable of collapsing all trajectory and/or mixing data (see Section 1.1.2.4 for a discussion on mixing). There are many variations among supposedly comparable flowfields, which include the velocity profiles of the jet and crossflow, the elevation of the jet injection plane with respect to the crossflow boundary layer, asymmetries associated with the experimental setup and the resulting flowfield dynamics that affect trajectory, the jet's proximity to the injection wall of the tunnel, and the Reynolds numbers of the jet, Re_j, and crossflow, Re_∞.

Another, more recent scaling law formulation attempts to generate a physics-based scaling parameter that can be applied to the jet in crossflow (Forliti et al., 2015). The scaling parameter, B, is derived by applying a control volume analysis on the jet and summing the contributions of the net drag force applied to the jet by the crossflow, and the effect of jet momentum reorientation associated with crossflow fluid entrainment. Applying the control volume analysis and solving for the scaling parameter, one obtains the formulation for B

shown in Equation 1.5.

$$B = \frac{J}{\frac{2C_D}{\pi} + C_e J^{1/2}} \tag{1.5}$$

In Equation 1.5, C_D and C_e are the entrainment and drag coefficients, respectively, which are empirical quantities extracted from experimental data. Unfortunately, quantifying these parameters for a variety of different momentum flux ratios and Reynolds numbers can be difficult. Moreover, the control volume analysis applied to derive this scaling parameter is only valid for thin crossflow boundary layers. These limitations restrict the application of the physical space scaling parameter B to a specific subset of the transverse jet parameter space where the drag and entrainment coefficients can be estimated and the crossflow boundary layer is thin. As demonstrated in Forliti et al. (2015), when the limitations of the scaling parameter are satisfied, scaling physical space by BD yields excellent trajectory collapse.

1.1.2.4 Centerplane Mixing Trends of the JICF

Since the JICF has been implemented in various applications that require rapid mixing of two fluid streams, the mixing characteristics in the centerplane of this flowfield have been studied extensively. Some previously utilized common mixing quantification parameters include centerline jet fluid concentration decay (Smith and Mungal, 1998; Su and Mungal, 2004), and centerline velocity decay (Fearn and Weston, 1974). The work of Smith and Mungal (1998), Su and Mungal (2004), and Fearn and Weston (1974) all suggest an exponential decay of their respective measurement quantities outside the potential core of the jet, the rate of which is dependent on flowfield conditions and configuration. Moreover, although it has been suggested by some (Smith and Mungal, 1998) that the equidensity ($S = 1.00$) transverse jet centerline concentration decays at a rate that is greater than the free jet in the near-field ($s_c^{-1.3}$ transverse jet decay rate as opposed the the free jet decay rate of s_c^{-1}, where s_c is the distance along the jet centerline), the work of Su and Mungal (2004) shows an s_c^{-1} decay rate in the near field of an $R = 5.7$ jet in crossflow . The experimental data of Smith and Mungal (1998) suggests that for $10 < R < 25$, there exists a transition of concentration decay rate from the superior $s_c^{-1.3}$ rate in the near-field to a slower, R-dependent decay

rate in the far-field. In contrast to Smith and Mungal (1998), Su and Mungal (2004) show an s_c^{-1} decay rate in the near field of the jet with no clear transition to a slower decay rate in the far-field for an $R = 5.7$ jet in crossflow. It should be noted that Smith and Mungal (1998) used a contraction nozzle that created a top-hat velocity profile at the jet exit, whereas Su and Mungal (2004) used a straight pipe to create an unverified parabolic velocity profile at the exit. It is also worthwhile to note that Su and Mungal (2004) found no obvious differences in decay rate between flush and protruding pipe injection, suggesting minimal effect of the crossflow boundary layer on mixing along a pipe-injected jet trajectory. However, as mentioned in Section 1.1.2.3, the crossflow boundary layer will almost certainly have an effect on the trajectory of the jet itself.

Other centerplane mixing metrics include the spread, δ, of the jet in either the vertical or trajectory-normal direction n, and the penetration, P, of the jet in the vertical direction (Davitian et al., 2010b; Getsinger, 2012). Both of these measurements are defined by deciding on a minimum jet fluid concentration level that can be considered as still being part of the jet itself (5% in Getsinger (2012), 20% in Su and Mungal (2004)). It is clear that higher J cases should penetrate into the crossflow more deeply, and this is indeed the result obtained in the work of Getsinger (2012) and Davitian et al. (2010b). Getsinger (2012) also found that for equivalent J at a fixed Re_j, jets with lower density ratio S penetrate into the crossflow to a lesser degree. This could be a consequence of the thinner crossflow boundary layer associated with the lower density ratio cases with fixed J and Re_j, which results in a higher transverse momentum flux at positions close to the jet injection wall. Yet Getsinger (2012) found that although the equivalent S, lower J cases spread less in the trajectory-normal direction (trajectory determination as outlined in Section 1.1.2.3), transverse jets with lower density ratio S of equivalent momentum flux ratio J penetrate less but spread more in the trajectory-normal direction, suggesting that jet penetration and spread are not always directly correlated as previously conjectured (Kamotani and Greber, 1972). Su and Mungal (2004) split their spread measurements to determine the difference between the spread on the lee side and windward side of the jet and found the spread on the lee side of the jet to be significantly higher than that of the windward side for the R=5.7 equidensity jet in

crossflow. This finding can possibly be attributed to jet fluid being deposited in the wake much more readily than being entrained in the windward crossflow due to pressure gradient considerations.

Because of the fact that most of the jet fluid lies outside the centerplane of the jet, it is highly doubtful that centerplane metrics such as spread and concentration decay are truly accurate measures of mixing; jet cross-sectional mixing quantification seems to be a more logical alternative for determining the mixing efficiency of the JICF. The thesis of Getsinger (2012) offers a preliminary look at the mean cross-sectional mixing characteristics of the JICF using several mixing parameters such as Unmixedness (Dimotakis and Miller, 1990) and Spatial Mixing Deficiency (Bockhorn et al., 2010). A more in-depth look at various cross-sectional mixing quantification parameters can be found in Section 1.2.

1.1.3 Recent Studies on Strategic JICF Control

1.1.3.1 Upstream Shear Layer Stability Characteristics

It is only recently that in-depth studies concerning the stability of the jet in crossflow configuration have been undertaken. A sizeable portion of this body of work is concerned with characterizing the stability of the upstream shear layer between the jet and crossflow. The shear layer vortex formation around the round jet column has generally been attributed in the past to an instability similar to the familiar Kelvin-Helmholtz instability (Fric and Roshko, 1994; Kelso et al., 1996). The reorientation of these shear-layer vortices as they are tilted and deformed by the crossflow has been linked to the formation of the CVP (Kelso et al., 1996; Cortelezzi and Karagozian, 2001). On the other hand, at very low jet Reynolds numbers ($Re_j = 100$) and for jet-to-crossflow velocity ratio $R < 3$, wake-like vortical structures coupled to the CVP dominate the flow, while for $R > 3$, jet-like rings dominate the flow (Camussi et al., 2002). Camussi et al. (2002) thus suggest that the jet's shear layer is not of the Kelvin-Helmholtz type. Blanchard et al. (1999) make similar claims for a slit-generated jet in crossflow; they see stable jets without shear layer oscillations for $Re_j < 300$ or $R < 3$.

Recent studies at UCLA have been aimed at characterizing the nature of the instability

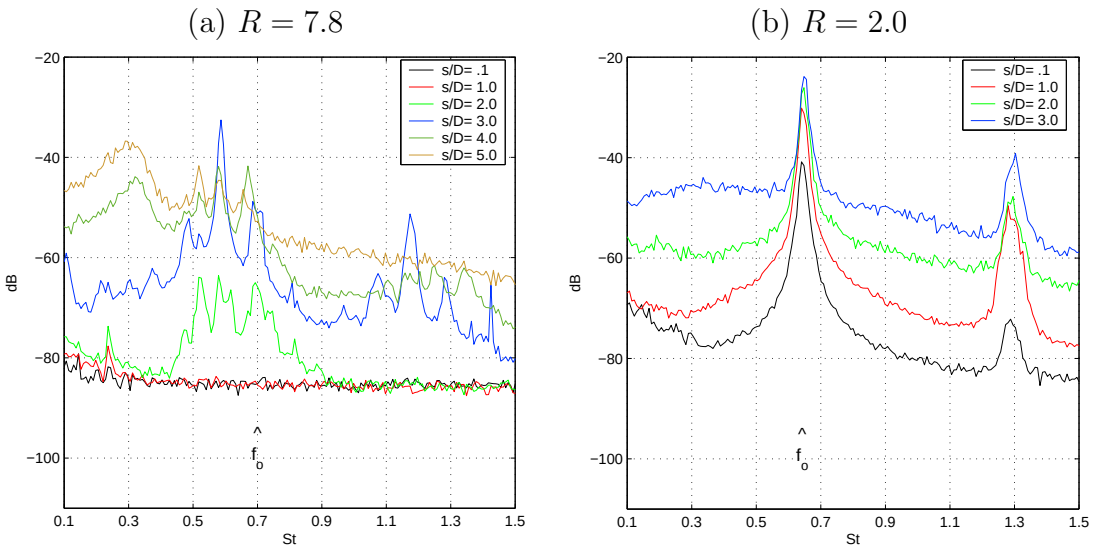


Figure 1.2: Vertical velocity spectra in the equidensity transverse jet at two R conditions, one each above and below the apparent transition in spectral character. Spectra are measured within the jet shear layer at varying distance s/D from the jet exit. Conditions correspond to $Re_j = 2000$. From Megerian et al. (2007).

of the upstream shear layer of the JICF. The work of Megerian et al. (2007) focused on the spectral character of the upstream shear layer for the equidensity ($S = 1.00$) jet in crossflow at $Re_j = 2000$ and $Re_j = 3000$ with both flush and elevated injection over a jet-to-crossflow velocity ratio range $\infty > R > 1.15$ (R based on jet centerline velocity and crossflow freestream velocity). This investigation shows that as R is lowered below a transitional value of around 3.2-3.5 for flush injection and around 1.2 for elevated injection, the nature of the instability of the upstream shear layer changes dramatically. Figure 1.2 shows the change in character of the vertical velocity spectra in the upstream shear layer obtained from the hotwire as it is traversed along the upstream shear layer with distance s/D. The oscillations seem to shift from relatively weak and broadband with multiple spectral peaks, shown in Figure 1.2a, to strong and pure-tone spectral characteristics with evidence of energy contained in higher harmonics, shown in Figure 1.2b. Moreover, in the high R regime, the fundamental mode, f_0, was observed to shift in frequency or Strouhal number ($St = \frac{f_0 D}{U_j}$) as the hotwire was traversed along the shear layer, suggesting high susceptibility to outside perturbations. This frequency-shifting was not apparent in the low R case. The fundamental

instability for jets with velocity ratios below the apparent transition of instability character was also observed to initiate much closer to the jet exit and persist all along the shear layer at the same frequency. This and other evidence for a transition in the character of the shear layer instability such as jet lock-in behavior and fundamental mode amplitude growth (Davitian et al., 2010a) suggest that the shear layer becomes absolutely unstable for $R \lesssim 3.1$.

A similar type of transition in the upstream shear layer instability character is found in the work of Getsinger et al. (2012). For a constant $Re_j = 1800$ with flush injection, spectral measurements of the upstream shear layer are made for the momentum flux ratio range $\infty > J > 5$ and density ratio range $1 > S > 0.14$. It is found that for a fixed S above a critical value (approximated to be around 0.4-0.45), the transition from weak, broadband oscillations to strong, pure-tone oscillations occurs as momentum flux ratio is lowered below a critical value of around $J \approx 10$. Since, for an equidensity jet in crossflow, $R = \sqrt{J}$, this critical momentum flux ratio agrees favorably with the critical velocity ratio determined from the work of Megerian et al. (2007) and Davitian et al. (2010a). Moreover, the work of Getsinger (2012) reveals that below the transitional density ratio of around $S \approx 0.45$, all momentum flux ratio conditions exhibit similar strong pure-tone oscillations, including the $J \to \infty$ condition corresponding to the free jet. This finding is in accordance with the low density jet experiments of Hallberg and Strykowski (2006), who find the transitional value of S to create a globally unstable shear layer to be in the range $0.27 \lesssim S \lesssim 0.5$ for the Re_j and D/θ values associated with the flow conditions in the thesis of Getsinger (2012). Hence both J and S play a critical role in the shear layer oscillation character of the jet in crossflow. The shear layer response variation to single-tone acoustic forcing as R is varied described in Davitian et al. (2010b) is similar to the shear layer response variation in Getsinger et al. (2012) for reduction of S. However, as shown in Fig. 1.3, there seems to be a difference in the degree of unforced vortex pairing inhibition when decreasing the density ratio (Figure 1.3c vs. Figure 1.3d) as compared to the inhibition seen when decreasing momentum flux ratio (Figure 1.3a vs. Figure 1.3b), suggesting differences between the nature of the transition as these two control parameters are varied independently.

The transition of the shear layer spectral character from broadband, weak oscillations at

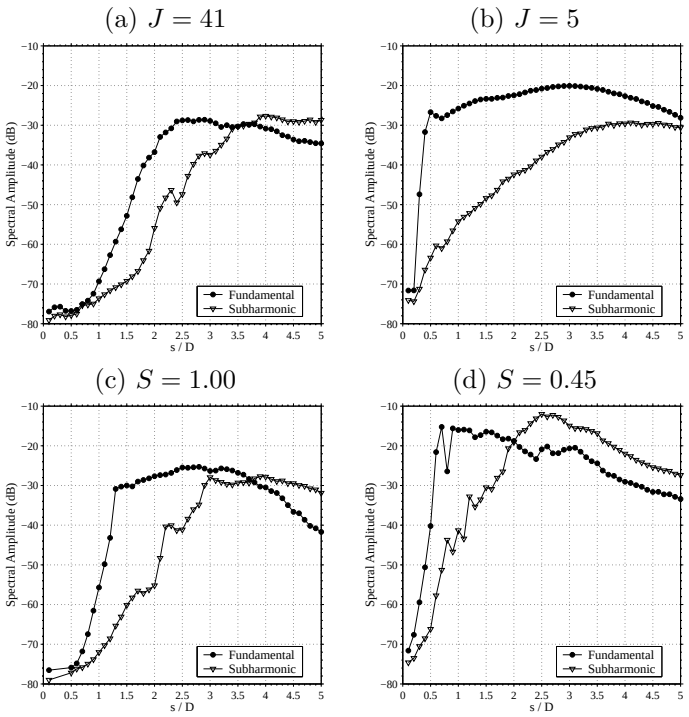


Figure 1.3: Comparison of the development along the shear layer of the fundamental and subharmonic modes as (a & b) momentum flux ratio is lowered for an $S = 1.00$ jet and (c & d) density ratio is lowered for a $J = 20$ jet. From Getsinger (2012).

high R or J values to strong, pure tones with higher harmonics at lower R or J values is among extensive evidence that the flow undergoes a transition from convective instability to absolute instability (Megerian et al., 2007; Davitian et al., 2010a). Absolute instability is defined as the condition where a disturbance in the flow propagates both upstream and downstream in time, typically resulting in a very strong and pure-tone oscillation. A shear flow that is locally absolutely unstable in a sufficiently large region often demonstrates temporally growing global modes. This type of instability growth is found in bluff-body wakes (Provansal et al., 1987) and low-density jets (Monkewitz et al., 1990; Kyle and Sreenivasan, 1993). Flows that are locally convectively unstable everywhere are sometimes called amplifiers since perturbations introduced upstream amplify only as they travel downstream, whereas flows with sufficient pockets of local absolute instability that give rise to a global instability are sometimes called oscillators since they fluctuate at their own intrinsic frequency. It should be noted that not all flowfields can be analyzed using local concepts of instability

since many are strongly nonparallel (velocity profile changes are on the same order as the instability wavelength). These flows require global eigenmode analysis to accurately capture the flowfield dynamics (Chomaz, 2005).

Both simulation and experimentation can shed light on transition in shear layer instability characteristics. Formally determining whether a flow is globally unstable experimentally requires a non-intrusive measurement of the transient response of the flowfield in question to the impulsive change of a control parameter. If the flowfield is globally unstable, the time-plot of the velocity fluctuation as the control parameter is varied will show an initial linear increase and then eventual saturation as the flowfield enters a limit cycle with an intrinsic, natural frequency. This was attempted by Strykowski (1986) for a cylinder wake using hotwire anemometry to detect oscillations in the flow. However, most experimental diagnostics do not allow the transient response to variation in flow conditions to be characterized easily. Time series hotwire measurements in Davitian et al. (2010a) for the transverse jet do show a significant increase in fluctuation amplitude as R is dropped below around 3.2. If direct transient measurement is impossible, there are numerous measurements that try to characterize the periodic behavior of globally unstable flow. These include, in increasing order of strength of evidence for global instability, single-point spectra showing pure-tones with higher harmonics, steady-periodic forcing to detect lock-in phenomena (forcing of the jet in crossflow will be discussed in Section 1.1.3.2), low-level forcing at the suspected global mode frequency to determine if linear amplification is possible, and the measurement of the saturation amplitude as a function of a flow control parameter (Huerre and Monkewitz, 1990). If no forcing is applied, the least convincing evidence of the presence of global instability is single-point spectra because a clean spatial instability could result in a peaky spectrum similar to that of a global instability.

A more convincing unforced piece of evidence for global instability is measuring the saturation amplitude at the suspected global mode frequency near the value of the control parameter that seems to be changing the character of the spectrum. If a global instability is present, the saturation amplitude near the bifurcation point, J_{cr}, should follow a similar

trend to the saturation amplitude resulting from the Landau equation (Eq. 1.6).

$$|A|_0 \approx c_3(J_{cr} - J)^{\frac{1}{2}} \tag{1.6}$$

This trend is found for the transverse jet using the root mean square of the vertical velocity fluctuation as measured by a hotwire in the upstream shear layer of a $Re_j = 2000$, $S = 1.00$ jet in crossflow in Davitian et al. (2010a), although different values of the measured critical control parameter, R_{cr}, depending on measurement location along the shear layer, is found. This variation in R_{cr} may be attributed to the inability of the Landau equation to encapsulate the total spatial amplification of localized disturbances (Getsinger, 2012). The transition to global instability completely changes the character of the fluctuation spectrum, which suggests that a subsequent change in the nature of the nonlinear interaction between modes and eventual energy transfer to dissipative scales in inertia-dominated jets could have a significant effect on the overall mixing of the jet in crossflow.

Sinusoidal excitation of the jet in crossflow can also help to verify stability characteristics. If a flowfield is globally unstable, exciting it at a frequency, f_f, near the global mode, f_0, could potentially result in the forcing frequency overtaking the fundamental shear layer instability. Yet such "lock-in" to the applied frequency f_f might require higher amplitude forcing if f_f is not close to f_0. This phenomenon is intrinsic to many non-linear systems, including coupled pendulums swinging at frequencies close to each other. The work of Davitian et al. (2010a) found lock-in behavior in the equidensity jet in crossflow at low velocity ratio R with the amplitude of forcing required for lock-in of the natural mode to the forcing frequency to be linearly proportional to the difference between the two frequencies ($|f_f - f_0|$), suggesting a Hopf Bifurcation to a global mode (see Huerre and Monkewitz (1990) for a description of this type of bifurcation). The work of Getsinger et al. (2012) found similar behavior for the low-density ($S = 0.55$) jet in crossflow with an increase in the amplitude required for lock-in as the control parameter J is lowered below $J_{cr} \approx 10$ for a fixed S, suggesting strengthening of the apparent global instability as momentum flux ratio is decreased. This behavior is shown in Figure 1.4 for an $S = 0.55$ transverse jet.

Simulations of the jet in crossflow have also explored instability characteristics of this

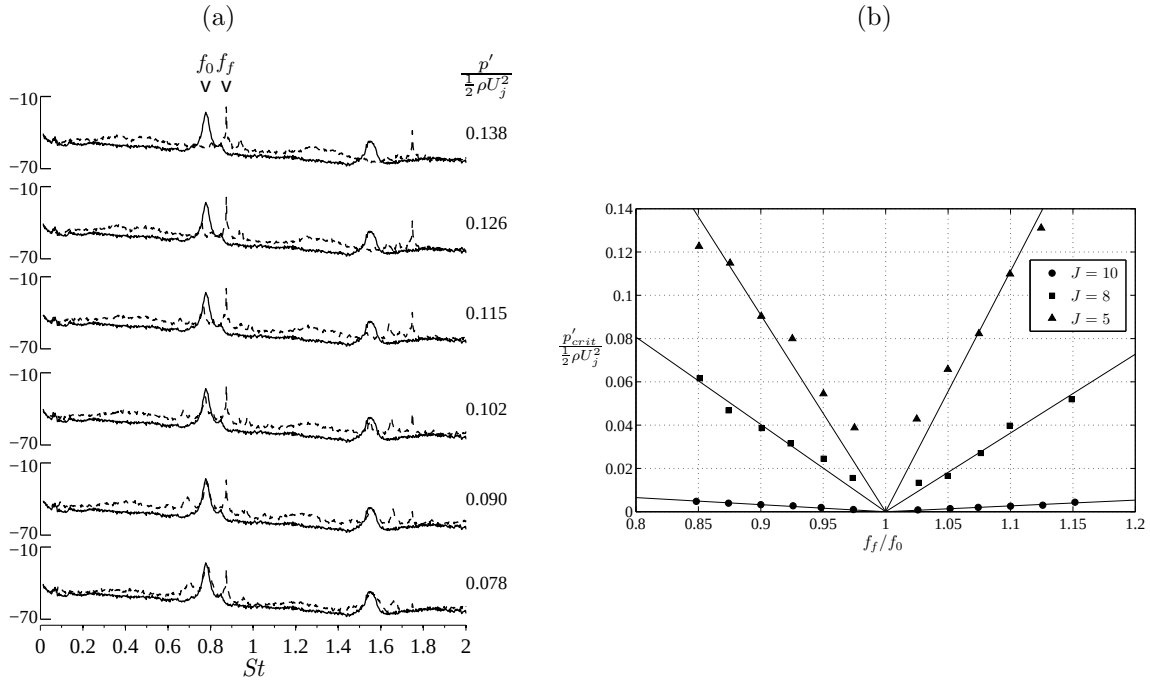


Figure 1.4: (a) Power spectra (amplitude in dB) as measured at $s/D = 2.0$ in the $(J, S) = (5, 0.55)$ transverse jet shear layer at several normalized forcing amplitudes. The dashed lines represent the spectra of the forced shear layer, and the solid line represents the unforced shear layer spectra. Forcing is applied at $f_f = 2528$ Hz and the fundamental frequency is $f_0 = 2248$ Hz. (b) Forcing amplitude at which lock-in to the forcing frequency is achieved, as a function of forcing frequency f_f, for several values of J at $S = 0.55$. Data from Getsinger et al. (2012).

flowfield. The work of Bagheri et al. (2009) found laminar pipe and crossflow inlet conditions to result in a linearly globally unstable flow at velocity ratio $R = 3$ using selective frequency damping of a full DNS simulation of the JICF to yield a base flow over which eigenvalue analysis was administered to determine the global eigenmodes. Global instability was also found in the work of Ilak et al. (2012) by the same group, with the appearance of several bifurcations yielding different globally unstable eigenmodes that depend on the velocity ratio of the flow. However, it is important to note that neither of these simulations resolved the flow in the jet pipe. This is a severe deficiency since at low velocity ratios, the crossflow has been shown to flow into the pipe both experimentally (Kelso et al., 1996), and computationally (Muppidi and Mahesh, 2007). Reversed flow of this sort can significantly change the upstream shear layer instability characteristics and increase velocity profile gradients resulting in severe alteration of growth rates, which is most likely the reason the work of

Ilak et al. (2012) shows a lack of coherent upstream shear layer roll-up near the jet exit for all cases studied ($0.675 < R < 3$).

1.1.3.2 Controlled Excitation of the Jet in Crossflow

Aside from attempting to characterize the instability using excitation, another use for forcing the jet in crossflow is to alter the penetration and mixing characteristics. The work of Johari et al. (1999) applied full modulation to a turbulent water jet in crossflow at velocity ratios of 5 and 10 with varying frequency and duty cycle of forcing. This experiment showed drastic increases in penetration and molecular mixing for conditions of forcing that resulted in distinct vortex rings with sufficient separation. Coherent vortex rings were generated when short injection times and low duty cycles of forcing were applied, resulting in distinct impulses of vorticity that penetrated deeply due to the self-induced velocity fields (Chang and Vakili, 1995), but were also sufficiently separated so pairs of vortices did not interact with each other in such a way that reduced the overall penetration and mixing benefits. The forced liquid jet in crossflow studies by Eroglu and Breidenthal (2001) showed similar behavior.

The work of M'Closkey et al. (2002) is the first to have used open loop control to form more precise temporal waveforms. These researchers also found increased spread and penetration for an $R = 2.58$, $Re_j = 1500$ gaseous jet in crossflow forced using square wave excitation at frequencies corresponding to subharmonics of the fundamental mode and duty cycles corresponding to prescribed pulse widths. Shapiro et al. (2006) linked these optimal pulse widths to the ideas of Gharib et al. (1998) concerning an optimal excitation piston stroke length-to-diameter ratio, $L/D \approx 4$, for coherent vortex ring formation. Shapiro et al. (2006) determined that corresponding optimal stroke ratios for transverse jet excitation produced the deepest-penetrating periodic vortex structures for $R = 2.58$ and $R = 4.0$. Sinusoidal excitation did not produce significant differences in jet spread or penetration in the work of Shapiro et al. (2006) or M'Closkey et al. (2002). Yet sine-wave forcing of an $R = 6$, $Re_j = 5000$ gaseous jet in crossflow administered by Narayanan et al. (2003) found the jet to be more susceptible to lower frequency forcing, with evidence of amplification of the forced

frequency along the jet, increased mixing, and eventual nonlinear effects highlighted by the appearance of higher harmonics.

These prior studies (M'Closkey et al., 2002; Shapiro et al., 2006) demonstrate that convectively unstable and globally unstable flows respond very differently to induced perturbations, although at the time this distinction was not understood. Since then our group has proposed that the temporal waveform associated with forcing a jet in crossflow should be altered strategically, depending on the unforced shear layer instability characteristics that appear to be present in the configuration of interest. This proposal is validated in the work of Davitian et al. (2010b) who found the convectively unstable jet in crossflow to respond to low-level sinusoidal forcing easily and with improved spread, but that globally unstable jets do not appear to be impacted by sinusoidal excitation, except at very high forcing amplitudes, especially at frequencies close to the natural mode, f_o. However, square wave forcing at optimal stroke ratios was found to affect globally unstable jet penetration and spread. Hence the stability characteristics of the unforced jet in crossflow can have a profound effect on its optimized control strategy.

1.2 Mixing Quantification of Fluid Flows

Determining the optimal mixing metric best suited for transitional or turbulent flowfields has been a topic of discussion in the fluid dynamics community for decades. To quantify mixing of the jet in crossflow, some rely on the mean and fluctuating quantities associated with centerplane of the jet, e.g., centerline concentration decay (Smith and Mungal (1998)). However, with the majority of jet fluid being contained outside the centerplane, this method of mixing quantification cannot possibly be regarded as a true measure of mixing. Others rely on mean quantities such as scalar concentration decay and spread/penetration of the jet using jet cross-sectional images (Niederhaus et al., 1997). This method is a bit more informative, but it still does not completely characterize the mixing efficiency of the jet in crossflow.

In order to quantify mixing correctly, first a formal definition of what it means to be

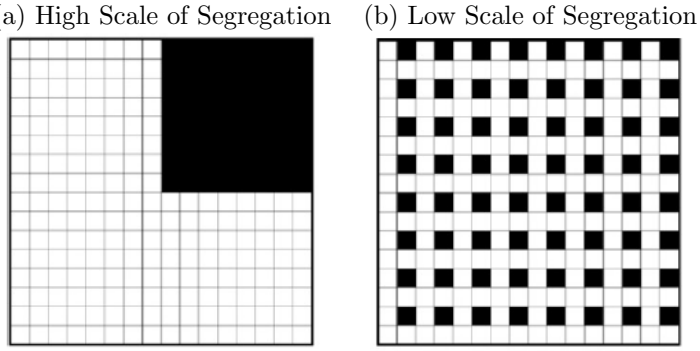


Figure 1.5: Comparison of high and low scales of segregation with constant intensity of segregation. Adapted from Kukukova et al. (2009).

fully mixed must be supplied. Unfortunately, this is not as simple as it sounds. Kukukova et al. (2009) define mixing in terms of three key process variables: intensity of segregation, scale of segregation, and exposure. The intensity of segregation can be thought of as a standard deviation or variance measurement; a perfectly mixed fluid should be so uniformly close to the mean value of the parameter of interest that the variance is negligible. The scale of segregation can be thought of as the clustering that occurs in any turbulent mixing process. An informative method of visualizing this parameter is shown in Fig. 1.5. The two checkerboard patterns have the same intensity of segregation since the number of black and white squares are the same between them, but (b) has a much smaller scale of segregation. The structures (clusters of black squares) are much smaller in (b) than they are in (a). This is the reason why both intensity and scale of segregation measurements are important; two completely different flowfields could have similar variance about the mean but radically different scales of segregation, or they could have similar size of the structures but highly different intensities of segregation. The third process variable, exposure, can be thought of as the potential to decrease the intensity of segregation by diffusive mixing. The more contact area and/or the larger the gradient of the concentration of the fluids, the more potential for diffusive mixing. It is immediately apparent that none of these process variables are completely independent of each other, and Kukukova et al. (2009) found their relationships difficult to define in a cause and effect manner.

The work of Dimotakis (2000) defines turbulent mixing in terms of a cascade of consec-

(a) Large-Scale Structures (b) Vortex Breakdown to Smaller Scales

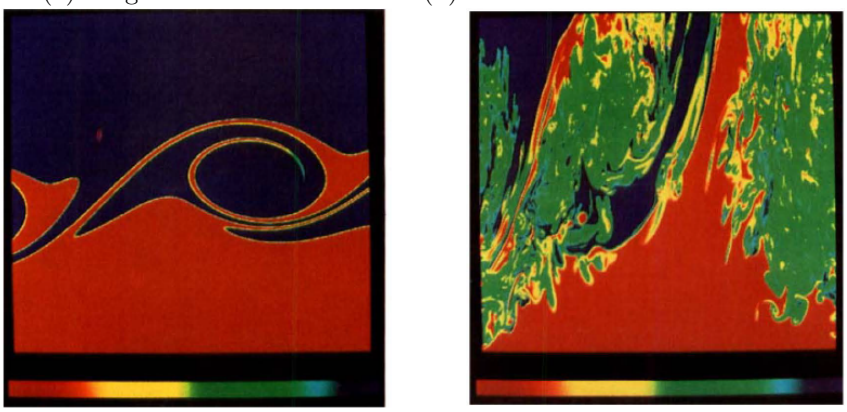


Figure 1.6: The evolution of a mixing layer from (a) large, coherent structures to (b) smaller scales. From Koochesfahani and Dimotakis (1986).

utive processes in the flowfield itself. These steps can all be explained by examining the evolution of a shear layer. First, due to the velocity-induction effect of the Biot-Savart Law, the vortex structure in the shear layer engulfs some of the fluid from both the jet and the crossflow. This process is associated with large scales (low wave-numbers). Now that fluid has been engulfed, the nonlinearity of the Navier-Stokes equations results in energy transfer to higher wave-numbers (smaller scales) and distortion of the mean flow that leads to secondary instabilities of smaller scales. This energy transfer and mean flow distortion, as well as the growth of other unstable frequencies, is manifested physically by the appearance of progressively smaller structures on top of the large structures. This evolution is what is referred to as turbulent stirring; energy transfer from small to intermediate wavenumbers and secondary instability growth manifested as a chaotic reorganization of the fluid particles. Fig. 1.6 is a visualization of the fluid engulfment (a) and subsequent emergence of smaller scales (b). The third and final process of turbulent mixing occurs at the smallest scales (highest wavenumbers), which is characterized by the dissipation associated with molecular momentum diffusivity, ν, molecular thermal diffusivity, α, or molecular mass diffusivity, D, depending on the flowfield parameter of interest. It is immediately obvious from this view of turbulent mixing that large scale flow features such as mean gradients and initial shear layer instabilities have a direct effect on the efficiency of mixing of the flowfield.

Comparing the flowfield (Dimotakis, 2000) and process variable (Kukukova et al., 2009) methods for defining mixing yields striking similarities. If all pertinent length scales are resolved in a measurement (so molecular-level mixing is captured), the intensity of segregation can be regarded as a measure of the molecular mixing, and the scale of segregation can be regarded as a measure of the turbulent stirring. There is no direct analog to the exposure process variable, but that is because the "exposure" is a result of all three physical mixing processes combined. The large scale fluid motion, the turbulent stirring, and the molecular mixing in the diffusion regime all affect the potential for further molecular mixing. It is because of this reason that most mixing quantification parameters fall into either the intensity or scale of segregation categories. As explained in Shan and Dimotakis (2006), mean quantities such as the average spread or concentration decay of a jet can be regarded as measures of the fluid entrainment. Therefore, a complete characterization of the physical mixing process requires a mean measure of entrainment, a measure of the turbulent stirring, and a measure of the molecular mixing. Unfortunately, as demonstrated by (Kukukova et al., 2009), these processes are intricately connected with each other, and there is no immediately apparent method of measuring them separately. For instance, a variance based measurement intended to characterize molecular mixing applied to a highly turbulent flow could be dominated by the effect of turbulent stirring. It should also be noted that although it is desirable, it is not strictly necessary to resolve all scales down to the Kolmogorov (or Batchelor) scale to distinguish efficiency between molecular mixing processes; it is only necessary to resolve the flowfield parameter being measured down to the scales at which diffusion becomes important (diffusive regimes in the wavenumber spectrum). A more in-depth look at the scales and resolution associated with the present experiments will be given in Chapter 4.

There are many different mixing quantification parameters that can be utilized to characterize the jet in crossflow in terms of the three mixing processes discussed earlier. Measures of the entrainment or large-scale flow reorganization that are pertinent to this flowfield include the mean concentration decay and the mean spread of the jet. These two parameters can be defined in different ways; the concentration decay could be along the centerline of the jet as in Smith and Mungal (1998) and Su and Mungal (2004), or it could be a tem-

porally and spatially-averaged concentration decay of the jet cross-section as one moves the measurement plane downstream of jet injection. The spread could also be measured using different methods. Variations of this parameter quantification include the spread of the jet on the centerplane in the vertical (Davitian et al., 2010b) or trajectory-normal (Smith and Mungal, 1998; Getsinger, 2012) directions, or the spread of the jet cross-section in either the vertical or lateral direction. A more complete quantification of the jet spread, as utilized in Niederhaus et al. (1997), is the diameter of a circle containing the same area as the jet cross-section.

Parameters for quantifying the intensity of segregation, which can be applied to jet cross-sectional slices, are typically of the variance-type. For instance, Unmixedness (Equation 1.7) is a parameter commonly used as a quantification of mixing (Danckwerts, 1952; Dimotakis and Miller, 1990; Smith et al., 1997; Getsinger, 2012).

$$U = \frac{1}{L_y L_z} \int \int \frac{(C/C_o - \overline{C}/C_o)^2}{\overline{C}/C_o(1 - \overline{C}/C_o)} dydz \tag{1.7}$$

In Equation 1.7, C/C_o is the local concentration value in the instantaneous concentration field, and $\overline{C}/C_o$ is the average of this concentration over the entire spatial domain, $L_y L_z$. The Unmixedness, as defined in Equation 1.7, is essentially a variance measurement about a spatial mean, scaled by the variance that would arise from completely unmixed fluids with the same mean value. A completely molecularly mixed fluid would have zero variance about the mean, resulting in a zero Unmixedness. Another measurement of the intensity of segregation is the Spatial Mixing Deficiency (SMD), as outlined in Equation 1.8.

$$SMD = \{\frac{1}{L_y L_z} \int \int [\frac{C/C_o - \overline{C}/C_o}{\overline{C}/C_o}]^2 dydz\}^{1/2} \tag{1.8}$$

These two measurements are very similar. The only significant difference is found in the normalization. Spatial mixing deficiency is a direct measure of the variance about the mean, and is therefore scaled by the mean. Unmixedness, however, takes into account the fact that the concentration can only vary between zero and one (Dimotakis and Miller, 1990). This small discrepancy can result in significantly different trends as evidenced by the work of Getsinger (2012) for the low density transverse jet. It should be noted that because of

the difference in normalization between these two parameters, Unmixedness is sensitive to the actual concentration values relative to the jet concentration value of one, whereas SMD is independent of actual concentration due to its scaling. However, when the mean value is matched, these two intensity of segregation metrics yield similar trends in mixing.

Another measure of the intensity of segregation is the spatial probability density function (pdf) of the concentration (Smith and Mungal, 1998; Shan and Dimotakis, 2006), as calculated using a histogram of the concentration data. For a theoretically perfectly mixed fluid, the spatial probability density function would reveal a Dirac delta function δ at the mean value. For a completely unmixed fluid, two separate Dirac delta functions would be found at concentrations values of zero and one. An increase in mixing or a decrease in intensity of segregation can be visualized in the probability density function by an increase in the peak (most probable concentration) and a subsequent development of valleys in the pdf, as shown in Figure 1.7 from the data of Shan and Dimotakis (2006). The pdf and Unmixedness calculations can be applied to instantaneous images and the values obtained can be averaged over the entire set of images, or they can be applied to a specific region of the flow over time. As long as the method of application is consistent and the resolution is sufficient, these mixing metrics should be able to differentiate between degrees of mixing. The method of application of these mixing metrics in a meaningful way for an open-boundary system such as the jet in crossflow will be summarized in Chapter 4.

Another, more fundamental method of measuring molecular mixing is by inducing a chemical reaction. Chemical reaction precludes the need to resolve measurements down to the smallest scales in order to quantify molecular-level mixing since the reaction itself occurs at the molecular level. Quantification of mixing via reaction is most commonly used in studies examining acid-base reactions, e.g., in dilute liquid jets in crossflow (Broadwell and Breidenthal, 1984; Johari et al., 1999; Eroglu and Breidenthal, 2001). If the chemical reaction is not highly endothermic or exothermic, no significant alterations to the flowfield are expected, and the degree of reaction completeness, e.g., acid neutralization by base, can be regarded as a direct measure of molecular mixing. Unfortunately, the chemical reactions that can be generated in a gaseous flowfield are typically highly exothermic, resulting in significant

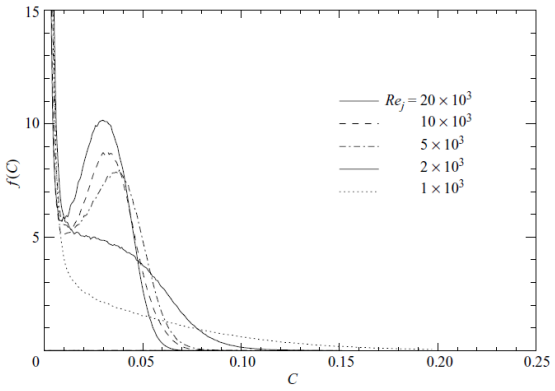


Figure 1.7: Concentration probability density function of a jet in crossflow with increasing Reynolds number indicating increase in mixing. From Shan and Dimotakis (2006).

density and transport property alterations that can distort the mixing characteristics of the non-reactive case. There are two-tracer methods that yield accurate measurements of molecular mixing such as NO-Planar Laser-Induced Fluorescence (PLIF) and acetone-PLIF, but these methods require two separate excitation sources (Meyer et al., 2002).

Because the stirring of the flowfield is an inherently turbulent process, the scale of segregation can only be quantified using instantaneous data. There are several different measures of this mixing metric present in the literature. One of the more physically intuitive measures is the scalar dissipation rate, χ, (Smith et al., 1997; Su and Clemens, 1999). The scalar dissipation rate, as defined in Eq. 1.9 (D is molecular diffusivity), is essentially a measure of the destruction rate of scalar energy $\frac{1}{2}\zeta^2$.

$$\chi \equiv D\nabla\zeta \cdot \nabla\zeta = D|\nabla\zeta|^2 \tag{1.9}$$

The higher the scalar dissipation rate, which is similar to a local rate of strain, the larger the scalar gradients in the flowfield, and hence the smaller the scales of segregation. If this scalar destruction or dissipation rate is low, large quantities of turbulent stirring are not present in the flowfield. This could be either because the flow has been molecularly mixed sufficiently, or because the flow is still fairly laminar, which reveals once again that a true quantification of mixing for a highly turbulent process needs both an intensity of segregation metric and a scale of segregation metric. Bothe (2010) used a spatially-averaged scalar dissipation rate

calculation to determine an integral scale of segregation. A more in-depth look at the scalar dissipation rate and its relation to the mixing/reaction processes in fluid flows will be given in Section 1.3.

Another possible measure for the scale of segregation is a probability density function of the scalar difference for a given separation distance between two points of measurement along a specific direction (Shan and Dimotakis, 2006). However, this method only gives the probability for a given separation distance; it cannot be used as a global scale of segregation metric. A more informative calculation is the integral length scale from statistical turbulence theory. Defined in Eq's 1.10 and 1.11, using a correlation function called the correlogram, $R(h)$, for a given separation distance, h, and integrating $R(h)$ yields a length scale that can be used as a measure of the average size of structures in the flowfield (Danckwerts, 1952).

$$R(h) = \frac{1}{N(h)} \sum_{N(h)} \frac{(C_i(x) - \overline{C})(C_i(x+h) - \overline{C})}{\sigma^2} \tag{1.10}$$

$$L_R = \int_0^{\frac{1}{2}A_{int}} R(h)dh \tag{1.11}$$

For a scalar distribution with very small structures, the correlation function $R(h)$ would fall to zero much faster than in a flowfield with larger structures, which would result in a smaller integral length scale. However, this method does not work well for flows with large-scale segregation since points far from each other will be negatively correlated.

A recently formulated mixing metric known as the Mix-Norm (Mathew et al., 2005; Gubanov and Cortelezzi, 2010) attempts to rectify the inability of variance-based measures of mixing such as the Unmixedness to capture small-scale variations in chaotic and turbulent flows. When the flow is highly turbulent, most of the fluctuation energy content is contained within the large scales. However, since diffusion in these flows occurs as the smallest scales, the level of molecular mixing quantified by these variance-based mixing measures could be overshadowed by the large-scale turbulent stirring. An attempt at applying the Mix-Norm to the mixing quantification of the current JICF study resulted in identical results to the Unmixedness quantification, suggesting that the Reynolds number of this study is not high enough for significant scale separation between the stirring and mixing processes to be

present within the flowfield. This contention will be verified with a study on the variation of Unmixedness with probe resolution summarized in Chapter 4.

1.3 Velocity Field Strain and Scalar Dissipation

In both laminar and turbulent flowfields, the fundamental mechanism of fluid mixing is molecular mass diffusion. The rate at which diffusion acts to enhance uniformity of concentration is dependent on the gradient of concentration of the fluid being mixed, and it also depends on the total interfacial area between the dissimilar fluids. Transitioning from laminar to turbulent flow enhances both of these mechanisms by modifying the underlying strain rate field that transports and contorts the scalar field. The strain rate field, ϵ, is characterized by the symmetric portion of the velocity gradient tensor, ∇u, as defined in Equation 1.12

$$\epsilon_{ij} = \frac{1}{2}(\frac{\partial u_i}{\partial x_j} + \frac{\partial u_j}{\partial x_i}) \tag{1.12}$$

Variations in strain rate cause variations in scalar dissipation rate (Equation 1.9), altering the local mixing rate of the flow.

Many studies have delved into the relationship between scalar dissipation rate and strain rate in turbulent flowfields. The two-part study of Buch and Dahm concerning the relationship between the scalar dissipation structure and the strain rate field in a fully turbulent free jet (Buch and Dahm, 1996, 1998) showed that the effect of the underlying strain field on the scalar dissipation field depends on the local Schmidt number, Sc. As mentioned in Section 1.1.1, the Schmidt number is a dimensionless parameter that relates the momentum diffusivity of a flowfield to its mass diffusivity. In liquid flows, $Sc = O(1000)$, while in gaseous flows, $Sc = O(1)$. Thus, neighboring scalar dissipation layers in turbulent liquid flows experience essentially uniform strain rate whose variation with spatial coordinate along each layer can be neglected in the modeling of these flows, although strain rate variations in time can still be important, especially in highly turbulent flows. As shown in (Buch and Dahm, 1996), the low spatial variance of the strain rate in liquid flows results in reduced folding and contortion of the scalar dissipation structures. Moreover, neighboring dissipation layers

tended to align parallel to each other, and had a layer-like topology. Similar results were found for $Sc = O(1)$ in the work of Buch and Dahm (1998), although the scalar dissipation fields exhibited more contorted structures and variation in scalar gradient direction owing to the spatially varying strain field. The resulting layer-like topologies of the scalar dissipation rate fields in both of these studies suggested that the scalar gradient preferentially aligned with the minimum principal compressive axis.

Orientation of the scalar gradient in relation to the strain field has been studied extensively in turbulent flows. The numerical studies of isotropic turbulence and shear flows by Kerr (1985), Ashurst et al. (1987), and Vedula et al. (2001) concluded that the scalar gradient structures tend to align perpendicular to line-like vortex tubes, along the most compressive component of the strain-rate tensor. The highest scalar dissipation rates in these studies were found in regions where the angle between the principal compressive axis and the scalar gradient was negligible. The four-dimensional scalar and velocity field experimental measurements of Su and Dahm (1996) found large degrees of preferential alignment between the scalar gradient direction and the maximum principal compressive strain axis. Moreover, this work showed further increases in preferential alignment between the scalar gradient and maximum principal compressive strain when the data was conditioned to the highest scalar gradient values, verifying the numerical results mentioned previously. Similar results were found in the simultaneous PLIF/PIV measurements of nonreactive turbulent free jets, and reacting turbulent flames in the work of Rehm and Clemens (1999). These studies suggest a simplified model of the local strain rate and its relationship to the local conserved scalar dissipation rate could be generated and applied to turbulent flowfields.

1.3.1 Strained Laminar Layer Models for Turbulence

Due to the complexity of turbulent flows, various models have been formulated in an attempt to simplify the flowfield structure for simulation purposes. Modeling is particularly important for turbulent combustion, as the species transport equations can be formulated in a conserved mixture fraction form that could be modeled in the non-reacting reference frame. Many of

the turbulent mixing models attempt to structure the flow as a set of one-dimensional, quasi-steady, strained laminar diffusion layers. One of the more well-known models is the flamelet model for analysis of turbulent combustion (Marble and Broadwell, 1977; Peters, 1986). Assuming a thin flame, asymptotic expansion and order of magnitude arguments result in a one-dimensional conservative advection-diffusion equation that can be applied to a turbulent combustion process. However, since this model assumes fast chemistry, departures from equilibrium result in erroneous conclusions about the flowfield structure. Another, more broadly applicable formulation is described in the Strained Dissipation and Reaction Layer (SDRL) analysis of Bish and Dahm (1995). Assuming a locally one-dimensional, layer-like structure of the scalar dissipation rate field (which is consistent with the experimental findings for turbulent scalar mixing summarized in Section 1.3), and applying a quasi-steady simplification of the resulting advection-diffusion equation, an equation relating the spatially uniform compressive strain rate normal to the layer to the scalar dissipation rate can be extracted:

$$\epsilon_{SDRL} = 2\pi \left(\frac{\chi}{(\zeta^+ - \zeta^-)^2} \right) e^{2\left(erf^{-1}\left(\frac{\zeta - 0.5(\zeta^+ + \zeta^-)}{0.5(\zeta^+ - \zeta^-)} \right) \right)^2} \tag{1.13}$$

Strictly speaking, Equation 1.13 only applies to flows in which the compressive strain rate normal to the layer can be approximated as being spatially uniform. If two-dimensional, planar, conserved scalar measurements are utilized to calculate the compressive strain rate from the scalar dissipation rate, errors can result from three-dimensional effects. Any deviations from the one-dimensional approximation, such as significant velocity or scalar variation along the layer, high surface curvature, or significant out-of-plane velocity/scalar variation, could affect the results.

Transient effects are another potential source of deviation between the compressive strain rate calculated from the scalar dissipation rate and the actual local compressive strain rate in the flow. Unsteadiness and its effect on the correlation between strain rate and scalar dissipation rate in turbulent flows has been studied extensively by Kothnur and Clemens (2005). This work compared simultaneous 2D PLIF/PIV measurements of strain rate and scalar dissipation rate to the laminar diffusion layer model with an imposed, harmonically varying strain rate. The response time of the scalar dissipation layer thickness to the imposed strain

rate depended on the strain rate fluctuation amplitude and frequency. Comparisons between the model and experiments suggested that the finite response time had a non-negligible effect on the highly turbulent flow scalar dissipation structures. The scalar dissipation layers with greater than average strain rate tended to be thicker than predicted by the quasi-steady state theory, whereas the layers with lower than average strain rate tended to be thinner, which is consistent with the finite dissipation structure response time. Moreover, it was also shown that the model agreed best with the experimental results when the strain normal to the layer in the model was allowed to become extensive for a portion of the harmonic cycle, suggesting that scalar dissipation structures in turbulent flows do experience significant extensive strain during their lifetimes. However, since there is no quasi-steady state solution for extensive principal strain normal to a scalar dissipation layer, a scalar dissipation structure will not persist in the presence of continuous extensive strain.

1.3.2 Strain, Dissipation, and Reaction

As mentioned previously, many of the studies and models concerning strained scalar dissipation layers are motivated by the fact that the mixing process in a non-reactive flow can be related to the combustion process in an equivalent reactive flow. However, when the time-scales associated with the combustion process become important, more complex, time-varying behavior can result. For instance, when the strain field normal to a diffusion flame gets so large that the finite-rate kinetics cannot sufficiently burn the reactants into products fast enough to sustain a high temperature reaction zone, flame extinction can occur. This type of complex interaction between reaction and flow processes is very common in highly turbulent flows. For an excellent review of finite-rate reaction processes such as ignition, liftoff, and extinction in gaseous diffusion flames, refer to Linan et al. (2015).

Several studies have explored finite reaction-rate behavior in turbulent, reacting jets in crossflow. Steinberg et al. (2013) explored the structure and stabilization of heated H_2/N_2 jet flames in heated air crossflows using PIV and OH-PLIF. They found two flame branches in the centerplane of the jet: one on the windward side, and one on the lee-side. The lee-side

flame was relatively stable, and its stability increased with increasing jet speed, a result they attributed to a strengthening of the lee-side recirculation zone created by the interaction between the crossflow and the jet. In contrast to the lee-side, there was little positional stability of the windward-side flame branch, although the windward-side flame branch did seem to reside immediately downstream of regions with high extensive principal strain. In the work of Sullivan et al. (2014) that studied a reacting transverse jet in vitiated crossflow, average windward-side standoff location was shown to depend on momentum flux ratio J, with increasing standoff distance as J increased. These results suggest significant dependence of the flame characteristics of the reacting jet in crossflow on the underlying velocity and scalar field characteristics.

1.4 Focus of Current Studies

The previous sections have emphasized the importance of the mixing characteristics of the jet in crossflow. The work summarized seems to show a distinct difference in mixing efficiency as governing parameters are varied and different stability characteristics are encountered. Unfortunately, the mixing efficiency data available for the low Reynolds number and low momentum flux ratio regime for different density ratio jets is scarce and does not fully quantify the various processes associated with mixing. Moreover, different mixing metrics for quantification of the mixing progress in open-boundary systems have not been compared in a systematic and methodical method that is applicable for variable mass/molar ratio flows. Additionally, attempts to extract strain rate from scalar dissipation rate in transverse jets have not be undertaken.

This dissertation describes research on low density and equidensity non-reactive jets in crossflow in our laboratory. Building on studies by Getsinger (2012), an examination of the relationships among jet structure, symmetry/asymmetry, instabilities, and mixing was administered using non-intrusive optical diagnostics such as acetone-PLIF and stereo PIV, as well as hot wire anemometry. Both flush-mounted and elevated nozzles were utilized, and a flush-mounted straight pipe injector was characterized for its structure and mixing efficiency

as well. This study characterized mixing efficiency using various measures of entrainment, stirring, and molecular diffusion for low Reynolds number, low momentum flux ratio jets in crossflow at various density ratios and how this efficiency varied in different shear layer stability regimes. The effect of transverse jet evolution on the local strain rates, and scalar dissipation rates, in the flowfield were also studied. The strain field has important implications for the ability of the transverse jet to ignite and sustain a combustion reaction, as noted previously. Moreover, the ability to quantify strain rates from scalar field measurements (via acetone PLIF) and velocity field measurements (via stereo PIV) could provide important insights into the application of the strained dissipation and reaction layer approach in studying transitional flowfields.

CHAPTER 2

Experimental Setup and Diagnostics

2.1 The Jet in Crossflow Experimental Setup

The transverse jet flowfield configuration is generated using a low speed blower-type wind tunnel, as shown in Fig. 2.1. An adjustable frequency electric motor was used to drive a centrifugal blower in order to provide the crossflow of air. Before entering the 9:1 area ratio contraction section, the air from the blower was conditioned using honeycombs and screens of decreasing cell and mesh sizes in order to break down turbulent structures to smaller (dissipative) scales. For a brief overview of the effect honeycombs and screens have on flow uniformity and turbulence, refer to Barlow et al. (1999). Measurements of the crossflow suggest that after flow conditioning and contraction, the maximum attainable free-stream crossflow velocity, U_∞, was 7.00 m/s with a maximum turbulence intensity of less than 1.5% in the freestream. The exit of the contraction section was fitted flush with the 30 cm x 12 cm x 12 cm test section, which was spray painted black with barbecue grill paint to minimize optical reflections. Since light in the ultraviolet range of the spectrum was to be utilized for the non-intrusive measurements (see Section 2.3.1), the top window of the test section was made out of quartz. A plexiglass window was used for the side of the test section that required optical access, and a black side panel was used for the side that did not require optical access. During hotwire measurements, this black side panel was replaced with one that had appropriate cutouts for hotwire traversal. One additional test section of equal dimensions (without optical access) was mounted flush with the end of the primary test section. The second test section was followed by a 30 cm x 30 cm x 30 cm wooden chamber with an exhaust duct attached to the top. This wooden box was fitted with a 90 mm x 90

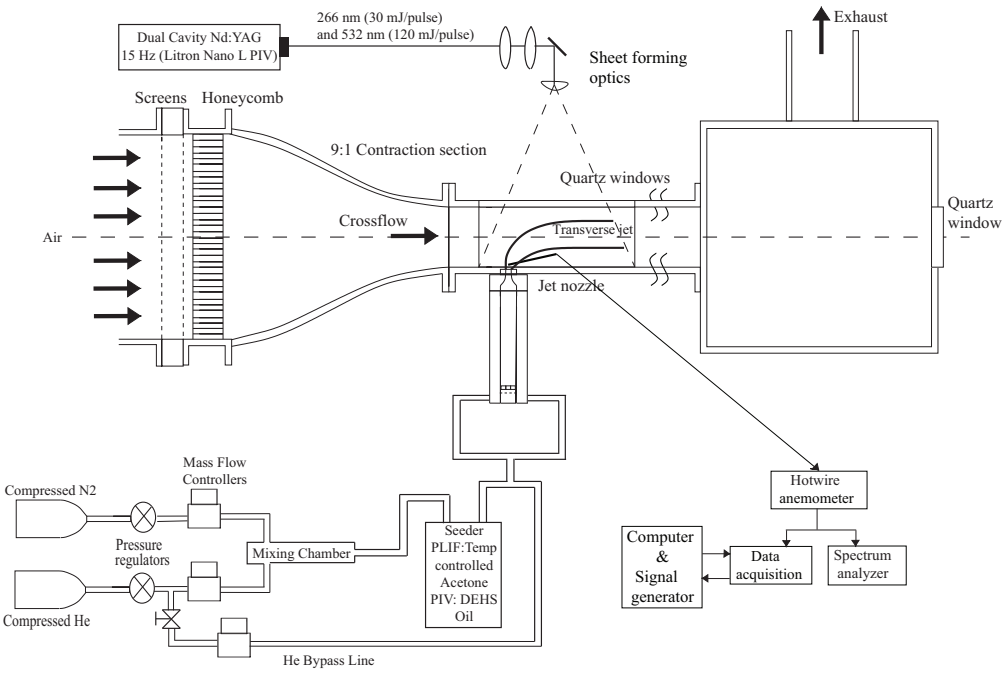


Figure 2.1: Variable density transverse jet wind tunnel, with associated data acquisition and optical diagnostic apparatus. One additional tunnel section, of identical dimensions, was situated downstream of the test section shown.

mm quartz window that allowed optical access from downstream looking upstream in the $-x$ direction for jet cross-sectional (yz-plane) imaging.

Tylan (model FC-260, (1) 0-5 NLPM N_2 and (1) 0-5 NLPM He, 1% calibration accuracy, 0.2% repeatability) and MKS (model GM50A, 0-70 NLPM He, 1% calibration accuracy, 0.3% repeatability) mass flow controllers were used to provide the appropriate proportions of helium and nitrogen to form a jet with the desired jet Reynolds number, Re_j, and jet-to-crossflow density ratio, S. The gas flows from these controllers were mixed in a passive mixing chamber. The output of this chamber was fed directly to four symmetrically oriented injectors attached to a plexiglass pipe just upstream of the nozzle (see Section 2.3 for modifications to fluid piping during optical measurements). Beneath this plexiglass pipe was a plexiglass plenum, housing either a loudspeaker or a piston-based actuator, used in separate studies to apply controlled longitudinal acoustic excitation (M'Closkey et al., 2002; Davitian et al., 2010b; Hendrickson and M'Closkey, 2012).

Some flow conditioning was administered between the 4-way injection point in the plexi-

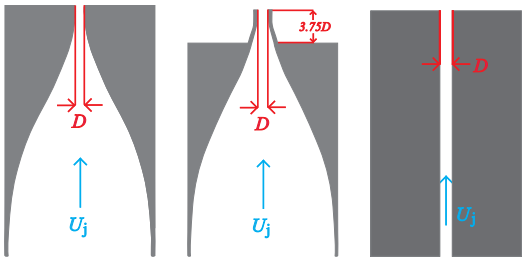


Figure 2.2: Alternative jet injectors studied: (a) flush nozzle (b) elevated nozzle (c) straight pipe.

glass pipe and the entrance of the nozzle. A honeycomb flow straightener of 0.3 cm cell size and 2.5 cm length, along with a 0.9 m length of straight PVC pipe were used to enhance the uniformity and symmetry of the velocity profile at the inlet of the nozzle. The PVC pipe length was sufficient enough to create a fully developed laminar velocity profile at its exit, alleviating any potential flow asymmetries or non-uniformities upstream of the nozzle. The well-conditioned gas flow exiting the PVC pipe was fed into the jet injector threaded into the test section.

Three separate types of injectors were used in this study: a flush-mounted nozzle, an elevated nozzle, and a flush-mounted pipe, each with an approximately 4 mm exit diameter (shown in Fig. 2.2). Uncertainties in the machining process resulted in slight differences in the exit diameter between the elevated and flush nozzles (4.04 mm diameter exit for the flush nozzle, 3.94 mm diameter exit for the elevated nozzle). The nozzles were machined with similar fifth-order polynomial contractions that generate essentially identical thin jet boundary layers at the jet exit in the absence of crossflow. However, as documented in Megerian et al. (2007), the jet exit velocity profile is considerably altered for both flush and elevated nozzles, with an increased upstream momentum thickness, for jet-to-crossflow velocity ratios below 4 (approximately). The only significant difference between the two nozzles was that the exit plane of one was mounted flush with the tunnel floor (hereafter referred to as the flush nozzle), whereas the exit plane of the other nozzle protruded into the test section by 3.75 jet diameters (hereafter referred to as the elevated nozzle). The protrusion length of the elevated nozzle was large enough such that all crossflow conditions currently studied had

boundary layer thickness significantly below the jet exit plane ($\delta_{99\%}/D \approx 2.3$ for the lowest crossflow velocity condition explored here, $U_\infty = 1.01\ m/s$). The third injector consisted of a straight pipe made of aluminum mounted flush with the test section floor (3.77 mm exit diameter). In order to thread this injector into the test section, the PVC pipe mounted between the plexiglass plenum and either of the nozzle injectors was necessarily removed due to space constraints, although the pipe alone was more than long enough to create a fully developed velocity profile at the jet exit, verified via hotwire anemometry, for the Reynolds numbers studied in this experiment without the need for utilization of the PVC pipe ($L/D = 155$). The jet fluid density and the mixture viscosity were determined using the constraints on Re_j and the density ratio S (viscosity determined by the Wilke formulation (Bird et al., 1960)). Gas mixture density relations were previously validated down to $S = 0.55$ using an acoustic waveguide in our laboratory (Canzonieri, 2009; Canzonieri et al., 2009).

The jet Reynolds number was kept constant at $Re_j = 1900$ for the mixing efficiency studies here, whereas jet-to-crossflow density ratio S was varied to determine the effect of this parameter on structure and mixing efficiency ($0.35 \leq S \leq 1.00$). Some results at other jet Reynolds numbers will be shown to emphasize the effect of this parameter on the jet cross-sectional structure. Jet-to-crossflow momentum flux ratio J was varied independently of density ratio by varying the speed of the crossflow. For a given density ratio, jet fluid flowrates were identical among different momentum flux ratios, and very similar for different injectors. The slight differences in jet exit diameter resulted in small mean jet velocity differences, however. Yet, given the transverse jet's strong dependence on momentum flux ratio J (Kamotani and Greber, 1972; Smith and Mungal, 1998; Megerian et al., 2007) and lesser dependence on jet Reynolds number (Megerian et al., 2007), small differences in mean jet exit velocity with fixed J, Re_j, and S are not expected to significantly affect comparisons among different injectors.

2.2 Hotwire Measurements

The mean velocity profile at the jet exit plane, the crossflow velocity profile just upstream of the jet exit, and the spectra of the upstream shear layer of the jet were measured using a single component, boundary-layer type hotwire probe (Dantec 55P15) that was situated on a linear stage platform capable of traversal in all directions with 1 µm accuracy. The hotwire was also used for spectral measurements during the stability characterization in previous experiments (Megerian et al., 2007; Davitian et al., 2010a; Getsinger, 2012). The output from the hotwire was fed to a Dantec constant temperature anemometer module, whose resulting signal was quantized and analyzed using a dSPACE 1104 DSP data acquisition (DAQ) board in conjunction with Matlab software.

When the thermal transport properties of the fluid mixture being analyzed were negligibly different from that of air, the hotwire was calibrated using a pitot tube and the crossflow. The pitot tube was attached to a 0-3″ H_2O differential pressure transducer for high velocity calibration, and a 0-0.25″ H_2O transducer for improvement of low velocity characterization. This method was also used to calibrate the centrifugal blower's electric motor frequency to crossflow velocity.

2.3 Optical Diagnostics

While a hotwire provides high temporal resolution measurements of velocity and illuminates the nature of the instability of the transverse jet shear layer, the inherently intrusive nature of this measurement tool casts doubts on the data obtained. Because optical diagnostic techniques have the advantage of minimizing perturbations to the flowfield during measurement, they have become a highly desired interrogation method for experiments in fluids. Optical imaging can be separated into two distinct categories: line-of-sight and planar. Light of sight measurements such as smoke visualization and OH-chemiluminescence imaging have the advantage of being relatively inexpensive, but the inherent integration over optical rays these methods utilize can lead to misleading quantitative conclusions. Planar measurements,

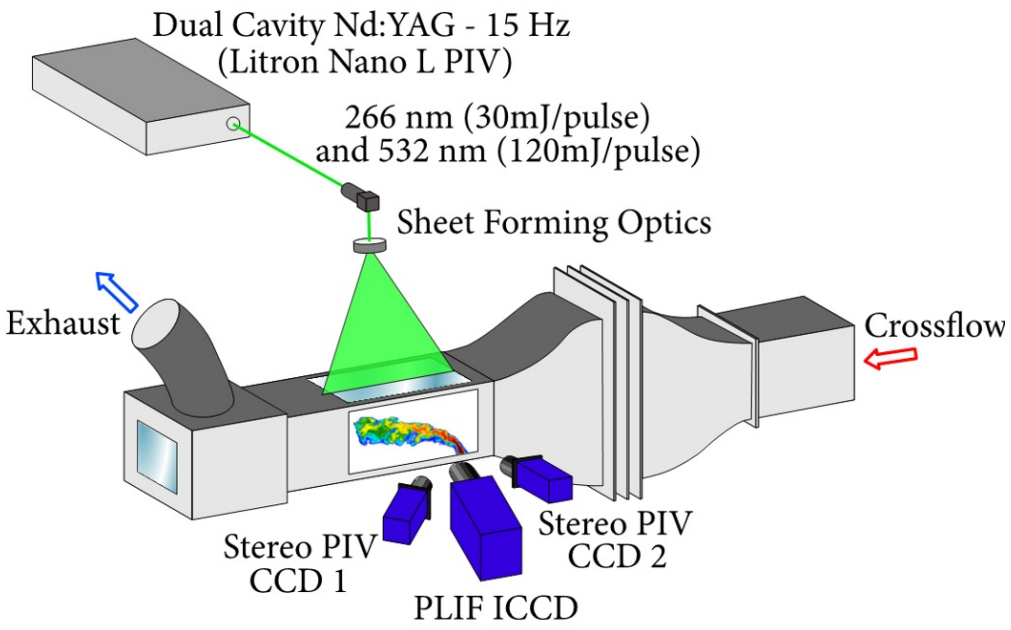


Figure 2.3: Schematic of the basic excitation and imaging setup for stereo PIV and acetone PLIF measurements in the transverse jet wind tunnel test section.

although usually more expensive, produce data that is only integrated over the thickness of the light sheet along an optical ray. In the limit of negligible sheet thickness compared to relevant length scales in the flowfield, much more highly resolved two dimensional data sets are produced when compared to line-of-sight measurements. Because of the obvious advantage of a planar measurement, this was the technique used for the present non-reactive experiments. The planar measurement technique utilized for structure and mixing characterization in this experiment was planar laser-induced fluorescence (PLIF) of acetone, and stereo particle image velocimetry (PIV) was used for velocity, vorticity, and strain field quantification.

A schematic of the general setup for planar imaging in the transverse jet is shown in Fig. 2.3. Monochromatic laser light at 1064 nm was produced by a dual cavity Q-switched Nd:YAG laser (Litron Nano L PIV). This infrared light was passed through second and fourth harmonic generators producing concentric beams at 532 nm and 266 nm. These beams were formed into a sheet by a combination of two spherical lenses, a turning mirror, and a $f = -10$ mm cylindrical lens. The sheet could be rotated with respect to the z-axis

for switching between centerplane and cross-sectional imaging, and the entire wind tunnel could be traversed in the direction of the crossflow using a stepper motor connected to a linear stage and controlled by the DAQ with Matlab. The purpose of traversing the wind tunnel was to image cross sections of the flowfield at several positions downstream of jet injection. Each cavity of the laser was capable of producing 8ns FWHM pulses with 30 mJ at 266 nm and 120 mJ at 532 nm. The maximum repetition rate of the laser was 15 Hz, although standard operation was well below this threshold (typically 2-7.5 Hz). Control of the laser and synchronization of the imaging was achieved using an external programmable timing unit and LaVision's DaVis 8.2 software.

2.3.1 PLIF

Planar laser-induced fluorescence (PLIF) is an optical measurement technique that exploits a tracer species' ability to fluoresce after it has been excited to a higher electronic energy state by a wavelength of light that falls in the fluorescence band of that species. When returning to its ground state, a significant portion of the excited molecules emit light at a wavelength different from the incident wavelength. This light can be captured with an appropriate imaging tool. The sensitivity of this fluorescence signal to incident light energy and tracer species concentration make it a very attractive concentration measurement method. Moreover, the fluorescence intensity decays very rapidly (on the order of ns), making this measurement technique useful for short time-scale phenomena such as high speed and/or reactive flows. For more information about the development of PLIF techniques for reactive flows, refer to Hanson et al. (1990).

There are many molecules that become excited and fluoresce in wavelength bands that are advantageous for experiments in fluids. In numerous reactive flowfields, the tracer molecule is a natural by-product of the reaction, such as NO or OH. When the naturally occurring species in the flowfield do not fluorescence or their excitation/fluorescence bands cannot be exploited properly, a seeded molecule is typically added to the flowfield. Some commonly used seeding species for fluorescence measurements are rhodamine or fluorescein dyes, I_2,

acetone, or biacetyl. In this experiment, acetone ($CH_3 - CO - CH_3$) is used for a number of reasons, not the least of which is its relatively mild toxicity and low cost. Other advantages of acetone as a seeded tracer molecule include high vapor pressure resulting in high seeding concentrations, low fluorescence lifetime (4 ns), and a broad excitation wavelength band as well as good separation between excitation and emission bands (excitation band: 225-320 nm, emission band: 300-500 nm). Moreover, acetone fluorescence is not quenched by the presence of oxygen like the phosphorescence of biacetyl, which is another tracer species used to characterize concentration in low speed flows due to its high quantum efficiency (15%). Fortunately, the phosphorescence lifetime of acetone is 200 µm which makes gated imaging a natural choice for capturing the fluorescence signal and minimizing contamination from the phosphorescence. Moreover, the presence of oxygen strongly quenches the phosphorescence of acetone. The combining effects of gating around the fluorescence signal and strong quenching of the phosphorescence signal in flow regions with oxygen concentration render the effect of the phosphorescence signal on the fluorescence images negligible. For a thorough summary of the photophysics of acetone and biacetyl, see Lozano (1992), Lozano et al. (1992), and van Cruyningen (1990).

For the PLIF measurements shown here, before being formed into a sheet, the 532 nm and 266 nm beams from the Nd:YAG laser were aimed towards a set of two 266 nm dichroic mirrors in order to turn the 266 nm but pass the 532 nm into beam dumps attached to the back of each dichroic mirror. This was done to remove most of the green light for purposes of increasing the signal-to-noise ratio (SNR) in the PLIF images. A 3 mm thick UV grade fused silica window was also situated between the exit of the dichroic mirror set and the entrance of the sheet forming optics set. The purpose of this window was to deflect a portion of the UV light (approximately 7%) to a pyroelectric joulemeter (Newport 818E-10-50-S) for pulse-to-pulse energy measurement to be used for PLIF image correction.

The 266 nm light sheet thickness was measured using the pyroelectric joulemeter and a razor blade that was traversed through the sheet using the hotwire's traversal mechanism (see Section 2.2). The resulting $1/e^2$ thickness ranged between 400-900 µm in the camera's field of view (FOV) for the structure and mixing quantification data sets. For the simultane-

ous PLIF/PIV data sets, the UV sheet thickness ranged between 1.4-1.9 mm. For the high resolution centerplane PLIF images, the thickness ranged between 360-450 µm. The simultaneous PLIF/PIV measurements required a thicker laser sheet so as to ensure reasonable PIV interrogation window correlation (see Section 2.3.2 for more details). Unfortunately, this could significantly affect the gradient measurements calculated from this data. However, gradient measurements from 2D data inherently assume small variations in the out-of-plane concentration and velocity, so it is assumed that flow measurements with large in-plane gradients have smaller out-of-plane components i.e. the gradient vector is approximately aligned with the measurement plane.

Since the PLIF signal captured by the camera can be thought of as a set of fluorescence data integrated in all three dimensions over each pixel, and the physical size of the portion of the measurement domain that each pixel is mapped to is typically much smaller than the thickness of the UV light sheet, the natural conclusion is that the lowest resolution direction of the PLIF data is the direction perpendicular to the measurement plane. The light sheet is not necessarily the limiting resolution, however, since concentration and velocity gradients in all directions are not equal. For instance, in the jet shear layer, near the potential core of the jet, in the centerplane ($y/D = 0$) images, $|\partial C/\partial y| << |\partial C/\partial x|$, where C is the concentration of any of the gas constituents of the jet. The variation in partial derivative magnitude that depends on direction is an important point to consider when determining the limiting resolution; it is obvious from the example given that the limiting resolution could be the pixel width in certain parts of the flow (e.g. near the jet potential core). More precisely, the combined effect of the optical transfer function of the entire imaging system acts as a smoothing filter on the concentration gradients in the plane of measurement. Therefore, a study of the effect of both pixel width variation and sheet thickness variation near the jet exit on the quantities calculated should give a reasonable estimate of the effect of resolution degradation on the results. Such an exploration will be summarized in Chapter 4 for the mixing results, and in Chapter 5 for the scalar dissipation rate/strain rate results.

Fluorescence images were captured with two different cameras. When stereo-PIV images were not to be taken simultaneously with the PLIF (which was the case for all the concen-

tration data used for mixing quantification), a 14-bit CCD camera (LaVision Imager proX) with 1600x1200 pixel resolution equipped with an external image intensifier (LaVision IRO) to boost signal was used to image the fluorescence. The external intensifier's optical setup resulted in the imposition of a centered circular aperture on the CCD array with a diameter of approximately 1500 pixels. The pixels that were outside this aperture were masked during post-processing. For experiments where stereo-PIV data was taken simultaneously with the PLIF data, the PLIF signal was captured with a 12-bit internally-intensified CCD camera (LaVision NanoStar) with 1280x1024 resolution. There was no circular aperture imposed on the CCD array for this internally-intensified camera. Four different camera lenses were used depending on the data set. For the centerplane images taken from the side of the tunnel through a plexiglass window, a Nikon 50 mm lens at f/2.0 equipped with a Vivitar +2 dioptre close-up lens was used for the mixing and structure data sets. The higher resolution (smaller FOV) centerplane PLIF data was taken with a 60 mm Nikon lens at f/2.8. The PLIF portion of the simultaneous PLIF/PIV data sets was taken with a 90 mm Sigma AF at f/2.8 equipped with a Vivitar +2 dioptre close-up lens. For the cross-sectional data taken through the quartz window attached to the exhaust box at the end of the wind tunnel (see Section 2.1), a Nikon 200 mm f/4.0 was fitted to the imaging camera. Regardless of the camera or lens used, all PLIF signals were first refined by a bandpass optical filter to remove background light but pass the fluorescence band wavelengths.

The in-plane resolution of the centerplane PLIF images taken for the structure and mixing studies ranged from 140 μm to 170 μm per pixel after 2x2 hardware binning was administered to increase the SNR. This resolution variation was necessary to capture enough downstream data for the higher-penetrating pipe flow configuration. The resolution of the smaller FOV centerplane PLIF images was 34 μm per pixel (no binning administered). The resolution of the PLIF portion of the simultaneous PLIF/PIV data was 65 μm per pixel after 2x2 hardware binning. Cross-sectional data resolution ranged from 120 μm to 160 μm per pixel after 2x2 hardware binning. The image intensifiers were gated for 200 ns around the fluorescence signal (0.1% of phosphorescence lifetime). For the PLIF data shown here, both laser cavities were fired with a 50ns temporal spacing in order to nearly double the incident light energy

within the gated period but still allow sufficient spacing between pulses to eliminate nonlinear interaction between the two laser firing processes that had been shown to result in a decrease in overall energy output. The 50 ns temporal spacing is several orders of magnitude smaller than any pertinent flow timescale resulting in negligible blurring (temporal averaging) of the fluorescence signal.

Since acetone is not a molecule that is inherently present in our flowfield, PLIF imaging necessitates the addition of a seeding apparatus in the fluid piping shown in Fig. 2.1. The seeding was accomplished by passing the N_2/He mixture exiting from the mixing chamber through sintered spray nozzles that were exhausted at the bottom a 7" tall x 7.5" diameter steel chamber 3/4 full with liquid acetone. This chamber was insulated from the ambient air and temperature controlled using a refrigerant re-circulator that pumped water through copper coils that spiraled through the center of the steel chamber. The coil dimensions were chosen to maximize surface area for heat transfer while simultaneously heating approximately equivalent volumes of acetone on either side of the coil spiral. The seeder temperature was measured using a Type T thermocouple inserted into the liquid acetone (Omega, with Analog Devices 2B50A Isolated Thermocouple Conditioner, 1°C max uncertainty). The pressure of the seeder was measured using a pressure transducer (Omega PX409-015G5V, 0-15 PSIG, 0.08% BSL calibration accuracy). In order to ensure saturation of the gas flow with acetone vapor, an additional seeder was added upstream of the temperature-controlled, pressure-monitored seeder.

Accurately quantifying the temperature and pressure of seeding is vital for determining the acetone concentration of the jet after seeding. Assuming acetone vapor saturation of the gas flow, the temperature of the acetone can be related to its vapor pressure (relation can be found in Lozano (1992)). The ratio of the vapor pressure to the total pressure in the seeder results in a measure of the molecular concentration of acetone in the jet. Controlled temperatures ranged between 12-20^{o}C depending on desired jet density, corresponding to acetone concentrations ranging between about 11-24% by volume (or mole fraction). The effect of adding acetone to the jet density and viscosity was taken into account using the Reichenberg method (Poling et al., 2001). Control of the molecular concentration of acetone

was an iterative process where a seeding pressure at a desired temperature was guessed and all gas flowrates were revised until convergence of pressure was attained. The refrigerant recirculator/copper coil combination was capable of regulating the temperature of the liquid acetone to within $\pm 0.2^{o}$C of the desired temperature, which resulted in negligible variations in vapor pressure. It should be noted that although the seeder was temperature-controlled, the tubing leading from the seeder to the injectors attached to the plenum was not. Because of the length of tubing in this portion of the fluid piping, it is reasonable to assume that the gas equilibrated with the ambient temperature by the time it reached the exit of the nozzle. The target seeding temperature, as measured by the thermocouple, was always kept below the room temperature to ensure that no acetone condensation occurred.

The raw images obtained from the CCD array need to go through a number of post-processing steps to be considered an accurate measure of jet fluid concentration. Some of the common corrections include bias error subtraction, shot-to-shot energy fluctuation normalization, and flat field (white image) correction. The bias errors taken into account include the mean camera dark noise and the mean background light signal. Shot-to-shot fluctuation of dark noise and background light are considered to be a part of the uncertainty in the final measurement. Another added complexity is the need to correct for laser sheet profile non-uniformity. Because the sheet produced by the forming optics is not collimated, the intensity can vary significantly along the length of the sheet. Moreover, because our excitation wavelength (266 nm) falls in the high absorption band of acetone, sheet energy absorption corrections also need to be administered.

The raw data captured by each pixel, S_i, is a combination of the acetone fluorescence, F_i, the camera dark noise, $B_{i,dark}$, which is highly dependent on the temperature of the CCD array (the cameras used in this experiment all have temperature-controlled CCD arrays to minimize dark noise), and the background signal associated with any light sources that are not a part of the fluorescence signal, $B_{i,light}$. All of these quantities are a function of the specific pixel as well as its position on the CCD array. The fluorescence can therefore be found using Equation 2.1 (time-averaged quantities denoted by an overbar):

$$F_i = S_i - \overline{B}_{i,dark} - \overline{B}_{i,light} \tag{2.1}$$

This fluorescence intensity has to be corrected for shot-to-shot energy fluctuations, light sheet profile differences, and light absorption when propagating through acetone. The resultant concentration of acetone C_i can be solved for by using Equation 2.2:

$$C_i = k\frac{S_i - \overline{B}_i}{\overline{L}_i - \overline{LB}_i} \tag{2.2}$$

The variable k is what takes into account all the efficiencies and shot-to-shot fluctuations of energy (as determined by the joulemeter) associated with this system. Its value is chosen such that the average concentration in a rectangular collection of pixels situated completely in the potential core of the jet is unity for all images taken. When the potential core of the jet was not in the camera's field of view such as in the cross-sectional yz-plane images, an attempt was made to compare a common line of data in the ensemble-averaged yz-plane images with the ensemble-averaged centerplane ($y = 0$) images and normalize appropriately to relate cross-sectional concentration to potential core concentration. This method resulted in satisfactory correction for the lower momentum flux ratio (J) cases but the asymmetrical and non-regular structure of the higher momentum flux ratio cases resulted in significant errors from this technique when taking data in the higher momentum flux ratio regime. For all PLIF data shown, concentration values are only reported when all corrections could be administered accurately. In Equation 2.2, $\overline{B}_i$ is a mean background image (ensemble average of 200 images with laser fire but no jet fluid in test section). It should be noted that both S_i and $\overline{B}_i$ have a mean dark image subtracted (ensemble average of 100 images with the lens cap on the camera). A flat field correction was applied to the resulting images in order to account for the system's response to a uniform input at the front of the camera lens. The uniform input was simulated using an ensemble average of 100 images of an LCD monitor that was positioned perpendicular to the camera and out of focus to further increase the uniformity of the incoming light. Warping of the images to map to real world coordinates was accomplished by imaging a two-plane calibration plate (LaVision Type 7) situated at a known position inside the test section and DaVis 8.2's built-in warping algorithm (camera

pinhole model). $\overline{L}_i$ and $\overline{LB}_i$ are the ensemble-averaged laser sheet image (200 image average), and the ensemble-averaged laser sheet background image (100 image average), respectively. For a summary of how to generate these two quantities and the modifications to $\overline{L}_i$ that result in corrections for both sheet energy profile nonuniformity and absorption, refer to Getsinger (2012).

Unfortunately, the lack of a fast-response energy measurement technique negated the possibility of accurate absorption correction of the PLIF portion of the simultaneous PLIF/PIV data sets, since the PLIF signal was recorded using only the first pulse of the two-pulse image capture required for PIV. It should be noted, however, that since these data sets were only used for local scalar gradient measurements, order of magnitude arguments render the effect of the absorption on the results extracted from these measurements negligible. Image-to-image normalization to the potential core was utilized as the sole means of global shot-to-shot laser energy fluctuation correction for the PLIF portion of the simultaneous PLIF/PIV measurements.

Fig. 2.4 shows the progression of the correction scheme for an example fluorescence image. Fig. 2.4 (a) is the raw data obtained from the CCD array. The effect of absorption and sheet energy profile variation is shown in the potential core of the jet in this image by a decrease in intensity when moving towards the bottom-left of the core. Fig. 2.4(b) shows the image after the background light and dark noise are removed, whereas (c) shows the effect of the white image correction and the image mapping to real-world coordinates. Fig. 2.4(d) is the result after normalization by the modified light sheet image to account for absorption and energy profile variation. This correction increases the signal intensity in the far field and results in a uniform concentration in the potential core. After multiplication by the scalar factor k which is determined by the method described previously, the resultant image can be regarded as a true measure of the jet fluid concentration in the light sheet plane. Steps (a)-(c) are performed in DaVis 8.2, and step (d) along with the k-factor multiplication is completed using a code written in Matlab. Multi-pass median filters were applied to the processed PLIF data sets in order to reduce noise in the images, while preserving gradients in the flow (see Ghandhi (2006) for a description of median filter effects on measured data).

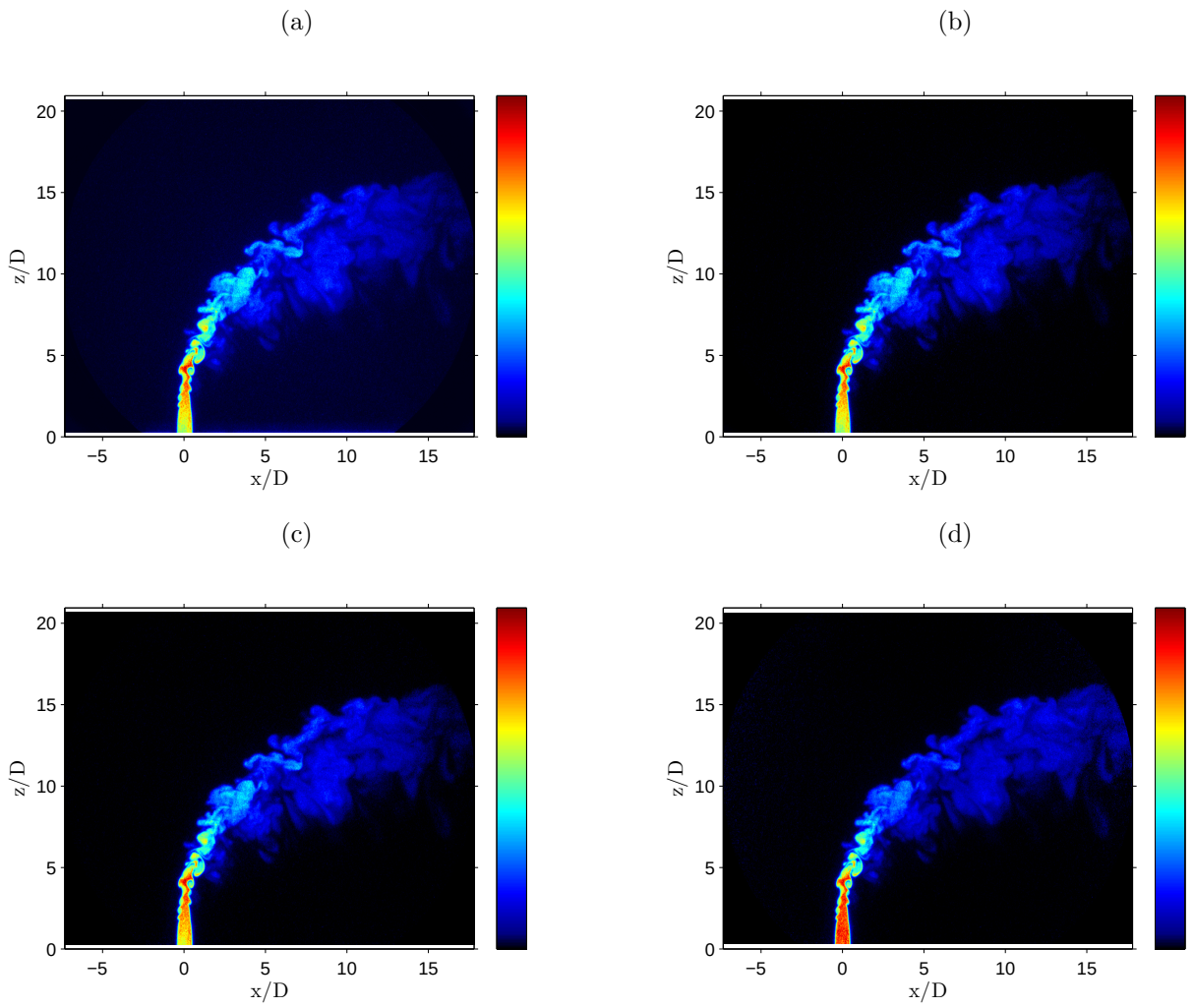


Figure 2.4: An example of several steps in the PLIF image correction process: (a) The raw image, (b) Background subtracted (c) Flat-field corrected and warped (d) Laser sheet profile and absorption corrected. Data from Getsinger (2012)

After processing and filtering, the signal-to-noise ratio (SNR) for the jet centerplane PLIF images was determined by dividing the average signal in a box contained within the potential core of the jet by the standard deviation of the data within that box for each individual image, and then averaging this SNR value over all images for a given set of measurements. For the high resolution centerplane PLIF images, minimum potential core SNR among all cases was 40. For the lower resolution centerplane PLIF images used for mixing quantification, minimum SNR was 55. For the PLIF portion of the simultaneous PLIF/PIV measurements, minimum SNR was 25. It should be noted, however, that the

SNR is actually a variable throughout a given image.

2.3.2 PIV

Particle image velocimetry (PIV) exploits the basic definition of velocity (distance traveled per unit time) to characterize the velocity field on a light sheet plane. In PIV measurements, two pulses of visible light of known time separation are used to illuminate seeded particles in the flow. These particles must be small enough to follow the flow and not be significantly influenced by Stokes Drag, but large enough to scatter enough light to be accurately tracked. The Mie scattering of the two pulses of light off of these particles is captured by a CCD camera using either a single frame with double exposure (auto-correlation), or two frames with single exposure (cross-correlation). The resulting images are then split into interrogation windows defined by specified blocks of pixels. The sizing of these interrogation windows has a direct effect on the accuracy of the data obtained. The interrogation windows must be large enough to contain a significant number of particles with a significant displacement within the interrogation window at the specified time separation, but they also must be small enough so that rotational displacements are negligible compared to translational movement and flow gradients are not averaged out significantly. Assuming that only translational displacements are present within an interrogation window, an FFT algorithm correlation is administered on the data to find the average displacement of all particles in the interrogation window. For a more in-depth review of the principles and modern developments in the field of PIV, see Adrian and Westerweel (2011).

The excitation source described Section 2.3 was chosen specifically to allow both PLIF and PIV measurements. The 532 nm output from that source is the light used in PIV measurements. Naturally, this means the dichroic mirror set and beam-sampler/joulemeter combination described in Section 2.3.1 are removed during PIV measurements to allow the 532 nm to form a sheet in the test section measured to be 1.4-1.6 mm thick. The crossflow is seeded by introducing glycol-based smoke fluid particles of 0.2µm mass-median diameter from a commercial smoke generator (Pea Soup Rocket) into the blower inlet. The jet was

seeded by diverting part of the gas flow through a TSI particle generator filled with Di-Ethyl-Hexyl-Sebacat (DEHS) oil. Seeding density was determined by how much of the jet gas flow was diverted into the seeder.

As shown in Fig. 2.3, our experiment utilized a stereoscopic PIV setup. This system yielded values for all three velocity components by using the two dimensional velocity field determined from the images taken by each camera separated by a rotation angle about the axis perpendicular to the jet injection plane (60° for this experiment). By mapping these two velocity fields to real-world coordinates and comparing the two-dimensional velocities determined by each camera with the geometrical setup of the imaging system, the out-of-plane component of velocity was determined. Stereo-PIV also has the added benefit of removing bias errors in the in-plane components of velocity caused by large out-of-plane displacements. This method of three-component-PIV is referred to as the 2D3C technique as opposed to more complex methods of determining all three components of velocity such as tomographic-PIV, which uses a volume illumination of the flowfield along with significantly more cameras (typically four). The cameras used to capture the scattered light distribution of each pulse are two 14-bit cross-correlation CCD cameras (LaVision Imager proX, 1600x1200 pixel resolution) fitted with Nikon 60mm lenses at f/11.0, 532nm narrowband filters, and Scheimpflug lens mounts used to tune the angle between the lens plane and the CCD array plane in order to keep the entire field of view in focus at the large viewing angle associated with this stereoscopic setup. The fields of view of each camera were mapped to real-world coordinates using a 3^{rd} order polynomial model built in to the DaVis 8.2 software and a LaVision Type 7 two-plane calibration plate placed in the light sheet. To account for discrepancies between the position and orientation of the light sheet with respect to the calibration plate, a self-calibration was administered using the crossflow (Wieneke, 2005).

Velocity fields were calculated using the code included in LaVision's DaVis 8.2 software. Before any vectors were calculated, the images obtained from each CCD array were first mapped to real-world coordinates. The resulting images were preprocessed to enhance the visibility and contrast of the particles by subtracting a global background image for each laser pulse, subtracting an 8 pixel-scale local sliding background, and utilizing 8 pixel-scale

min/max filtering. Multi-pass stereo cross-correlation was utilized, with decreasing interrogation window size for accuracy enhancement (2 passes at 32x32 pixel interrogation area size, and 4 passes at 24x24 interrogation area size). The relatively small interrogation area size was chosen to increase vector yield and accuracy of gradient measurements such as vorticity and strain. The time-separation between the two pulses Δt was 17.5 μs for the equidensity ($S = 1.00$) flush nozzle data sets, 15 μs for the equidensity ($S = 1.00$) flush pipe data sets, and 6 μs for the flush nozzle $S = 0.35$ data sets. These Δt were chosen to be within the range of the well-known rule of thumb for particle movement of less than or equal to 1/4 of the initial interrogation area size (Adrian and Westerweel, 2011) throughout the entire field of view. A similar rule of thumb is typically utilized for the out-of-plane component of velocity; the maximum particle displacement in the y-direction was kept within 1/4 of the measured sheet thickness. However, since there is no method to visualize the out-of-plane particle displacement directly from the images, the maximum crossflow speed was utilized as a conservative estimate of the maximum out-of-plane velocity that was encountered. Post-processing at each step of this multi-pass technique removed spurious vectors (vectors with low correlation values and/or significant deviations from neighboring vectors), replaced them with interpolated velocities, and applied smoothing/median filters.

CHAPTER 3

Transverse Jet Structure and Stability

Portions of this chapter are modified sections from Getsinger et al. (2014)

3.1 Flowfield Features

An important step in any fluid dynamics experiment, especially when the data will be used as validation for a numerical code, is determination of flow parameters and boundary conditions. For the non-reactive jet in crossflow, this includes a characterization of the jet Reynolds number, Re_j, the crossflow Reynolds number, Re_∞, the jet-to-crossflow momentum flux ratio, J, the jet-to-crossflow density ratio, S, and the velocity profiles of both the jet and the crossflow at key locations, allowing calculation of jet and crossflow momentum thicknesses, θ_j and θ_∞, respectively. Table 3.1 summarizes the range of values for the governing flow parameters associated with this experimental setup. The jet Reynolds number was fixed at $Re_j = 1900$ for the majority of the transverse jet flowfield explorations summarized here, aside from the study concerning Reynolds number effects on the asymmetry of the transverse jet cross-section (see Section 3.3.2). Re_j was determined using the bulk (profile-averaged) jet velocity, U_j, which was slightly different depending on injector diameter, D. It should be noted that care must be taken when comparing data from different research groups because many other jet experimentalists define Re_j by the centerline velocity of the jet. $Re_j = 1900$ was chosen to facilitate stability exploration (Davitian et al., 2010a; Getsinger, 2012), and thus was kept constant here in order to compare mixing and symmetry characteristics with the stability characteristics.

Since the jet Reynolds number, Re_j, was kept constant, the jet velocity, U_j, varied with

Parameter	Range
S	$1 \geq S \geq 0.35$
J	$41 \geq J \geq 2$
U_∞ (m/s)	$0.91 \lesssim U_\infty \lesssim 7.48$
θ_∞/D	$0.22 \gtrsim \theta_\infty/D \gtrsim 0.089$
Re_∞	$255 \lesssim Re_\infty \lesssim 2100$
$Sc_{acetone \rightarrow air}$	$1.3 \lesssim Sc_{acetone \rightarrow air} \lesssim 4.6$

Table 3.1: Governing flow parameter ranges explored in this experiment. Here, θ_∞ is the crossflow boundary layer momentum thickness, measured on the centerplane of the jet, 5 diameters upstream of the center of the jet exit at $(x/D, y/D) = (-5, 0)$.

changes in the jet-to-crossflow density ratio, S, the temperature in the laboratory during testing, T_{room}, the temperature in the acetone seeder, T_{seed}, and injector diameter, D. The actual jet and crossflow velocity values vary slightly from day to day depending on the temperature in the laboratory. The crossflow velocity range and the corresponding Reynolds number and momentum thickness ranges given in Table 3.1 correspond to variation from the slowest crossflow speed capable with accurate calibration of the crossflow, which corresponds to a $(S, J) = (1, 50)$ transverse jet injected from the flush nozzle for $Re_j = 1900$ during PLIF measurements, to the fastest crossflow speed capable with the current experimental setup, which corresponds to a $(S, J) = (1, 1.4)$ jet injected from the flush nozzle for $Re_j = 1900$ during PLIF measurements. The crossflow momentum thickness (θ_∞) range was calculated using a Blasius boundary layer fit to the velocity profiles at the minimum and maximum U_∞ given in Table 3.1 (see Figure 3.1 for a plot of these profiles and the Blasius fit corresponding to each U_∞; this will be discussed below). The free jet's momentum thickness for the flush nozzle injector was calculated previously (Getsinger, 2012) to be $\theta_j/D = 0.0142$. The upstream side of the transverse jet momentum thickness is a function of J and Re_j, as quantified in Megerian et al. (2007).

The crossflow Reynolds number was calculated using the freestream velocity value, U_∞, and the jet diameter, D. The Schmidt number Sc range given in Table 3.1 was calculated using the mixture kinematic viscosity for the jet fluid at the jet exit derived using the Wilke formulation (Wilke, 1950), and, following Reid et al. (1977), the molecular diffusivity of acetone into air at $(T, P) = (21°C, 1atm)$ $(D_{ace \rightarrow air} = 0.101 cm^2/s)$. Only the acetone

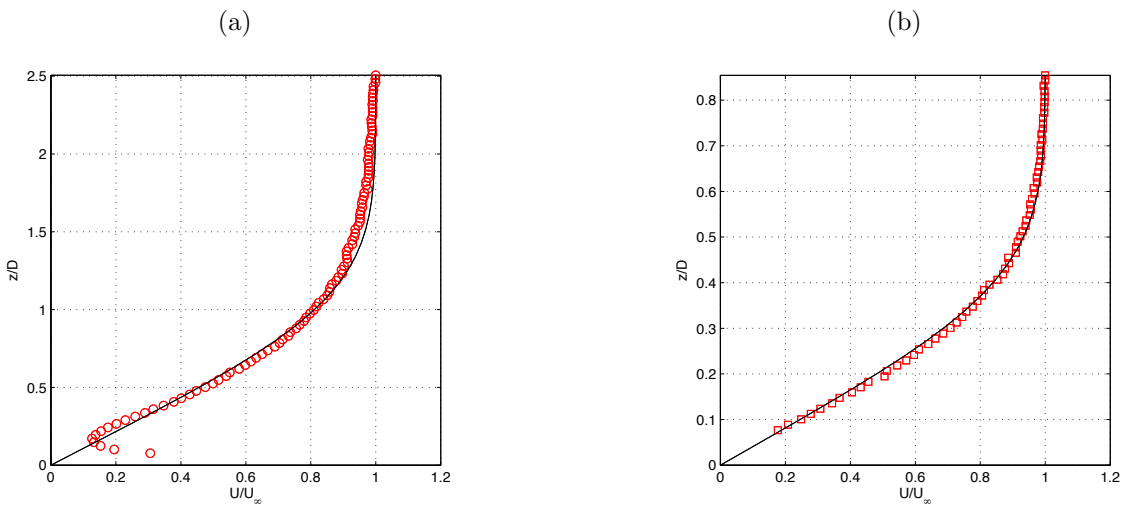


Figure 3.1: Crossflow boundary Layer measurements for (a) $U_\infty = 0.909m/s$ and (b) $U_\infty = 7.48m/s$ at $(x/D, y/D) = (-0.5, 0)$. Solid line is Blasius solution.

molecular diffusivity is directly relevant for this experimental setup since acetone-PLIF is being utilized for mixing metric calculation. It should be noted here that as the jet fluid mixes and equalizes with the crossflow for the low density ratio cases, the Schmidt number will decrease due to the increase in local density.

For both flush and elevated injection cases, the momentum flux ratio, J, is calculated using the bulk velocity of the jet, U_j, and the free-stream velocity of the crossflow, U_∞. Since the momentum thickness for a laminar free jet exit profile is only a function of the Reynolds number, the density ratio, S, has been surmised to have no effect on the exit momentum thickness for a constant Reynolds number jet (Hallberg and Strykowski, 2006). The bulk velocity of the jet is used to calculate the momentum flux as opposed to a direct integration of the velocity profile because the crossflow has a significant effect on the exit velocity profile of the jet (Megerian et al., 2007).

The free jet scaled momentum thickness was calculated to be $D/\theta = 70$ from a numerical integration of the velocity profile at the jet exit quantified via hotwire anemometry (Getsinger, 2012). According to the work of Hallberg and Strykowski (2006), the transition from convective to absolute instability for a low density free jet at $D/\theta = 70$ and $Re_j = 2000$ (Re_j based on centerline velocity) is between $0.27 \lesssim S \lesssim 0.5$. The transitional density ratio

found in the work of Getsinger (2012) and Getsinger et al. (2012) was around 0.45, which is consistent with the range suggested by Hallberg and Strykowski (2006).

Figure 3.1 shows the crossflow boundary layer profiles for two separate freestream velocities, U_∞, taken with a hotwire at the upstream edge of the nozzle with a Blasius boundary layer solution shown for reference. Both the low speed ($U_\infty = 0.909m/s$) and high speed ($U_\infty = 7.48m/s$) profiles follow the Blasius solution reasonably well, with larger deviation from the Blasius solution occurring for the lower speed case as to be expected due to the decrease in accuracy of hotwire measurements at lower speeds. The slight increase in velocity for the lower speed case (shown in Figure 3.1a) as the hotwire is brought closer to the floor can be attributed to heat conduction to the tunnel walls (Durst and Zanoun, 2002). It is worthwhile to note that the boundary layer thickness for the low velocity case is especially large when compared to the diameter of the jet, suggesting a non-negligible effect on the jet trajectory by the crossflow boundary layer. Further exploration of the crossflow boundary layer properties and spanwise variation will be described in Section 3.3.

3.2 Upstream Shear Layer Stability and Vortex Rollup

Most optical diagnostic techniques suffer from either low temporal or spatial resolution. Full resolution measurements from which spectral plots can be deduced are difficult and expensive to obtain using non-intrusive optical methods. Because of this limitation, hotwire measurement is still used to determine spectral character in a variety of flowfields. Fortunately, PIV measurements can be compared to hotwire measurements as a method of determination of the correspondence between the vortex structures and the hotwire data.

Stability characteristics for transverse jet shear layers quantified in the past via hotwire measurements (Megerian et al., 2007; Davitian et al., 2010a; Getsinger et al., 2012) show significant alterations in the upstream shear layer's spectral characteristics as velocity ratio R or momentum flux ratio J is reduced for a fixed set of jet Reynolds numbers. PIV in the present studies indicated a strong correspondence between shear layer stability conditions and shear layer vorticity rollup.

The first column in Figure 3.2, for example, shows the vertical velocity power spectra measured by the hotwire at several positions along the upstream shear layer (scaled distance s/D) for the equidensity JICF created by the flush nozzle. Here $Re_j = 1900$ was fixed, so that varying crossflow velocity U_∞ produced a range of jet-to-crossflow momentum flux ratios, $J = 41$ down to $J = 2$. The shear layer's frequency spectra is scaled in terms of the Strouhal number, $St \equiv fD/U_j$. As in prior studies, these power spectra demonstrated clear evidence for convectively unstable shear layers at high J values, with relatively weak and broadband peaks, multiple modes created by tonal interaction with the hotwire (Getsinger et al., 2012), and the generation of subharmonic instabilities. Such tonal interactions were not observed for the free jet, $J \to \infty$ (Megerian et al., 2007). When J was reduced below around 10 (R below approximately 3.1 for the equidensity case) by increasing the velocity of the crossflow and fixing that of the jet, the shear layer began to demonstrate typical absolutely unstable characteristics, with strong single tone oscillation and higher harmonics, along with a weakening and eventual absence of subharmonics at lower J. The second column in Fig. 3.2 provides a more detailed representation of the power spectra on a finer spatial grid ($\Delta s/D = 0.1$) via spectral magnitude contour plots, indicating the strength of the instabilities and corresponding Strouhal number for various locations along the shear layer. These contour plots enable distinctive characteristics of the transverse jet shear layer to be identified, contrasting more clearly the convective and absolute instability differences, as done in prior studies (Megerian et al., 2007; Davitian et al., 2010a; Getsinger et al., 2012).

A direct comparison of the nature of shear layer vortex roll-up and instabilities/pairing observed by the hotwire and stereo PIV measurements may be made via column (c) in Figure 3.2, which shows representative instantaneous fields of ω_y vorticity, normalized by U_j/D. The agreement here is excellent; for all cases, the locations along the upstream shear layer at which the initial onset of the instabilities became apparent in the hotwire spectrum correspond quite well with the initial shear layer vorticity roll-up locations in the PIV measurements. At $J = 41$, the initially laminar shear layer began to roll up on its upstream side at about $z/D = 2.0$ to 2.5, consistent with the initiation of the shear layer instability in the hotwire measurements at about $s/D = 2.0$. Beyond $z/D \approx 3.0$

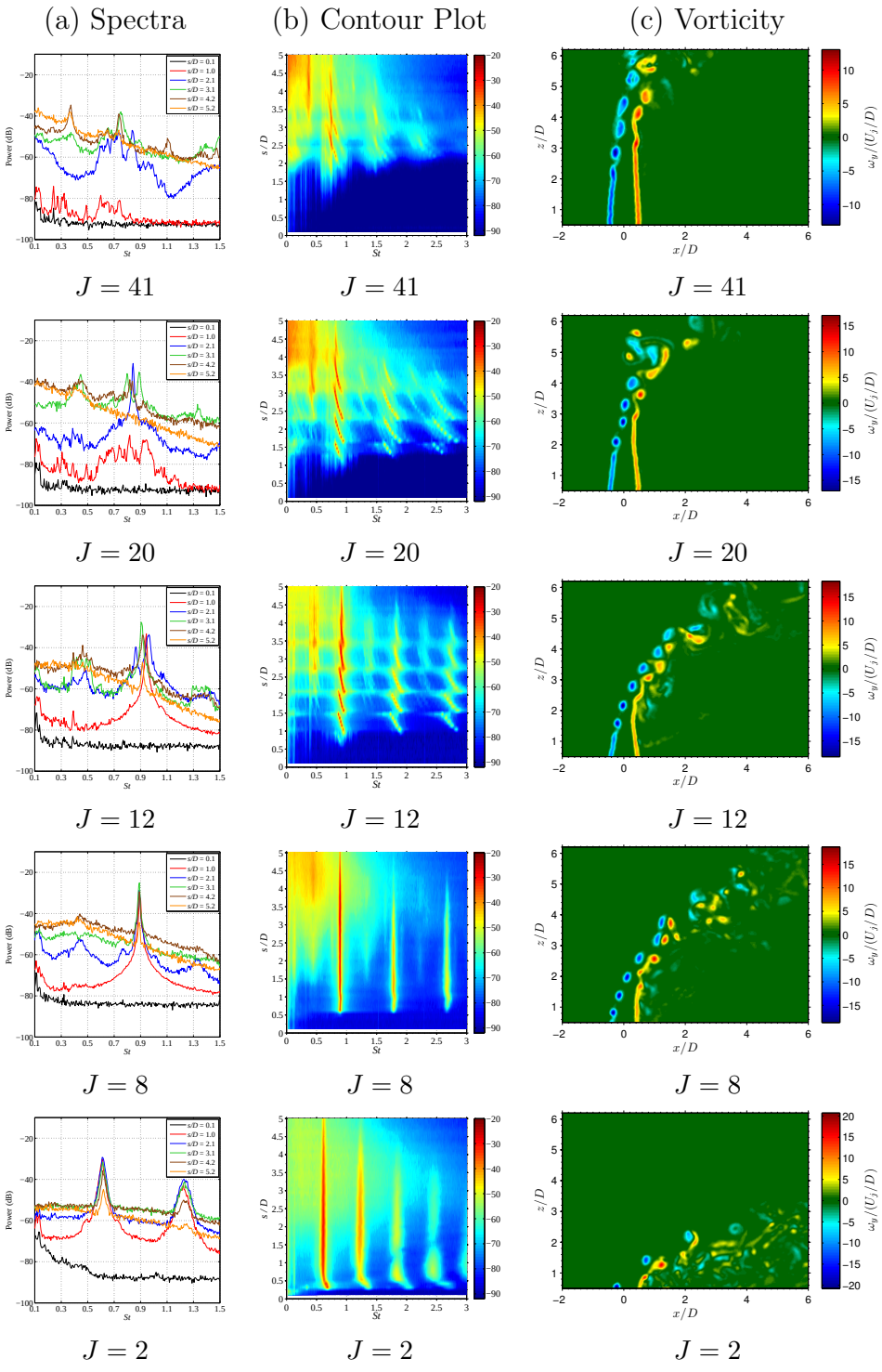


Figure 3.2: For the flush nozzle with $Re_j = 1900$, $S = 1.0$, and varying momentum flux ratios J, (a) Shear layer spectra at various locations s/D, (b) equivalent spectral contour plots with magnitude of instability strength (in dB) for various s/D locations and Strouhal numbers, and (c) scaled instantaneous spanwise vorticity field ω_y measured via PIV. Data for columns (a) and (b) are from Getsinger (2012).

for this flow condition, vortices on the upstream and downstream sides of the jet were observed to pair and merge, eventually breaking down into a turbulent free shear layer. This behavior was also demonstrated by the growth of a subharmonic peak in the hotwire power spectrum (near $St = 0.38$) at about $s/D = 3.0$. Similar agreement was found for the other momentum flux ratios in the convectively unstable regime, $J = 20$ and $J = 12$. At each of these successively lower momentum flux ratios, the location of shear layer roll-up and subsequent vortex pairing moved closer to the jet exit, and the spacing between adjacent vortices was reduced, consistent with an increasing oscillation frequency of the shear layer. At $J = 8$, which created shear layer conditions at which the flow was globally unstable per hotwire measurements, little evidence of vortex pairing was seen in the PIV-based vorticity field. A distinct spacing between adjacent shear layer vortex structures was maintained for a considerable distance downstream along the upstream layer, before eventual turbulent breakdown took place. This nearly constant vortex spacing was consistent with self-excitation of the jet shear layer at a pure-tone frequency observed here and in prior hotwire-based equidensity JICF shear layer studies (Megerian et al., 2007; Davitian et al., 2010a). This spacing also increased when J was lowered to 2, consistent with hotwire-based trends suggesting a lowered frequency of oscillation at lower momentum flux ratios under absolutely unstable conditions. Near-immediate shear layer rollup seen in the vorticity field image for $J = 2$ was also consistent with detection of the strong absolute instability via the hotwire probe. It is noted that the strongly periodic vortex rollup shown in column (c) at low momentum flux ratios ($J = 2$ and 8) was quite similar to that observed via smoke streaklines for $J = 4$ and $Re_j = 7600$ by Fric and Roshko (1988).

Stability characteristics for straight pipe-generated transverse jets have not been studied to any significant degree, as noted previously. Figure 3.3 shows the power spectra measured along the upstream shear layer via hotwire anemometry for the JICF injected from the flush pipe (first column), with a fixed Reynolds number and unity density ratio, and with successively decreasing values of J. Corresponding spectra at the same flow conditions for the flush nozzle and elevated nozzle are shown in columns (b) and (c), respectively, for comparison. Again, with a fixed set of jet conditions (S, Re_j), lowering J corresponds to increasing the

crossflow velocity U_∞, hence for each flow condition given in Fig. 3.3, bulk jet and freestream crossflow velocities are virtually the same among the three injectors. At higher momentum flux ratios corresponding to $J \geq 12$, the flush pipe-generated jet was observed to have considerably weaker shear layer instabilities as compared with the flush nozzle-generated JICF. The frequency-shifting tonal interactions with the hotwire probe, observed for both the flush and elevated nozzle-generated JICF (and not for free jets), were completely absent for the flush pipe-generated JICF. As documented in prior experiments (Megerian et al., 2007), the significant deflection of the flush nozzle-injected jet by crossflow (as U_∞ was increased), and the attendant increase in the flush nozzle's upstream jet momentum thickness at injection, contributed to the stronger, more rapidly initiated convective shear layer instability observed at $J \geq 12$ in Fig. 3.3. Linear stability analysis of the flush nozzle-generated JICF (Alves et al., 2008) predicts the variation of spatial growth rates as well as initial Strouhal numbers with decreasing J in the range $J > 10$; these predictions compare well, both qualitatively and quantitatively, with experimental findings as initial jet momentum thickness increases. The flush pipe, however, already had a fully developed velocity profile and thus a large initial jet momentum thickness in the absence of crossflow; hence increasing U_∞ in the range $J \geq 12$ in the present experiments appeared to have relatively little effect on the shear layer spectra.

Remarkably, as the momentum flux ratio for the flush pipe was reduced below 10 in Fig. 3.3, the flush pipe-generated upstream shear layer exhibited strong instabilities initiated very close to the jet exit, with clear higher harmonics and weakening subharmonic modes, as did the flush nozzle. Such spectral changes suggested a rather abrupt transition to absolute instability occurring near $J \approx 10$ in the flush pipe, the same condition as for shear layer transition in the flush nozzle. For the two flush injectors, each set of flow parameters in Fig. 3.3 produced the same crossflow conditions to which the jet was exposed, consisting of a Blasius boundary layer adjacent to the injection wall. The fact that the transition to absolute instability for the flush pipe and flush nozzle appeared to occur at similar momentum flux ratios likely was related to the strong crossflow's deflecting and entering into the upstream side of the jet exit itself, as determined in numerical simulations of the flush nozzle-generated

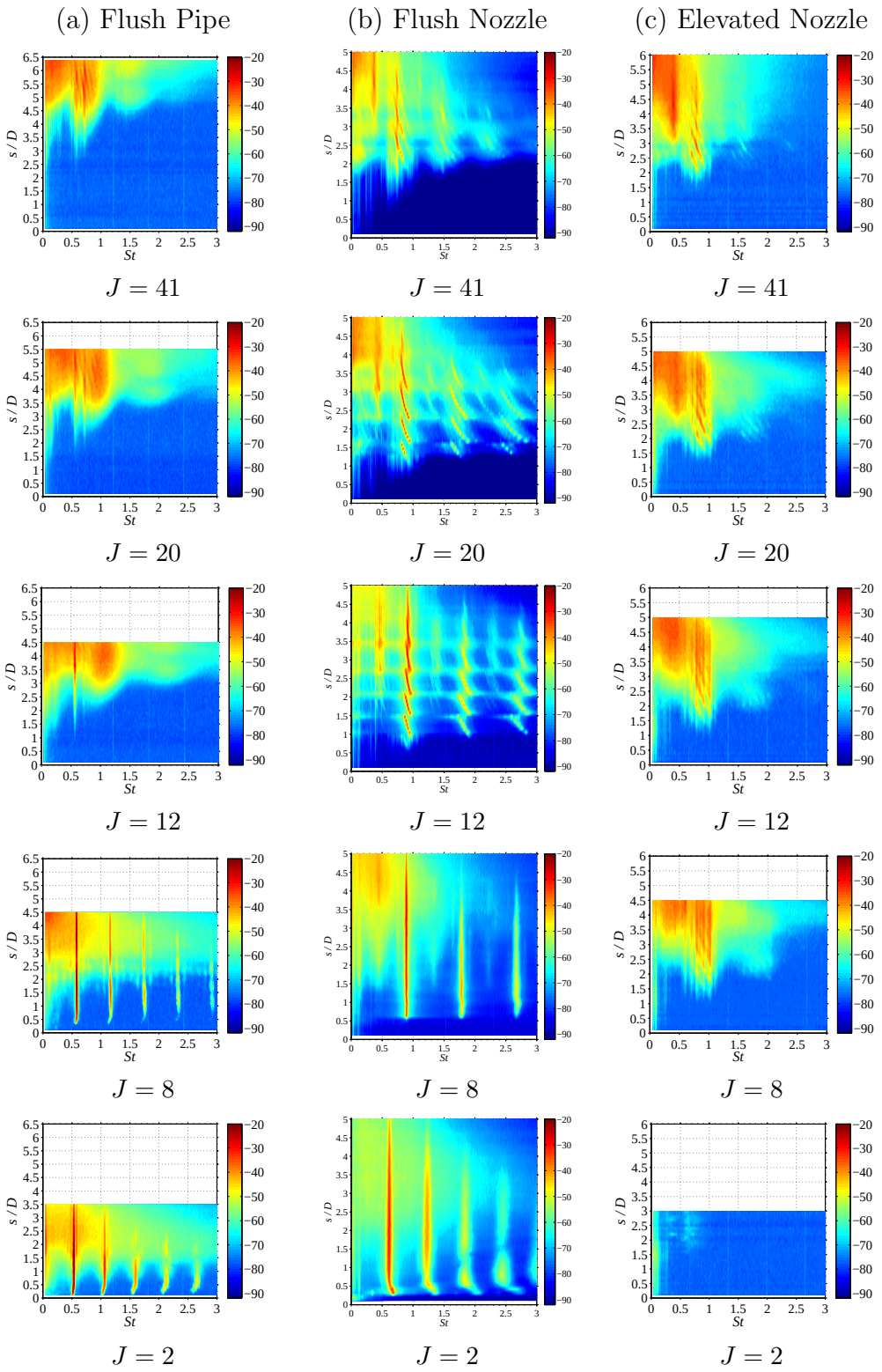


Figure 3.3: Contour plots of upstream shear layer spectral characteristics with $Re_j = 1900$ and density ratio $S = 1.0$: (a) flush straight pipe injector (b) flush nozzle injector, and (c) elevated nozzle injector. Data are shown for varying momentum flux ratios $J = 41$, 20, 12, 8, and 2. Data for column (b) is from Getsinger (2012).

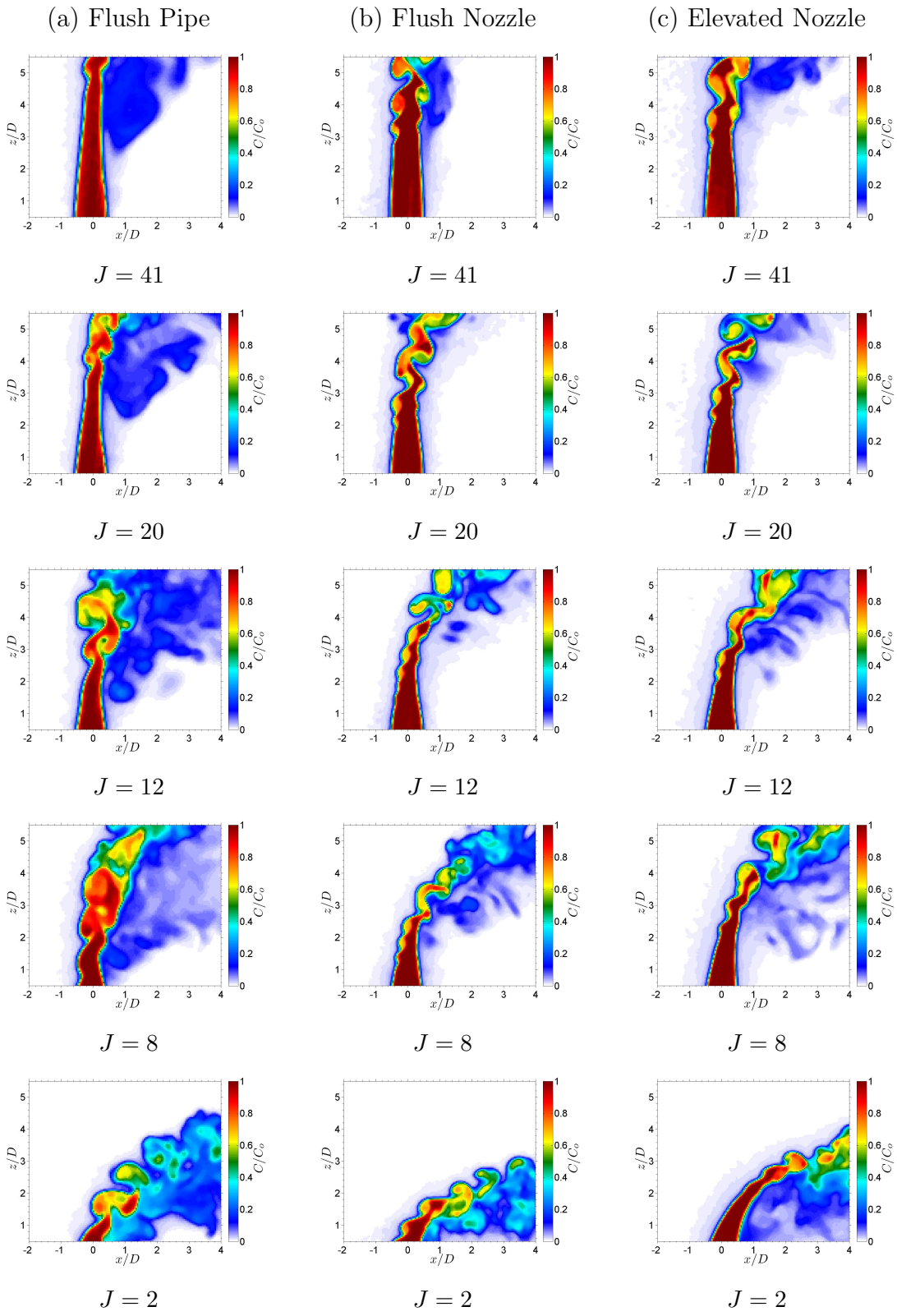


Figure 3.4: Centerplane (side) instantaneous acetone concentration fields of the JICF nearfield with $Re_j = 1900$ and density ratio $S = 1.00$: (a) flush straight pipe injector (b) flush nozzle injector, and (c) elevated nozzle injector. Data are shown for varying momentum flux ratios $J = 41$, 20, 12, 8, and 2.

transverse jet (Mahesh and Iyer, 2013). The present diagnostics (e.g., PIV in Figure 3.2) were not able to visualize flow within the jet nozzle or pipe, however, so this phenomenon could not be verified in the present experiments.

The elevated nozzle-generated JICF shown in column (c) of Fig. 3.3 exhibited similar shear layer characteristics to those of the flush nozzle for higher momentum flux ratios ($J \gtrsim 20$), as observed previously. But as documented in Megerian et al. (2007) at lower J values and thus higher crossflow velocities, the magnitude of vertical velocity exterior to the upstream side of the elevated nozzle increased, creating co-flow which is known to stabilize a jet's shear layer (Jendoubi and Strykowski, 1994). For the range of flow conditions shown in Fig. 3.3, the elevated jet did not exhibit a transition to absolute instability, principally due to the influence of this co-flow, although prior studies indicate that transition may indeed occur after the elevated jet is deflected substantially by crossflow, for $J \lesssim 0.93$.

Figure 3.4 shows instantaneous nearfield centerplane acetone PLIF concentration fields corresponding to the flow conditions for the spectral data in Fig. 3.3, for all three injectors. As with the PIV vorticity fields, the initial upstream shear layer vorticity rollup in these PLIF measurements corresponded well to the initiation of instabilities quantified in Fig. 3.3. Interestingly, while there was initiation of vortex rollup relatively close to the exit plane of the flush pipe-generated JICF for $J < 10$, it showed larger and less organized vortical structures than exhibited by the flush nozzle, which had strong periodic vorticity generation and a relative lack of vortex interactions for $J < 10$. Thus, while the pipe-generated JICF appeared to become absolutely unstable in the same flow regime as the flush nozzle-generated JICF, differences in the jet's exit conditions did appear to cause nearfield jet structural differences at all momentum flux ratios explored here.

3.3 Transverse Jet Cross-Sectional Characteristics

3.3.1 Constant Jet Reynolds Number, Equidensity

To determine the impact of the stability characteristics of the upstream shear layer on the overall jet structure (in particular on the formation of the CVP), a detailed examination

utilizing JICF yz-planar imaging was undertaken for all three injectors at $Re_j = 1900$ and $S = 1.00$. Figure 3.5 shows ensemble-averaged acetone PLIF concentration fields obtained in cross-sectional slices of the flush nozzle-generated JICF at a fixed location $x/D = 10.5$ downstream of injection. These images were averaged over 300 instantaneous flowfield snapshots, and are shown for the same flow conditions as in Figs. 3.3 and 3.4, and thus may be compared. For each average yz-plane PLIF image, the concentration scale ranges from zero to the maximum value within each image, and actual concentration values are only indicated when scaling to jet fluid concentration was possible.

At $x/D = 10.5$, there were a number of flow conditions for which the jet cross-section was asymmetric and/or without a typical CVP shape. The asymmetric cases appeared for all three injectors at larger momentum flux ratios ($J = 41$), cases in which the upstream shear layer was found to be convectively unstable and, as documented in Megerian et al. (2007) for both nozzles, more susceptible to the effects of small disturbances than were jets with absolutely unstable shear layers at lower values of J. The flush nozzle's asymmetric mean cross-section also included the presence of a tertiary vortical structure below the main jet structure, similar to structures observed by Kuzo (1995) and Shan and Dimotakis (2006). For the flush pipe at $J = 41$, even though its shear layer instability magnitude was weaker than that for the flush nozzle (Fig. 3.3), with relatively delayed initial shear layer rollup (Fig. 3.4), the mean jet cross-section downstream of injection also appeared to resemble a distorted, asymmetric CVP. In contrast, for smaller values of J, especially for the flush injection and/or for which the shear layer was absolutely unstable, per Fig. 3.3, an essentially symmetric CVP was observed. Such mean structures were seen for both flush pipe and flush nozzle cases at $J \leq 8$, and for the flush nozzle at $J = 12$, a condition for which shear layer rollup and vorticity initiation appeared considerably stronger than for larger J values.

For the elevated nozzle cases, none of the flow conditions in Fig. 3.5 appeared to create a clear cross-sectional CVP structure, except for the $J = 20$ condition, which had similar shear layer instability and rollup features to that of the flush nozzle at this flow condition (Figs. 3.3 and 3.4). It should be noted that the principal difference in flow conditions between elevated and flush nozzles at $J = 20$ was that the elevated jet was injected outside

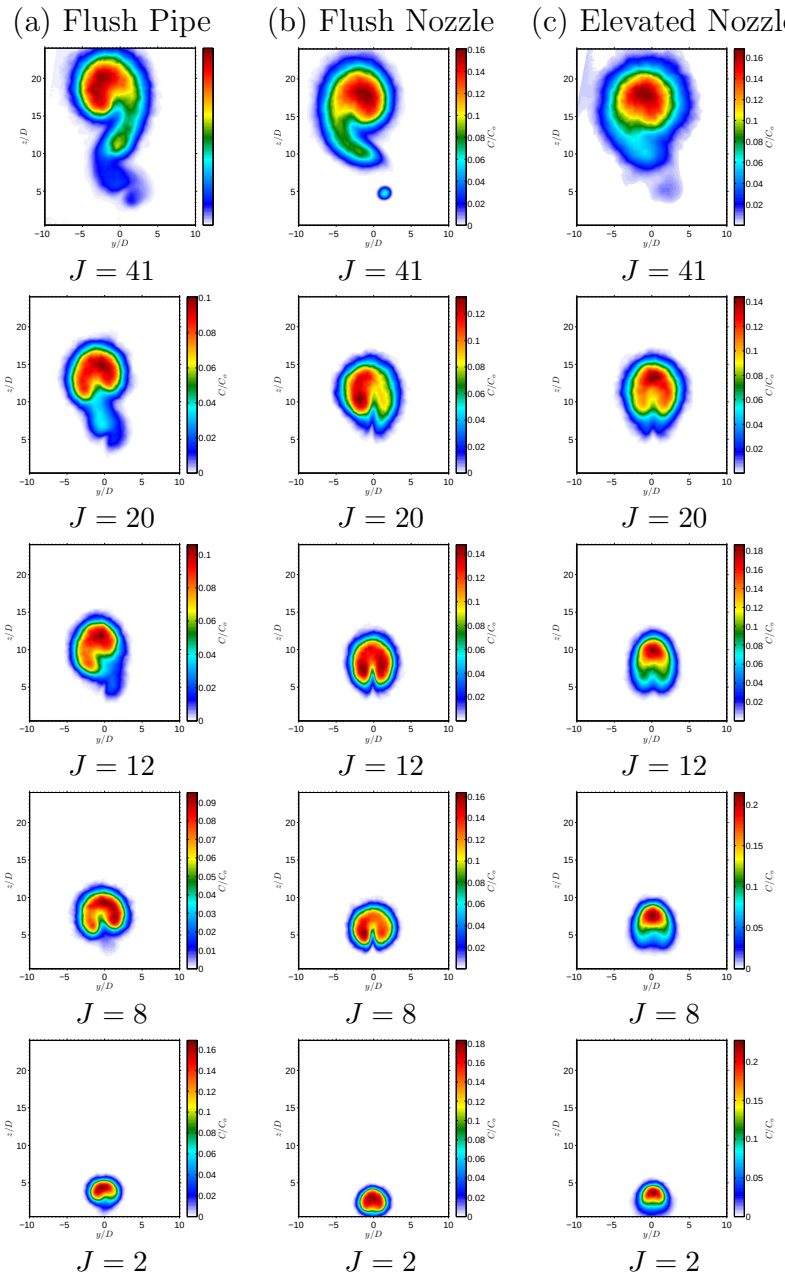


Figure 3.5: Cross-sectional jet slices at $x/D = 10.5$, visualized via acetone PLIF, with $Re_j = 1900$ and density ratio $S = 1.0$, averaged over 300 images: (a) flush straight pipe injector, (b) flush nozzle injector, and (c) elevated nozzle injector. A linear colormap is used. Data are shown for varying momentum flux ratios $J = 41$, 20, 12, 8, and 2.

of the wall (crossflow) boundary layer and, in addition, that there was a low level of vertical co-flow upstream of the elevated jet. This vertical co-flow velocity was approximately 5% of the peak jet velocity at $J \approx 20$, according to the equidensity measurements for this Reynolds number regime in Megerian et al. (2007). This degree of co-flow increased for $J < 20$ and thus affected shear layer spectra, weakening the instabilities, as indicated in Figs. 3.3 and 3.4. Instantaneous concentration fields for the cross-sections of the elevated nozzle-based JICF, especially at the higher value of $J = 41$, did show a temporal deflection of the jet cross-section to one side or the other about the $y = 0$ plane. While there was sufficient positive and negative oscillation in the y-direction as to produce a somewhat more symmetric-looking jet structure in the mean, instantaneous cross-sectional images for the flush injectors at $J = 41$ appeared to prefer one orientation, producing the more skewed image in the mean. Sample instantaneous cross-sectional images for all three injectors at two distinct times are shown in Fig. 3.6 and Fig. 3.7.

The structural asymmetry/symmetry for given flow conditions was observed from the nearfield of the jet and persisted downstream, as shown, for example, in Fig. 3.8 for the flush nozzle at downstream locations $x/D = 2.5,\ 5.5$, and 10.5. Those conditions producing mean structural asymmetry in the farfield, e.g., for $J = 41$ at $x/D = 10.5$, also showed an asymmetric structure, even with a tertiary vortex, very close to injection. Although the cross-sectional asymmetry for the flush nozzle at $J = 20$ was greatly reduced in the nearfield as compared with the other clearly convectively unstable case, $J = 41$, the flow condition did not produce the more cleanly symmetric CVP structures in the cross-section as observed for the cases that had absolutely unstable upstream shear layers ($J = 8$ and 2), or those with significant nearfield shear layer rollup close to absolutely unstable conditions ($J = 12$). Extensive modifications were made to the present injection system in an attempt to eliminate these asymmetries at higher J values. Additional flow straighteners upstream of the nozzle or pipe, an additional length of upstream pipe, rotation of the four-way injection system and even elimination of some of the orifices in the four-way system, as well as other alterations, were all tested. None had any significant effect on the mean jet cross-sectional shapes shown in Figs. 3.5 and 3.8. These results showed a consistent (and repeatable)

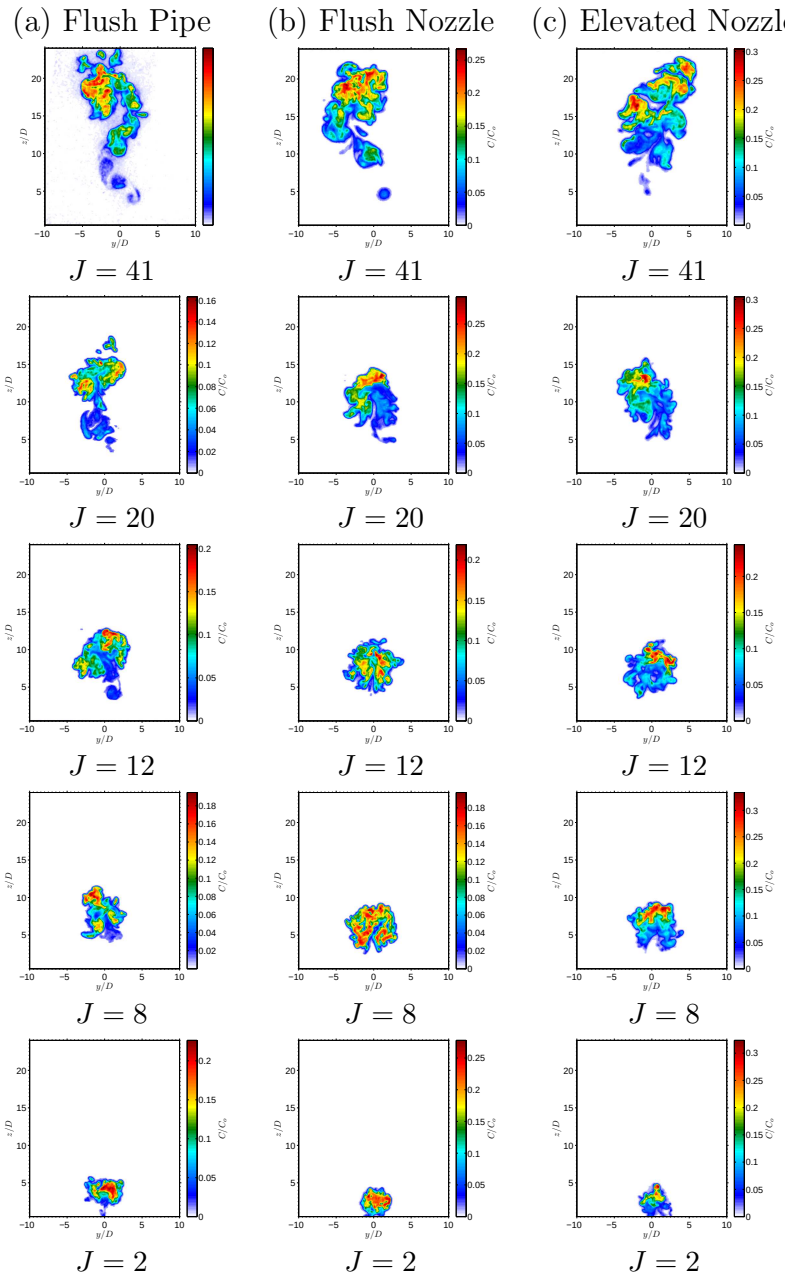


Figure 3.6: Instantaneous cross-sectional jet slices at $x/D = 10.5$, visualized via acetone PLIF, with $Re_j = 1900$ and density ratio $S = 1.0$: (a) flush straight pipe injector, (b) flush nozzle injector, and (c) elevated nozzle injector. A linear colormap is used. Data are shown for varying momentum flux ratios $J = 41$, 20, 12, 8, and 2.

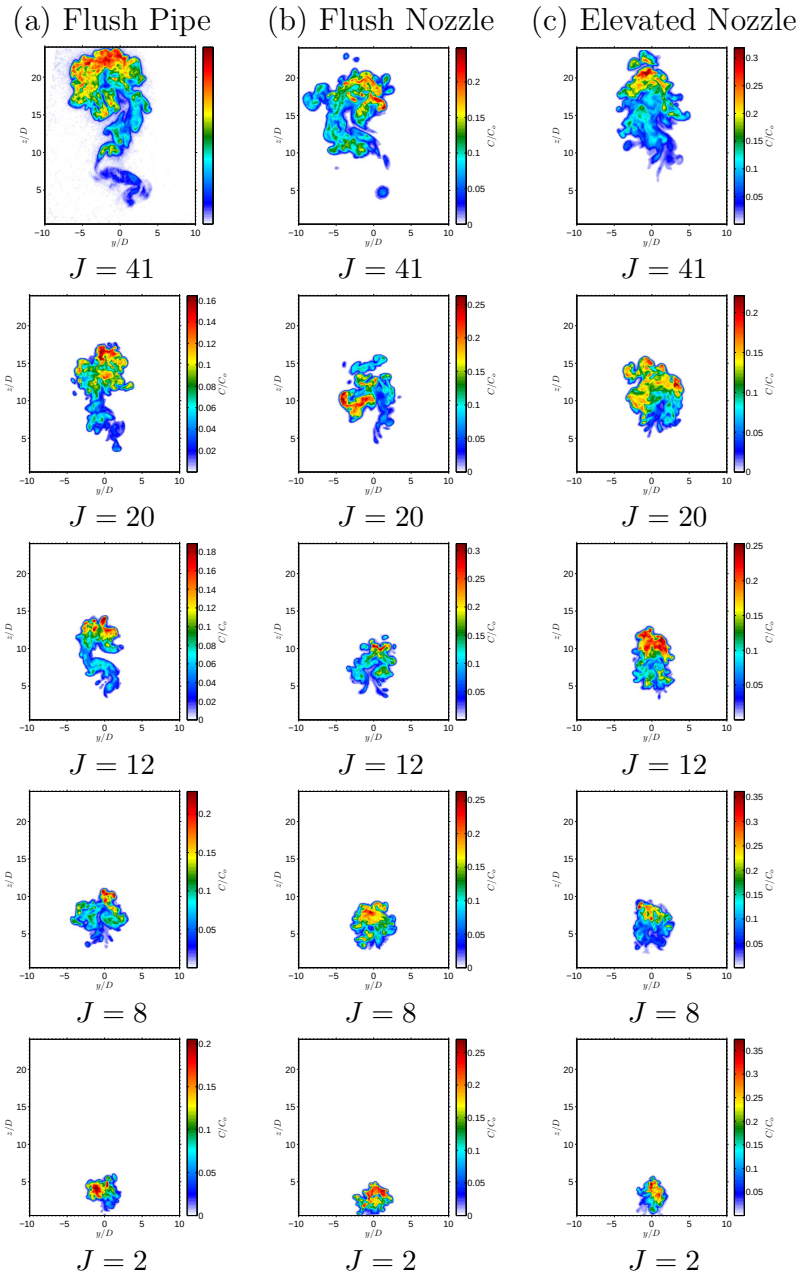


Figure 3.7: Instantaneous cross-sectional jet slices at $x/D = 10.5$, visualized via acetone PLIF, with $Re_j = 1900$ and density ratio $S = 1.0$, at a separate time distinct from the images in Figure 3.6: (a) flush straight pipe injector, (b) flush nozzle injector, and (c) elevated nozzle injector. A linear colormap is used. Data are shown for varying momentum flux ratios $J = 41$, 20, 12, 8, and 2.

correspondence between strong upstream shear layer rollup and formation of a symmetric CVP, while asymmetric cross-sectional structures corresponded to higher J values and thus to convectively unstable shear layer conditions.

In the above cases for a fixed jet Reynolds number and density ratio, and with successively reduced momentum flux ratio J (Figs. 3.3-3.5), the crossflow velocity U_∞ was necessarily increased. To explore the separate influence of the crossflow on jet structure, hotwire-based tunnel boundary layer measurements were made at a location five diameters upstream of the jet orifice, in the absence of jet flow. These showed a clear laminar Blasius velocity profile for the full range of crossflow conditions. Yet at very low crossflow velocities, corresponding to the highest momentum flux ratio case in the above-noted figures, a very small degree of crossflow asymmetry in the spanwise-(y-)direction was detected within the wall boundary layer.

Figure 3.9 shows a sample upstream wall boundary layer (velocity) profile for $U_\infty = 1.01$ m/s, corresponding to $J = 41$ for the $Re_j = 1900$, equidensity ($S = 1.0$) condition. A small asymmetry across the spanwise distance $-3.0 \leq y/D \leq 3.0$ was detected in the magnitude of local crossflow velocity within the boundary layer at an elevation of $z/D = 0.5$ and at 5 diameters upstream of the flush orifice ($x/D = -5.0$). This spanwise asymmetry in local crossflow velocity virtually disappeared beyond the edge of the wall boundary layer, above $z/D = 3.0$, where the percentage deviation in the local velocity across the spanwise length shown, 1.7%, was only slightly higher than the documented uncertainty in the measurement (1.2% of $U_\infty = 1.01$ m/s, per Megerian et al. (2007)). The degree of crossflow asymmetry within the boundary layer, at $z/D = 0.5$, was a proportionately larger fraction of the local velocity, with a percentage deviation of approximately 7.3% in the spanwise direction. Yet precision uncertainties in this single-component hotwire-based velocity measurement at very low velocities, near the tunnel injection wall, were also higher than at the boundary layer edge, based on trends in Megerian et al. (2007). At freestream crossflow velocities exceeding $U_\infty = 1.01$ m/s, the spanwise asymmetries within the wall boundary layer were typically smaller than those documented in Fig. 3.9, although a complete study of the crossflow boundary layer for all flow conditions was not conducted.

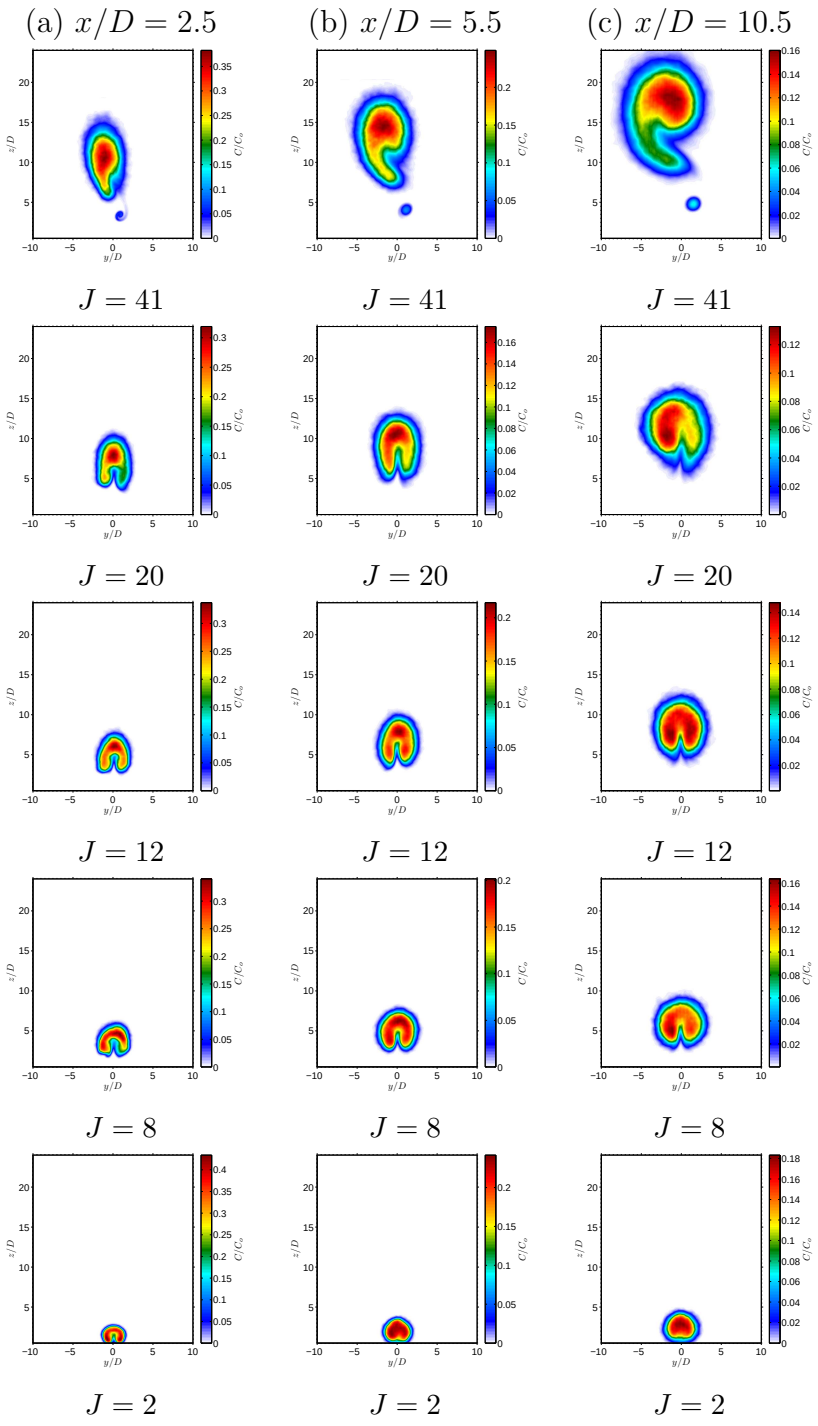


Figure 3.8: Evolution of cross-sectional jet slices of the flush nozzle-generated JICF, visualized via acetone PLIF, with $Re_j = 1900$ and density ratio $S = 1.0$, averaged over 300 images at different downstream locations: (a) $x/D = 2.5$ (b) $x/D = 5.5$ and (c) $x/D = 10.5$. Data are shown for varying momentum flux ratios $J = 41$, 20, 12, 8, and 2.

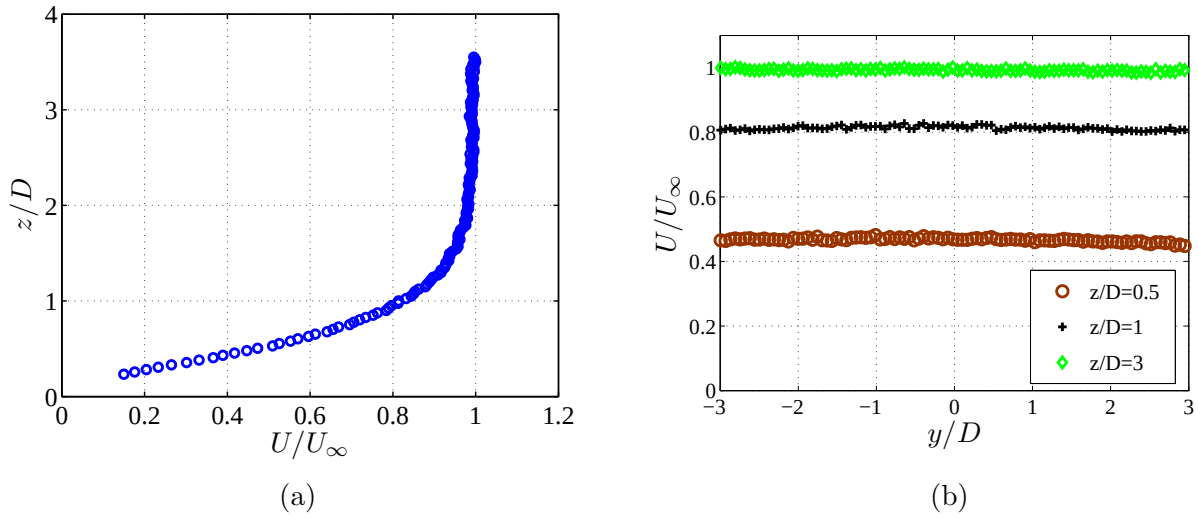


Figure 3.9: Crossflow boundary layer velocity measurements via hotwire: (a) Velocity profile upstream of the jet nozzle, at $x/D = -5.0$ and $y/D = 0.0$; (b) Local streamwise velocity measured at several different locations relative to the tunnel wall ($z/D = 0.5, 1.0, 3.0$) at $x/D = -5.0$ with variable spanwise location y/D. Conditions correspond to crossflow velocity in the freestream $U_\infty = 1$ m/s, with the jet flow turned off.

3.3.2 Variable Jet Reynolds Number, Equidensity

All previously mentioned experiments were conducted at $Re_j = 1900$. Thus, jet Reynolds number was also varied to determine the effect of this parameter on the jet structure. An examination of the effect of the previously mentioned crossflow asymmetry, or any undetected asymmetry associated with the crossflow, was conducted at a fixed value of $U_\infty = 1.01$ m/s, while varying the jet Reynolds number, and thereby also varying the momentum flux ratio. By fixing the crossflow conditions, one essentially fixes any asymmetric properties that the crossflow may have had at $U_\infty = 1.01$ m/s while exploring jet responses under different injection conditions (different injectors and flow conditions), and thus, for different jet shear layer stability characteristics. At a fixed downstream location $x/D = 10.5$, averaged yz-plane PLIF images for the flush nozzle are shown in the first column of Fig. 3.10; here jet fluid was injected directly into the incoming crossflow boundary layer (and hence into an upstream separation region created by the jet's interaction with crossflow, per Kelso and Smits (1995) and Kelso et al. (1996)). Mean cross-sectional images for the elevated nozzle, where the jet was injected above/outside of the wall boundary layer, are shown in the second

column of Fig. 3.10.

For the flush nozzle in Fig. 3.10, at higher momentum flux ratios and Reynolds numbers ($J \geq 25$ and $Re_j \geq 1500$) for which present and prior studies showed a convectively unstable shear layer and delayed shear layer vorticity rollup, the jet cross-sections were quite asymmetric, with a skewed CVP structure. For $J = 11$, however, the jet cross-section became much more symmetric for the flush nozzle-generated jet, with a CVP structure appearing at conditions typically approaching an absolutely unstable upstream shear layer.

For the elevated nozzle cases in Fig. 3.10, most of the flow conditions shown produced somewhat more symmetric jet cross-sections, although none corresponded to a clear, symmetric CVP. At very high values of $J = 71$ and $Re_j = 2500$, the asymmetry for the elevated nozzle was rather pronounced, and was similar to the asymmetric CVP for the flush nozzle at the same conditions. According to data in Megerian et al. (2007), at $J \approx 71$ in this Reynolds number range, the degree of vertical co-flow upstream of the elevated nozzle is quite small, less than 3% of the peak jet velocity at the nozzle exit plane. Hence the shear layer spectral characteristics were virtually identical between the flush and elevated nozzles under these conditions. The only other difference in flow conditions between the two nozzles at $J = 71$ was the very small spanwise crossflow asymmetry to which the flush nozzle-injected jet may have been exposed, as compared with a slightly more symmetric freestream crossflow for the elevated nozzle (Fig. 3.9). Neither of these effects appeared to have a substantial effect on altering the degree of cross-sectional asymmetry at $J = 71$. For the elevated nozzle at lowered values of J and Re_j in Fig. 3.10, all of which produced successively weaker shear layer instabilities due to the increasing external vertical co-flow, there were few conditions that actually produced a counter-rotating vortex pair shape in the mean, although the cross-sections became more symmetric at lower J values. As noted previously for the elevated jet in Fig. 3.5, instantaneous images showed there was a deflection of the jet cross-section to one side or the other in the y direction, with sufficient flipping back and forth in time as to produce a generally symmetric jet structure in the mean, but without the distinctive CVP shape. The weakening upstream shear layer instabilities for the elevated nozzle with reduced J, documented here and in previous studies (Megerian et al., 2007), corresponded to the

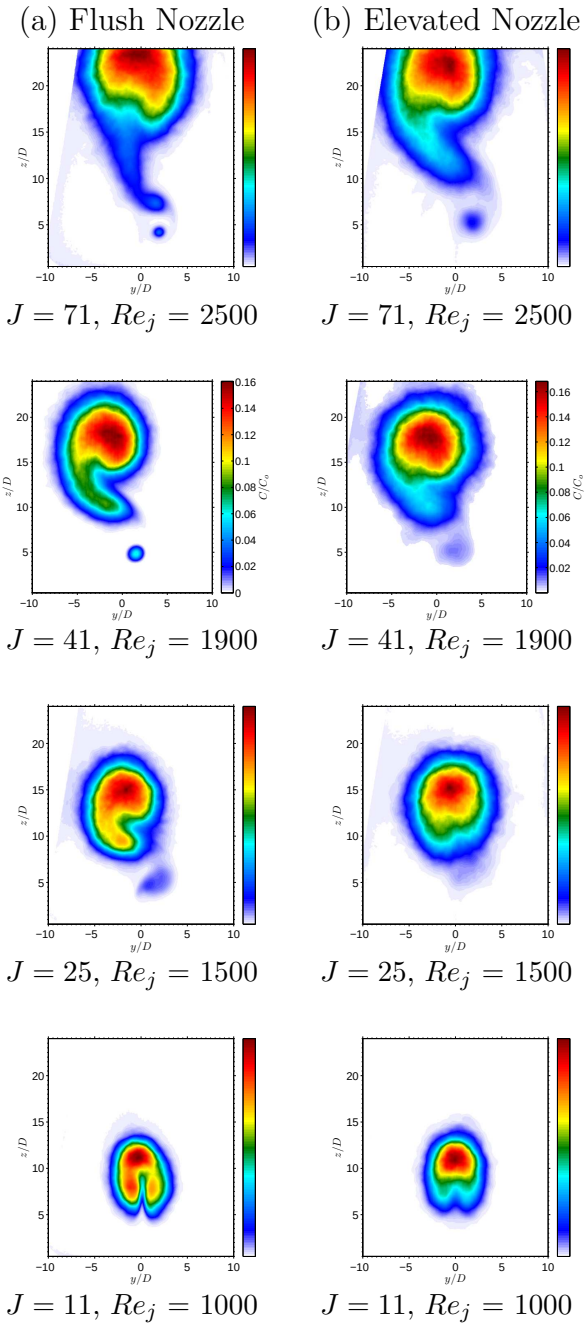


Figure 3.10: Cross-sectional jet slices (location $x/D = 10.5$) visualized via acetone PLIF, with fixed $U_\infty = 1.01$ m/s, density ratio $S = 1.0$, averaged over 300 images: (a) flush nozzle injector and (b) elevated nozzle injector. Data are shown for varying momentum flux ratios and jet Reynolds numbers as given.

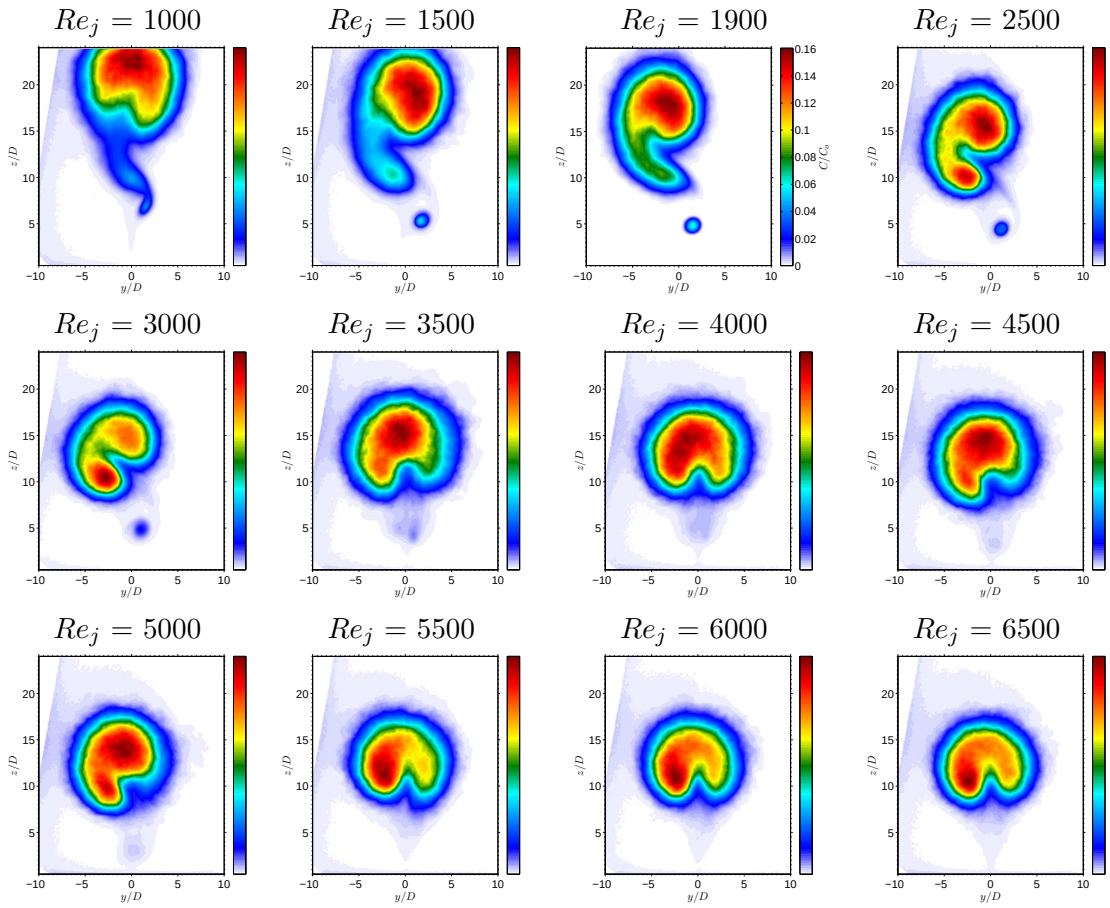


Figure 3.11: Cross-sectional jet slices at location $x/D = 10.5$, visualized via acetone PLIF, with fixed $J = 41$ and density ratio $S = 1.0$, averaged over 300 images for the flush nozzle-generated jet. A linear colormap is used. Data are shown for varying jet Reynolds numbers as indicated.

jet's lessened ability to sustain shear layer vorticity rollup and thus form a clear CVP for $J \lesssim 41$. Hence it is likely that these weakened shear layer instabilities for the elevated nozzle, rather than the small spanwise asymmetries in crossflow boundary layer profiles, produced the differences between flush and elevated nozzle mean cross-sectional images observed in Fig. 3.10. But the fact that the crossflow conditions upstream of jet injection were the same for all images shown in Fig. 3.10 suggested that it was the response of the transverse jet to the crossflow, and not the crossflow in and of itself, that created different jet flow structures. The cross-sectional asymmetries were most strongly correlated with the nature of jet shear layer instabilities, as created by differing injectors and momentum flux ratios.

Other researchers have observed that the jet Reynolds number itself could have a degree

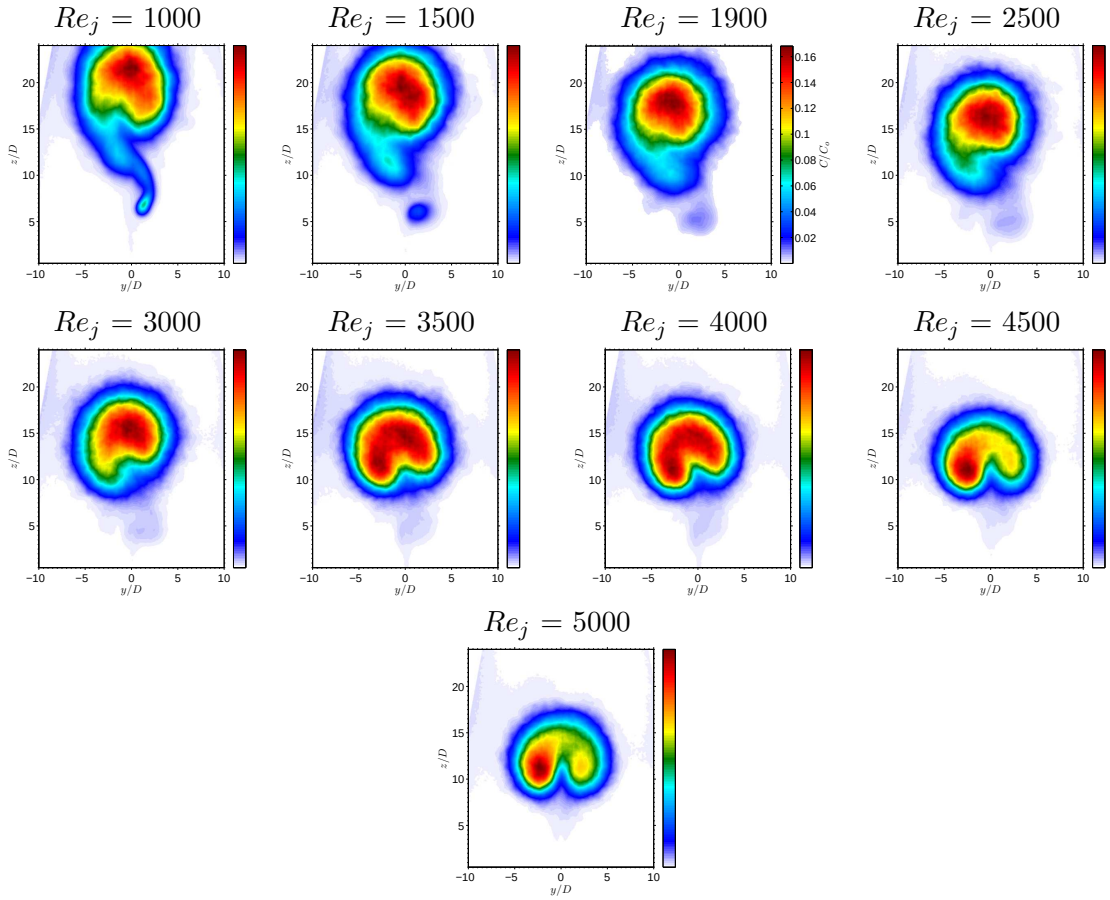


Figure 3.12: Cross-sectional jet slices at location $x/D = 10.5$, visualized via acetone PLIF, with fixed $J = 41$ and density ratio $S = 1.0$, averaged over 300 images for the elevated nozzle-generated jet. A linear colormap is used. Data are shown for varying jet Reynolds numbers as indicated.

of influence on jet cross-sectional symmetry (Kuzo, 1995; Shan and Dimotakis, 2006). For a fixed value of $J = 41$ and variable jet Reynolds numbers $1000 \leq Re_j \leq 6500$, shown in Fig. 3.11 for the flush nozzle and Fig. 3.12 for the elevated nozzle, the present studies showed that the jet cross-section was indeed asymmetric, with the presence of a tertiary vortex structure, for lower Reynolds numbers in the range $Re_j \lesssim 3500$. Transverse jets in this lower Reynolds number range have been documented (Megerian et al., 2007) to produce convectively unstable shear layers. At Reynolds numbers above 3500, the transverse jet cross-section became generally more symmetric in Fig. 3.11, with mean shapes that were closer to the expected CVP and without the tertiary vortical structure. Unequal distributions of jet fluid did appear to be present on either side of the CVP-like structures for such conditions, however. In fact, the slightly asymmetric CVP structure at $Re_j \gtrapprox 5500$ and $J = 41$ ($R = 6.4$) for the flush nozzle was similar to that observed at $Re_j = 5000$ and $R = 6$ in the experiments of Narayanan et al. (2003) and in the corresponding simulations of Muldoon and Acharya (2010), and is reminiscent of cross-sectional structures observed at higher Reynolds numbers and momentum flux ratios by Smith and Mungal (1998).

3.3.3 Constant Jet Reynolds Number, Low Density

The effect of jet-to-crossflow density ratio S on cross-sectional structure of the jet was also studied for $Re_j = 1900$ transverse jets. Similar transition in cross-sectional structure to the more symmetric CVP for a fixed density ratio S and reduced momentum flux ratio J was also observed when S was reduced below unity, with fixed J and Re_j. Figure 3.13 shows instantaneous centerplane images of jets injected from the flush nozzle at various density and momentum flux ratios for $Re_j = 1900$. When $S \lessapprox 0.40$, the jet's shear layer becomes absolutely unstable, as documented in Getsinger et al. (2012). Centerplane concentration fields in Fig. 3.13 showed, for absolutely unstable shear layer conditions ($S = 0.35$), a relatively rapid initiation of strong shear layer vorticity. This rapid initiation of rollup correlated with a more symmetric CVP-like cross-sectional structure in the mean (Fig. 3.14), albeit with some persistence of a lower vortical structure for $J = 41$. Hence, regardless of whether absolute instability in generated by lowering density ratio or momentum flux ratio,

there does seem to be strong correlation with the rapid shear layer rollup associated with absolutely unstable transverse jets and a symmetric jet cross-section. Additional mean cross-sectional PLIF images for the JICF for a range of J and S values are shown in Appendix A.

3.4 Structure and Mixing

The variation in the transverse jet centerplane and cross-sectional structure and vorticity distribution with variations of momentum flux ratio, density ratio, and injector type suggest a potential effect on the mixing efficiency of this flowfield. Alterations in stretching and folding of the mixing layers generated between jet and crossflow fluid could potentially result in significant alteration of the local mixing rate, resulting in variations in total mixing efficiency that need to be characterized. Moreover, the asymmetric cross-sectional jet fluid distribution observed could have a significant effect on the mixing efficiency. The asymmetric jet fluid distribution could also affect the correspondence between mixing metrics calculated from centerplane data and those calculated using cross-sectional data. These issues will be explored in detail in the next chapter.

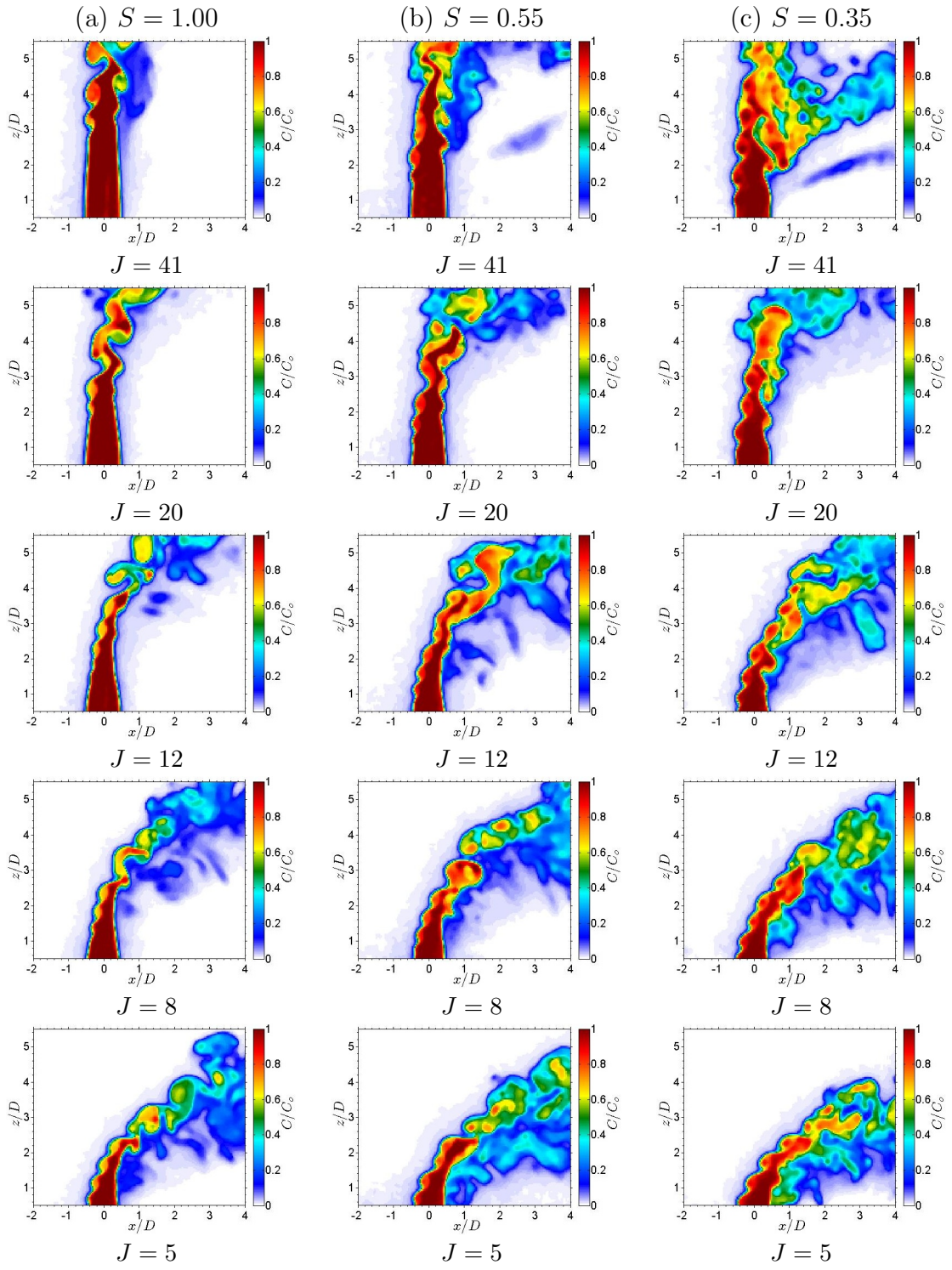


Figure 3.13: Instantaneous centerplane ($y = 0$) jet slices of the flush nozzle-generated JICF nearfield, visualized via acetone PLIF, with $Re_j = 1900$ and density ratios: (a) $S = 1.00$, (b) $S = 0.55$, and (c) $S = 0.35$. Data are shown for varying momentum flux ratios $J = 41$, 20, 12, 8, and 5.

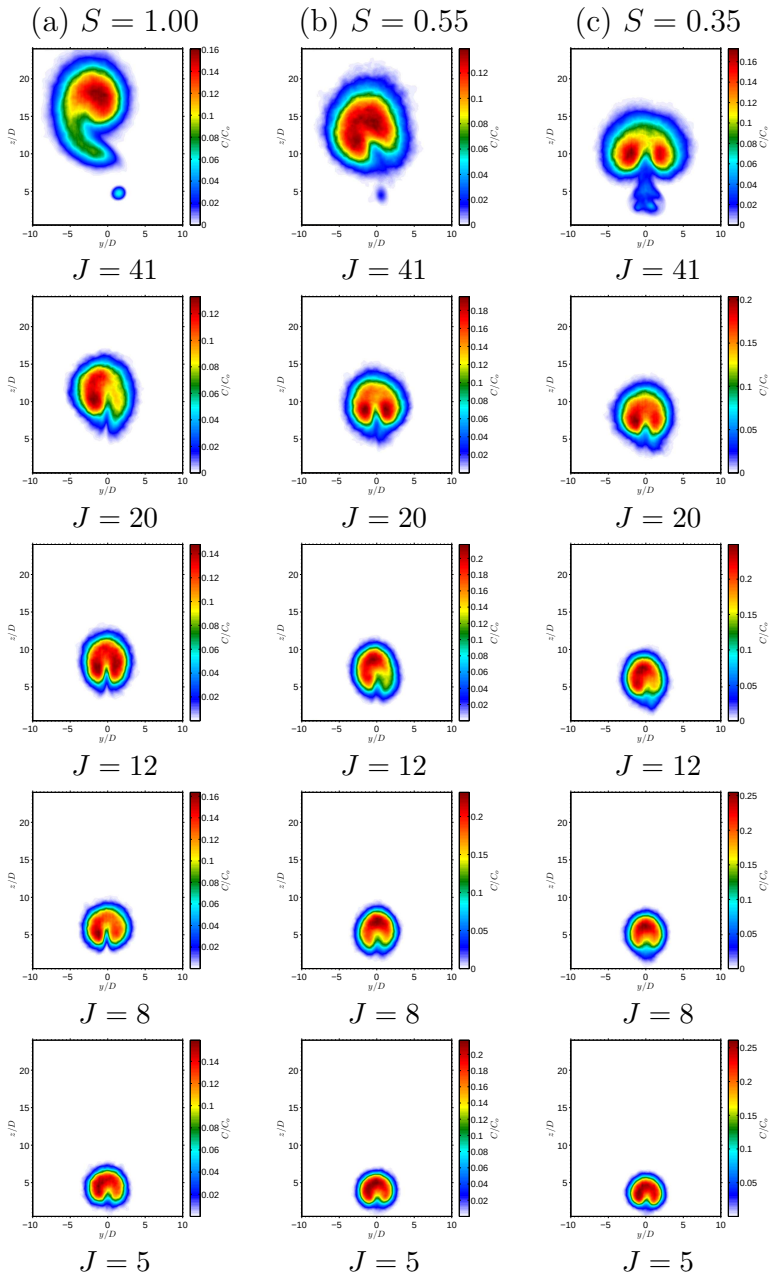


Figure 3.14: Cross-sectional jet slices for the flush nozzle-generated JICF at $x/D = 10.5$, visualized via acetone PLIF, with $Re_j = 1900$ and density ratios: (a) $S = 1.00$, (b) $S = 0.55$, and (c) $S = 0.35$. Images averaged over 300 snapshots. A linear colormap is used. Data are shown for varying momentum flux ratios $J = 41$, 20, 12, 8, and 5.

CHAPTER 4

Transverse Jet Mixing

This chapter focuses on characterizing the mixing efficiency of the jet in crossflow in various instability regimes. As outlined in Section 1.2, the three main processes that are thought to be associated with the mixing characteristics of any transitional or turbulent flowfield are large-scale entrainment, turbulent stirring, and molecular diffusion (Eckart, 1948; Broadwell and Breidenthal, 1984; Broadwell and Mungal, 1991; Dimotakis, 2000). The large-scale entrainment is what brings the two fluids into contact with each other in a high-shear environment. The turbulent stirring is what increases the surface area between the two fluids. The molecular diffusion occurring at the interfaces between the two fluids is what mixes the fluids molecularly. The work outlined here is a preliminary characterization of the mixing that results from these three processes. However, before any calculations are administered, the small scales associated with the transverse jet flowfield need to be characterized in order to be able to analyze the results effectively.

4.1 Scales and Resolution

The smallest scale associated with the characterization of transverse jet mixing using scalar measurements is the Batchelor scale, λ_B. In order to fully characterize molecular mixing, the visualization of the flowfield must resolve the Batchelor scale. Unfortunately, the Batchelor scale is typically much too small to be able to resolve without sacrificing visualization of the large-scale flow features. However, it is not strictly necessary to fully resolve the flowfield down to the smallest length scale in order to distinguish between mixing efficiency characteristics in the diffusive regime. It is only necessary to resolve the scales at which diffusion becomes significant.

Unfortunately, the complexity of the low Reynolds number transverse jet flowfield and the

variation of density and viscosity render calculation of the smallest pertinent length scale at every measurement position associated with the current set of experiments impossible. This difficulty arises, in part, from the fact that the low Reynolds number jet is transitioning to turbulence. This transition results in an interplay between the reduction of scales associated with the transition, and an increase in the size of structures associated with the combined effect of the jet spreading and the velocity difference between the jet and the crossflow decreasing. However, assuming fully developed turbulence, a conservative estimate of the smallest resolution required to capture diffusive effects can be calculated.

Following the work of Shan and Dimotakis (2006), Equation 4.1 is used to calculate the scalar diffusion scale, λ_D, which is the multiple of the Batchelor scale at which diffusive effects become important (deviation from $-5/3$ power law in the scalar spectrum).

$$\frac{\lambda_D}{\delta} \simeq 50 Re_\delta^{-3/4} Sc^{-1/2} \tag{4.1}$$

Manipulating Equation 4.1 to separate all properties, Equation 4.2 is the resultant equation.

$$\lambda_D \simeq 50 \delta^{1/4} \mu^{1/4} \rho^{-1/4} D_{ace \rightarrow air}^{1/2} U^{-3/4} \tag{4.2}$$

In Equation 4.2, δ is a length scale associated with the large-scale dynamics, μ is the dynamic viscosity, ρ is the density, $D_{ace \rightarrow air}$ is the molecular mass diffusivity of acetone into air, and U is a velocity scale associated with the large-scale dynamics. There is no definitive method for calculation of these parameters for a variable density, transitional, anisotropic flowfield like the jet in crossflow explored presently, but for the sake of underestimation of λ_D, conservative values of these parameters associated with the lowest density ratio case explored ($S = 0.35$) will be used. The length scale used for δ is the diameter of the flush nozzle, D. The dynamic viscosity, μ, used in Equation 4.2 is the value of the jet fluid mixture at the jet exit; this value is very close to that of air and is not expected to change significantly as the jet evolves. The density used is also the density of the jet fluid mixture at the jet exit for the $S = 0.35$ case. It is important to note that as the jet travels downstream and mixes with the crossflow, the density will increase. However, since the velocity will be decreasing, and λ_D depends more on variations in velocity than density (as evidenced by Equation 4.2),

the calculated length scale is still expected to be an underestimate. The velocity scale used is the centerline velocity at the jet exit for the $S = 0.35$ case, determined from PIV.

These conservative estimates result in a scalar diffusion scale value of $\lambda_D \simeq 300\mu m$, suggesting that a resolution of 150µm is enough to satisfy the Nyquist criterion. Assuming gradients in all directions tend to be similar, the limiting resolution in the PLIF measurements is the laser sheet thickness, which varies from 400-900µm in the camera's field of view for the data sets utilized for mixing quantification. Unfortunately, the laser sheet thickness within the field of view is a resolution that is around 3-6 times the diffusion scale resolution requirement calculated using these conservative estimates. However, it is once again noted how conservative these estimates are, and, as mentioned previously, the scalar gradients in all directions will not be equal near the jet exit. In fact, near the jet exit, the limiting resolution is the pixel width. Moreover, U decreases significantly with downstream distance, and the turbulence is not well developed near the jet exit, where the length scale δ is the smallest. Therefore, the measurements could still be considered to be resolved enough that the difference of diffusive mixing efficiency among different (J, S) transverse jets is captured reasonably well. To verify this contention, a significantly higher resolution PLIF data set for the flush nozzle injector was taken as well. The variation in the mixing efficiency trends quantified utilizing the low resolution and high resolution data sets was found to be negligible. These results will be shown in Section 4.7.

4.2 Differential Diffusion Effects

A common assumption associated with experimental scalar measurements such as acetone PLIF used to quantify mixing in turbulent flows is that all scalar quantities such as concentration and temperature will be transported in a similar fashion. This assumption is usually applied because the scalar transport equations render diffusivity negligible at high Reynolds number. This view of a turbulent flowfield is most likely correct for the transport of mean and large-scale scalar structures at high Reynolds number. However, in any experiment where molecular mixing is being quantified, particularly in one at low Reynolds number, the

diffusive regime becomes important, and differential diffusion can no longer be neglected. The Rayleigh scattering experiments of Brownell and Su (2008) showed significant differential diffusion effects on gas-phase free jet mixing quantification of helium-propane mixtures into air. As expected, helium diffuses much more readily than propane.

The mixing efficiency quantification of the relatively low Reynolds number jet in crossflow studied in the present experiment with acetone PLIF measurement has the potential to be affected by the differential diffusion amongst helium and the other gases in the jet (nitrogen and acetone). Molecular diffusivities into air are relatively similar between acetone and nitrogen, suggesting that differential diffusion between these two gases can be neglected to reasonable accuracy. However, helium molecular diffusivity into air is typically an order of magnitude larger than acetone or nitrogen. Therefore, although they would be located at the same positions in the flowfield since they are being stretched and convected by the same velocity field, the acetone gas structures visualized using acetone PLIF in this experiment could possibly be significantly smaller than the helium structures. This discrepancy should be kept in mind at all times. All the acetone PLIF mixing quantification data embodies the mixing efficiency of a scalar with a diffusivity that is comparable to the molecular mass diffusivity of acetone. Fortunately, molecular mixing quantification is most important for combustion systems, and the molecular mass diffusivity into air of common combustion fuels such as methane and propane are close to the diffusivity of acetone into air. Therefore, the mixing quantification at the diffusive and molecular levels using acetone PLIF can be considered as a relatively accurate measure of diffusive and molecular mixing of propane or methane, although direct comparison between mixing efficiency in a non-reactive flow and combustion efficiency in the reactive counterpart can only be administered experimentally due to heat release and its effect on all field quantities, including molecular mass diffusivity.

4.3 Jet Trajectory Comparison

As shown in Chapter 3 by means of acetone PLIF visualization, there is high correspondence between the transverse jet's upstream shear layer stability characteristics and the formation,

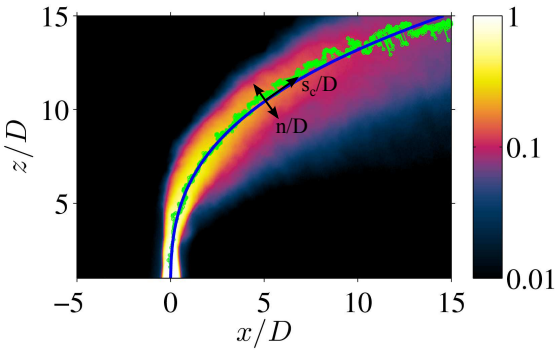


Figure 4.1: Mean scalar concentration image in the $y = 0$ centerplane, with colorbar values corresponding to local concentration C/C_o, for the $J = 20$, $S = 1.00$ transverse jet. Averaging takes place over 300 images. Green data points on this mean jet image show the loci of scalar maxima, while the blue line shows the power law curve fit, with corresponding normal (n) and trajectory s_c coordinates scaled by diameter D. Data from Getsinger (2012)

symmetry, and evolution of the vorticity distribution of the jet cross-section. The PLIF data sets shown in Chapter 3 (along with additional sets shown in Appendices A and B) were also utilized to quantify the mixing efficiency of this flowfield. Before the mixing along the jet is quantified, however, the trajectory of the jet must be determined. As outlined previously, the trajectory of the jet is defined as a power law fit to the loci of maximum jet fluid concentration values. An example of such a fit is shown in Fig. 4.1. This fitting is accomplished by first fitting a power law to the maximum concentration values along vertical columns of data at different positions downstream of the jet exit, and then using that initially calculated trajectory to determine the maximum concentration values along the jet trajectory-normal (n) direction. This second fit is then iterated on until the fit coefficients have converged, which takes 3 iterations on average. The distance along this trajectory curve is designated as the s_c coordinate. Comparisons among mixing trends in the $x-z$ coordinate system and the $n-s_c$ coordinate system will be shown in Sections 4.5.1 and 4.6. The $x-z$ coordinate system trends may be more useful in certain applications that require efficient downstream mixing. However, in order to accurately compare mixing efficiency of jets of various momentum flux and density ratios, the $n-s_c$ coordinate system is more appropriate as it is along the jet trajectory itself.

The trajectory fits calculated using the method outlined can be compared as a measure of the effect of variation of flow parameters on jet trajectory. For instance, Figure 4.2 shows the trajectory variation when density ratio is varied for $Re_j = 1900$ transverse jets at various momentum flux ratios in the range $41 \geq J \geq 5$. For all momentum flux ratios, lowering the density ratio decreased the jet penetration into the crossflow. As has been demonstrated in Chapter 3 and in the work of (Getsinger et al., 2012), the transverse jet in this regime undergoes transition to absolute instability when either the density ratio is lowered below $S \sim 0.45$, or the momentum flux ratio is lowered below $J \sim 10$. Therefore, for the $J = 41$ case, lowering the density ratio has a significant effect on the upstream shear layer, possibly resulting in a reduction of the jet trajectory. Another likely contributor to the reduced trajectory as density ratio is lowered is the reduction of the crossflow boundary layer thickness. In order to match Re_j and J for variable S, the crossflow and jet velocities need to be increased. The increase in the crossflow velocity results in a decrease of the crossflow boundary layer thickness, and thus a more immediate influence of the crossflow on turning the jet. It is worthwhile to note that the effect of reducing S on the jet trajectory seems to diminish as momentum flux ratio is lowered, particularly for the $J < 10$, absolutely unstable cases. This could be associated with the fact that all density ratios are absolutely unstable when $J < 10$.

Figure 4.3 shows the effect of variation of injector type on the trajectory of an $Re = 1900$, $S = 1.00$ transverse jet for a variety of momentum flux ratios. As demonstrated in Chapter 3, in Figure 4.3, the only absolutely unstable cases are the $J = 5$ cases for flush injection. The similar trajectory between flush nozzle and elevated nozzle injection for $J = 41$ and $J = 12$ are a product of the similar upstream shear layer stability cases among these two jets. It is worthwhile to note that for $J = 41$, the elevated nozzle is injected outside the wall boundary layer, and therefore is exposed to higher crossflow speeds near its exit plane. Yet comparing the trajectories of the flush and elevated nozzle injection cases suggests the injection above the crossflow boundary layer has minimal effect on the trajectory in this flow regime. Therefore, the shear layer stability characteristics seem to be the dominant factor in determining the level of penetration of the jet into the crossflow for the nozzle

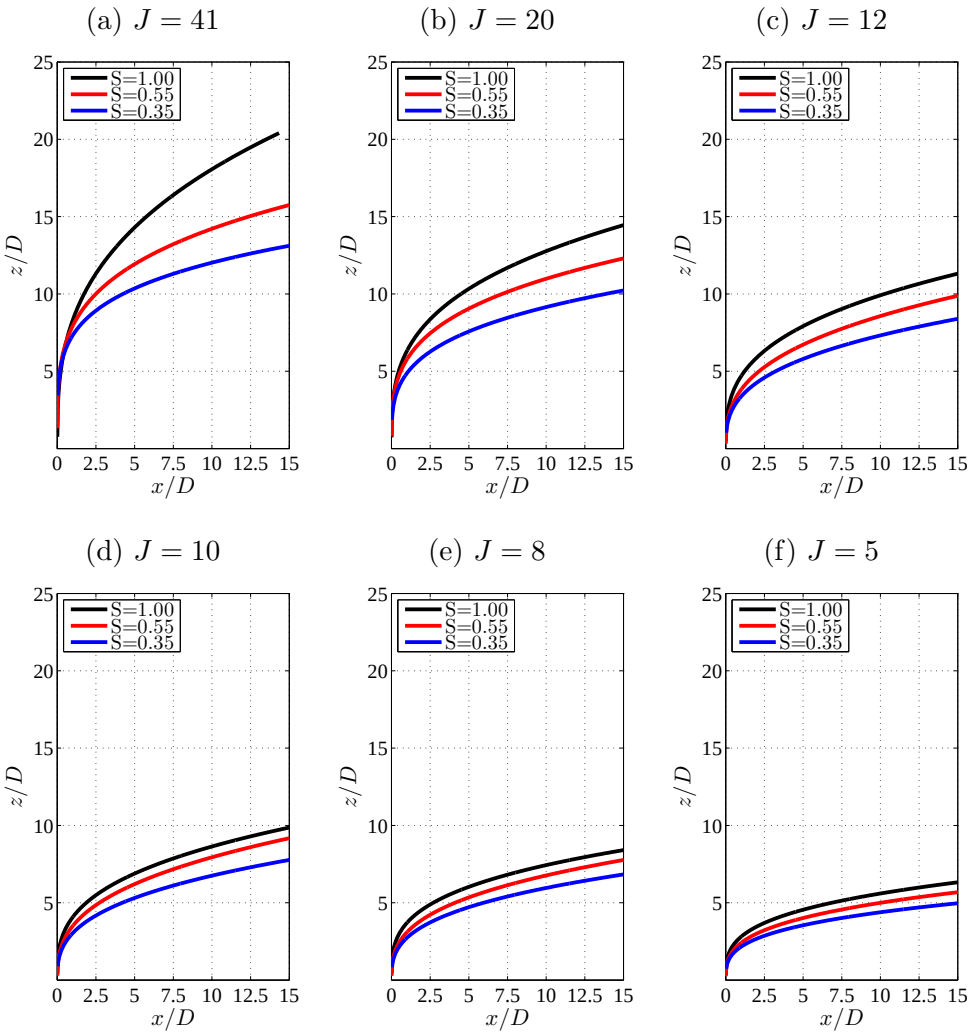


Figure 4.2: Scalar centerline trajectories of flush nozzle-injected transverse jets of various density ratios ($1.00 \geq S \geq 0.35$) and momentum flux ratios ($41 \geq J \geq 5$) as indicated.

injection cases. This contention is further supported by analyzing the trajectory variation between flush and elevated nozzle injection at $J = 5$. For $J = 5$, the jet injected from the elevated nozzle actually penetrates further into the crossflow than the jet injected from the flush nozzle. This increase in penetration can be attributed to the vertical co-flow along the elevated nozzle-injected jet that acts to stabilize the upstream shear layer at higher crossflow speeds, as documented in Megerian et al. (2007), and verified using hotwire anemometry measurements of upstream shear layer spectra shown in Chapter 3.

It is worthwhile to note that the flush pipe-injected jet penetrated deeper into the crossflow than both the flush nozzle and elevated nozzle-injected jets for all momentum flux ratios. This finding is consistent with the work of Muppidi and Mahesh (2005), who found the trajectory of the transverse jet to depend on the jet exit velocity profile. The increase in penetration for flush pipe injection was most apparent for $J \geq 12$, when the jets were convectively unstable. Interestingly, the variation of penetration between the flush pipe-injected jets and the nozzle-injected cases was reduced when the flush-injection cases were absolutely unstable, as in $J = 5$. The significant increase in crossflow speed associated with the absolutely unstable cases profoundly alters the jet exit velocity profile. In fact, recent simulations (Mahesh and Iyer, 2013) suggest that crossflow fluid may travel into the flush jet orifice at such strong crossflow conditions. It should also be noted that momentum flux ratio was matched among the jets using mass-averaged velocity, not momentum-averaged velocity. This fact could also be contributing to the variation in penetration among the flush pipe-injected jets and the nozzle-injected jets, since the center-line of the flush pipe-injected jet has a significantly higher velocity than that of the nozzle-injected jets.

Figures 4.2 and 4.3 scale physical space by the diameter D. It is apparent from these figures that the diameter of the jet is not the only factor affecting the evolution of the jet. In fact, as outlined in Section 1.1.2.3, considerable work has been done in determining an appropriate large scale of the jet to utilize in physical-space scaling and potentially yield data collapse. Figure 4.4 highlights the effect of scaling the jet trajectory using the D, JD, and $\sqrt{J}D$ length scales utilized by others (Keffer and Baines, 1963; Broadwell and Breidenthal, 1984; Smith and Mungal, 1998; Hasselbrink, 1999; Muppidi and Mahesh, 2005). If any of

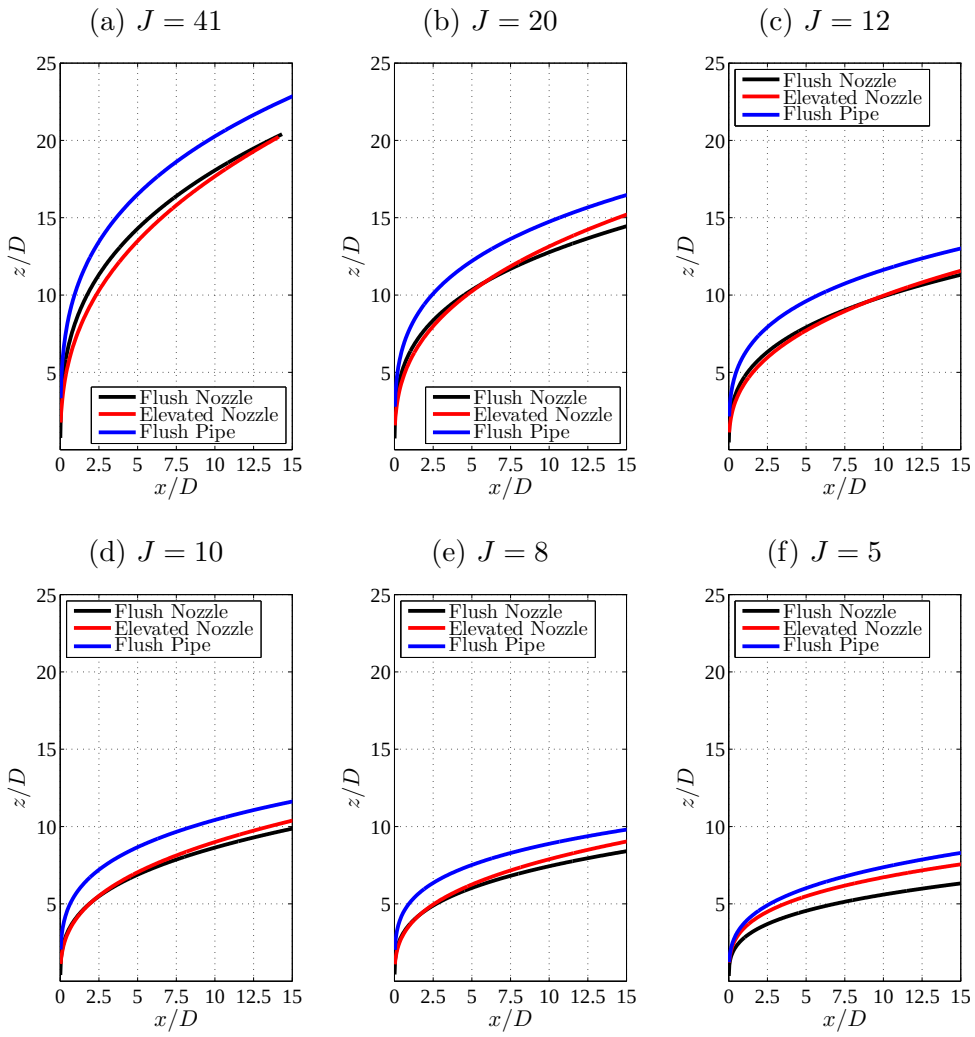


Figure 4.3: Scalar centerline trajectories of $S = 1.00$ transverse jets injected from flush nozzle, elevated nozzle, and flush straight pipe injector configurations. Data shown for momentum flux ratios is the range $41 \geq J \geq 5$ as indicated.

these scaling parameters fully captured the variation in the physical processes associated with this flowfield that affect jet trajectory (e.g. entrainment variation and/or pressure differences), the data would collapse onto a single curve and the jet could be considered to be self-similar. It is apparent from these plots that none of these scaling parameters yield acceptable data collapse, which could be due to a variety of factors. For instance, the relatively low Reynolds number of the jet could affect the trajectory scaling, since entrainment characteristics are significantly different between laminar and turbulent flows. This is especially important for transitional flows like the one studied here, where the turbulence level has significant dependence on distance along the jet. Moreover, the JD and $\sqrt{J}D$ scaling parameters assume that crossflow boundary layer thickness variation does not affect the jet trajectory. However, as outlined in Chapter 3, since large variations in crossflow boundary layer thickness are present in this experiment due to the fact that the jet conditions are fixed and the crossflow conditions are varied, this assumption does not necessarily apply here. The jet momentum thickness also plays a role in this flow that is not captured by either scaling parameter, as evidenced by comparing the data collapse variation between the flush pipe-injected jets, and the flush nozzle-injected jets. Finally, the relatively low momentum flux ratio regime in the present study suggests that proximity to the test section floor could also be affecting trajectory data collapse.

4.4 Mean Entrainment Measures

4.4.1 Maximum Mean Concentration Decay

As outlined in Section 1.2, mean measures of mixing such as the mean concentration decay along the jet centerline can be considered to be indirect/imperfect measures of crossflow fluid entrainment into the jet. This entrainment decreases the local concentration of jet fluid within a given measurement volume (pixel size multiplied by light sheet thickness), which results in a decrease of fluorescence signal. Figure 4.5 highlights the maximum mean concentration decay (C_m/C_o) along the jet centerline coordinate, s_c, scaled by D, JD, and $\sqrt{J}D$ for an equidensity transverse jet injected from all three injectors at a variety of mo-

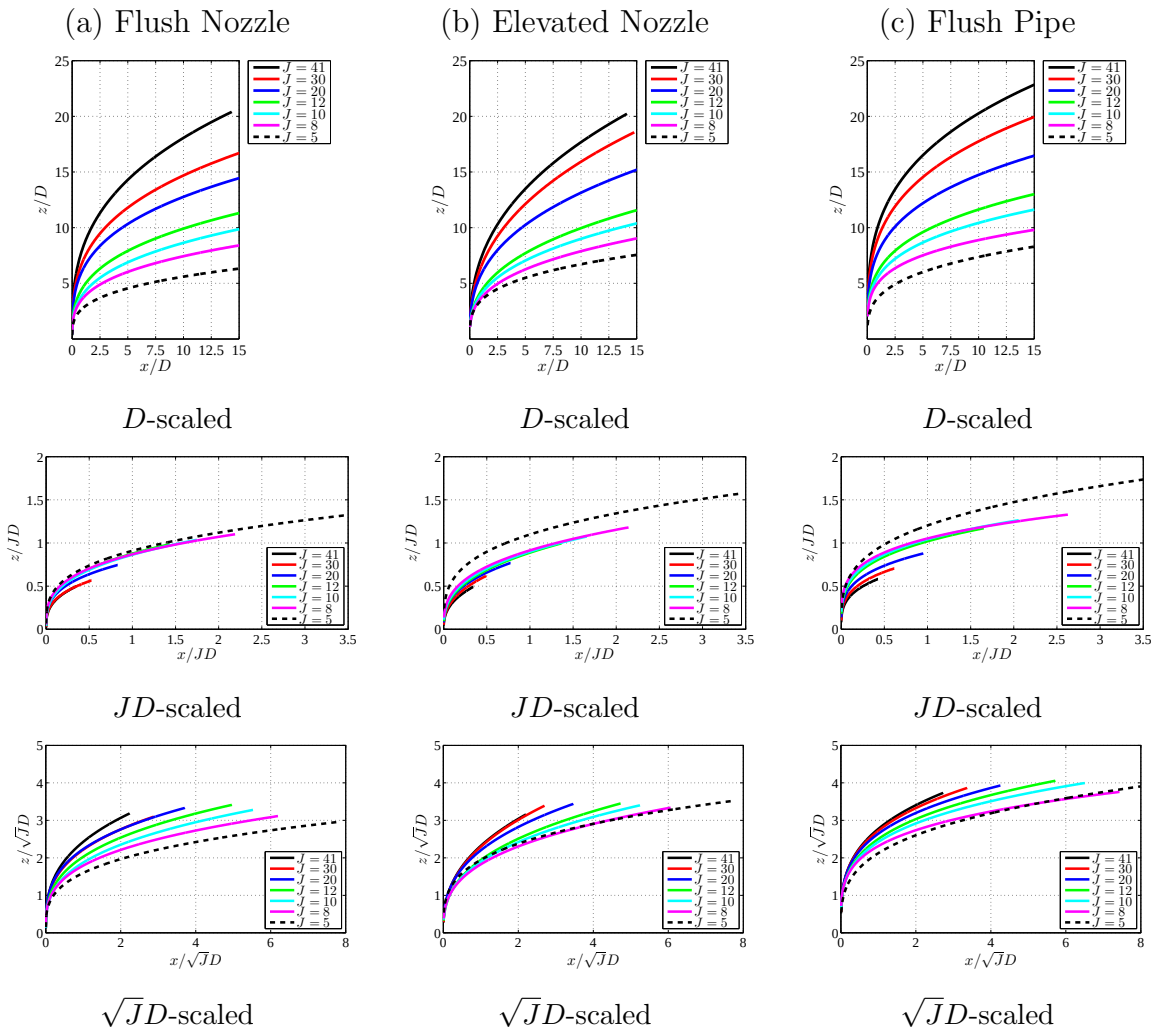


Figure 4.4: Scalar centerline trajectories of $S = 1.00$ transverse jets for various momentum flux ratios. (a) flush nozzle injector (b) elevated nozzle injector (c) flush straight pipe injector. Data are shown for various physical coordinate scalings (D, JD, and $\sqrt{J}D$).

mentum flux ratios. In the top row of Figure 4.5, the s_c/D position at which C_m/C_o starts to decay is a measure of the length of the potential core. The potential core length is an indicator of the degree of engagement between jet and crossflow fluid in the near-field of the transverse jet. Figure 4.5 shows that for the flush-injection cases, lowering momentum flux ratio decreases the potential core length. This is consistent with the increase in near-field vorticity generation as J is lowered for both the flush nozzle and flush pipe-injected jets. The elevated nozzle-injected jet potential core lengths, however, seem to decrease significantly more slowly as J is lowered when compared to the flush-injected jets. In fact, a slight increase in potential core length is observed for elevated nozzle-injected when comparing $J = 8$ to $J = 5$. This finding is consistent with the vertical co-flow along the upstream side of the elevated nozzle-injected jets acting to stabilize the shear layer and reduce vorticity generation, resulting in a reduction of near-field crossflow fluid entrainment into the jet.

Similar to the jet trajectory comparison (Figure 4.4), scaling physical space with JD and $\sqrt{J}D$ did not result in acceptable data collapse along the entire jet, as shown in the second and third row of Figure 4.5. It should be noted, however, that $\sqrt{J}D$ scaling did produce some potential core length collapse for the flush nozzle and flush pipe-injected cases, which is consistent with the work of Smith and Mungal (1998) for a turbulent, flush nozzle-injected transverse jet with $25 \leq J \leq 100$. This potential core collapse suggests that $\sqrt{J}D$ is a significant parameter for determination of the near-field entrainment characteristics of the transverse jet.

The potential core collapse with $\sqrt{J}D$ scaling also enables more direct comparison of the concentration decay trends after potential core breakdown. The various reference lines on Figure 4.5 correspond to known concentration decay rates for different types of flows. The $s_c^{-1.3}$ decay rate is what has been observed in the work of Smith and Mungal (1998) for high J transverse jets. The s_c^{-1} decay rate is what is predicted for turbulent free jets, and it is what is observed for pipe-generated transverse jets at high J in the work of Su and Mungal (2004). The $s_c^{-2/3}$ decay rate is what is expected for wake-like flows, and the work of Hasselbrink and Mungal (2001) predicts transition from jet-like behavior in the near-field to wake-like behavior in the far-field of strong (high J) transverse jets. It is immediately

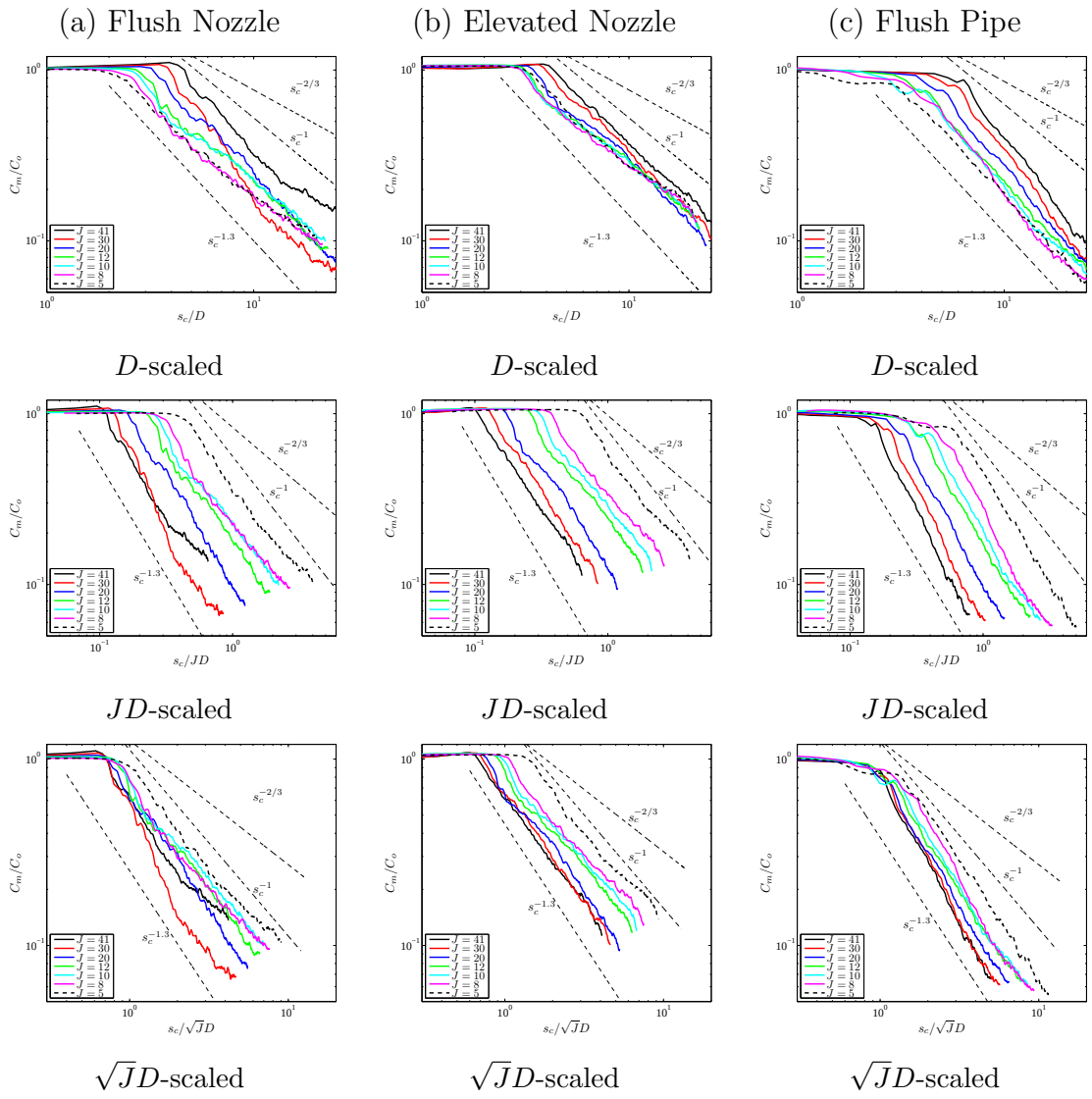


Figure 4.5: Maximum mean concentration decay trends along the scalar centerline trajectory coordinate s_c for equidensity transverse jets at various momentum flux ratios. (a) Flush nozzle injector (b) elevated nozzle injector (c) flush straight pipe injector. Data are shown for various physical coordinate scaling (D, JD, and $\sqrt{J}D$).

apparent from the $\sqrt{J}D$-scaled, flush nozzle data that the decay rate of $J = 41$ and $J = 30$ transverse jets does exhibit "branch point"-behavior, branching from a higher decay rate to a lower decay rate at a given downstream s_c/D location. Smith and Mungal (1998) found the branch point to occur at $s/JD = 0.3$, very close to the branch point observed in the present studies for $J = 41$ and $J = 30$ ($s/JD \approx 0.33$). It should be noted, however, that the decay rates before and after the branch point seem to be highly dependent on the momentum flux ratio. Moreover, no branch point behavior was observed for flush pipe-injected, or elevated nozzle-injected flows, suggesting that both the jet exit velocity profile and the crossflow velocity profile play an integral role on the appearance of the branch point. Branch-point behavior was not observed for the pipe injection studies of Su and Mungal (2004).

Due to the significant variation in concentration decay rate along the jet associated with a variation in momentum flux ratio, significant crossing of decay lines among different momentum flux ratio jets is observed. For instance, the first row of Figure 4.5a shows that for $s_c/D < 10$, the $J = 5$, flush nozzle-injected case has a lower maximum mean concentration than $J = 30$. However, for $s_c/D > 10$, $J = 30$ has the lower C_m/C_o. The crossing over of decay lines in the maximum mean concentration decay trends was postulated by Smith and Mungal (1998) to be the physical mechanism for the minimum flame length behavior observed to occur at specific values of jet-to-crossflow velocity ratio R in reactive transverse jet experiments. This flame length variation depending on J has significance for applications where a designated maximum concentration level is required to be reached quickly (e.g. pollutant dispersal). For instance, in this experiment, if the target $C_m/C_o = 0.2$ and a flush nozzle injector is used, $J = 8$ and $J = 5$ would be considered to be the best mixers. In contrast, if the target $C_m/C_o = 0.1$, $J = 30$ would be considered to be the best mixer. Comparing the different injector decay trends, the degree of crossing over of decay lines also seems to be highly dependent on injector type.

For the flush nozzle-injected jets, the average decay rate along the jet after potential core breakdown for $J \leq 20$ lied between the free jet rate of s_c^{-1} and the high J transverse jet rate of $s_c^{-1.3}$, with the lower momentum flux ratio jets having decay rates closer to s_c^{-1}. Above $J = 20$, the decay rate varies significantly along the jet, with portions along the trajectory

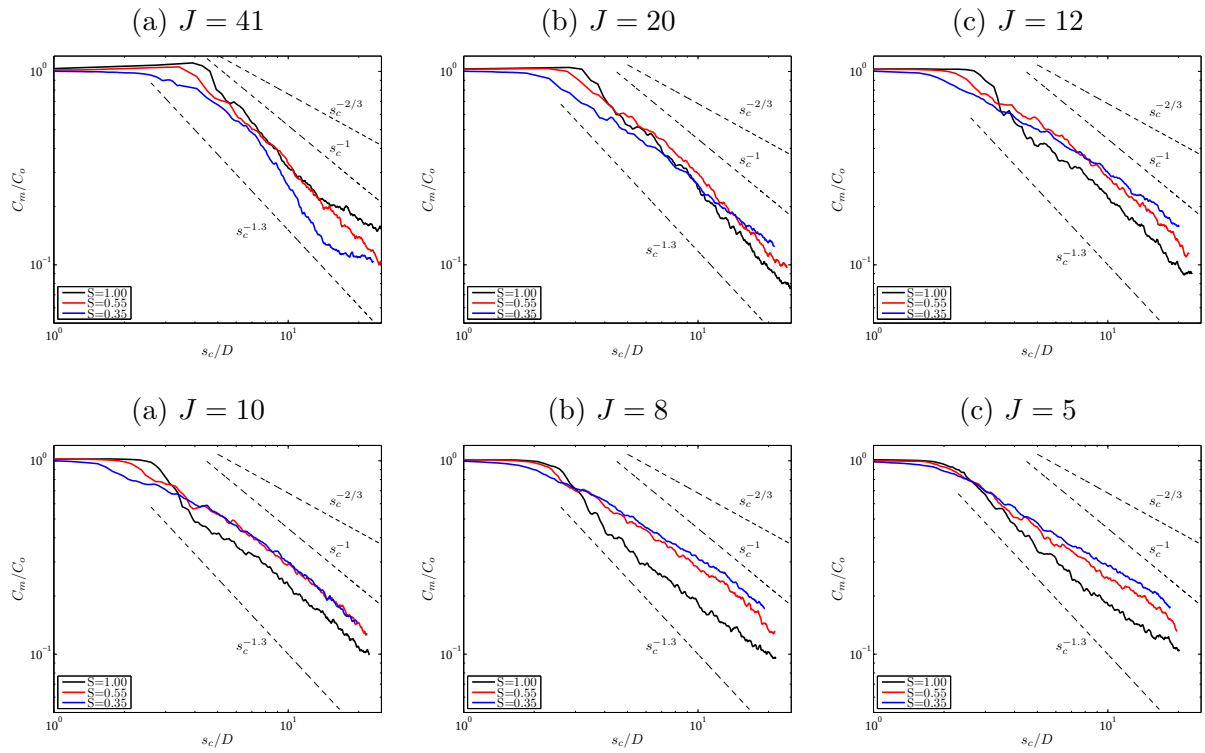


Figure 4.6: Maximum mean concentration decay as a function of centerline trajectory coordinate s_c/D for flush nozzle-injected transverse jets of various density ratios ($1.00 \geq S \geq 0.35$) and momentum flux ratios in the range $41 \geq J \geq 5$, as indicated above each plot.

of the $J = 30$ and $J = 41$ jets having a decay rate higher than $s_c^{-1.3}$, as evidenced by the JD-scaled plots (second row of Figure 4.5a). In contrast, C_m/C_o for $J = 41$ and $J = 30$ jets injected from the elevated nozzle have a less variable decay rate along their trajectory. The decay rate for the elevated nozzle injection cases seem to decrease to s_c^{-1} and lower as J is reduced, although the majority of the elevated nozzle-injected cases were closer to s_c^{-1} than $s_c^{-1.3}$, consistent with the weakened jet shear layer associated with the vertical co-flow mentioned previously. The flush pipe-injected C_m/C_o decay rates after potential core breakdown all lied between $s_c^{-1.6}$ and $s_c^{-1.3}$, suggesting potential increases in mixing as compared to the flush nozzle-injected jets. This finding is significant and will be verified with other mixing metrics, as pipe injectors are significantly easier to machine and model.

Figure 4.6 highlights the C_m/C_o decay trends for flush nozzle-injected jets at fixed J, while

varying density ratio S in the range $0.35 \leq S \leq 1$. For the cases shown here, all $J < 10$ jets and all $S = 0.35$ jets are absolutely unstable. Otherwise, increases in either J or S result in reduced upstream shear layer vorticity associated with weakened, convectively unstable shear layers. As can be seen from Figure 4.6, the density ratio S has an effect on transverse jet evolution that is not fully captured by the momentum flux ratio. For high $J = 41$, lowering the density ratio and transitioning the flow to absolute instability ($S < 0.4$) reduced C_m/C_o. This finding is consistent with the significant increase in instability and vorticity generation near the jet exit for high momentum flux ratio cases when lowering the density ratio. Similar to the $S = 1$, $J = 41$ case, a branch point was also observed for the $S = 0.35$, $J = 41$ case, although its location was further along the jet trajectory ($s/JD \approx 0.36$). Interestingly, no branch point was observed for $S = 0.55$. Therefore, it would seem as though the appearance and location of the branch point is a function of J, S, and injector type.

As the momentum flux ratio is lowered (i.e. $J = 12$), and particularly for the cases that are already absolutely unstable (i.e. $J < 10$), lowering the density ratio actually reduces the C_m/C_o decay rate. In fact, lowering the density ratio for $J = 5$ reduces the decay rate below the rate found in wake flows ($s_c^{-2/3}$). This is a somewhat unexpected result, and it will be explored in detail using instantaneous images and mixing metrics of both the centerplane and cross-section of the jet in following sections.

Figure 4.7 directly highlights the effect on C_m/C_o of varying the injector type for equidensity transverse jets at fixed J. For $J = 41$, the flush nozzle-injected and elevated nozzle-injected jets show very similar C_m/C_o trends near the jet exit, consistent with the highly similar upstream shear layer stability characteristics of these two nozzles at high J outlined in Chapter 3. In contrast, as J is lowered (i.e. $J \leq 12$), the potential core of the elevated nozzle is elongated and the decay rate is reduced due to the vertical co-flow along the shear layer. For $J = 41$, the pipe injected jet exhibited a delayed potential core breakdown, consistent with the delayed onset of upstream shear layer instability summarized in Chapter 3. The average decay rate along the entire jet after potential core break-down, however, was consistently high for the pipe-injected cases as compared to the other injectors for all J cases shown here, suggesting the pipe to be the best overall mixer among all injectors.

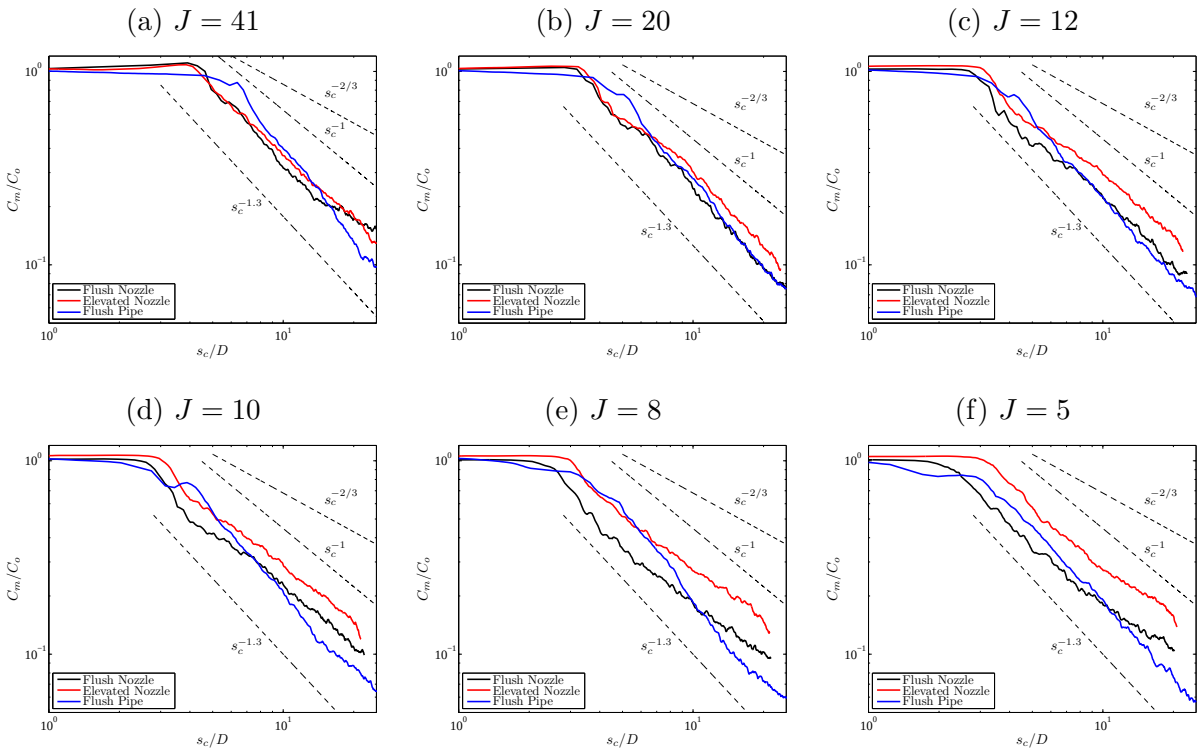


Figure 4.7: Maximum mean concentration decay as a function of scalar centerline trajectory coordinate s_c/D for equidensity transverse jets injected from the flush nozzle, elevated nozzle, and flush straight pipe injector configurations, with momentum flux ratios in the range $41 \geq J \geq 5$, as indicated above each plot.

However, instantaneous mixing metrics need to be applied in order to verify this contention. Moreover, the centerplane is not necessarily a good indicator of the total entrainment and mixing characteristics of the entire jet cross-section, especially since there are high levels of asymmetry in the jet cross-sectional structure for certain cases, as summarized in Chapter 3. It is for this reason that comparisons among the various mixing metrics utilized in this study to characterize the jet using both centerplane and cross-sectional data will be administered.

4.4.2 Mean Jet Spread

As summarized in Section 1.1.2.4, another commonly utilized measure of mean entrainment of crossflow fluid into the jet is the spread of the transverse jet, δ, at a given jet trajectory

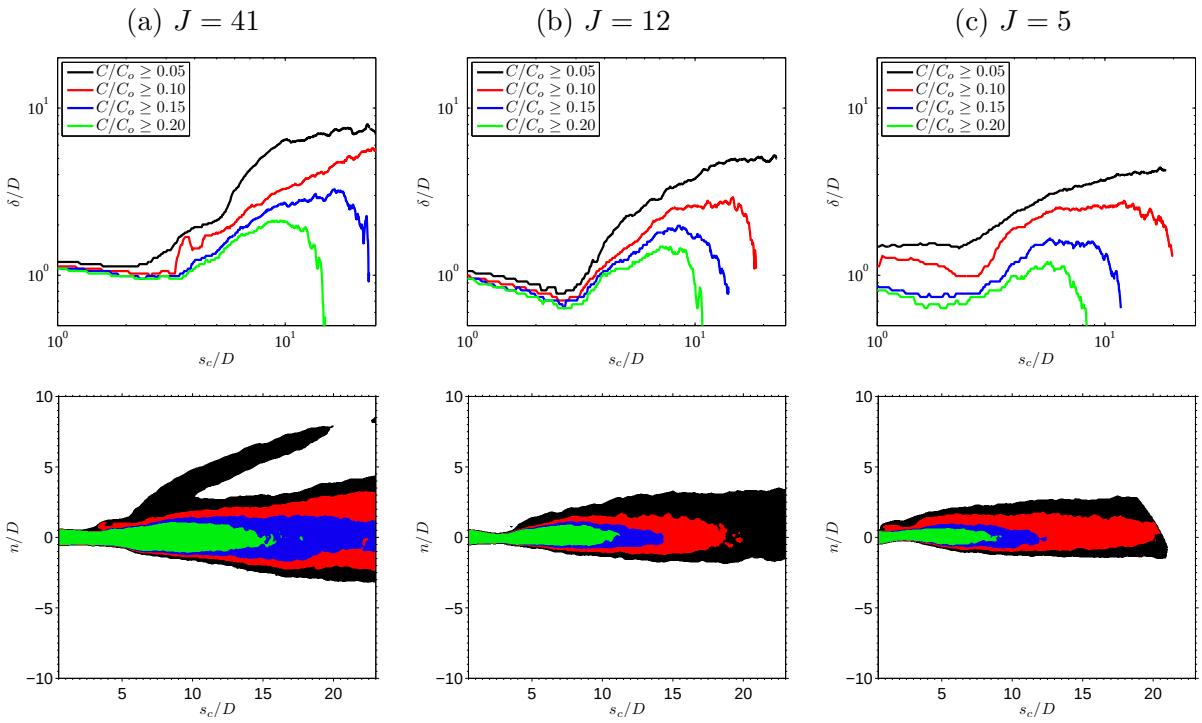


Figure 4.8: Top row: normalized mean jet spread, δ/D, in the jet trajectory normal direction, n, as a function of normalized centerline trajectory coordinate, s_c/D, for flush nozzle-injected, $S = 1.00$ transverse jets. Bottom row: mean jet spread visualization images for various threshold concentrations as indicated in the legend of the plots in the top row. Data shown for momentum flux ratios (a) J=41 (b) J=12 (c) J=5.

location, s_c, in the trajectory-normal direction, n, with positive values of n corresponding to the lee side of the jet (see Figure 4.1 for coordinate system). To quantify this for the current study, after determination of the $s_c - n$ coordinate system, a coordinate transformation was administered using the power law fit to the jet trajectory and MATLAB's interp2 function with cubic interpolation. The resolution input to the MATLAB function was kept constant and equal to the pixel resolution of the original data. After the coordinate transformation, the data was set to a value of unity for concentrations above the spread threshold concentration, and set to zero for concentrations below the threshold. The spread was then quantified using a summation of the vector from the resulting binary data matrix at each jet trajectory location (s_c/D).

The top row of Figure 4.8 shows spread data for flush nozzle-injected transverse jets at $J = 41$, $J = 12$, and $J = 5$ utilizing the concentration thresholds $C/C_o \geq 0.05$, $C/C_o \geq 0.10$, $C/C_o \geq 0.15$, and $C/C_o \geq 0.20$ to define the boundaries of the jet. The bottom row of this figure is a direct visualization of the spread boundaries, in the $s_c - n$ coordinate system, of the data in the top row. It is immediately apparent from these images that the trends in the spread are dependent on threshold concentration. For instance, as evidenced by column a in Figure 4.8, the lee-side lobe (positive n/D) of the asymmetric, $J = 41$ jet seems to be contributing significantly to the total spread when a threshold concentration $C/C_o \geq 0.05$ is utilized to define the boundaries of the jet. The effect of the lee-side lobe for $J = 41$ disappears when the threshold concentration is increased to $C/C_o \geq 0.10$, however. This lee-side lobe disappears completely for the structurally symmetric jets ($J \leq 20$).

Comparing the spread trends to the concentration decay trends, there seems to be discrepancy between the two metrics. For instance, according to the spread plots, $J = 41$ has the best entrainment characteristics as it seems to spread the most when the δ/D values are compared to those of $J = 12$ and $J = 5$ at a given spread concentration threshold (e.g. $C/C_o \geq 0.05$). This is in direct contrast to the concentration decay plots, which suggest that the $J = 5$ case has the best entrainment characteristics for $s_c/D < 10$, as evidenced by the top row of Figure 4.5a. This discrepancy is due to the inherently asymmetric nature of the transverse jet. Unlike the free jet, since the transverse jet is not generally axisymmetric about its centerline, the centerplane spread is not as good an indicator of entrainment characteristics as it is for the free jet. In the case of the axisymmetric free jet, the decay of C_m/C_o would directly correlate with the spread of the jet due to mass conservation considerations. This correlation is not necessarily true for transverse jets, however, as the concentration distribution (and hence spread) could vary in different directions about the centerline. It is for this reason that this author considers the centerplane spread of the transverse jet to be a poor indicator of its entrainment characteristics.

Although the spread is not a good indicator of the entrainment characteristics of the jet, concentration threshold visualizations like those shown in the bottom row of Figure 4.8 do have value in determining the minimum flame length trends for the transverse jet, as a

means of predicting reactive JICF behavior, and as an improved indicator of the entrainment efficiency of this flowfield as compared to the centerplane spread. For instance, comparing the data for $J = 41$, $J = 12$, and $J = 5$ for the concentration threshold $C/C_o \geq 0.2$, the visualizations in the bottom row of Figure 4.8 show that the $J = 5$ case has the shortest flame length among these three cases, which is consistent with the C_m/C_o trends in the top row of Figure 4.5a. The C_m/C_o trends show that the $J = 5$ case drops to $C_m/C_o = 0.2$ at $s_c/D \approx 8$), which agrees well with the top row of Figure 4.8c, and it is also consistent with the flame length visualization of the bottom row of Figure 4.8c. In contrast to the $C/C_o \geq 0.2$ trends, the $C/C_o \geq 0.1$ trends in the spread plots shown in Figure 4.8 suggest that $J = 12$ has a shorter flame length than $J = 5$, consistent with the minimum flame length characteristics caused by the crossing over of C_m/C_o decay lines discussed in Section 4.4.1. Thus, spread visualization plots like those shown in the bottom of Figure 4.8 can be utilized as an alternative, and somewhat more informative, method to visualize the flame length and concentration distribution of this flowfield at a given target threshold concentration.

Figure 4.9 highlights flame length visualizations similar to those in the bottom row of Figure 4.8 for $S = 1.00$ transverse jets injected from all three injectors studied at momentum flux ratios $J = 41$, $J = 12$, $J = 8$, and $J = 5$. It should be noted again that in this coordinate system, positive n/D corresponds to the lee side of the jet. The minimum flame length for variable J mentioned in Section 4.4.1 can be directly visualized here. For instance, the flush pipe data in 4.9a suggests that if a maximum jet fluid concentration of $C/C_o = 0.1$ is desired (red "flames" in these images), the minimum flame length momentum flux ratio is $J \approx 8$. Consistent with the C_m/C_o decay plots, these images also show that the minimum flame length is dependent on injector type as well as target jet fluid concentration (or stoichiometry in the equivalent reactive case).

Figure 4.10 visualizes the flame length variation for transverse jets injected from the flush nozzle injector at several different density ratios $S = 1.00$, $S = 0.55$, $S = 0.35$. As seen in the C_m/C_o trends in Figure 4.6, there seems to be a shift in the flame length trends for lowering S as momentum flux ratio is varied. For the $J = 41$ cases, the flame length drops as density ratio is lowered, whereas for $J < 12$, the flame length increases as density ratio is lowered.

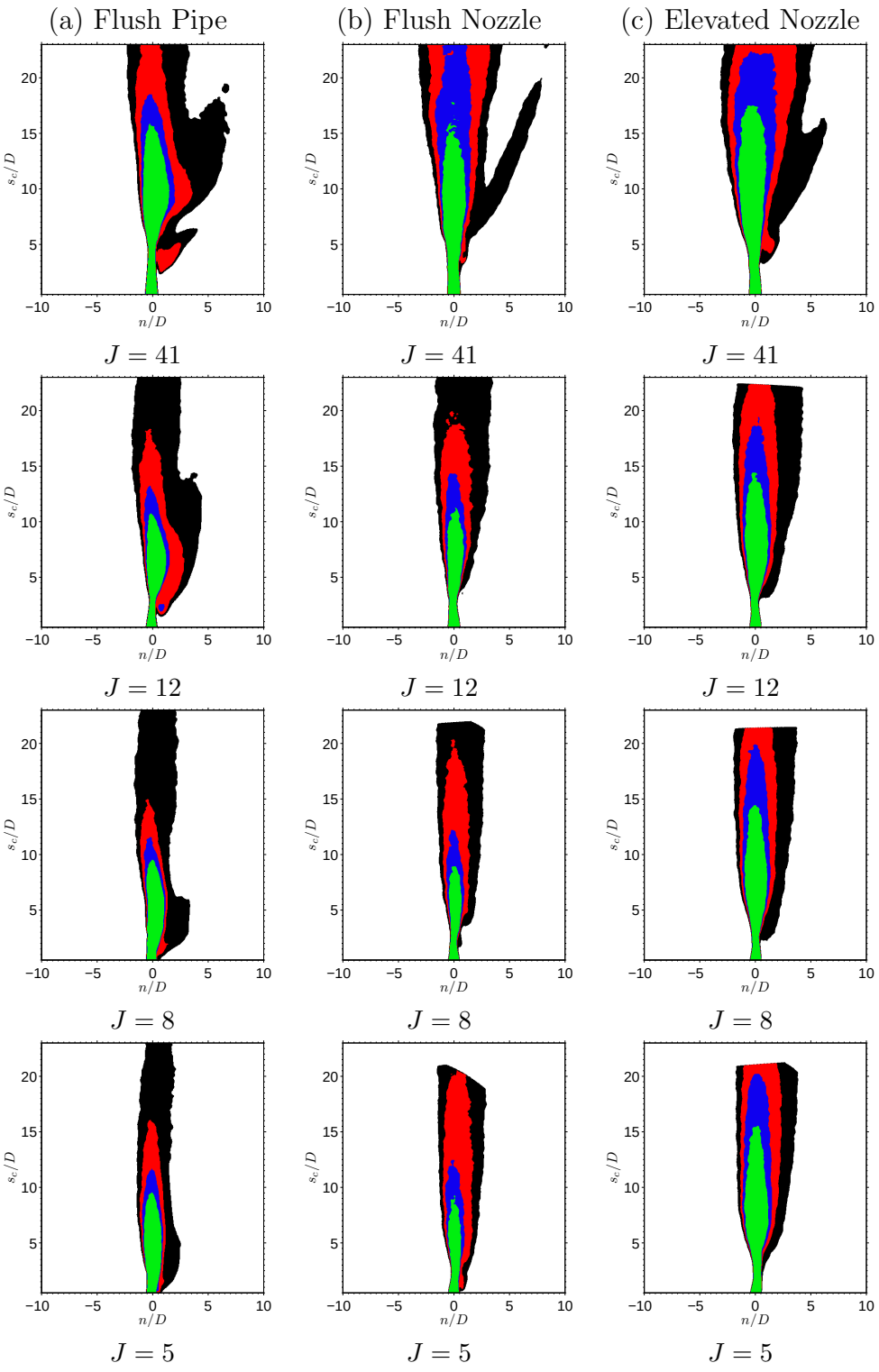


Figure 4.9: Mean spread and flame length visualization of the JICF with $Re_j = 1900$ and density ratio $S = 1.00$, transformed to the $s_c - n$ coordinate system and binarized according to a chosen target threshold concentration. (a) Flush straight pipe injector (b) flush nozzle injector, and (c) elevated nozzle injector. Data are shown for varying momentum flux ratios $J = 41$, 12, 8, and 5. Target threshold concentrations shown are $C/C_o \geq 0.05$ (black), $C/C_o \geq 0.10$ (red), $C/C_o \geq 0.15$ (blue), and $C/C_o \geq 0.20$ (green).

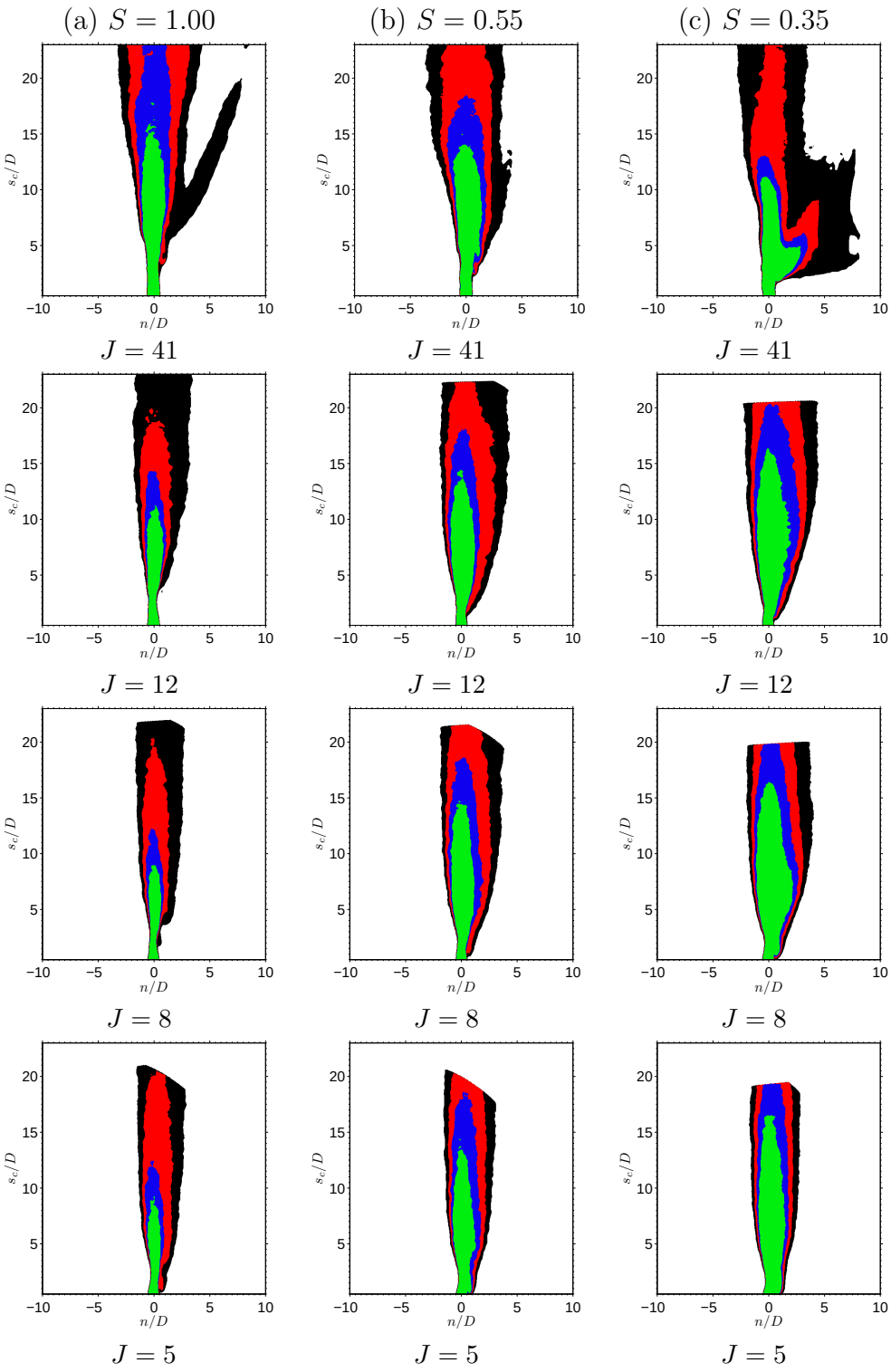


Figure 4.10: Mean spread and flame length visualization of the JICF with $Re_j = 1900$ injected from the flush nozzle at various density ratios, transformed to the $s_c - n$ coordinate system and binarized according to a chosen target threshold concentration. (a) $S = 1.00$, (b) $S = 0.55$, and (c) $S = 0.35$. Data are shown for varying momentum flux ratios $J = 41$, 12, 8, and 5. Target threshold concentrations shown are $C/C_o \geq 0.05$ (black), $C/C_o \geq 0.10$ (red), $C/C_o \geq 0.15$ (blue), and $C/C_o \geq 0.20$ (green).

It should also be noted that there seems to be a general increase in lee-side (positive n/D) spread as density ratio is lowered for $J \geq 8$. This increased lee-side spread with a reduction in S is not as apparent for $J = 5$, however, potentially due to the proximity of the jet to the test section floor for this lower momentum flux ratio case. It remains to be seen whether these variations in flame length and jet fluid distribution correlate well with more definitive measures of mixing applied to the centerplane as well as the cross-section of the jet.

4.5 Turbulent Stirring and Diffusion Measures

4.5.1 Cross-sectional Mixing Metrics

As mentioned previously, the variation in jet fluid distribution about the transverse jet centerline suggests that mixing metrics applied to the cross-section of the jet will result in more conclusive mixing efficiency data. To the knowledge of this author, a systematic method of mixing metric application for transverse jets with different J and S has never been developed. Complications arise due to the fact that the transverse jet is not a closed boundary system. A closed boundary system yields a constant global mass or concentration ratio at all mixing progress levels. This constant global mass/molar ratio is ideal for mixing metrics such as the Unmixedness or PDF, the probability density function of the concentration (see Section 1.2 for definitions of these metrics), since they are intended to measure variations about the global mean value. However, since the transverse jet is an open boundary system, the global mean value is not necessarily constant. As shown in the work of Shan and Dimotakis (2006), mass conservation applied to a control volume containing all of the jet fluid of the equidensity jet in crossflow results in a mean scaled jet fluid concentration value, $\hat{C}/C_o$, that depends on the jet-to-crossflow velocity ratio, R, the cross-sectional area of the jet exit, A_j, and the cross-sectional area of the control surface containing all of the jet fluid at a downstream location x, oriented in the y-z plane, A_{cs}:

$$\frac{\hat{C}(x)}{C_o} \simeq R\frac{A_j}{A_{cs}(x)} \tag{4.3}$$

The main assumption of Equation 4.3 is that the average component of the jet velocity perpendicular to the control surface is approximately equal to the crossflow speed, U_∞. This

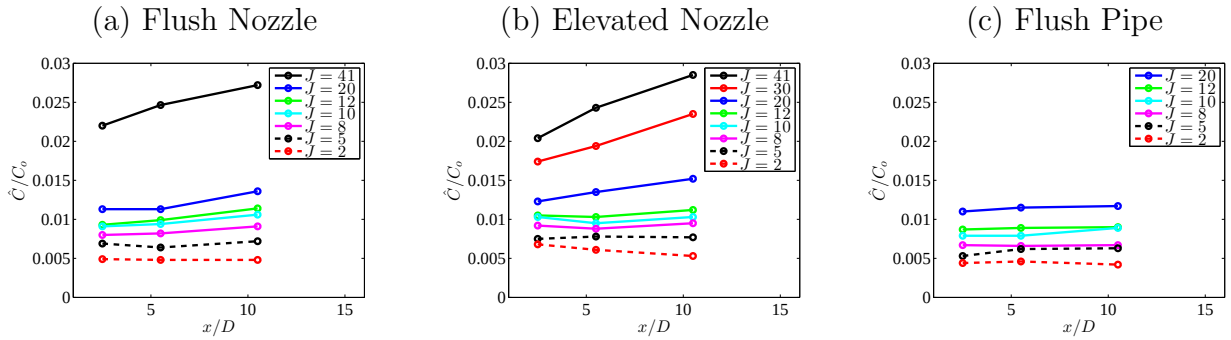


Figure 4.11: $\hat{C}(x)/C_o$ variation with downstream distance x and momentum flux ratio J for the equidensity JICF with $Re_j = 1900$ injected from the three different injectors: (a) Flush Nozzle (b) Elevated Nozzle, and (c) Flush Pipe. $\hat{C}(x)/C_o$, as defined in Equation 4.3, is calculated with $A_{cs} = 18D \times 18D$ for all J and x/D.

is a reasonably accurate assumption for $x >> D$, particularly for low R equidensity jets, and it can serve as a general reference for trends in concentration with variations in R. Equation 4.3 suggests that as long as the control volume cross-sectional area A_{cs} is kept constant and the assumption on jet velocity applies, $\hat{C}(x)/C_o$ should stay constant with downstream distance, x. The trends in $\hat{C}(x)/C_o$ with downstream distance x for equidensity transverse jets injected from the flush nozzle at various J (or R since $J = SR^2$) are shown in Figure 4.11. In this figure, $A_{cs} = 18D \times 18D$ for all $\hat{C}(x)/C_o$ calculated.

The trends in Figure 4.11 at a given x/D are consistent with Equation 4.3 for all injectors. As J is lowered, $\hat{C}(x)/C_o$ decreases when the control surface A_{cs} is kept constant. There is some deviation of $\hat{C}(x)/C_o$ for a given J at different x/D, however. This deviation is most apparent for high J. The trends in $\hat{C}(x)/C_o$ seem to suggest that at high J, the mean velocity perpendicular to the control surface is higher than the crossflow speed, especially near the jet exit. Cross-sectional PIV in this flow regime would verify this result.

The variation of $\hat{C}(x)/C_o$ with variations in J proposed by Equation 4.3, and verified by the data in Figure 4.11, suggests that comparing mixing trends among different J requires a method of matching the mean jet fluid concentration value, $\overline{C}/C_o$, over the selected interrogation area, A_i. Matching $\overline{C}/C_o$ for $S = 1.00$ effectively matches the global mass ratio between jet fluid and crossflow fluid, yielding concentration field data that can be utilized to quantify mixing metrics that are more suited for closed boundary systems like the spatial

PDF and Unmixedness. To accomplish this mean matching in the present study, the size of the cross-sectional interrogation area, A_i, enclosing the jet fluid within the plane of measurement, was varied such that the mean value of the scalar over this area, $\overline{C}/C_o$, was matched among all different momentum flux ratios at each instance of time (i.e. for each instantaneous PLIF image). It should be noted that when the jet density and crossflow density are not the same ($S \neq 1$), the mass ratio and molar ratio are not equal. The PLIF measurement technique visualizes molar ratios (more specifically, number density of acetone), and does not take into account the mass of the gas constituents. Therefore, when $\overline{C}/C_o$ is matched among different S, it is the molar ratio that is matched, not the mass ratio. A simple calculation could be done to convert from molar ratio to mass ratio based on the density ratio, but since no restrictions are placed on a desired mass ratio between jet fluid and crossflow fluid, in order to compare jet to crossflow mixing efficiency variation among different S, no attempt at such a conversion from molar to mass ratios was administered.

In order to match the $\overline{C}/C_o$ value among different cases, a reference mean must be chosen. The choice of reference mean was explored in detail in the present study. Two extremes of the reference $\overline{C}/C_o$ value were determined from the cross-sectional data: one was the mean value for the flush nozzle injected, $S = 1.00$, $J = 41$ case at $x/D = 10.5$ ($\overline{C}/C_o = 2.21 \times 10^{-2}$), the other was for the $S = 1.00$, $J = 2$ case at $x/D = 10.5$ ($\overline{C}/C_o = 3.89 \times 10^{-3}$). $\overline{C}/C_o$ was calculated for each case by averaging a $20D \times 20D$ square containing all the jet fluid in the mean image. These two reference values were used to compare trends among the mixing metrics. As mentioned before, the reference mean, $\overline{C}/C_o$, was matched among different cases at different instances of time by varying the interrogation area, A_i, for each instantaneous image. In practice, this was accomplished by sorting the data from the entire field of view (FOV) into a vector of concentration values from highest to lowest. This vector was then augmented by adding or subtracting zeros until the mean value of the vector was equal to $\overline{C}/C_o$. This method of mean matching was found to be the simplest and most easily automated, and since the Unmixedness value is not dependent on flow length scales (assuming adequate resolution), the method is equivalent to varying A_i.

Figure 4.12 compares the trends of cross-sectional Unmixedness, U_{yz}, calculated using the

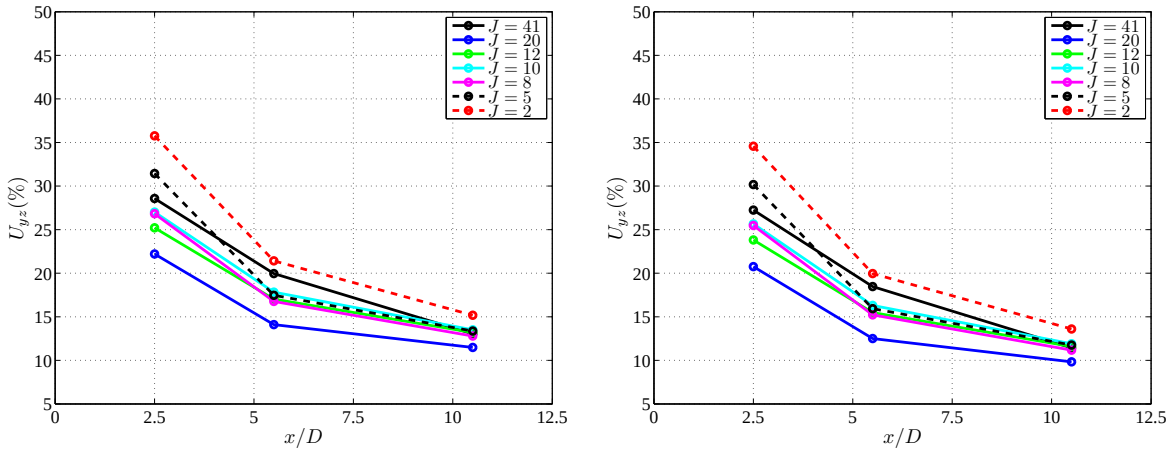


Figure 4.12: Cross-sectional (constant x/D)-based unmixedness, U_{yz}, for equidensity flush nozzle-injected transverse jets, plotted against downstream coordinate x/D. U_{yz} was calculated by matching each instantaneous image's spatial mean to the spatial mean value of the temporal mean image at $x/D = 10.5$ for two different flow conditions: (a) $J = 2$ and (b) $J = 41$. Results are shown for various momentum flux ratios.

two reference means mentioned (Figure 4.12a for $J = 2$, and Figure 4.12b for $J = 41$). The data are plotted against downstream coordinate x/D. The Unmixedness values in Figure 4.12 were calculated for $S = 1.00$ transverse jets injected from the flush nozzle injector for various momentum flux ratios in the range $41 \geq J \geq 2$ as indicated in the plot. As Figure 4.12 shows, although the values of Unmixedness drop slightly for a higher reference mean value (Figure 4.12b as compared to Figure 4.12a), the trends are identical between the two reference means. Thus, although the values of Unmixedness do change depending on the reference mean value, the trends do not, suggesting that the reference mean value can be arbitrarily chosen provided that all jet fluid is contained within A_i when the mean is matched.

Figure 4.13 compares the trends of the PDF with a variation in reference mean value for the same data used to quantify the Unmixedness values shown in Figure 4.12, that is, for the extreme values of the reference mean extracted from $J = 41$ and $J = 2$ at $x/D = 10.5$. Each column in Figure 4.13 is a different cross-sectional position as indicated, and each row corresponds to a different reference mean value. Similar to the Unmixedness trends, the PDF trends suggest that as long as all the jet fluid is contained within A_i, the reference

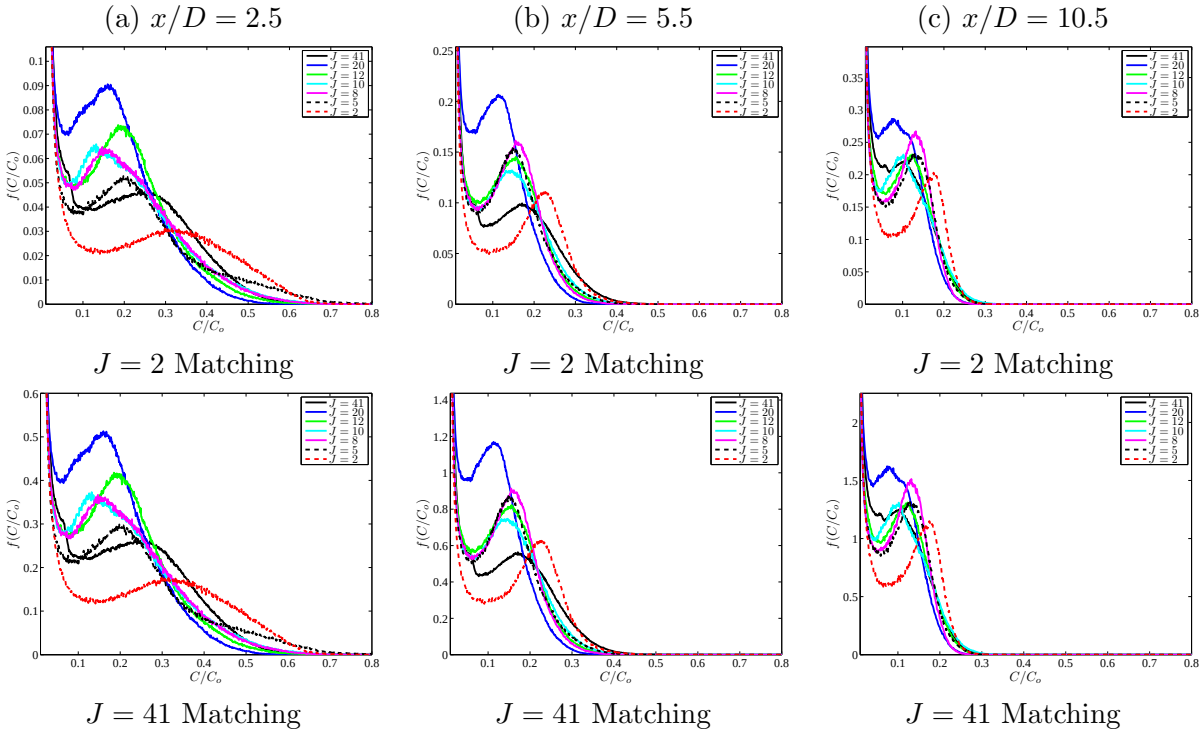


Figure 4.13: Cross-sectional (constant x/D)-based PDF, for equidensity flush nozzle-injected transverse jets, plotted at various downstream coordinates x/D as indicated. PDF was calculated by matching each instantaneous image's spatial mean to the spatial mean value of the temporal mean image at $x/D = 10.5$ for two different flow conditions: $J = 2$ (top row) and $J = 41$ (bottom row). Results are shown for various momentum flux ratios.

mean value has no bearing on the trends of mixing. For instance, according to Figure 4.13, both reference mean matching conditions suggest that the $J = 20$ case is the best-mixed case at every x/D location i.e. has the strongest peak in the PDF at C/C_o closest to the reference mean value, which is consistent with the trends of Unmixedness shown in Figure 4.12. The actual probability density value of the peak, however, does change with variations in $\overline{C}/C_o$. The variation in PDF peak value with variation in reference mean is consistent with the Unmixedness quantification in Figure 4.12, as a stronger PDF peak corresponds to a concentration field that is more uniform, resulting in a lower Unmixedness. Therefore, all cross-sectional mixing data shown in the rest of this thesis will utilize the reference mean value of the flush nozzle-injected, $S = 1.00$, $J = 2$ case at $x/D = 10.5$ ($\overline{C}/C_o = 3.89 \times 10^{-3}$) for determination of A_i. Similar sensitivity analysis to reference mean value of the centerplane Unmixedness calculation will be summarized in Section 4.6.

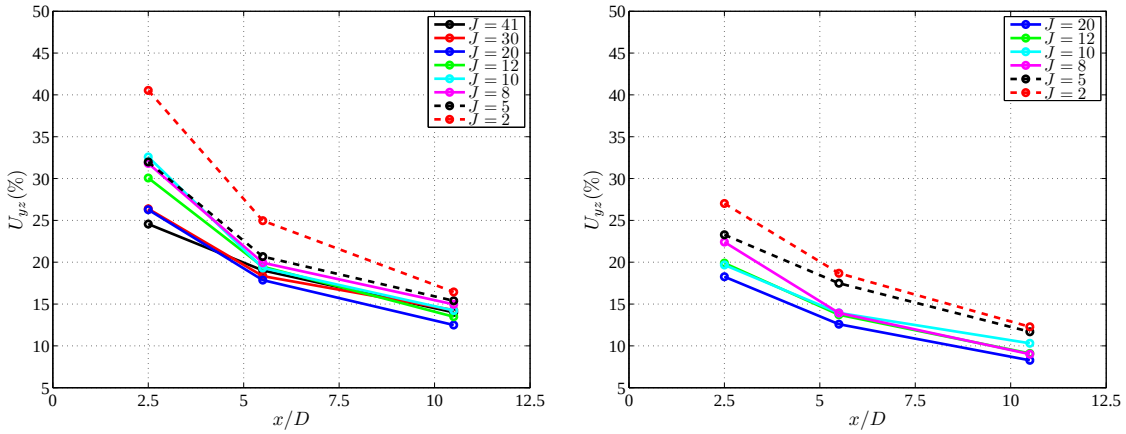


Figure 4.14: Cross-sectional (constant x/D)-based unmixedness, U_{yz}, for equidensity transverse jets at various momentum flux ratios as indicated, plotted against downstream coordinate x/D. U_{yz} was calculated by matching each instantaneous image's spatial mean to the spatial mean value of the temporal mean image at $x/D = 10.5$ for the flush nozzle-injected, $S = 1.00$, $J = 2$ jet. Results are shown for two different injectors: (a) Elevated Nozzle, and (b) Flush Pipe.

The consistency of the trends in PDF and Unmixedness was found to be the case for all cross-sectional PDF and Unmixedness data quantified. Figure 4.14 shows the cross-sectional Unmixedness trends at different downstream positions for equidensity transverse jets injected from the elevated nozzle (Figure 4.14a) and the flush pipe (Figure 4.14b) for a variety of momentum flux ratios in the range $41 \geq J \geq 2$. A comparison among the Unmixedness trends in Figure 4.14 to the PDF quantification shown in Figure 4.15 suggests that these two mixing metrics can be used interchangeably. For instance, as found for the flush nozzle injector data plotted in Figures 4.12 and 4.13, both metrics suggest that for all injectors studied, the $J = 20$ is the best downstream mixer up to $x/D = 10.5$. Additionally, $J = 2$ seems to be the worst downstream mixer for all injectors studied, as evidenced by its highest Unmixedness value and least compact PDF distribution at all measurement locations. Therefore, if efficient downstream mixing is required, $J = 20$ would be the optimum mixer for the equidensity momentum flux ratios shown here. $J = 20$ is not necessarily the best mixer along the jet trajectory coordinate s_c/D, however.

Figure 4.16 compares the mixing trends along the jet trajectory coordinate s_c/D of equidensity transverse jets for all injectors studied, with momentum flux ratios in the range

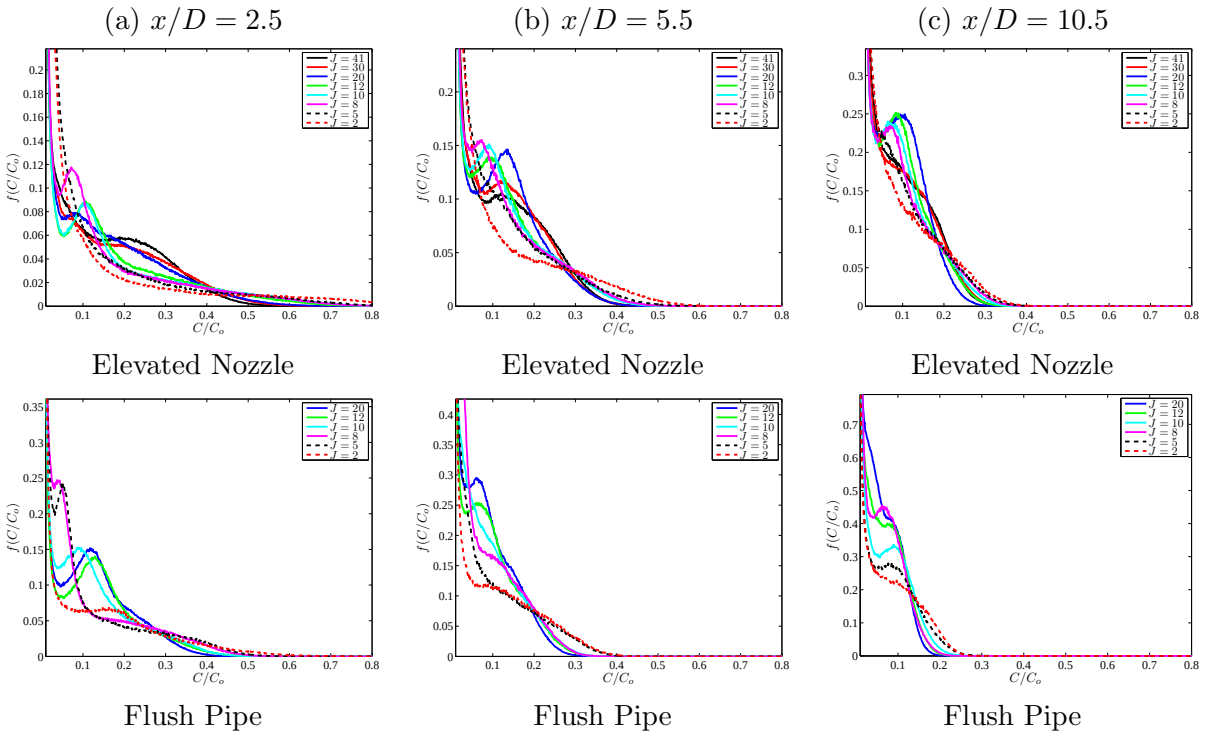


Figure 4.15: Cross-sectional (constant x/D)-based PDF, for equidensity transverse jets, plotted for various downstream coordinates x/D and momentum flux ratios as indicated. PDF was calculated by matching each instantaneous image's spatial mean to the spatial mean value of the temporal mean image at $x/D = 10.5$ for the flush nozzle-injected, $S = 1.00$, $J = 2$ jet. Results are shown for two different injectors: Elevated Nozzle (top row) and Flush pipe (bottom row).

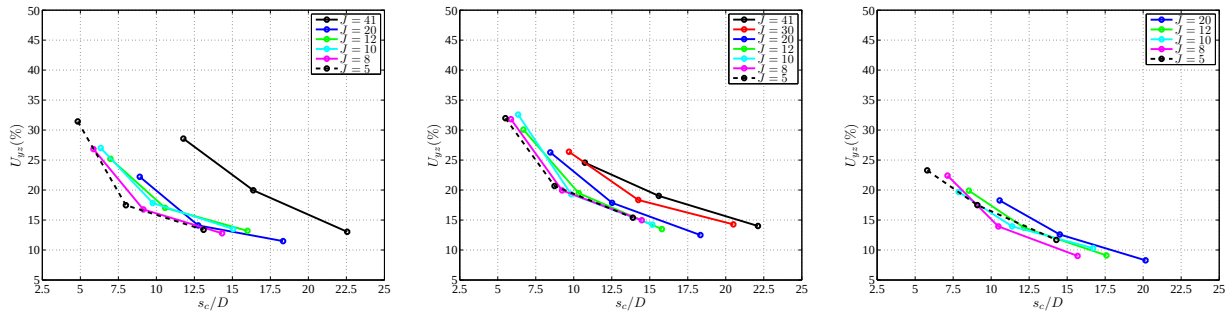


Figure 4.16: Cross-sectional (constant x/D)-based unmixedness, U_{yz}, for equidensity transverse jets at various momentum flux ratios as indicated, plotted against jet trajectory coordinate s_c/D. U_{yz} was calculated by matching each instantaneous image's spatial mean to the spatial mean value of the temporal mean image at $x/D = 10.5$ for the flush nozzle-injected, $S = 1.00$, $J = 2$ jet. Results are shown for three different injectors: (a) Flush Nozzle, (b) Elevated Nozzle, and (c) Flush Pipe.

$41 \geq J \geq 5$. The trends of U_{yz} vs. s_c/D in Figure 4.16 are markedly different from the trends of U_{yz} vs. x/D shown in Figures 4.14 and 4.12. The U_{yz} vs. s_c/D plots suggest that lowering the momentum flux ratio tends to increase mixing, whereas the U_{yz} vs. x/D plots suggested optimum mixing at $J = 20$. This discrepancy is to be expected, as higher momentum flux ratio jets have had longer time to mix with the crossflow at a given downstream position. Due to this discrepancy, most of the Unmixedness data shown here will be plotted against the jet trajectory coordinate, s_c/D, as this is the more natural coordinate for comparisons among different, J, S, and injector types. Figure 4.16 also suggests that the flush pipe tends to be the best mixer among all injectors, and the elevated nozzle tends to be the worst, consistent with the C_m/C_o decay trends summarized in Section 4.4.1.

Figure 4.17a-c shows the PDF trends at a constant downstream position $x/D = 10.5$ for flush nozzle-injected transverse jets of varying density ratio, at constant momentum flux ratios $J = 41$ (a), $J = 12$ (b), and $J = 5$ (c). Figure 4.17d shows trends of Unmixedness at $x/D = 10.5$ with varying density ratio for momentum flux ratios corresponding to the PDFs plotted in Figure 4.17a-c. The consistency between the Unmixedness value and the PDF is once again noted. Both metrics suggest that lowering density ratio below $S = 1.00$ decreases mixing at $x/D = 10.5$ for all momentum flux ratios. The reduction in mixing (increase in U_{yz}) associated with $S < 1.00$ is not as significant for the high $J = 41$ case as

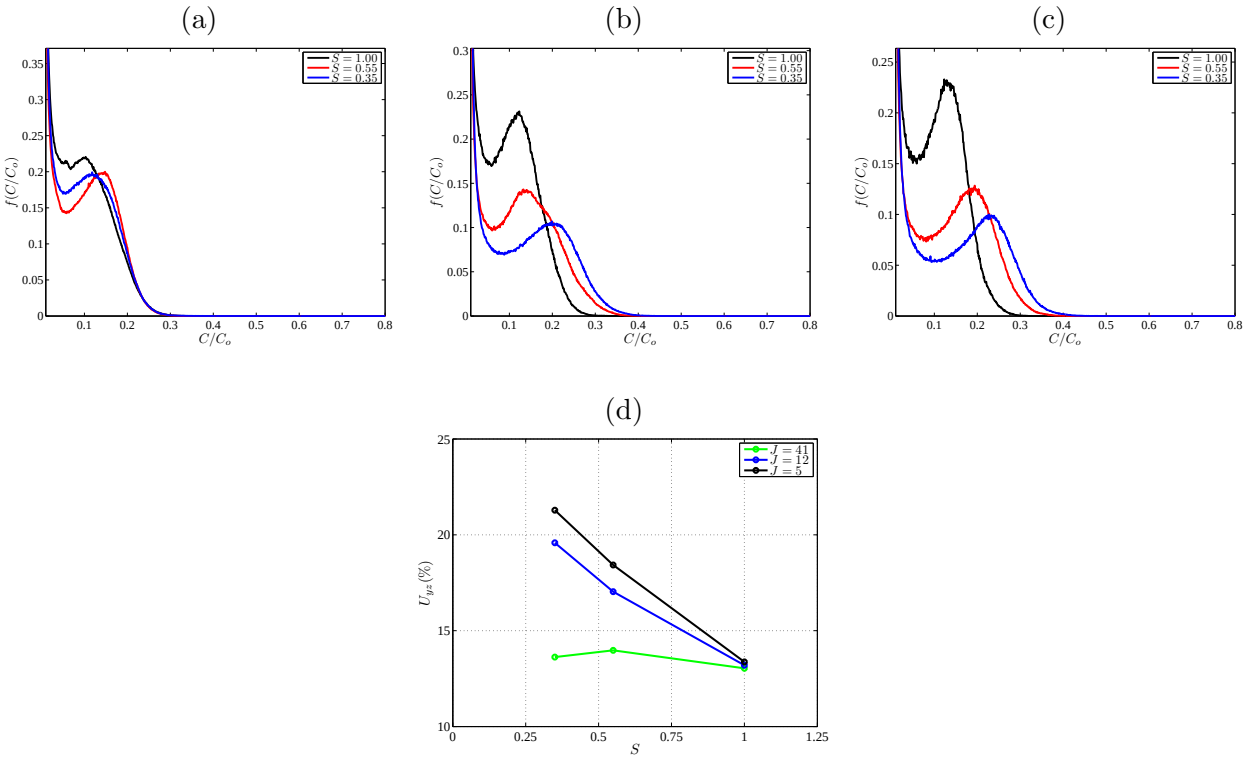


Figure 4.17: Cross-sectional (constant $x/D = 10.5$)-based metrics: (a-c) spatial probability density function (PDF) and (d) Unmixedness U_{yz} for flush nozzle-injected transverse jets with density ratios $S = 1.00$, $S = 0.55$, and $S = 0.35$. Data are shown for various momentum flux ratios: (a) PDF, $J = 41$, (b) PDF, $J = 12$, (c) PDF, $J = 5$, and (d) U_{yz} vs. S for various J values.

opposed to the lower momentum flux ratio cases, however. At first glance, this finding seems to be in contrast to the reduction in C_m/C_o for lowering S at $J = 41$ shown in Figure 4.6a. Yet trends at constant x/D do not necessarily translate to trends along the jet trajectory coordinate s_c/D, as mentioned previously. For $J = 41$, at $x/D = 10.5$, $s_c/D = 23$ for $S = 1.00$, $s_c/D = 20$ for $S = 0.55$, and $s_c/D = 18$ for $S = 0.35$. Therefore, the fact that the $J = 41$, $S = 0.35$ has reached a comparative level of mixing at a significantly lower s_c/D coordinate suggests that it is the best mixer for $J = 41$, consistent with the C_m/C_o trends. As evidenced by the trajectory plots in Figure 4.2, the variation in s_c/D at constant x/D is reduced for lower J, which is the reason why the trends of U_{yz} at constant x/D for $J = 12$ and $J = 5$ correspond well with the trends of C_m/C_o at $J = 12$ (Figure 4.6b) and $J = 5$ (Figure 4.6c). However, in order to enable more accurate comparison between centerplane and cross-sectional mixing trends, the Unmixedness must be directly applied to the centerplane images.

4.6 Centerplane and Cross-sectional Mixing Metric Comparison

Although the cross-section of the jet is the most relevant plane over which to determine transverse jet mixing efficiency, cross-sectional flowfield measurement can at times be difficult or impossible. Therefore, it is worthwhile to compare centerplane and cross-sectional mixing metrics and determine the level of correspondence. Since it has been determined that Unmixedness is an appropriate metric to use for the cross-section due to its formulation and its ability to capture the information contained in the PDF in a compact form, the Unmixedness was also utilized as a metric for the centerplane. Unmixedness quantification was applied to the centerplane using two different methods. The results from these methods will be designated as $U_{c,sn}$, and $U_{c,xz}$. In the first method, $U_{c,sn}$ was calculated utilizing the mean jet trajectory to transform the instantaneous centerplane images to the $s_c - n$ coordinate system, similar to the method applied to the mean spread images (see Section 4.4.2). $U_{c,sn}$ was evaluated on this transformed plane by using narrow slices of data oriented in the jet-normal direction n with a fixed interrogation area width of $0.25D$ in the s_c direction, as shown in Figure 4.18. The interrogation area was moved pixel by pixel in the s_c direc-

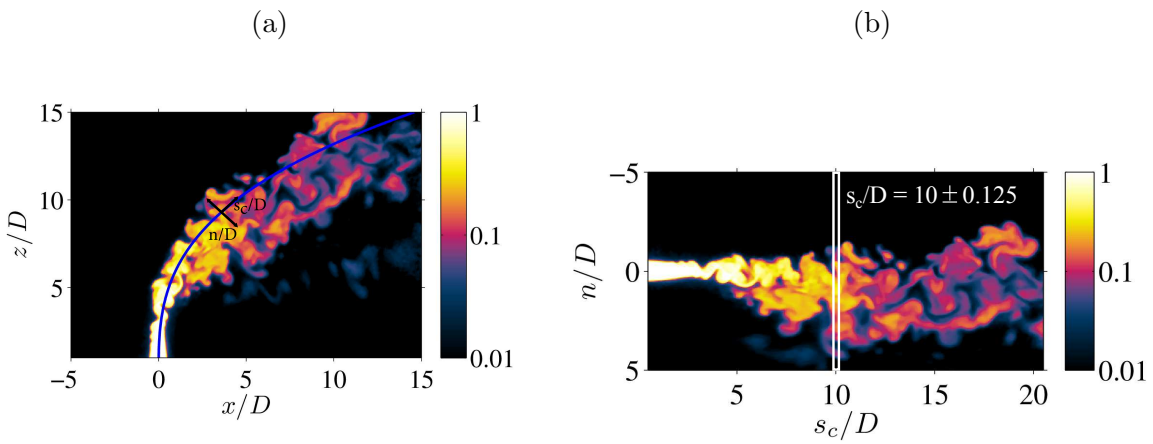


Figure 4.18: (a) Instantaneous scalar centerline trajectory in the $y = 0$ centerplane of the transverse jet for $J = 20$ and $S = 1.00$. As in Fig. 4.1, the blue line shows the power law curve fit for the corresponding mean jet image. (b) Instantaneous image transformed into the s_c/D, n/D coordinate system with an example of a thin interrogation area slice centered at $s_c/D = 10$, of total width 0.25, used to evaluate centerplane Unmixedness $U_{c,sn}$.

tion, resulting in trends of $U_{c,sn}$ vs. s_c/D. In the second Unmixedness calculation method, $U_{c,xz}$ was calculated from the un-transformed centerplane data using vertical slices in the z direction with constant interrogation area width $0.25D$ in the x direction.

Similar to the method of mean-matching utilized for the cross-sectional data, the data from the interrogation area extracted for either $U_{c,sn}$ or $U_{c,xz}$ calculation was sorted into a vector ordered from high to low concentration values, and zeros were added or subtracted from the vector in order to match the mean value to a reference mean. Since all of the jet fluid is not contained within the centerplane, this mean-matching method has less of a physical basis for the centerplane data, but it is still necessary in order to have a more appropriate comparison among jets of different J as it does match the ratio of jet fluid to crossflow fluid within the plane of measurement. A sensitivity analysis to the reference mean value, $\overline{C}/C_o$, was also administered for the centerplane data. Figure 4.19 compares the $U_{c,sn}$ and $U_{c,xz}$ trends for two extreme reference mean values quantified using an average of a $20D \times 0.25D$ block of pixels for $J = 41$ centered at $s_c/D = 20$ (bottom row of Figure 4.19) and $J = 5$ at $s_c/D = 15$ (top row of Figure 4.19). $J = 2$ was not used due to its poor trajectory fitting. Comparing the top row of Figure 4.19 to the bottom row, there

seems to be very little sensitivity to the reference mean, which is consistent with the cross-sectional Unmixedness sensitivity analysis summarized in Section 4.5.1. Slight variations exist for $J = 30$, however. Unfortunately, quantitative cross-sectional jet fluid concentration data were not obtained for $J = 30$, as the match between the centerplane data and the cross-sectional data were not accurate due to effects associated with the asymmetry. Since there were only minor variations for $J = 30$, the reference mean value calculated from the $J = 5$ data at $s_c/D = 15$ ($\overline{C}/C_o = 2.41 \times 10^{-2}$) was utilized as the reference mean for the remainder of the centerplane Unmixedness calculations shown here. It is also worthwhile to note the similarity between the $U_{c,sn}$ data (Figure 4.19a) and the $U_{c,xz}$ data (Figure 4.19b). Although the values do change between $U_{c,sn}$ and $U_{c,xz}$, there is very little deviation in trends, which justifies plotting cross-sectional Unmixedness against the centerline trajectory coordinate s_c/D, as the cross-sectional Unmixedness is calculated for vertical slices (similar to $U_{c,xz}$).

Figure 4.20 highlights the trends of $U_{c,sn}$ and $U_{c,xz}$ for $S = 1.00$ transverse jets, injected from the elevated nozzle and flush pipe injectors, with various momentum flux ratios in the range $41 \geq J \geq 5$. Similar to the flush nozzle injector data shown in the top row of Figure 4.19, the elevated nozzle $U_{c,sn}$ and $U_{c,xz}$ trends exhibit very little deviation from one another. There is, however, slightly more deviation between $U_{c,sn}$ and $U_{c,xz}$ trends for the flush pipe injector, as indicated by the $8 \leq J \leq 12$ cases plotted in the bottom row of Figure 4.20. This slight increase in deviation could be explained by the deeper penetration into the crossflow that the pipe-injected jets exhibit as compared to the nozzle-injected jets (e.g. see Figure 4.3).

The centerplane Unmixedness trends of the elevated nozzle and flush nozzle jets shown in Figure 4.20, along with the flush nozzle-injected jet trends highlighted in the top row of Figure 4.19, can be directly compared to the cross-sectional Unmixedness trends of these injectors shown in Figure 4.16. These results show remarkable consistency between the centerplane Unmixedness trends and the cross-sectional Unmixedness trends. Both planes of measurement suggest that mixing along the jet trajectory coordinate generally increases as the momentum flux ratio decreases, at least relatively near the jet exit ($s_c/D < 20$). There

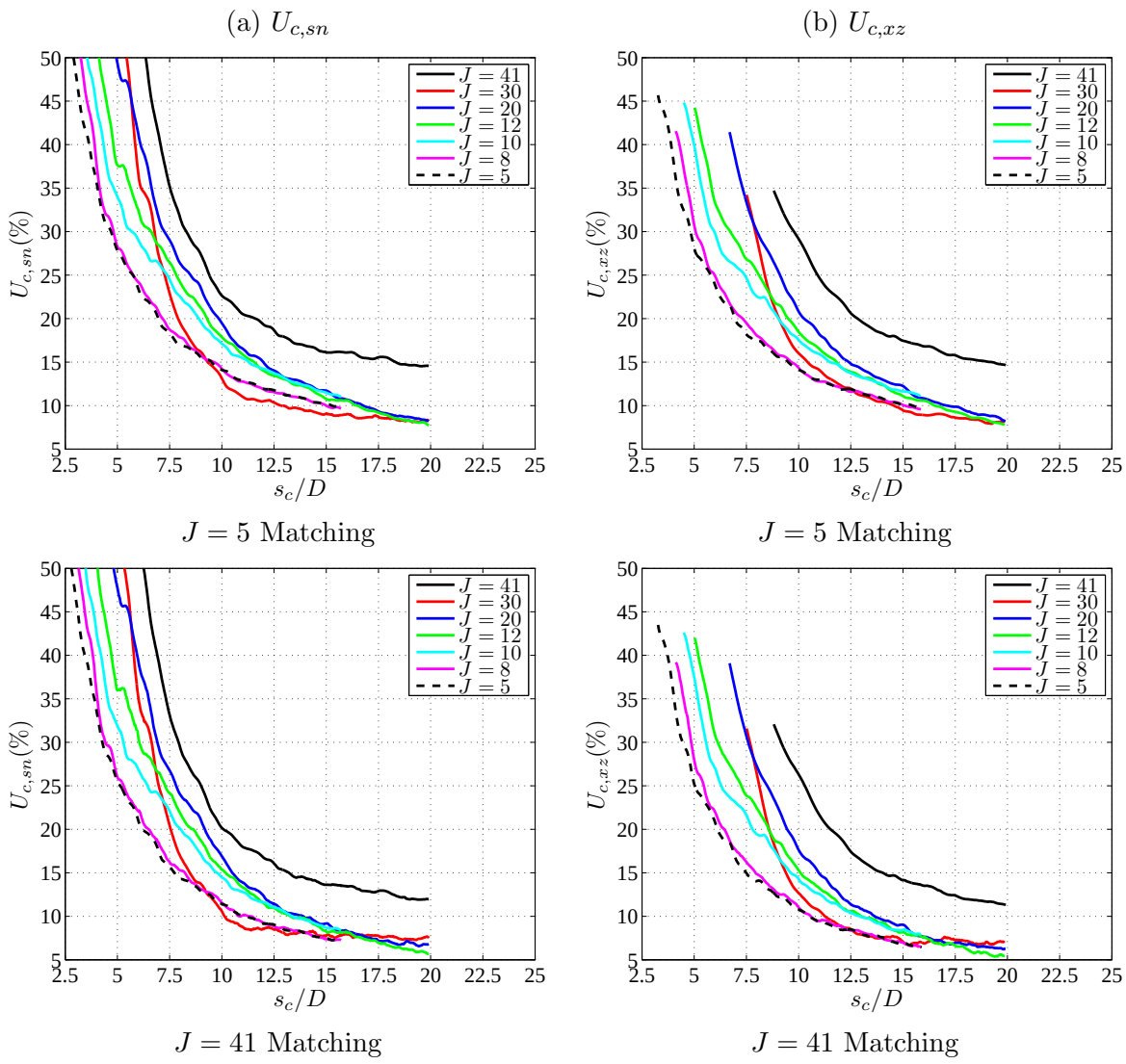


Figure 4.19: (a) $U_{c,sn}$ and (b) $U_{c,xz}$ trends at various J for $S = 1.00$, flush nozzle-injected jets with two different reference mean values utilized for mean-matching. Reference mean values were extracted from the $J = 5$ (top row) and $J = 41$ (bottom row) data for the flush nozzle-injected, $S = 1.00$ transverse jet.

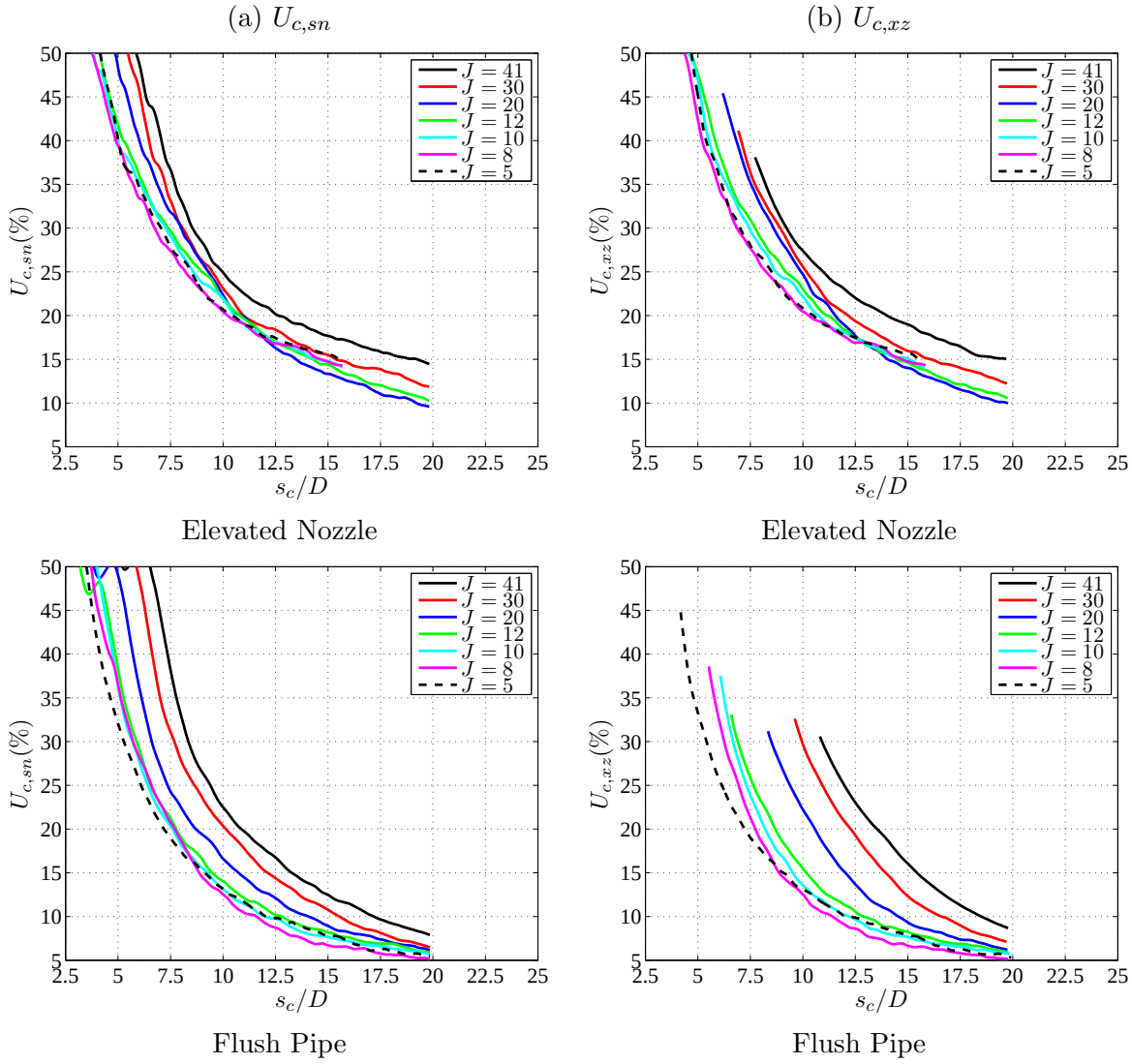


Figure 4.20: (a) $U_{c,sn}$ and (b) $U_{c,xz}$ trends at various J for $S = 1.00$ transverse jets. Data shown for the elevated nozzle (top row), and flush pipe injectors (bottom row). Reference mean value was extracted from the $J = 5$ data for the flush nozzle-injected, $S = 1.00$ transverse jet.

are some deviations from this rule, however, as evidenced by comparing the flush pipe $J = 8$ case to the $J = 5$ case in both the cross-sectional Unmixedness (Figure 4.16c) and centerplane Unmixedness (bottom row of Figure 4.20) calculations. Consistent with the cross-sectional results, the centerplane data also suggest that the flush pipe injector is generally the best mixer, and the elevated nozzle is generally the worst due to the upstream shear layer co-flow's reduction of upstream vorticity generation. The remarkable consistency between the jet centerplane Unmixedness and cross-sectional Unmixedness verifies the repeatability of the experiments, as the data for each cross-sectional downstream measurement location (each x/D) were taken on a different day. The centerplane data were taken on a separate day from the cross-sectional measurements as well.

The $U_{c,sn}$ trends may also be compared to the maximum mean concentration decay trends shown in the first row of Figure 4.5. Figure 4.21 plots the $U_{c,sn}$ trends in log-scale for $S = 1.00$ jets injected from all three injectors, so that direct comparisons to the log-log plots in the first row of Figure 4.5 can be made. Comparing these two sets of mixing metric trends suggests that even though the C_m/C_o metric is applied to the mean data, it seems to capture the mixing trends quite well. Both metrics suggest that the flush pipe injector has the fastest overall decay rate among all injectors at any momentum flux ratio studied here, as evidenced by the slopes of the $U_{c,sn}$ and C_m/C_o trends. Moreover, both metrics suggest a generally higher level of mixing for lower momentum flux ratios, even for the elevated nozzle injector. Both metrics also suggest that as the crossflow velocity is increased (J is reduced), the vertical co-flow along the elevated nozzle-injected jet's upstream shear layer acts to reduce the degree of mixing between the jet and crossflow as compared to the flush nozzle injector. The branch point and crossing of decay line behavior of C_m/C_o summarized in Section 4.4.1 is also apparent in the $U_{c,sn}$ trends shown in Figure 4.21.

Although the trends of $U_{c,sn}$ and C_m/C_o are generally similar, there is a significant advantage to the $U_{c,sn}$ metric. Since $U_{c,sn}$ incorporates the entire centerplane jet concentration profile within a thin interrogation area oriented in the $s_c - n$ plane into its calculation, it is able to directly illuminate the jet shear layer behavior near the jet exit, whereas the C_m/C_o metric only indirectly shows this behavior by showing the length of the potential core. For

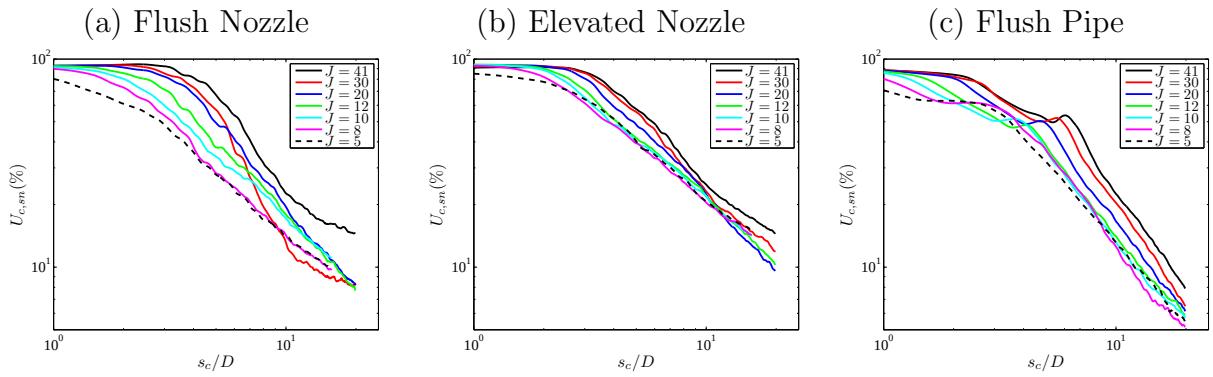


Figure 4.21: $U_{c,sn}$ variation along jet trajectory coordinate s_c/D for the momentum flux ratio range $41 \geq J \geq 5$. Data shown on log-log plots for $S = 1.00$ jets with $Re_j = 1900$ injected from the three different injectors: (a) Flush Nozzle (b) Elevated Nozzle, and (c) Flush Pipe.

instance, comparing the trends of C_m/C_o and $U_{c,sn}$ for the flush nozzle-injected, $J = 5$ jet (Figure 4.21a and the top row of Figure 4.5a, respectively), one can see that the $U_{c,sn}$ value begins to decay at the jet exit, whereas C_m/C_o starts to show variation near $s_c/D \approx 2.5$. Moreover, since the Reynolds number is relatively low for the mixing study administered here, the correspondence between C_m/C_o and $U_{c,sn}$ does not necessarily extend to the fully turbulent regime due to the separation of inertial (large) and viscous (small) scales associated with highly turbulent flows. Thus, $U_{c,sn}$ is a more conclusive and discerning measure of mixing than C_m/C_o. The C_m/C_o metric should only be used as an alternative to save computational time and complexity in the lower Reynolds number regime; any extension of the correspondence between these two metrics to fully turbulent jets in crossflow must be verified.

Figure 4.22 highlights the trends of $U_{c,sn}$ with variable density ratio at various momentum flux ratios for flush nozzle-injected transverse jets. Similar to the C_m/C_o (Figure 4.6) and U_{yz} trends (Figure 4.17), $U_{c,sn}$ seems to suggest a shift in the character of the mixing trends with S reduction for high J as compared to low J. When the density ratio is lowered, higher momentum flux ratios tend to mix better overall, especially near the jet exit. In contrast, when the density ratio is lowered for low momentum flux ratios, the overall mixing progress is reduced, especially for $J < 10$, when the upstream shear layer is absolutely unstable regardless of density ratio. This behavior can be explained by visual inspection of the PLIF

data.

Figure 4.23 shows high-resolution, instantaneous, centerplane PLIF images of $S = 1.00$, flush nozzle-injected jets for $J = 41$, $J = 12$, $J = 8$, and $J = 5$. Figure 4.24 shows high-resolution, instantaneous, centerplane PLIF images of $S = 0.35$, flush nozzle-injected jets at the same momentum flux ratios shown in Figure 4.23 for $S = 1.00$. These high resolution data sets are not the data utilized for the mixing study, but as it will be summarized in Section 4.7, $U_{c,sn}$ trends are very similar between the high resolution images shown here, and the lower resolution images utilized for the mixing study. Comparing the $S = 1.00$ images (Figure 4.23) to the $S = 0.35$ images (Figure 4.24), one significant difference is immediately apparent: the reduction of entrainment of crossflow fluid into the vortex cores. The equidensity transverse jet upstream shear layer vortices seem to be drawing a significant amount of crossflow fluid into their cores. However, the cores of the low density vortices seem to contain primarily jet fluid. This finding explains why the shift in character of mixing trends for S reduction occurs. For high J cases (e.g. $J = 41$), lowering the density ratio increases vorticity generation on both the upstream and downstream side of the jet, especially near the jet exit, as summarized in Getsinger et al. (2012). This increased vorticity generation enhances interfacial area generation and increases scalar gradients, resulting in an increase in local mixing rate. Moreover, there is more jet fluid in the wake of the $S = 0.35$, $J = 41$ jet as opposed to the $S = 1.00$, $J = 41$ case, which is consistent with the spread data shown in the first row of Figure 4.8ac. As the momentum flux ratio is lowered, however, the upstream shear layer generates vorticity closer to the jet exit for $S = 1.00$ due to the interaction between the jet and the crossflow. This vorticity generation mechanism results in enhanced crossflow fluid entrainment as opposed to the vorticity generation mechanism associated with lowering density ratio, as evidenced by comparing the PLIF images of $S = 1.00$, $J = 5$ to $S = 0.35$, $J = 5$ (Figure 4.23d as compared to Figure 4.24d).

Figure 4.25 directly visualizes the effect on mixing efficiency, as characterized by $U_{c,sn}$, of varying the injector type at fixed J for equidensity transverse jets. The $U_{c,sn}$ trends shown in Figure 4.25 may be directly compared to the C_m/C_o trends shown in Figure 4.7. As mentioned previously, the overall mixing enhancement of the flush pipe injector as compared

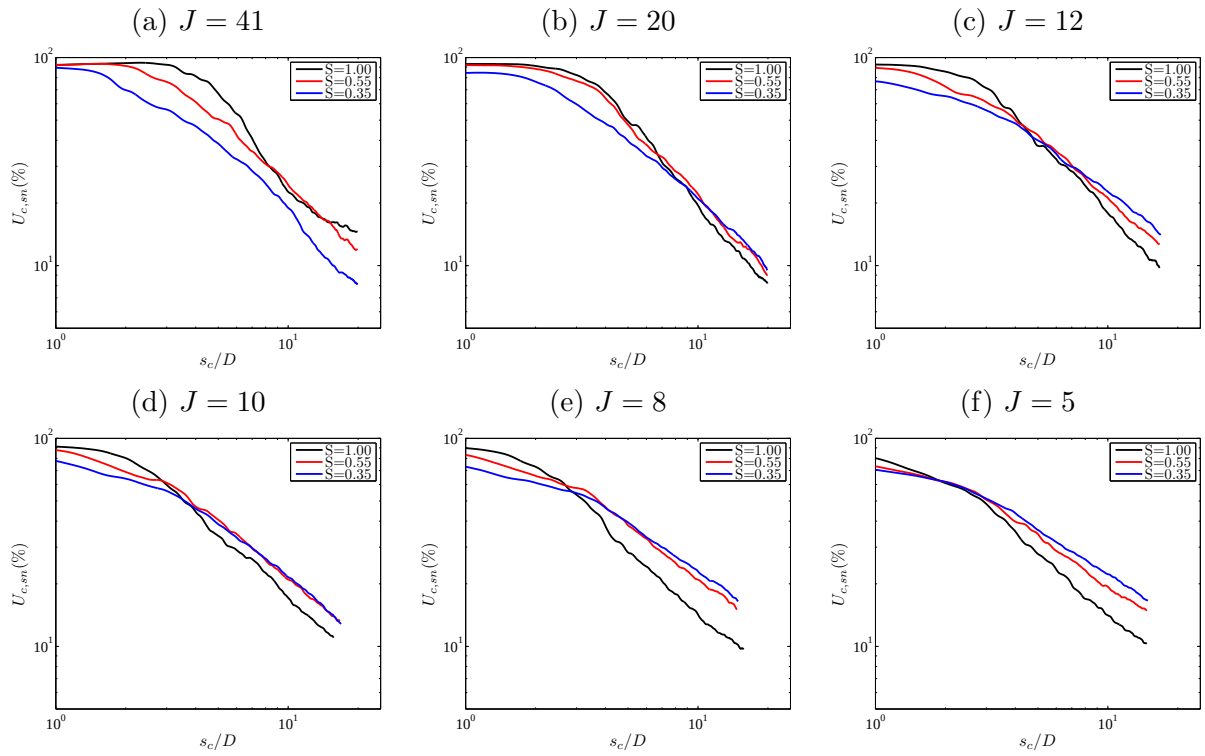


Figure 4.22: Transformed-plane Unmixedness, $U_{c,sn}$, as a function of centerline trajectory coordinate s_c/D for flush nozzle-injected transverse jets at various density ratios S, with $41 \geq J \geq 5$ as indicated.

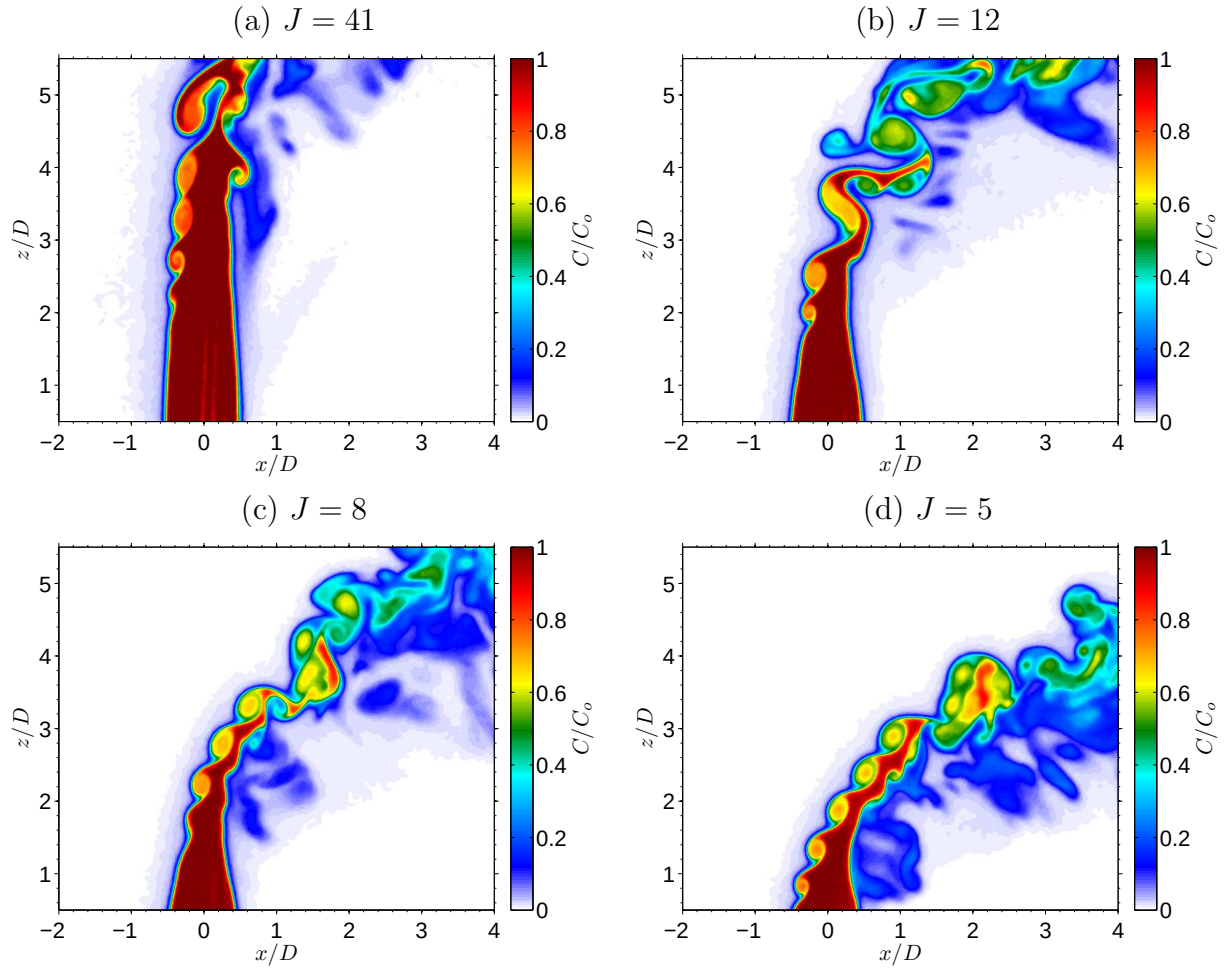


Figure 4.23: Instantaneous high-resolution centerplane (side view) acetone PLIF imaging of the $S = 1.00$, flush nozzle-generated JICF with varying momentum flux ratios in the range $41 \geq J \geq 5$ as indicated.

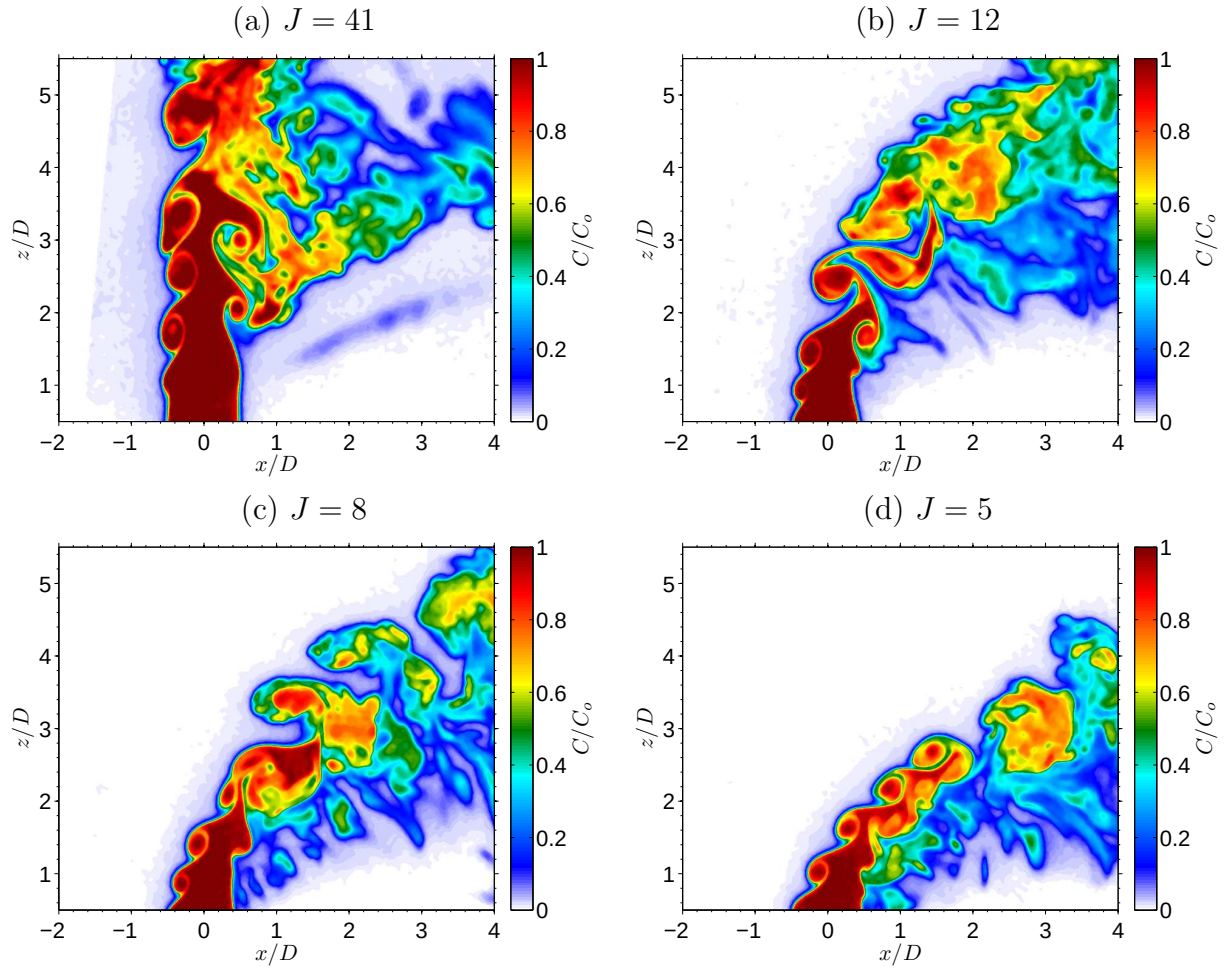


Figure 4.24: Instantaneous high-resolution centerplane (side view) acetone PLIF imaging of the $S = 0.35$, flush nozzle-generated JICF with varying momentum flux ratios in the range $41 \geq J \geq 5$ as indicated.

to the other injectors is apparent in both C_m/C_o and $U_{c,sn}$ trends. There does seem to be slight differences between the two mixing metrics, however. For instance, for $J = 41$, C_m/C_o (Figure 4.7a) suggests delayed mixing initiation for the flush pipe as compared to the flush nozzle (i.e. a longer potential core). In contrast, $U_{c,sn}$ (Figure 4.25a) suggests that the jet fluid and crossflow fluid start to mix significantly closer to the jet exit for the flush pipe injector than the C_m/C_o metric implies. High resolution images were also taken for the pipe flow and can help explain these phenomena. Similar to the flush nozzle-injected cases shown previously, the pipe data shown in Figure 4.26 was not utilized for mixing quantification. Comparing the $J = 41$ case for the flush pipe injector (Figure 4.26a) to the corresponding $U_{c.sn}$ trend in Figure 4.25a, one can infer that the cause for the reduction of $U_{c,sn}$ lies in the wake of the jet. There is a large deposit of jet fluid on the lee-side of the pipe-injected, $S = 1.00$, $J = 41$ transverse jet that is not present in the centerplane images of the flush nozzle-injected, $S = 1.00$, $J = 41$ jet (Figure 4.26a). This wake fluid deposit variation is not captured by C_m/C_o. Thus, the two dimensional nature of the $U_{c,sn}$ calculation makes it a more conclusive centerplane mixing metric as compared to C_m/C_o. The high resolution PLIF images of the pipe flow as compared to the nozzle flow also suggest that the increase in mixing associated with the pipe flow is caused by the formation and breakdown of the large-scale vortices generated by the pipe flow injector, as seen when comparing the evolution of the large, coherent vortices of the pipe flow-injected, $J = 5$ case shown in Figure 4.26d to those generated by the nozzle flow shown in Figure 4.23d. Additional high resolution centerplane-based PLIF images may be found in Appendix C.

4.7 Effect of Resolution on Mixing Results

Due to the resolution requirements summarized in Section 4.1, it is worthwhile to explore the effect of resolution on the mixing trends summarized in this section. A resolution effect study was administered by calculating $U_{c,sn}$ for certain key momentum flux ratios of the high resolution data shown in Figures 4.23 and 4.24. The $U_{c,sn}$ data obtained from these high resolution images was compared to the lower resolution results. $U_{c,sn}$ was chosen to be the mixing metric for resolution effect characterization since it is the only instantaneous metric

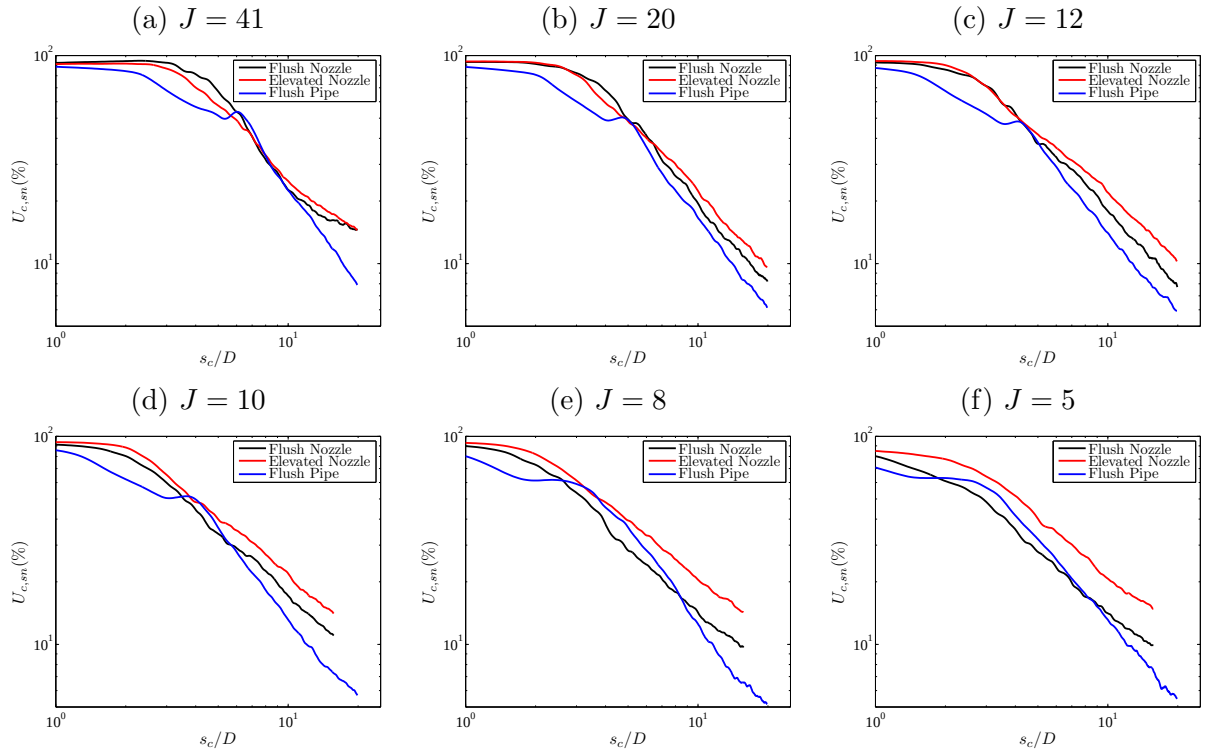


Figure 4.25: Transformed-plane Unmixedness, $U_{c,sn}$, as a function of centerline trajectory coordinate s_c/D for $S = 1.00$ transverse jets injected from flush nozzle, elevated nozzle, and flush pipe injectors, with $41 \geq J \geq 5$ as indicated.

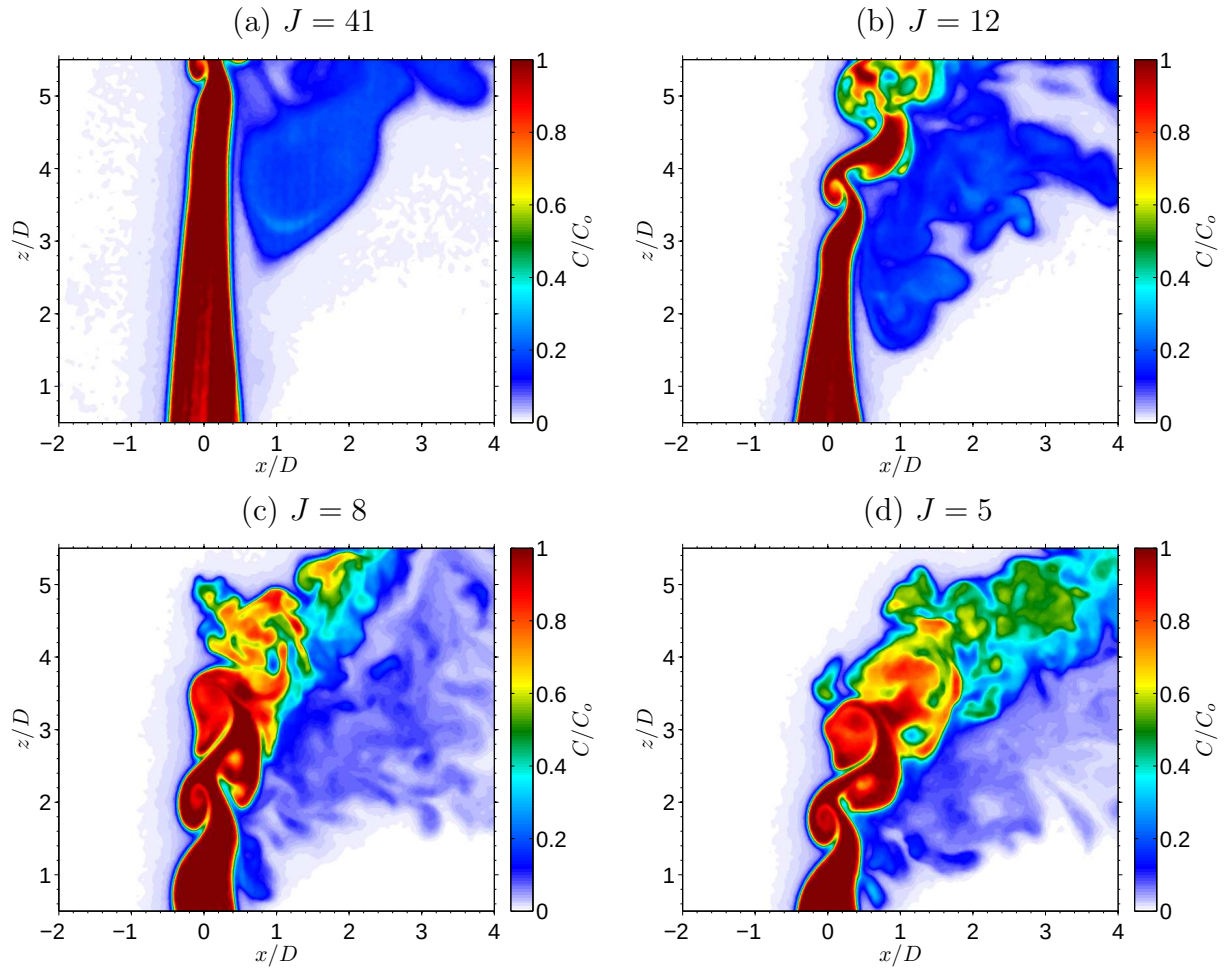


Figure 4.26: Instantaneous high-resolution centerplane (side view) acetone PLIF imaging of the flush pipe-generated JICF with varying momentum flux ratios in the range $41 \geq J \geq 5$ as indicated.

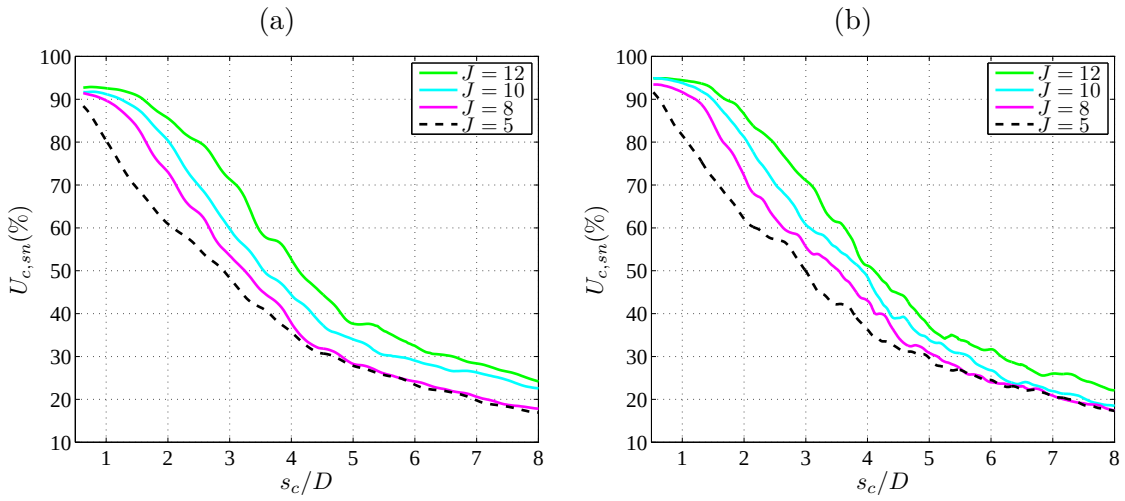


Figure 4.27: $U_{c,sn}$ trends for flush nozzle-injected, equidensity transverse jets at various momentum flux ratios as indicated, plotted against jet trajectory coordinate s_c/D. Results are shown for (a) low resolution data used for the mixing study, and (b) high resolution data used for jet near-field visualization.

applied to the near-field of the jet, where the resolution requirements would be highest. Figure 4.27 compares trends of $U_{c,sn}$ between the high resolution and low resolution data for flush nozzle-injected, $S = 1.00$ jets at $J = 12$, $J = 8$, and $J = 5$. The low resolution results (Figure 4.27a) show very similar trends to the high resolution results (Figure 4.27b), suggesting that resolution has minimal affect on the mixing trends summarized in this study for $S = 1.00$, although there are slight differences in the values of $U_{c,sn}$ between the high resolution and low resolution data sets (e.g. compare $J = 10$ for $s_c/D > 5$ in Figure 4.27ab). These slight variations in $U_{c,sn}$ do not seem to be caused by resolution, however, as the $U_{c,sn}$ value is higher for the lower resolution data, which is the opposite trend one would expect if resolution degradation was causing the discrepancy. It is unclear as to what the reason for this $U_{c,sn}$ variation is, although slight day-to-day variation of any of the pertinent parameters affecting this measurement is one possible explanation.

As summarized in Section 4.1, the strongest resolution requirement of the data shown in this study is associated with the $S = 0.35$ transverse jet. Thus, it is worthwhile to compare the $U_{c,sn}$ results for the high resolution data to the low resolution data for $S = 0.35$ as well, as shown in Figure 4.28 for $J = 12$, $J = 10$, $J = 8$, and $J = 5$. The data shown in Figure

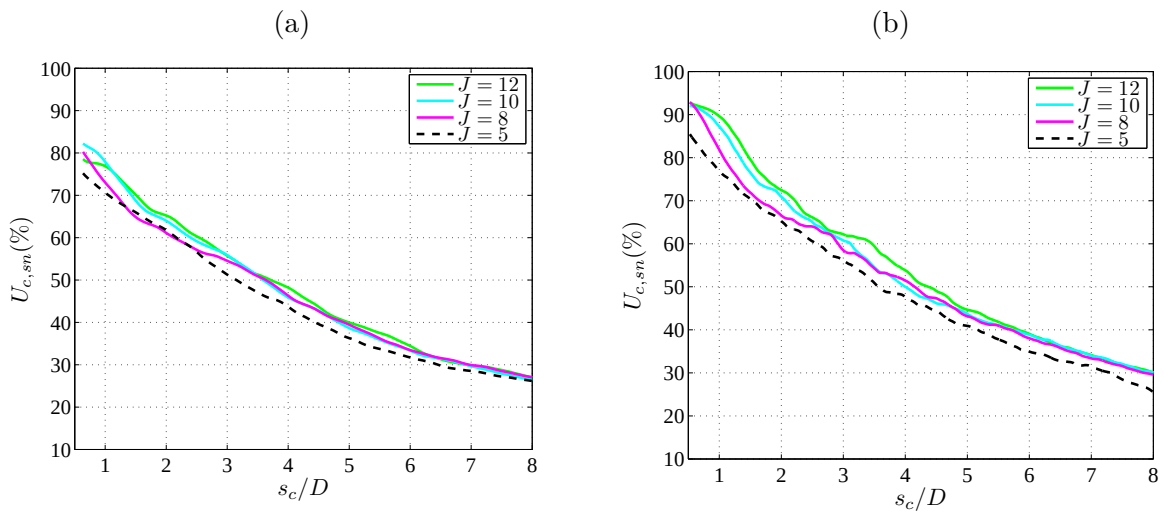


Figure 4.28: $U_{c,sn}$ trends for flush nozzle-injected, $S = 0.35$ transverse jets at various momentum flux ratios as indicated, plotted against jet trajectory coordinate s_c/D. Results are shown for (a) low resolution data used for the mixing study, and (b) high resolution data used for jet near-field visualization.

4.28 suggest a $\approx 10\%$ reduction of $U_{c,sn}$ for the low resolution data as compared to the high resolution data for all momentum flux ratios analyzed. This $U_{c,sn}$ reduction trend is what one would expect if resolution were affecting the $U_{c,sn}$ quantification. The trends among the high resolution cases are still consistent with the trends among the lower resolution cases, however (i.e. lowering the momentum flux ratio generally results in a reduction of $U_{c,sn}$). Moreover, as mentioned in Section 4.1, as the jet spreads and the jet velocity decays downstream of the jet exit, the local Reynolds number will be reduced, resulting in a relaxation of the resolution requirement to capture diffusive mixing. Thus, it can be assumed that the mixing data summarized in this chapter capture the trends of mixing with variations in J and S reasonably, albeit values of the mixing metrics could be affected by the resolution up to $\approx 10\%$ for the lower density ratio cases ($S < 1$).

4.8 Mixing and Scalar Dissipation

The mixing measures outlined in previous sections of this chapter suggest significant variation in mixing efficiency with variations in J, S, and injector type. This variation in mixing

efficiency is caused by reorganization of velocity field structures and its effect on scalar field structures. In order to analyze the velocity field in more detail and compare it to the scalar field, simultaneous PLIF/PIV data of the jet centerplane were taken; these data sets will be analyzed in the next chapter.

CHAPTER 5

Simultaneous Scalar and Velocity Field Characterization

The results from Chapters 3 and 4 suggest that there is significant correlation between the velocity field developed by the interaction between the jet and the crossflow, and the jet fluid distribution and mixing characteristics of the JICF flowfield. In order to characterize the interaction between the scalar field and velocity field in more detail, and to extract flow and scalar parameters that are relevant to reactive and mixing processes, simultaneous PLIF/PIV measurements were taken of the JICF near-field, on the jet centerplane. These simultaneous PLIF/PIV measurements will be analyzed in this chapter.

5.1 Simultaneous PLIF/PIV Measurements

Figures 5.1, 5.2, and 5.3 show sample instantaneous scaled vorticity and scaled scalar gradient magnitude images, where spanwise vorticity ω_y is obtained from the PIV and is scaled by the ratio of mean jet velocity to jet diameter (U_j/D), and the square of the local gradient magnitude in the concentration field, $|\nabla C|^2$, is obtained from acetone PLIF imaging and is scaled by $(C_o/D)^2$, where C_o is the concentration at the jet exit. Data are shown for $S = 1.00$ transverse jets injected from the flush nozzle (Figure 5.1), $S = 0.35$ transverse jets injected from the flush nozzle (Figure 5.2), and $S = 1.00$ transverse jets injected from the flush pipe (Figure 5.3). The data shown in these figures are for $J = 41$, $J = 12$, and $J = 5$; additional data sets at other momentum flux ratios can be found in Appendix D. All data sets in Figures 5.1, 5.2, and 5.3 show remarkable correspondence between the vorticity field (column a in these figures) and the scalar gradient magnitude field (column b in these figures). For the flush nozzle-injected, $S = 1.00$ transverse jets (Figure 5.1), as vortices form on the upstream shear layer due to interaction between the jet and the crossflow, low-

pressure vortex cores are generated, resulting in both jet and crossflow fluid being drawn into the cores. This vorticity generation increases the interfacial area between jet fluid and crossflow fluid and correlates with an increase in the concentration gradient magnitude in the upstream shear layer, as evidenced by the increase in $|\nabla C|^2/(C_o/D)^2$ when roll-up begins (e.g. near $z/D \approx 2.2$ for $J = 41$, shown in the top row of Figure 5.1). The initial increase in $|\nabla C|^2/(C_o/D)^2$ occurs closer to the jet exit when J is lowered, consistent with the increase in the strength of the shear layer instability and thus in shear layer vorticity near the jet exit with a decrease in J. However, as the jet fluid is mixed with the crossflow fluid further downstream at locations of high $|\nabla C|^2/(C_o/D)^2$ (mixing layers) and the vorticity diffuses, the concentration gradient relaxes and the local mixing rate decreases, as evidenced by the decrease in $|\nabla C|^2/(C_o/D)^2$ when vortices break down (e.g. $z/D > 5$ for $J = 12$, shown in the middle row of Figure 5.1). These findings are very consistent with the mixing results summarized in Chapter 4. The $S = 0.35$ data sets shown in Figure 5.2 suggest that the generation of secondary instability and turbulent vortex breakdown occurs closer to the jet exit when the density ratio is lowered (e.g. compare the $S = 0.35$, $J = 12$ vorticity field in the second row of Figure 5.2a to the $S = 1.00$, $J = 12$ vorticity field in the second row of Figure 5.1a). This finding is also consistent with the increase in hot-wire spectra background noise when density ratio is lowered, as evidenced by the shear layer instability measurements outlined in Getsinger et al. (2012).

The $S = 1.00$ flush pipe-injected JICF vorticity and scalar gradient magnitude images shown in Figure 5.3 provide useful insight into the evolution of the jet when the injector geometry is varied. For the convective unstable cases (e.g. $J = 41$ and $J = 12$), the pipe-injected jet has diffuse regions of symmetric vorticity in the upstream and downstream jet shear layers near the jet exit, consistent with what one would expect from flow ejected from a pipe. These distributed regions of vorticity become more compact and strengthen in magnitude farther along the jet, after which instability is manifested and vortices form. Similar to the $S = 1.00$ flush nozzle-injected jets, vortex generation for $J = 41$ and $J = 12$ tends to increase concentration gradients, as evidenced by the increase in $|\nabla C|^2/(C_o/D)^2$ after the onset of instability. For the flush pipe-injected, absolutely unstable, $J = 5$ case

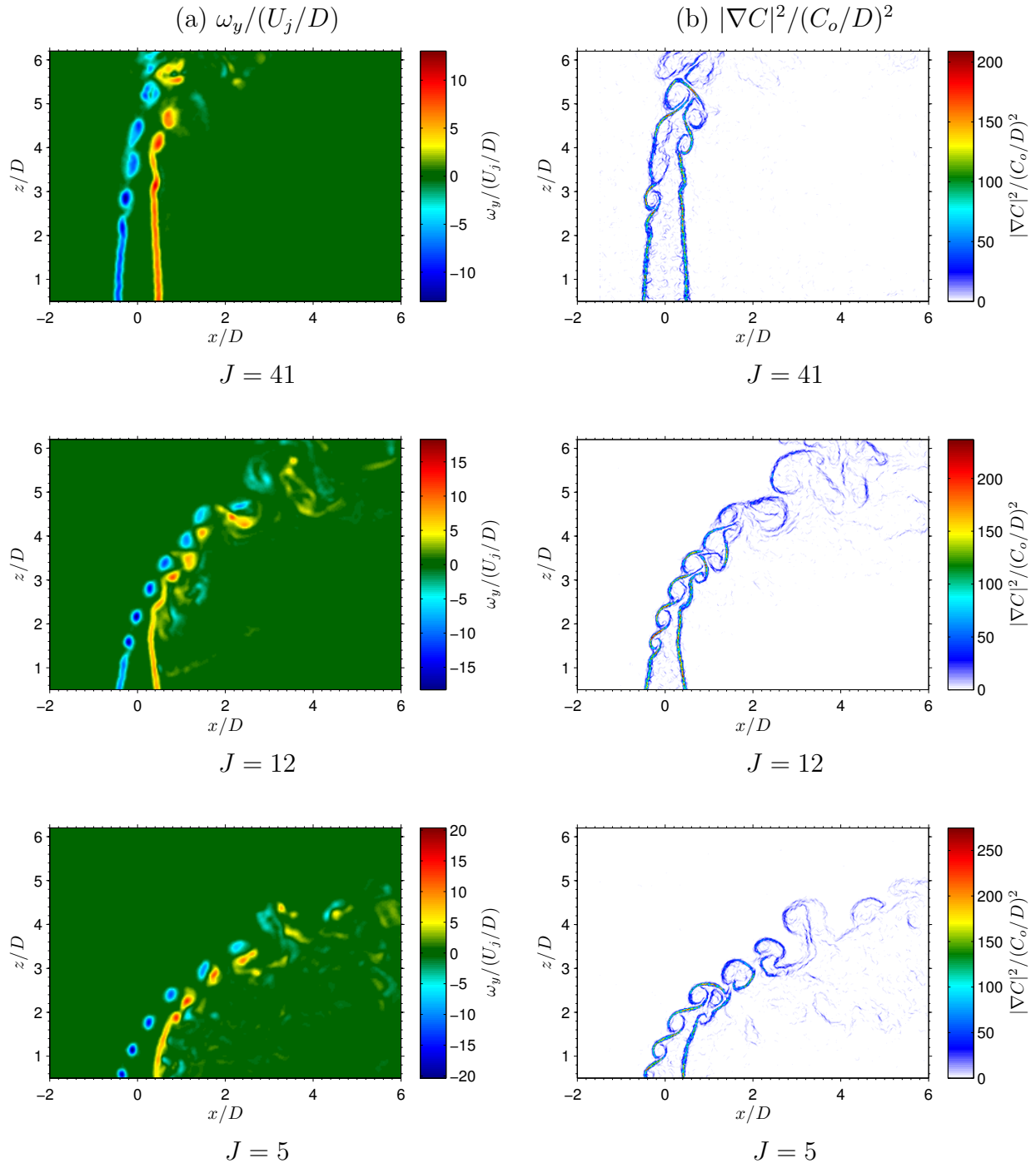


Figure 5.1: Instantaneous centerplane (side view) simultaneous PLIF/PIV imaging of $S = 1.00$, flush nozzle-generated JICF with varying momentum flux ratios: $J = 41$ (top row), $J = 12$ (middle row), $J = 5$ (bottom row). Data shown for (a) scaled vorticity $\omega_y/(U_j/D)$ and (b) scaled jet fluid concentration gradient magnitude $|\nabla C|^2/(C_o/D)^2$.

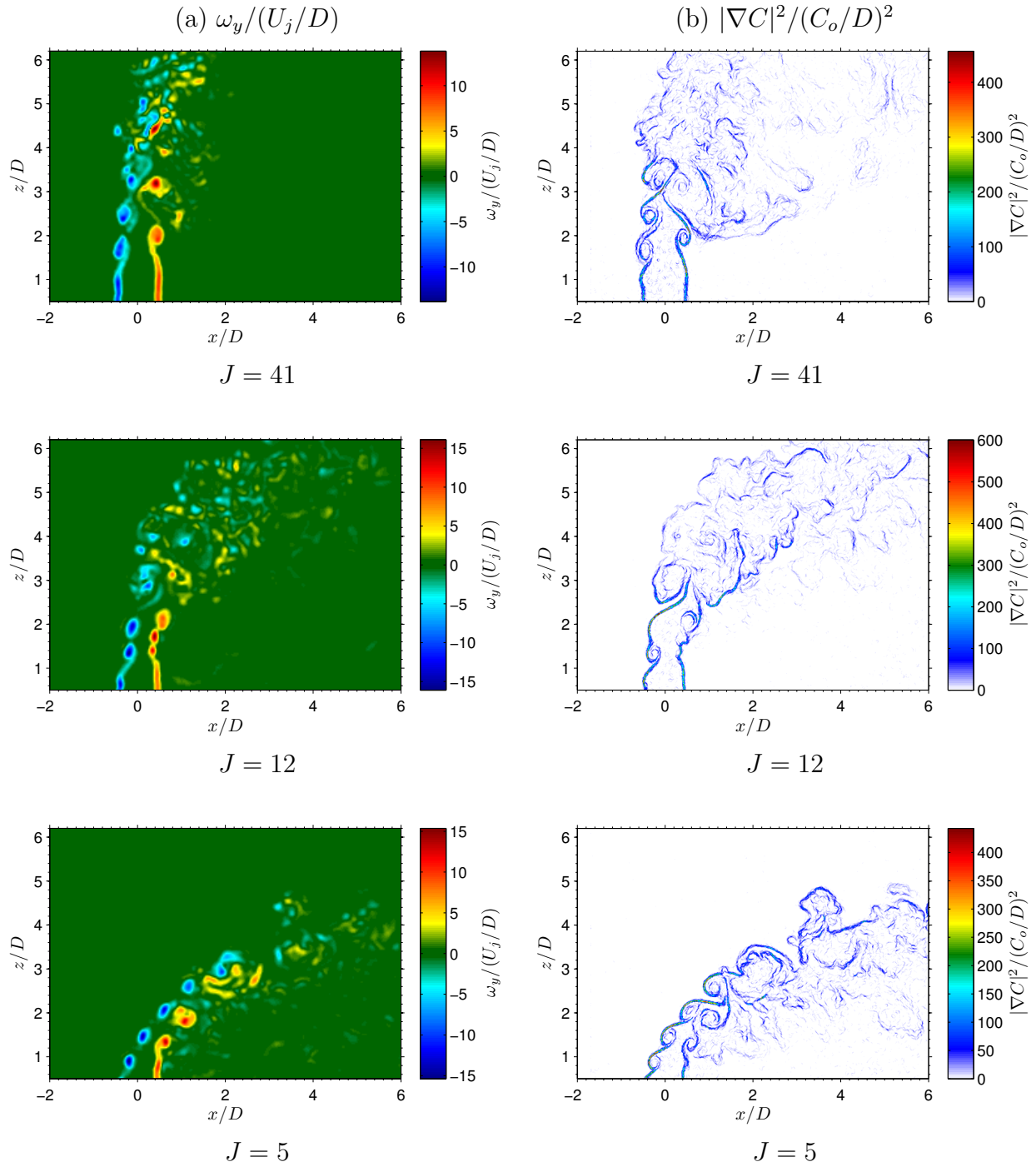


Figure 5.2: Instantaneous centerplane (side view) simultaneous PLIF/PIV imaging of $S = 0.35$, flush nozzle-generated JICF with varying momentum flux ratios: $J = 41$ (top row), $J = 12$ (middle row), $J = 5$ (bottom row). Data shown for (a) scaled vorticity $\omega_y/(U_j/D)$ and (b) scaled jet fluid concentration gradient magnitude $|\nabla C|^2/(C_o/D)^2$.

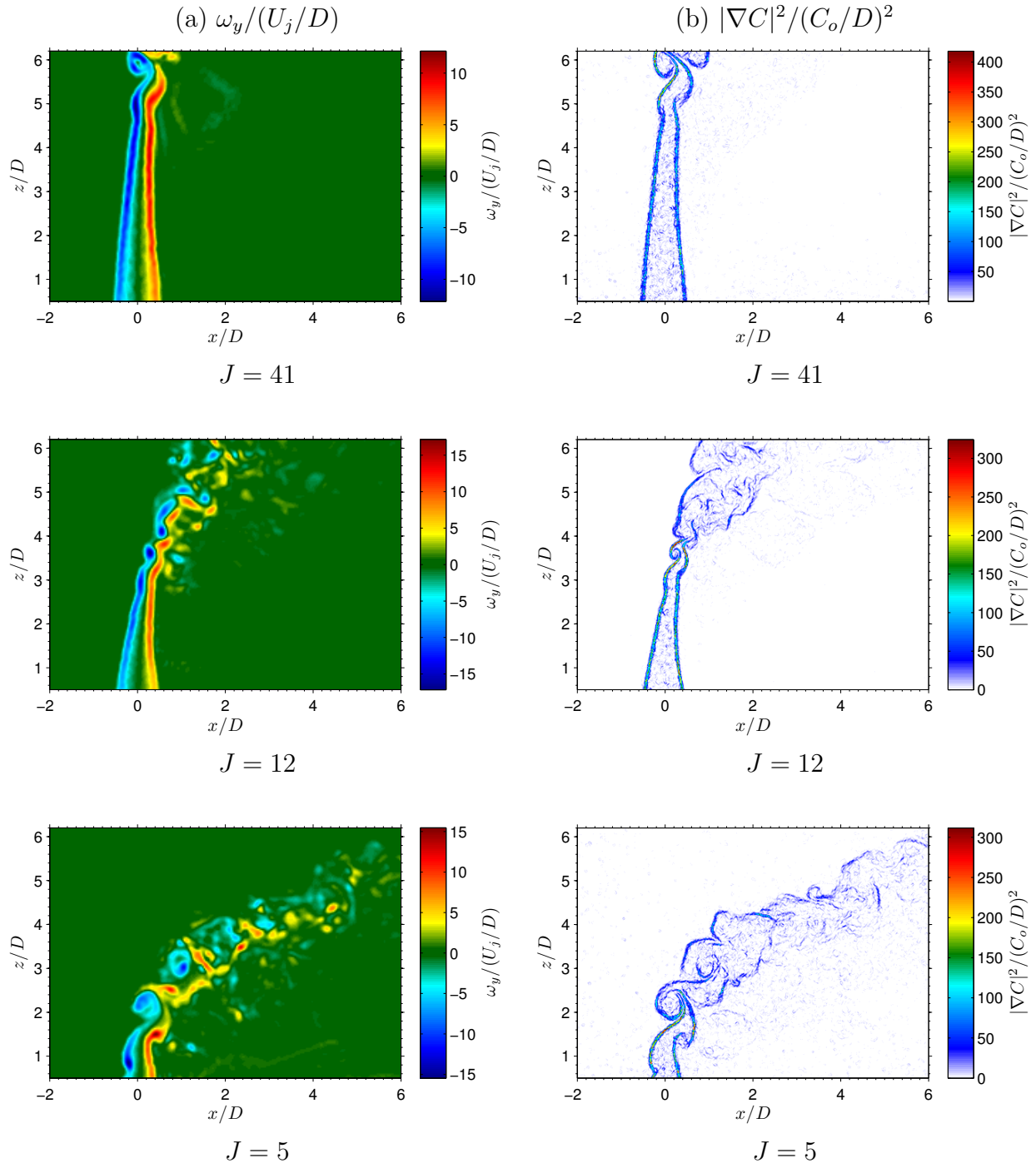


Figure 5.3: Instantaneous centerplane (side view) simultaneous PLIF/PIV imaging of $S = 1.00$, flush pipe-generated JICF with varying momentum flux ratios: $J = 41$ (top row), $J = 12$ (middle row), $J = 5$ (bottom row). Data shown for (a) scaled vorticity $\omega_y/(U_j/D)$ and (b) scaled jet fluid concentration gradient magnitude $|\nabla C|^2/(C_o/D)^2$.

shown in the bottom row of Figure 5.3, vortex generation is present near the jet exit, which is consistent with the flush nozzle-injected, $J = 5$ case shown in Figure 5.1. The vortices generated are significantly larger for the flush pipe-injected $J = 5$ jet as compared to the flush nozzle-injected $J = 5$ jet, however, suggesting that the velocity profile at the jet exit, which is different for the pipe injector as compared to the flush-mounted nozzle, can have a significant effect on both shear layer stability and structure. These data also suggest that there is a significant effect of jet shear layer instability characteristics on the mixing layer evolution. A number of other methods to characterize this correlation will be summarized in following sections.

5.2 POD Analysis

Proper Orthogonal Decomposition (POD), also known as Principal Component Analysis (PCA), has been used for decades as a method to extract the most dominant mode structures in a field of data obtained from a turbulent flow. One of the main advantages of POD analysis is that the structures extracted from the calculation are ordered according to fluctuation energy content, thus extracting important flow features from data that could otherwise be noisy or highly chaotic. For a thorough review of the POD method and its applications, see Berkooz et al. (1993). Snapshot-POD (Sirovich, 1987) can be used to extract mode structures from instantaneous snapshots of the flow, and therefore will be used as the method of POD calculation in this JICF study. Recently, a number of groups have utilized POD to analyze JICF velocity data (Meyer et al., 2007; Vernet et al., 2009; Schlatter et al., 2011). However, application of POD analysis need not be restricted to velocity data. Thus, a comparison between the POD mode structures and fluctuation energy distribution extracted from the velocity data to the POD mode structures and fluctuation energy distribution extracted from scalar data can provide insights into the correlation between the scalar field and the velocity field. POD analysis was applied to 500 snapshots of the simultaneous PLIF/PIV data taken for the cases shown in Figures 5.1, 5.2, and 5.3.

Figure 5.4 highlights the first four velocity mode structures and their corresponding

portion of the total kinetic energy fluctuation of the flow extracted from the PIV data for the equidensity, flush nozzle cases, for which vorticity fields are shown in Figure 5.1, while Figure 5.5 shows the first four scalar mode structures and their corresponding portion of the total scalar energy fluctuation of the flow extracted from the PLIF data for the same cases. As expected, both the velocity and scalar fields are dominated by shear layer structures, and the jet's upstream shear layer structures become more dominant and are initiated closer to injection as the momentum flux ratio is reduced and absolute instability in approached. The $J = 5$ case in particular shows strongly periodic upstream shear layer rollup that is initiated immediately at injection, in both PIV and PLIF-based POD modes 1 and 2. There are some wake structures present in the velocity field POD modes for lower momentum flux ratios ($J \leq 12$), as evidenced by the out-of-plane velocity fluctuation on the lee-side of the jet for $J = 12$ and $J = 5$ in Modes 3 and 4 (third and fourth rows of Figure 5.4bc). Some evidence for the effect of these wake structures on the scalar fluctuation can be seen in the PLIF POD as well (e.g. see Mode 3 and Mode 4 for $J = 5$ shown Figure 5.5c).

It is worthwhile to explore the similarity between Mode 1 and Mode 2 for most of the data shown in Figures 5.4 and 5.5. Following the work of Meyer et al. (2007), one can plot the POD coefficients of the first and second mode for all snapshots analyzed. If the coefficients of the first two modes plotted against each other yields a circle, then the structure in question is a periodic traveling wave that is characterized by linear combinations of modes 1 and 2. Figure 5.6 plots the coefficients of the first 2 modes (a_1 and a_2), extracted from the PIV and PLIF POD analyses applied to flush nozzle-injected, $S = 1.00$ jets with $J = 41$, $J = 12$, and $J = 5$. As expected, as the momentum flux ratio is lowered and the flow transitions to absolute instability (as noted above, yielding strongly periodic upstream shear layer vortex shedding), the coefficients of the first two modes plotted against each other begins to form a circular shape (e.g. compare the first row of Figure 5.6a to the last row). For $J = 5$, the coefficient plot also shows strong periodicity in the PLIF POD analysis (bottom row of Figure 5.6b), suggesting that upstream shear layer absolute instability dominates the evolution of both scalar and velocity fields for $S = 1.00$, absolutely unstable ($J < 10$) jets. The periodicity is not apparent in the PLIF POD coefficient plot for $J = 12$, however (see

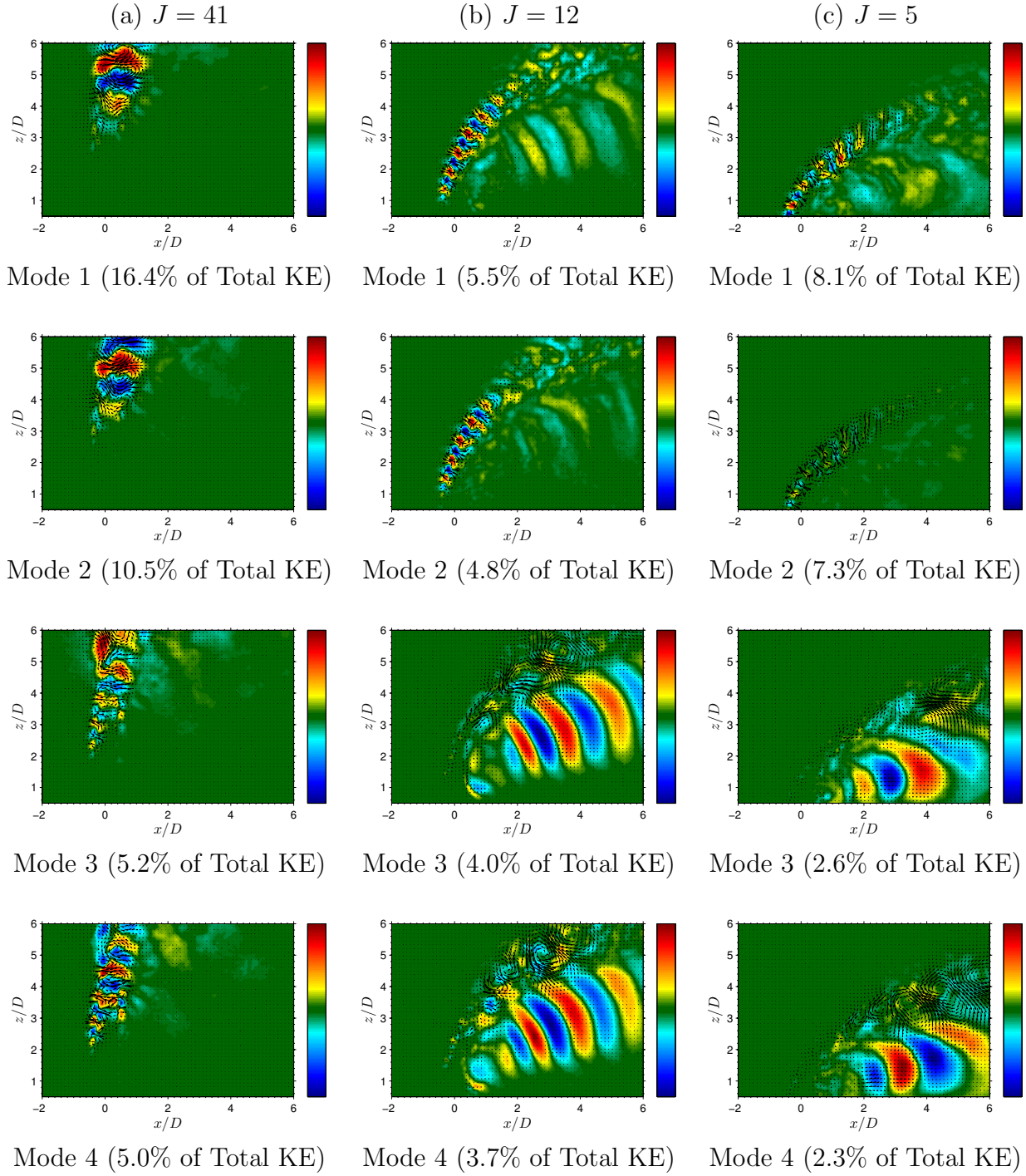


Figure 5.4: PIV POD mode structures extracted from instantaneous centerplane (side view) simultaneous PLIF/PIV imaging of $S = 1.00$, flush nozzle-generated JICF with varying momentum flux ratios: (a) $J = 41$, (b) $J = 12$, (c) $J = 5$. Data shown for Mode 1 (first row), Mode 2 (second row), Mode 3 (third row), Mode 4 (fourth row). Arrows in images indicate in-plane velocity component structure contribution, while colormap indicates out-of-plane velocity component structure contribution. Percent of total kinetic energy (KE) contributed by each mode is indicated below each image.

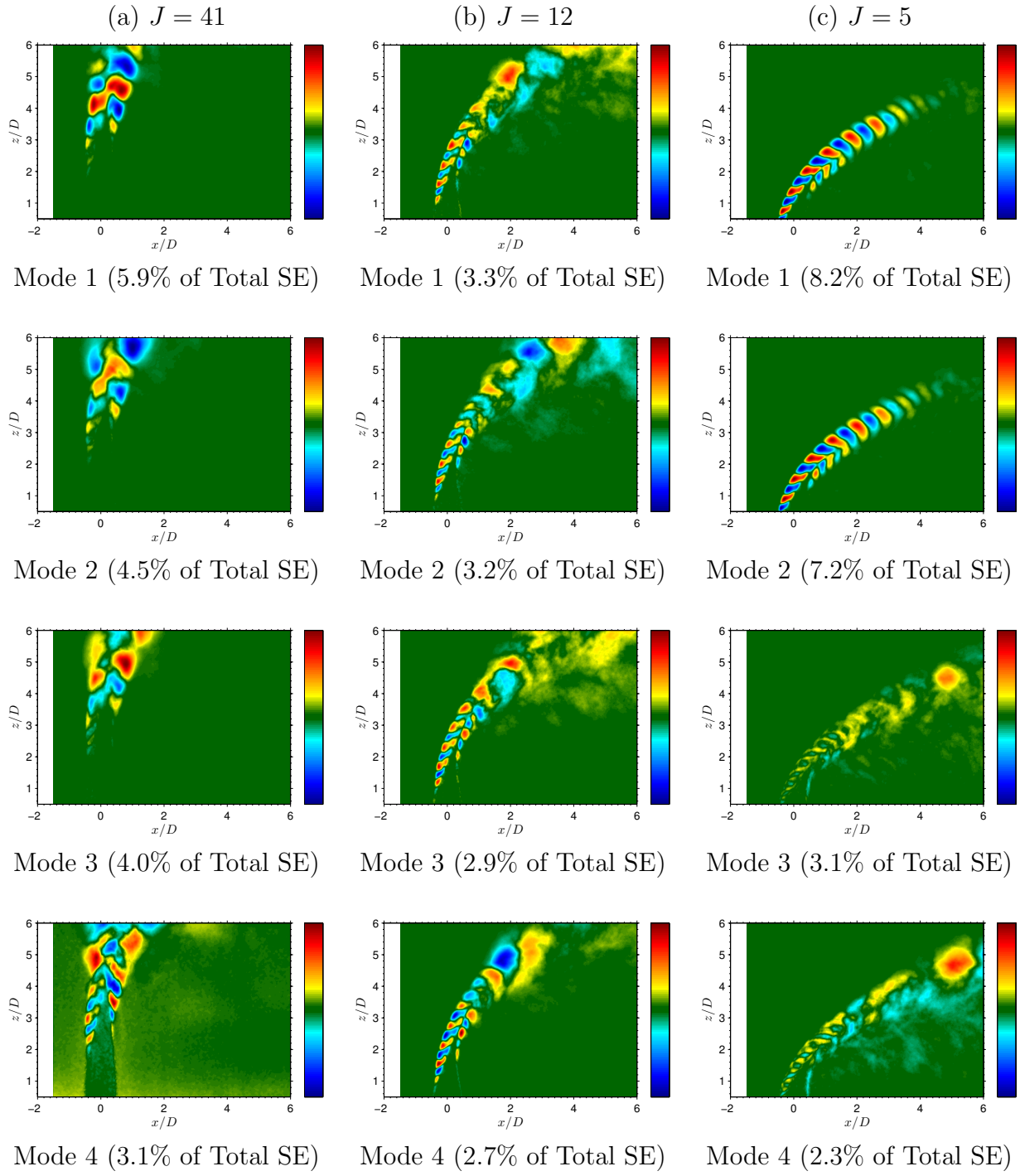


Figure 5.5: PLIF POD mode structures extracted from instantaneous centerplane (side view) simultaneous PLIF/PIV imaging of $S = 1.00$, flush nozzle-generated JICF with varying momentum flux ratios: (a) $J = 41$, (b) $J = 12$, (c) $J = 5$. Data shown for Mode 1 (first row), Mode 2 (second row), Mode 3 (third row), Mode 4 (fourth row). Percent of total scalar fluctuation energy (SE) contributed by each mode is indicated below each image.

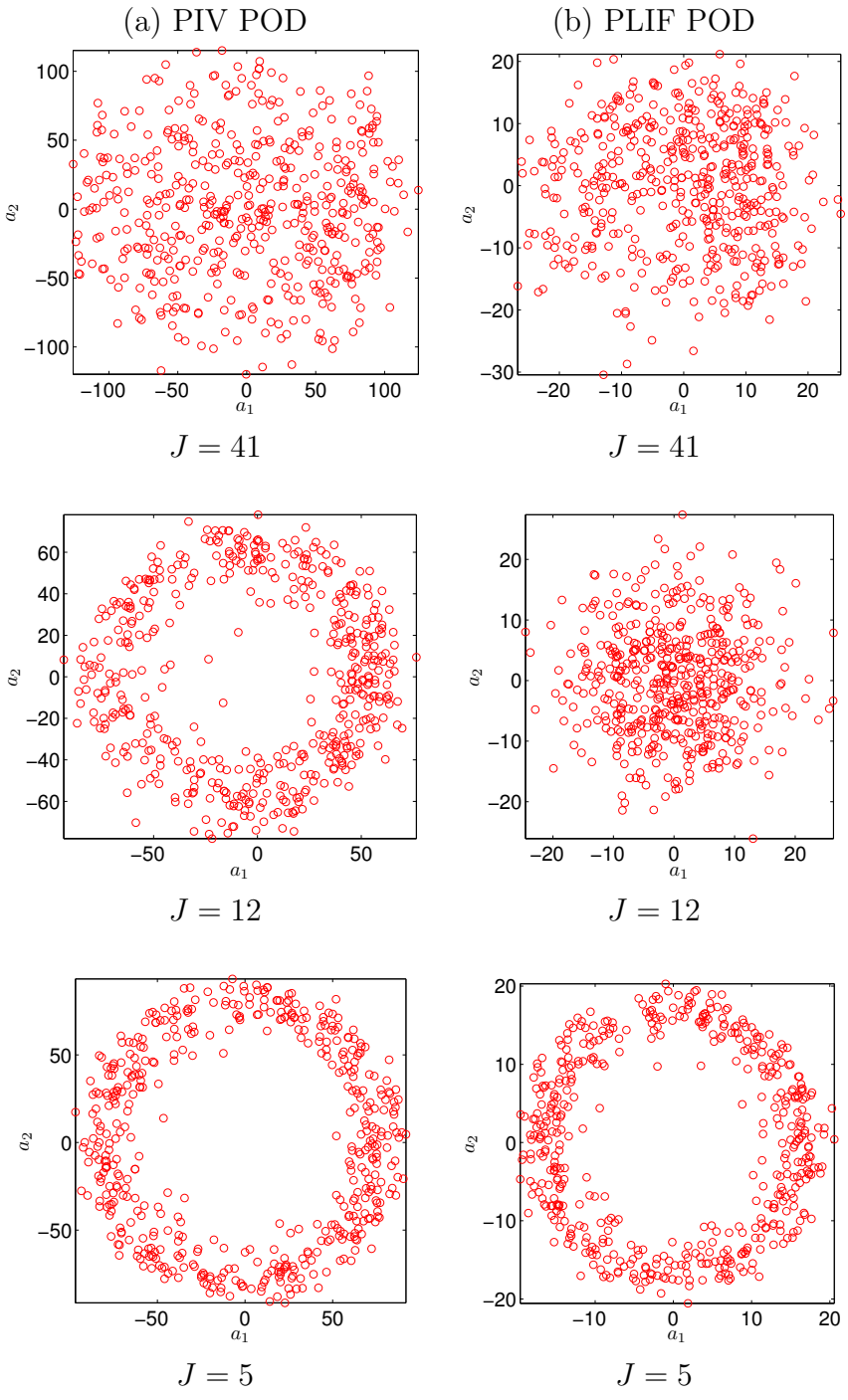


Figure 5.6: (a) PIV POD and (b) PLIF POD coefficients for the first two modes plotted against each other. POD analysis extracted from instantaneous centerplane (side view) simultaneous PLIF/PIV imaging of $S = 1.00$, flush nozzle-generated JICF with varying momentum flux ratios: $J = 41$ (top row), $J = 12$ (middle row), $J = 5$ (bottom row).

middle row of Figure 5.6b).

Figures 5.7 and 5.8 show visualizations of the first four modes extracted from the PIV and PLIF POD analyses applied to the $S = 0.35$, flush nozzle-injected transverse jets with $J = 41$, $J = 12$, and $J = 5$. Compared to the equidensity PIV and PLIF POD modes, the PLIF and PIV POD modes for the $S = 0.35$ case shown in Figures 5.7 and 5.8 have more chaotic and irregular structure. It is worthwhile to note that although the first two $S = 0.35$, $J = 41$ PIV POD modes are shear layer modes (first and second row of Figure 5.7a), the first two PLIF POD modes are actually wake modes (first and second row of Figure 5.8a). Thus, the wake of the $S = 0.35$, $J = 41$ jet has a significant impact on the scalar field distribution and fluctuation content, which is consistent with the high-resolution, near-field centerplane images for this condition shown in Figure 4.24a. As the momentum flux ratio is lowered for $S = 0.35$, the first two PLIF POD modes become shear layer modes (e.g. compare $J = 41$ to $J = 5$ in Figure 5.8). This transition from wake-behavior dominance to shear layer-behavior dominance in the scalar field for $S = 0.35$ jets could be contributing to the transition from enhanced mixing when lowering S at high J to reduced mixing when lowering S at low J, in addition to differences in the amount of crossflow fluid entrained within vortices between the two cases, as outlined in Section 4.5.

Figures 5.9 and 5.10 show visualizations of the first four modes extracted from the PIV POD and PLIF POD analyses applied to $S = 1.00$, flush pipe-injected transverse jets at $J = 41$, $J = 12$, and $J = 5$. Similar to the $S = 1.00$ PIV POD and PLIF POD modes shown in Figures 5.4 and 5.5, the first two PLIF and PIV POD modes for the flush pipe-injected jets shown in Figures 5.9 and 5.10 are composed primarily of shear layer structures. Another noteworthy correlation among the equidensity, flush nozzle-injected jets and the equidensity, flush-pipe injected jets is the variation in fluctuation energy distribution as momentum flux ratio is varied. For instance, for the flush nozzle-injected, $S = 1.00$ jets, as momentum flux ratio is lowered from $J = 41$ to $J = 12$, the percent contribution by PIV POD Mode 1 to the total kinetic energy fluctuation of the flow drops from 16.4% to 5.5%. As momentum flux ratio is lowered from $J = 12$ to $J = 5$, however, the percent energy contribution increases from 5.5% to 8.1%. This trend in energy content distribution is very similar to that of

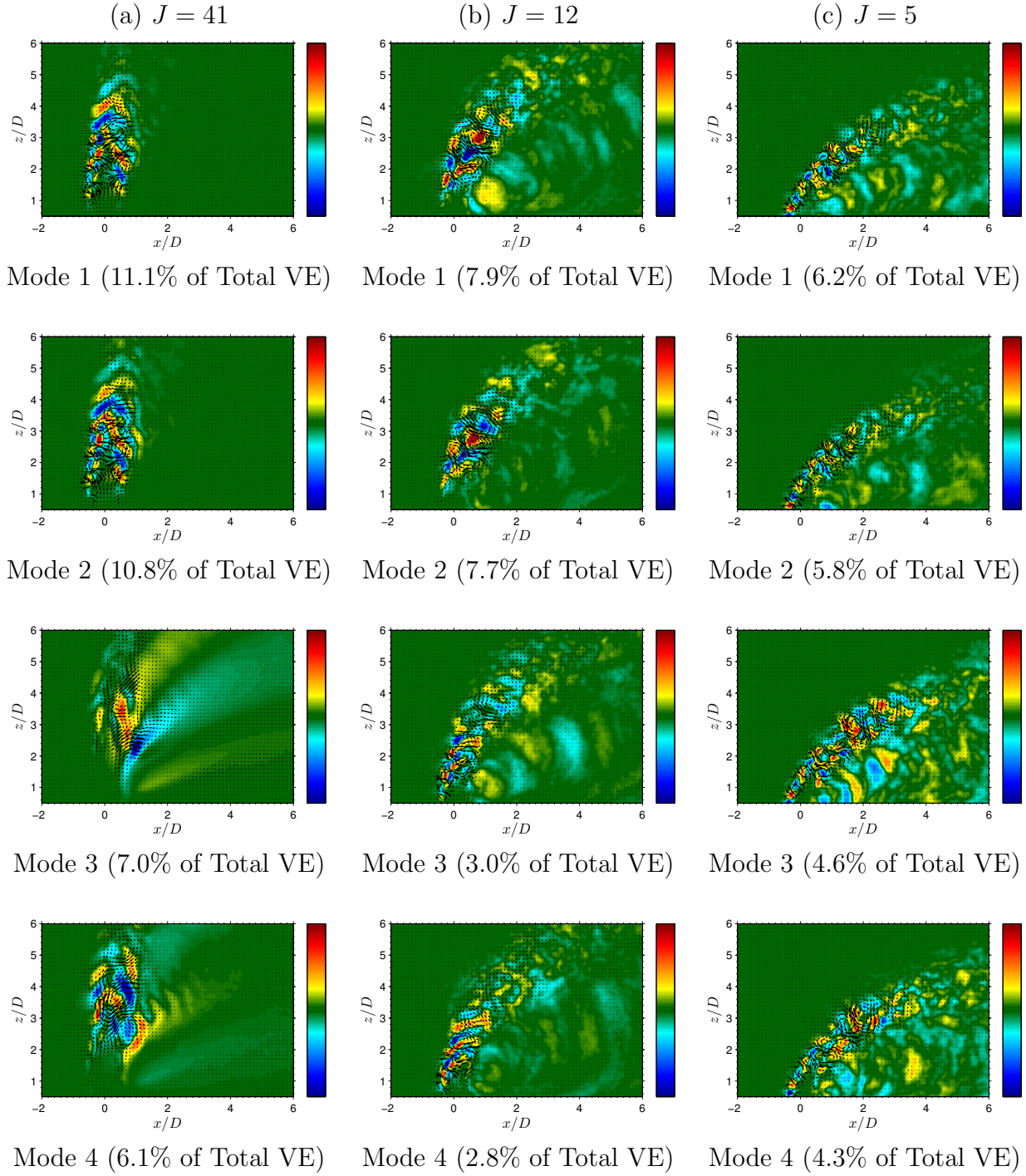


Figure 5.7: PIV POD mode structures extracted from instantaneous centerplane (side view) simultaneous PLIF/PIV imaging of $S = 0.35$, flush nozzle-generated JICF with varying momentum flux ratios: (a) $J = 41$, (b) $J = 12$, (c) $J = 5$. Data shown for Mode 1 (first row), Mode 2 (second row), Mode 3 (third row), Mode 4 (fourth row). Arrows in images indicate in-plane velocity component structure contribution, while colormap indicates out-of-plane velocity component structure contribution. Percent of total velocity fluctuation energy (VE) contributed by each mode is indicated below each image.

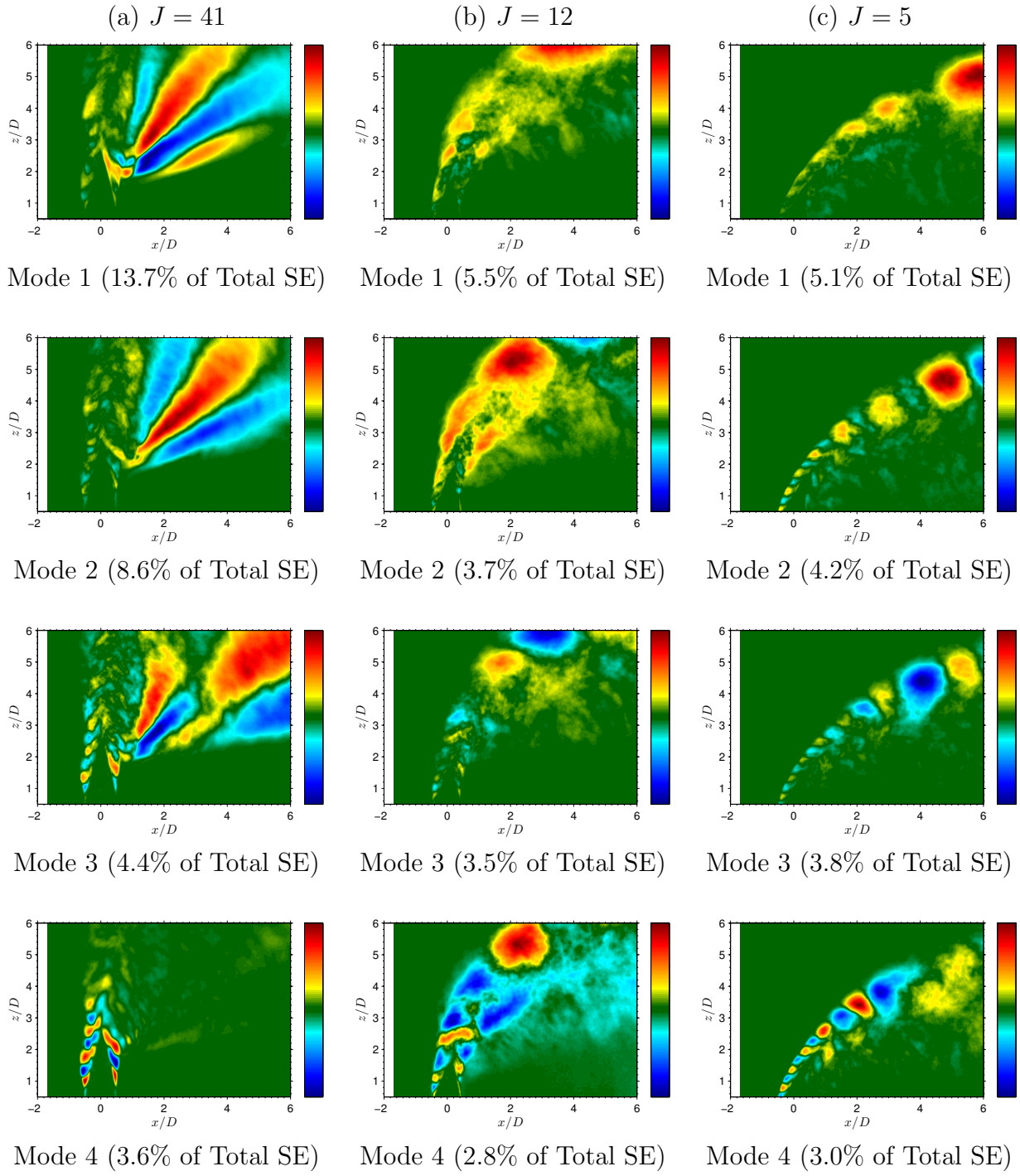


Figure 5.8: PLIF POD mode structures extracted from instantaneous centerplane (side view) simultaneous PLIF/PIV imaging of $S = 0.35$, flush nozzle-generated JICF with varying momentum flux ratios: (a) $J = 41$, (b) $J = 12$, (c) $J = 5$. Data shown for Mode 1 (first row), Mode 2 (second row), Mode 3 (third row), Mode 4 (fourth row). Percent of total scalar fluctuation energy (SE) contributed by each mode is indicated below each image.

the flush pipe-injected jets; percent kinetic energy fluctuation contribution, for flush pipe-injected transverse jets, by PIV POD Mode 1 is 20.0% for $J = 41$, 7.3% for $J = 12$, and 18.5% for $J = 5$. This similarity between the $S = 1.00$, flush nozzle and flush pipe-injected jets is related to the transition to absolute instability when lowering momentum flux ratio. The $S = 0.35$, flush nozzle-injected jets do not follow the same trend due to the fact that all $S = 0.35$ jets are absolutely unstable (e.g. see Mode 1 energy content in Figure 5.7).

5.3 Strain and Scalar Dissipation Rates

As outlined in Section 1.3, there is a direct link between the underlying strain field of any fluid flow where mixing of dissimilar fluids is taking place, and the scalar gradient field that is facilitating mixing. In this section, that link will be explored in detail by comparing the strain field ϵ, as defined in Equation 1.12, to the scalar dissipation rate field χ, as defined in Equation 1.9. It should be noted, however, that the simultaneous PLIF/PIV measurements taken in this study only yield 2-D strain rate/scalar dissipation rate data. Therefore, possible variations in the third dimension should be taken into account when analyzing the data. Measurement noise (e.g. shot noise, camera noise, background fluctuations, etc) could also have a significant effect on gradients calculated from the data. In order to reduce the effect of noise on the results, aside from the various filters applied to both the PLIF and PIV data, all gradient quantities are averaged over each set of images.

5.3.1 Mixing Layer Determination

In order to compare the velocity and scalar gradient quantities utilizing simultaneous acetone PLIF and stereo PIV measurements, a method for determining the location of the dominant upstream and downstream mixing layer between jet and crossflow fluid was developed. Utilizing the mean jet trajectory from the PLIF data, a transformation from the $x-z$ coordinate system to the $s_c - n$ coordinate system was implemented, similar to the method utilized for the centerplane spread and Unmixedness results (see Section 4.4.2 for an explanation of the transformation method). After the transformation was implemented, the mixing layer location was determined by tracking the position with the highest scalar dissipation rate at each

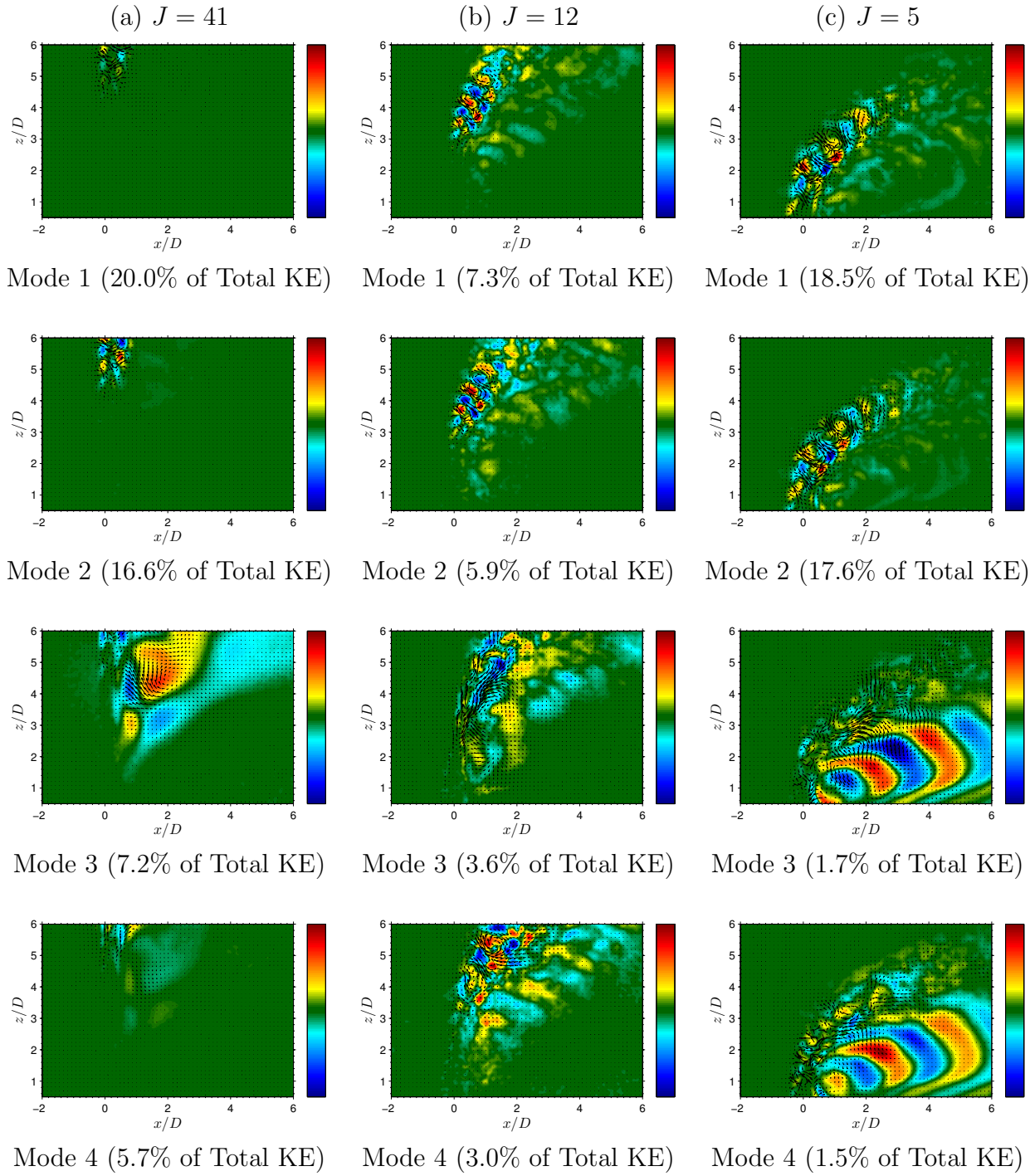


Figure 5.9: PIV POD mode structures extracted from instantaneous centerplane (side view) simultaneous PLIF/PIV imaging of $S = 1.00$, flush pipe-generated JICF with varying momentum flux ratios: (a) $J = 41$, (b) $J = 12$, (c) $J = 5$. Data shown for Mode 1 (first row), Mode 2 (second row), Mode 3 (third row), Mode 4 (fourth row). Arrows in images indicate in-plane velocity component structure contribution, while colormap indicates out-of-plane velocity component structure contribution. Percent of total kinetic energy (KE) contributed by each mode is indicated below each image.

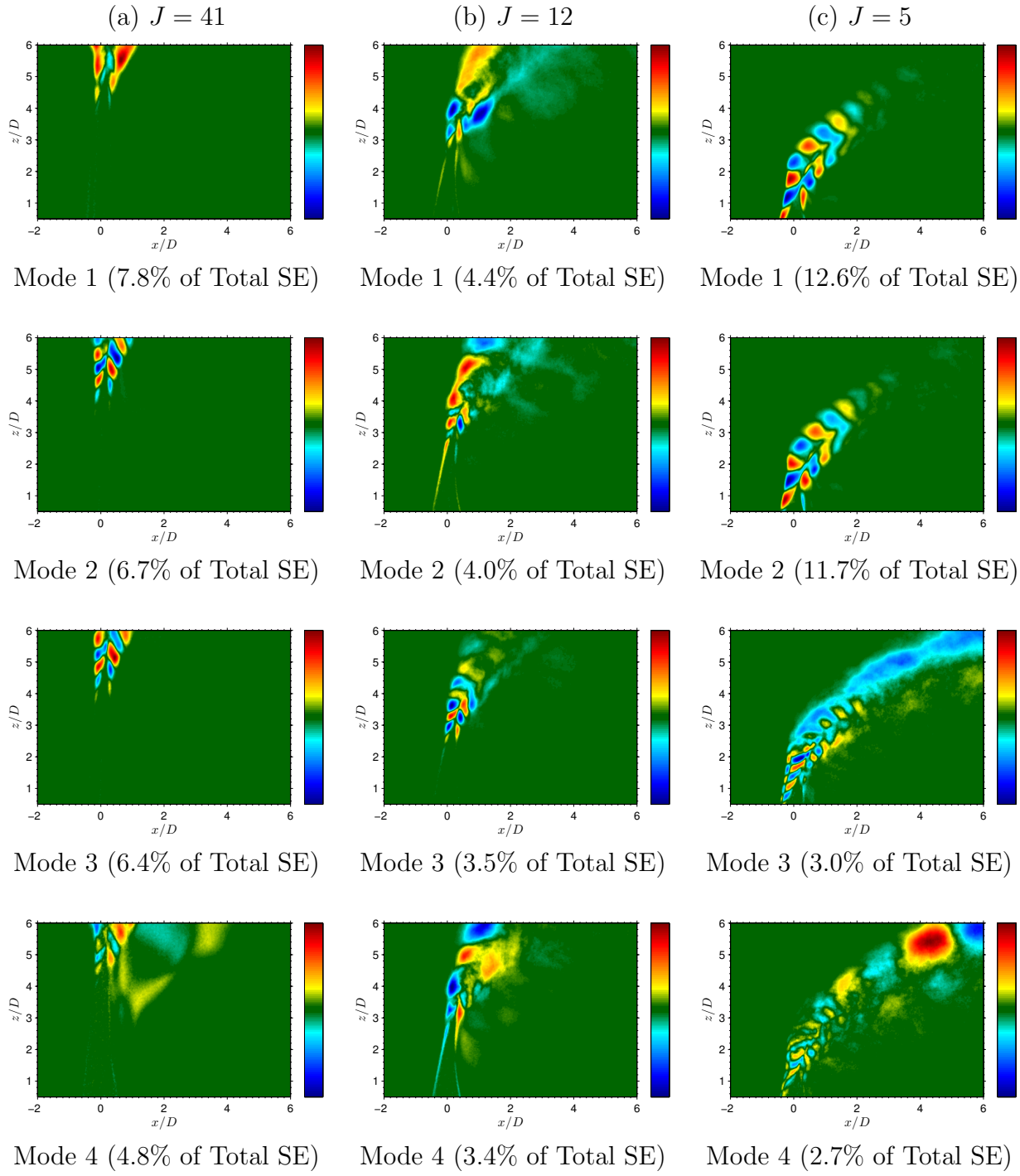


Figure 5.10: PLIF POD mode structures extracted from instantaneous centerplane (side view) simultaneous PLIF/PIV imaging of $S = 1.00$, flush pipe-generated JICF with varying momentum flux ratios: (a) $J = 41$, (b) $J = 12$, (c) $J = 5$. Data shown for Mode 1 (first row), Mode 2 (second row), Mode 3 (third row), Mode 4 (fourth row). Percent of total scalar fluctuation energy (SE) contributed by each mode is indicated below each image.

(a) C/C_o in $x-z$ (b) C/C_o in s_c-n (c) χ in s_c-n

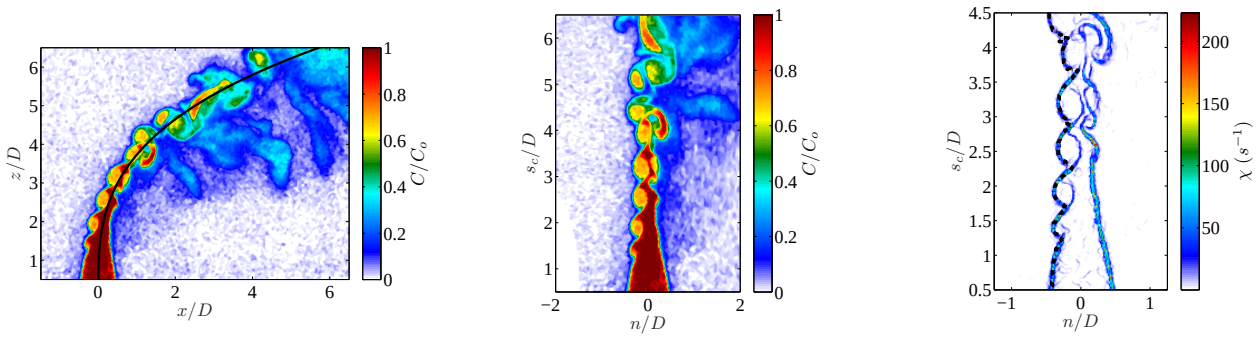


Figure 5.11: Example scalar field (C/C_o) image in $x-z$ coordinate system with mean jet trajectory overlapped onto image (a), transformed scalar field image in s_c-n coordinate system (b), and transformed scalar dissipation rate (χ) image used to track mixing layer location with upstream mixing layer overlapped onto image (c). Data shown for flush nozzle-injected, $S = 1.00$, $J = 12$ transverse jet.

s_c/D location. As an example, Figure 5.11 shows the scalar field obtained from simultaneous PLIF/PIV measurements of a flush nozzle-injected, $S = 1.00$, $J = 12$ transverse jet with the mean jet trajectory overlapped onto the image, the corresponding image transformed to the $s_c - n$ coordinate system, and the scalar dissipation rate tracking of the upstream mixing layer location. A similar method was utilized to track the downstream (lee-side) mixing layer location. All average scalar dissipation rates and strain rates shown in this study were calculated at the instantaneous mixing layer location determined from this method, and averaged over the set of images.

5.3.2 Maximum Scalar Dissipation Rate and Minimum Principal Strain Rate

As outlined in Section 1.3, scalar mixing structures in turbulent flows tend to exhibit a layer-like topology, with the scalar gradient direction aligned with the minimum principal (compressive) strain axis. Assuming this approximation of the underlying physics to be valid for the present JICF study, one can compare scalar dissipation rate calculated from the PLIF measurement to the minimum principal strain rate calculated from the simultaneous PIV data at the same location as the scalar dissipation rate calculation to see if there are any correlations among the trends. This comparison was administered for both the upstream and downstream mixing layers of flush nozzle-injected, and flush pipe-injected, equidensity

transverse jets at $J = 41$, $J = 12$, and $J = 5$. Figures 5.12 and 5.13 highlight the variation in scalar dissipation rate and minimum principal strain rate, on the upstream and downstream mixing layers, for the flush nozzle-injected (Figure 5.12) and flush pipe-injected (Figure 5.13) transverse jets. The data in Figures 5.12 and 5.13 result from averaging the χ and ϵ_{min} extracted from each instantaneous image at a given s_c/D. It is apparent from these plots that the minimum principal strain and scalar dissipation rate do not necessarily correlate with each other. This discrepancy is primarily due to the fact that the minimum principal axis does not necessarily align with the scalar gradient vector.

Figure 5.14 highlights the magnitude of the average angle difference, $|\alpha|$, between the minimum principal axis of strain from the PIV data and the scalar gradient vector direction from the PLIF data, for flush-nozzle injected and flush pipe-injected, equidensity transverse jets of momentum flux ratios $J = 41$, $J = 12$, and $J = 5$. Angle difference data is shown in Figure 5.14 for both the upstream mixing layer (UML) and downstream mixing layer (DML). If there were perfect alignment between the minimum principal axis and the scalar gradient vector direction, in a flowfield of pure straining, the average angle difference would be zero along the jet trajectory. The results are what one would expect for this relatively low Reynolds number, transitional transverse jet. Near the jet exit, before vortex formation for $J = 41$ transverse jets injected from either the flush nozzle injector, or the flush pipe injector, the magnitude of the angle difference is close to 45°, which is the angle difference one would expect in a shear-dominant environment, with a lesser degree of straining. Initial vortex formation tends to cause a drop in the angle difference (e.g. see the flush nozzle, $J = 41$ upstream shear layer angle difference data in Figure 5.14a at $s_c/D \approx 2.5$, or the flush nozzle, $J = 12$ upstream shear layer angle difference data in Figure 5.14b at $s_c/D \approx 1.5$). However, Figure 5.14 highlights the fact that the angle difference between the maximum scalar gradient vector and the minimum principal strain axis may not be close to zero. Therefore, a comparison of the scalar dissipation rate to the component of strain along the scalar gradient vector is a more appropriate comparison to make for the evolution of the scalar field in response to the stain field in this flow.

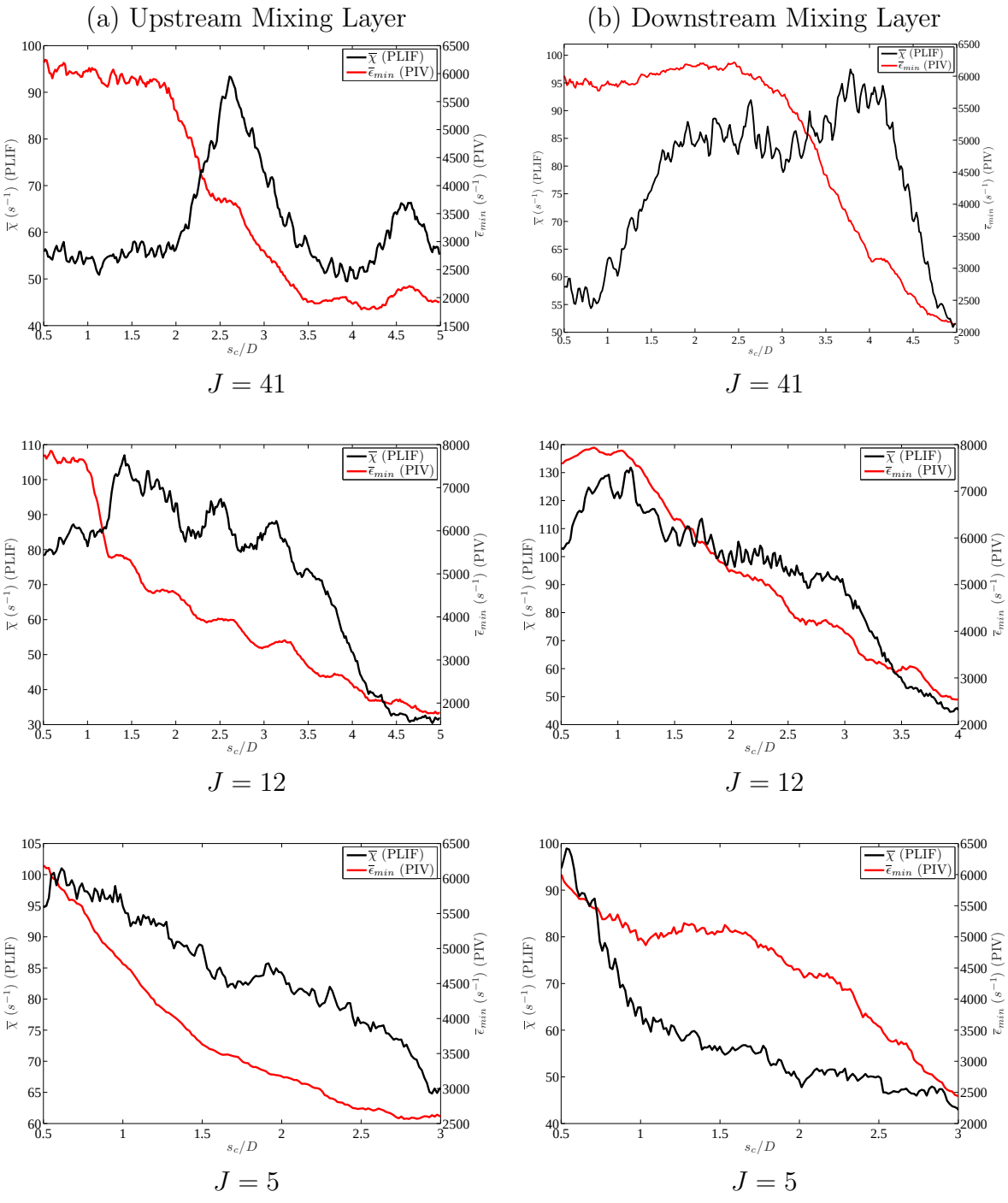


Figure 5.12: Mixing layer average maximum scalar dissipation rate $\overline{\chi}$ and average minimum principal compressive strain rate $\overline{\epsilon}_{min}$ of $S = 1.00$, flush nozzle-injected transverse jets with $J = 41$, $J = 12$, and $J = 5$ as indicated below each plot. Data shown for (a) upstream mixing layer, and (b) downstream mixing layer.

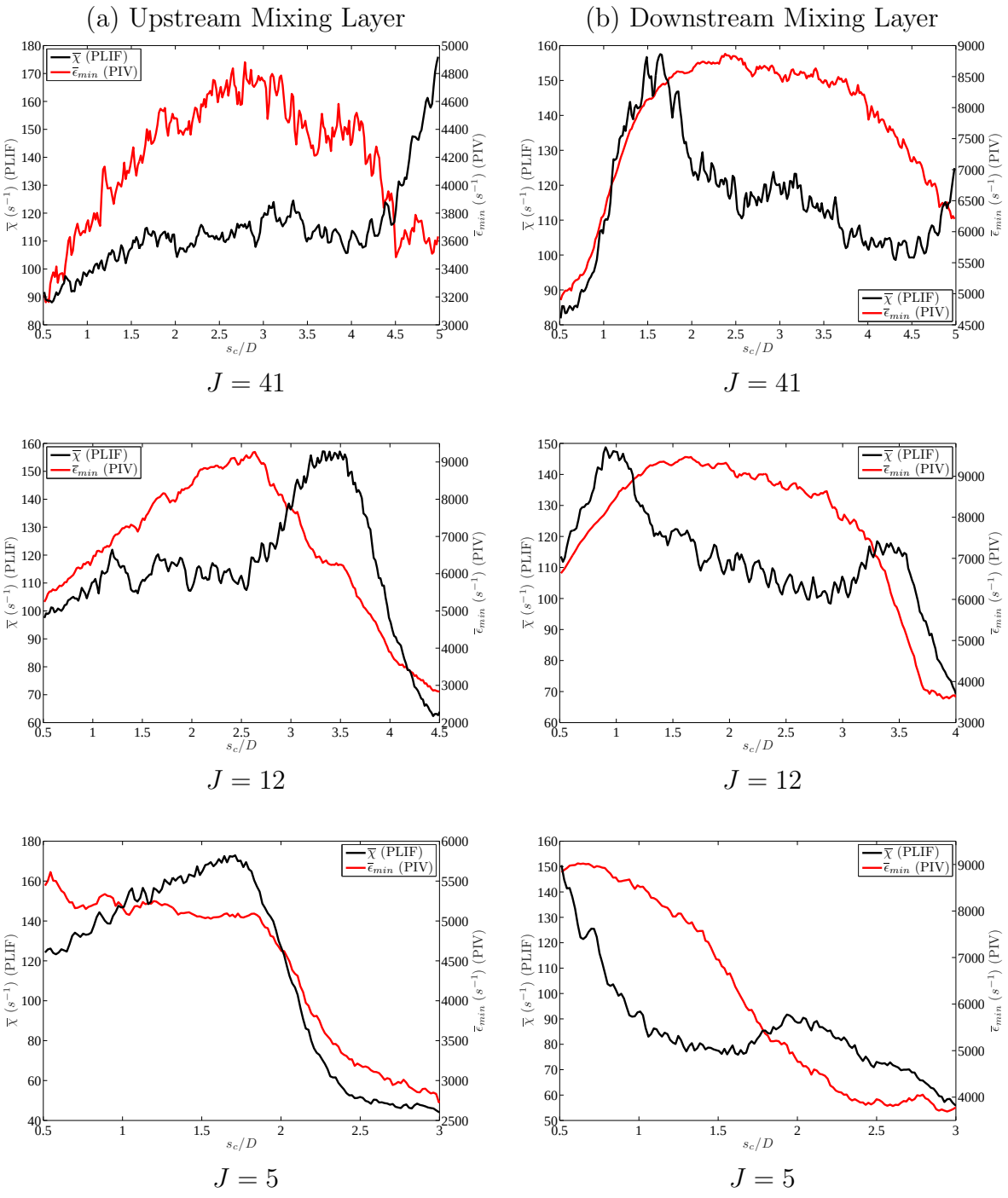


Figure 5.13: Mixing layer average maximum scalar dissipation rate $\overline{\chi}$ and average minimum principal compressive strain rate $\overline{\epsilon}_{min}$ of $S = 1.00$, flush pipe-injected transverse jets with $J = 41$, $J = 12$, and $J = 5$ as indicated below each plot. Data shown for (a) upstream mixing layer, and (b) downstream mixing layer.

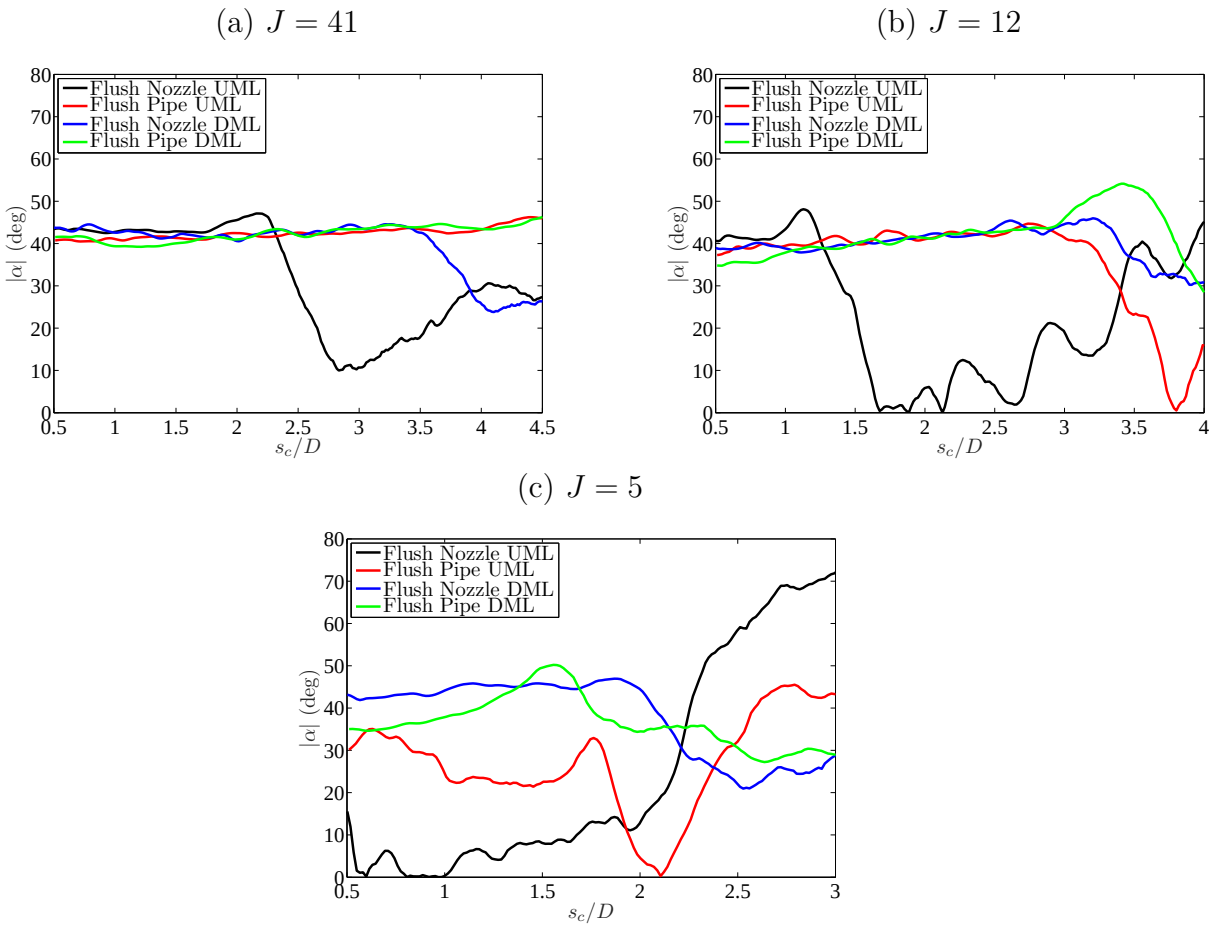


Figure 5.14: Magnitude of average angle difference, $|\alpha|$, between the minimum principal compressive strain axis, and the maximum scalar gradient vector. Data shown for both the upstream mixing layer (UML) and downstream mixing layer (DML) of flush nozzle-injected, and flush pipe-injected, $S = 1.00$ transverse jets with (a) $J = 41$, (b) $J = 12$, and (c) $J = 5$.

5.3.3 Maximum Scalar Dissipation Rate and Layer-Normal Strain Rate

As summarized in Section 1.3.1, assuming transient and three-dimensional effects are negligible and that compressive strain normal to a scalar dissipation layer dominates the evolution of the scalar dissipation rate, one can relate the scalar dissipation rate to the rate of strain. Therefore, direct comparison of the scalar dissipation rate to the strain rate in the scalar gradient direction could yield insights into JICF evolution and mixing. Without time-resolved data, the comparison between the scalar dissipation rate and strain rate normal to the layer is only valid when the strain rate normal to the layer is compressive, however. This is due to the fact that a quasi-steady state solution to the advection-diffusion equation of the scalar (Equation 1.13) is only possible when the molecular diffusion in the scalar gradient direction is balanced by compressive strain in the scalar gradient direction, and extensive strain along the layer (normal to the scalar gradient direction). If there is extensive strain in the scalar gradient direction, both strain and diffusion act to decrease the scalar dissipation rate and no quasi-steady solution to the advection-diffusion equation is possible. Therefore, in order to compare the trends among scalar dissipation rate and strain rate, any data points that had extensive strain in the scalar gradient direction were removed from the averaging process. Similar to the findings of Kothnur and Clemens (2005), extensive strain normal to the scalar gradient direction was found to be affecting the evolution of scalar structures quite often, especially at certain locations in the flow, primarily in regions immediately preceding vortex rollup (e.g. $z/D \approx 2.1$ for the flush nozzle-injected, $S = 1.00$, $J = 41$ jet, as shown in the top row of Figure 5.1). In order to ensure statistical significance, a qualifier was applied to the averaging process that required at least 200 data points to be contained within the average layer-normal strain rate and scalar dissipation rate calculation at each s_c/D location.

Figure 5.15 compares the trends of upstream and downstream mixing layer average scalar dissipation rates, and average layer-normal strain rates, for flush nozzle-injected, $S = 1.00$ transverse jets with $J = 41$, $J = 12$, and $J = 5$. It is apparent from these plots that the upstream mixing layer trends of scalar dissipation rate and strain rate (Figure 5.15a) generally correspond well with each other when one compares the PLIF and PIV data along

the scalar gradient vector direction. It is particularly worthwhile to note that increases in strain rate and scalar dissipation rate are highly coincident in regions of initial upstream shear layer vortex rollup (e.g. $s_c/D \approx 2.7$ for $J = 41$). The downstream mixing layer comparison between scalar dissipation rate and layer-normal strain rate (Figure 5.15b) only shows some correspondence for $J = 41$. For the conditions where $J = 12$ and $J = 5$, scalar dissipation rate trends do not correlate with the strain rate trends on the downstream mixing layer. In Figure 5.16, similar to the flush nozzle injector, the flush pipe injector scalar dissipation rate and layer-normal strain rate trends for $J = 41$, $J = 12$, and $J = 5$ show correspondence on the upstream mixing layer (Figure 5.16a). In contrast to the flush nozzle injector, on the downstream mixing layer of the flush pipe-injected jets (Figure 5.16b), $J = 5$ shows significant correspondence between the scalar dissipation rate and layer-normal strain rate. It is possible that these discrepancies could be due to three-dimensional or transient effects not incorporated in this two-dimensional, planar measurement that is not resolved in time.

5.3.4 SDRL Model Applied to the JICF

In order to directly determine the correlation between the scalar field and the underlying strain field in the JICF studied here, the strain rate predicted from the Strained Dissipation and Reaction Layer (SDRL) model (see Section 1.3.1) was calculated from the scalar field data and compared to the strain rate extracted from the velocity field data. The strain rate was calculated from the PLIF measurements by utilizing an automated method of error function fitting that was formulated and applied to each instantaneous scalar mixing layer location. Error function fitting was required in order to determine the boundary scalar values ζ^+ and ζ^- in Equation 1.13. If one solves the 1D scalar advection-diffusion equation, assuming quasi-steady behavior, and a locally uniform strain rate, the scalar (C/C_o or ζ) distribution takes the form shown in Equation 5.1.

$$C/C_o = 0.5(C/C_o^+ + C/C_o^-) + 0.5(C/C_o^+ - C/C_o^-)erf(n_l/\lambda_D) \tag{5.1}$$

In this equation, n_l is the layer-normal coordinate direction, which is assumed to be the two-dimensional scalar gradient direction determined from the PLIF measurements for each

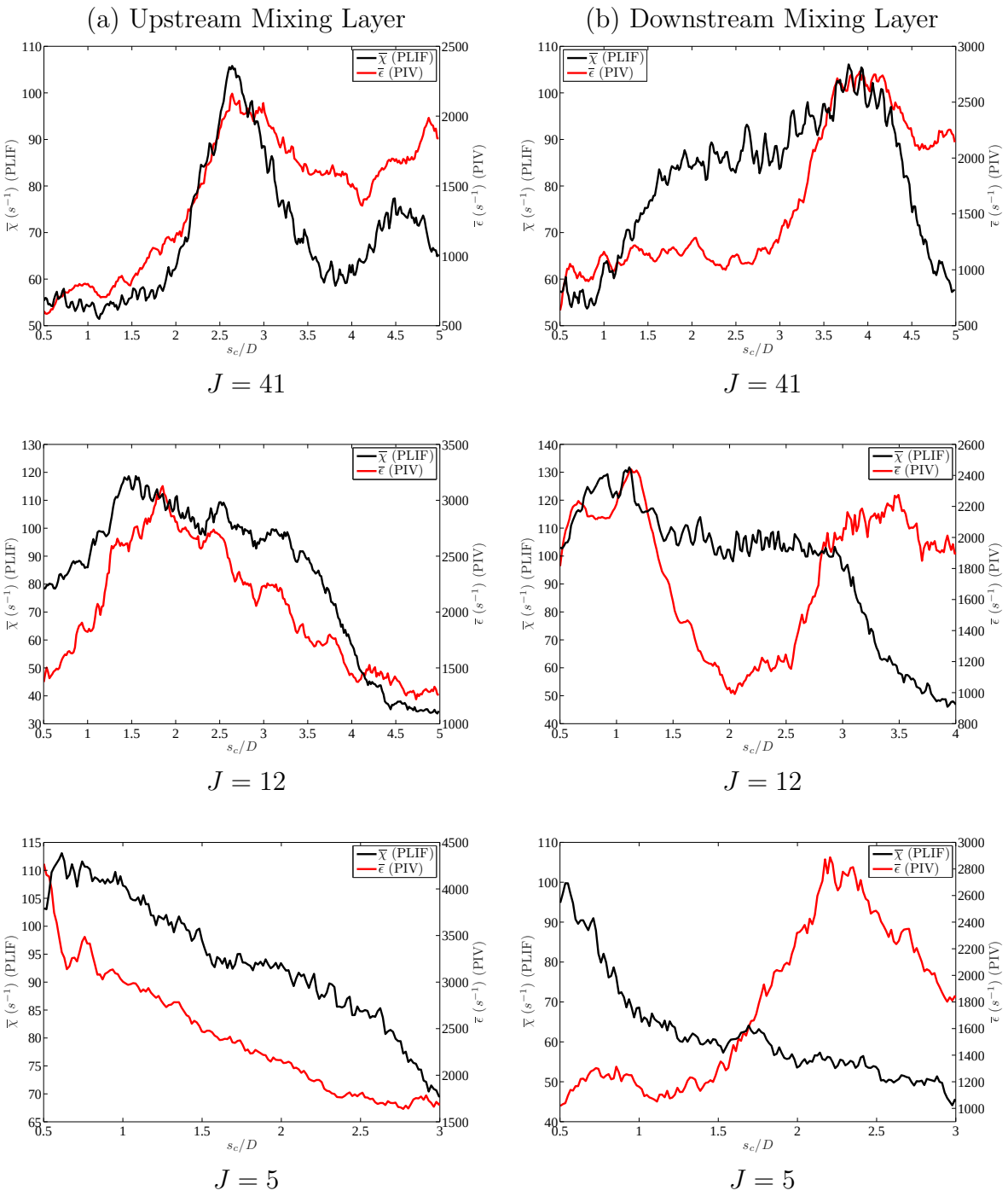


Figure 5.15: Mixing layer average maximum scalar dissipation rate, $\overline{\chi}$, and average strain rate normal to the scalar gradient direction, $\overline{\epsilon}$, of $S = 1.00$, flush nozzle-injected transverse jets with $J = 41$, $J = 12$, and $J = 5$ as indicated below each plot. Data shown for (a) upstream mixing layer, and (b) downstream mixing layer. Data points with extensive strain in the scalar gradient direction are removed from averaging process.

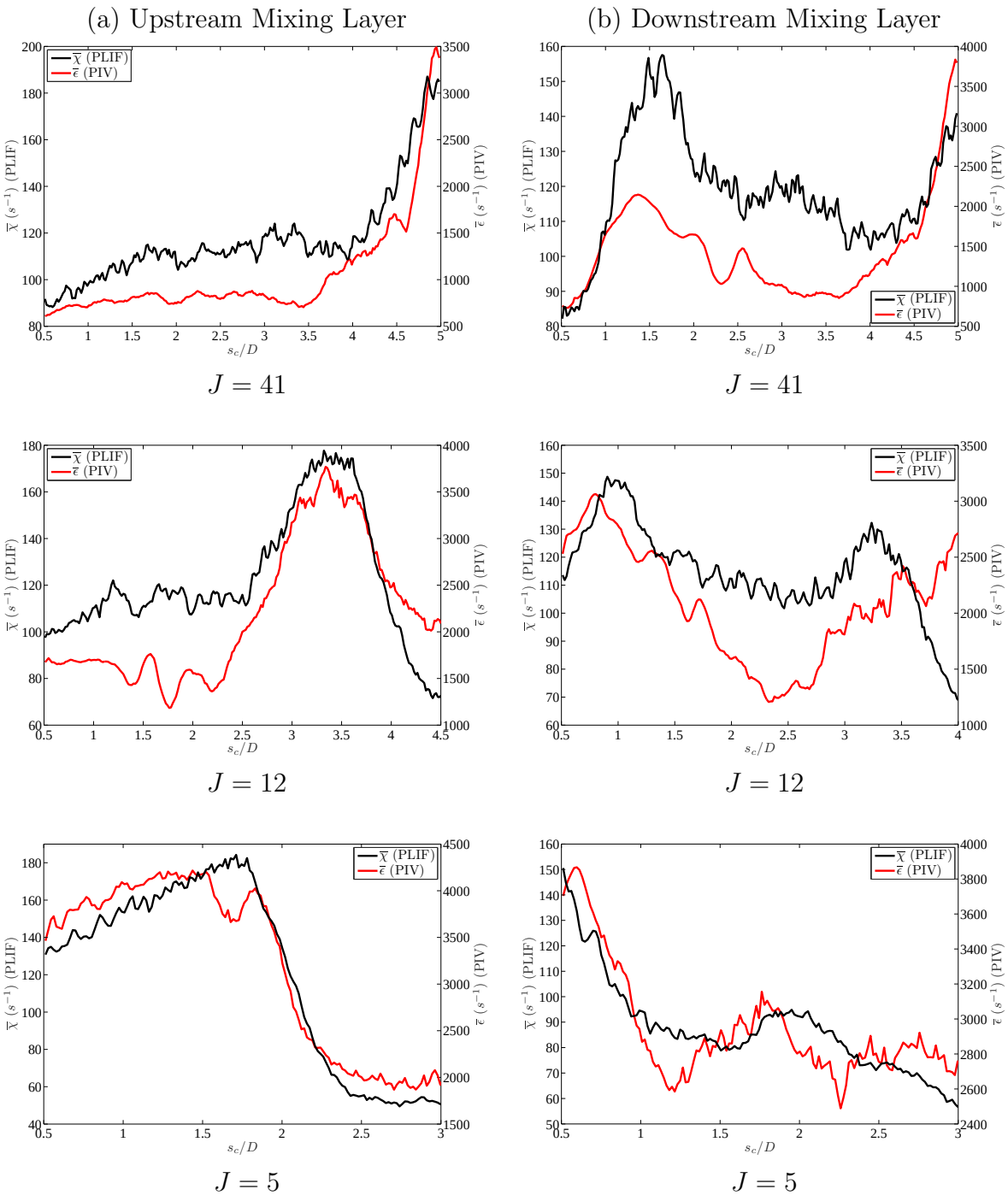


Figure 5.16: Mixing layer average maximum scalar dissipation rate, $\overline{\chi}$, and average strain rate normal to the scalar gradient direction, $\overline{\epsilon}$, of $S = 1.00$, flush pipe-injected transverse jets with $J = 41$, $J = 12$, and $J = 5$ as indicated below each plot. Data shown for (a) upstream mixing layer, and (b) downstream mixing layer. Data points with extensive strain in the scalar gradient direction are removed from averaging process.

(a) $J = 5$, PLIF from simultaneous PLIF/PIV (b) $J = 5$, high resolution PLIF

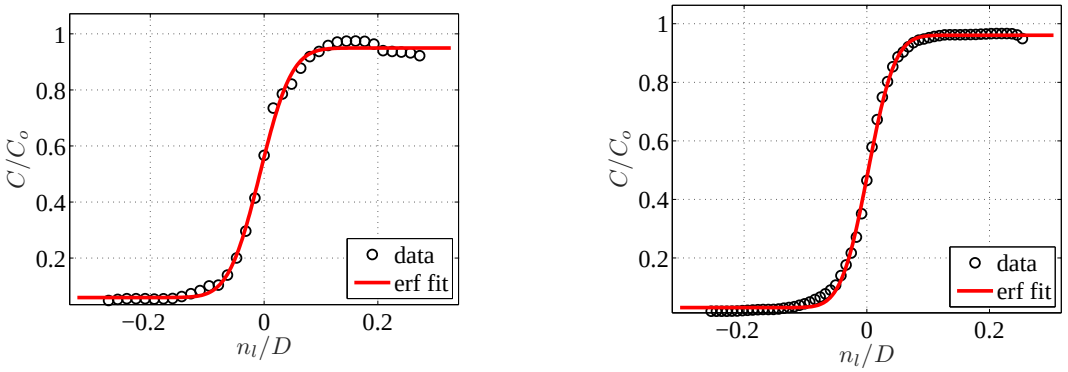


Figure 5.17: Example error function fits for flush-nozzle injected, $S = 1.00$, $J = 5$ transverse jets. Data shown for (a) PLIF portion of simultaneous PLIF/PIV, and (b) high-resolution PLIF measurements.

mixing layer location, and λ_D is the length scale that results from the competition between strain and diffusion ($\lambda_D = \sqrt{D/\epsilon}$ in the quasi-steady state limit, where D is the diffusion coefficient). In practice, an error function fit of the form shown in Equation 5.2 was applied to the C/C_o data in the layer-normal direction n_l.

$$C/C_o = a + b \times erf(\frac{n_l - c}{d}) \tag{5.2}$$

The boundary conditions $C/C_o^+ + C/C_o^-$ were determined by comparing the a and b coefficients of the fit in Equation 5.2 to Equation 5.1. In order to ensure accuracy and applicability of the fit, aside from requiring that the strain rate normal to the layer determined from PIV to be compressive, another qualifier in the averaging process was applied based on the Pearson correlation coefficient of the fit ($r > 0.99$). Similar to the data shown in Section 5.3.3, at least 200 data points for each s_c/D location were required to be incorporated into the averaging process in order to consider the average to be statistically significant. An example fit for the flush nozzle-injected, $S = 1.00$, $J = 5$ jet is shown in Figure 5.17a for the spatial resolution of the PLIF measurements shown thus far in this chapter.

Figure 5.18 compares the trends of mixing layer strain rate calculated from the scalar measurements, to the average layer-normal strain rate extracted from the PIV measurements, for flush nozzle-injected, $S = 1.00$ transverse jets with $J = 41$, $J = 12$, and $J = 5$. This comparison is administered for both upstream (Figure 5.18a) and downstream (Figure 5.18b)

mixing layers. For $J = 41$, the qualitative correspondence between the PIV and PLIF strain rates is remarkable on both upstream and downstream mixing layers (top row of 5.18). Quantitatively, the peak strain rate values for $J = 41$ along the jet trajectory coordinate s_c/D calculated from the PLIF for the upstream shear layer, approximately 1100 s^{-1}, are about half of the peak values extracted from the PIV, which are approximately 2100 s^{-1}. This discrepancy could be due to limitations associated with the experimental setup, such as resolution of the PLIF images. A study of the effect of resolution on the PLIF strain rate will be shown in Section 5.3.5. As the momentum flux ratio is lowered (e.g. $J = 12$ and $J = 5$), the correlation between the PLIF and PIV strain rate trends becomes poorer, especially in the downstream mixing layer of the jet. It is difficult to definitively determine the exact cause of this discrepancy without time-resolved, fully three dimensional measurements of the scalar and velocity fields. However, one likely explanation for the lack of correspondence on the downstream side of the jet for $J = 12$ and $J = 5$ is the increase in three-dimensional and transient effects on the lee side of the jet as momentum flux ratio is lowered, as evidenced by the transient wake vortices that appear in the structures of Mode 3 and Mode 4 calculated from the PIV POD (third and fourth rows in Figure 5.4bc). Another possible contributor to any lack of correspondence for all cases studied here is the finite response time of the scalar dissipation layer to changes in strain rate. As summarized in the work of Kothnur and Clemens (2005), the scalar dissipation layer response time is dependent on both amplitude and frequency of strain rate fluctuation, and it is also dependent on whether the strain rate is increasing or decreasing. It should be noted, however, that the observed trends in Figure 5.18 for the lower downstream PIV-based strain rates, as compared to upstream PIV-based strain rates, at $J = 12$ and $J = 5$, is consistent with trends for ignition of reactive jets in crossflow (Sullivan et al., 2014; Cetegen, 2015). Lowered strain rates suggest the propensity of more robust ignition, and for the transverse jet, this often occurs on the lee-side of the jet.

Figure 5.19 shows the trends of upstream and downstream mixing layer PIV and PLIF strain rates for flush pipe-injected, $S = 1.00$ transverse jets with $J = 41$, $J = 12$, and $J = 5$. Similar to the flush nozzle data, for $J = 41$, the upstream and downstream mixing layers (top

row of Figure 5.19) show remarkable qualitative correspondence between the PLIF-calculated and PIV-extracted strain rates. Quantitatively, the strain rate values are close to each other near the jet exit for both the upstream and downstream mixing layers of $J = 41$, but diverge significantly when PIV strain rate increases (e.g. at $s_c/D \approx 3.5$ for upstream mixing layer data shown in the top row of Figure 5.19a). Moreover, quantitative correspondence between the PLIF and PIV strain rates decreases with decreasing J. Thus, it would seem as though the strain rate calculated from the PLIF measurements in this study using the SDRL model can only be used as a qualitative measure of the general trends in strain rate. Quantitative correspondence between the PLIF-calculated strain rate to the strain rate extracted from PIV is rare among the cases analyzed, and only seems to be in regions where the strain rate is relatively low and the flow is fairly laminar with minimal three-dimensional effects (e.g. near the jet exit for the flush pipe-injected, $S = 1.00$, $J = 41$ jet). It could be possible that the resolution of the simultaneous PLIF/PIV data is affecting the quantitative correspondence significantly, however. The next section explores this possibility in more detail.

5.3.5 PLIF Resolution Effects on SDRL Model Application

In order to determine the effect of resolution on the results shown in Sections 5.3.3 and 5.3.4, the higher resolution PLIF measurements used to determine the effect of resolution on mixing in Section 4.7 were also analyzed using the methods outlined in Sections 5.3.3 and 5.3.4. It should be noted, however, that since no simultaneous PIV data were taken with the higher resolution PLIF data, mixing layer locations with extensive strain rate in the scalar gradient direction could not be removed from the averaging process. Here, the higher resolution PLIF images had an in-plane resolution of 34 μm/pixel, whereas the lower resolution PLIF portion of the simultaneous PLIF/PIV measurements had an in-plane resolution of 65 μm/pixel. The scalar dissipation rates calculated from both sets of PLIF measurements for the flush nozzle-injected, $S = 1.00$, $J = 41$ and $J = 5$ cases are shown in Figure 5.20. It can be seen from these plots that the general trends of scalar dissipation rate are similar between the higher resolution PLIF measurements and the lower resolution PLIF portion of the simultaneous PLIF/PIV measurements. The actual scalar dissipation

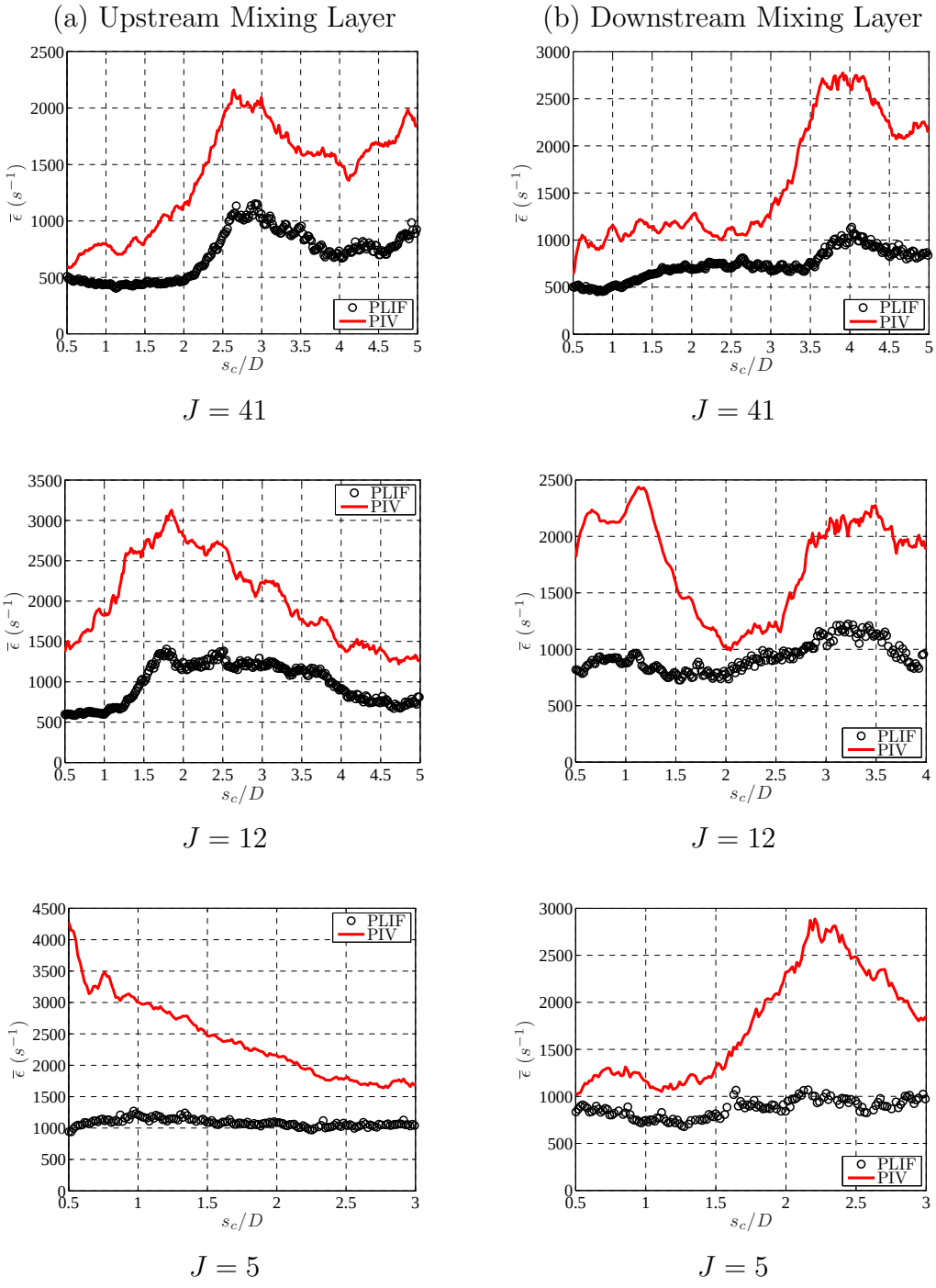


Figure 5.18: Average strain rate on the mixing layer calculated from scalar measurements using Equation 1.13, and average strain rate extracted from PIV in the direction normal to the scalar gradient direction, of $S = 1.00$, flush nozzle-injected transverse jets with $J = 41$, $J = 12$, and $J = 5$ as indicated below each plot. Data shown for (a) upstream mixing layer, and (b) downstream mixing layer. Data points with extensive strain in the scalar gradient direction are removed from averaging process.

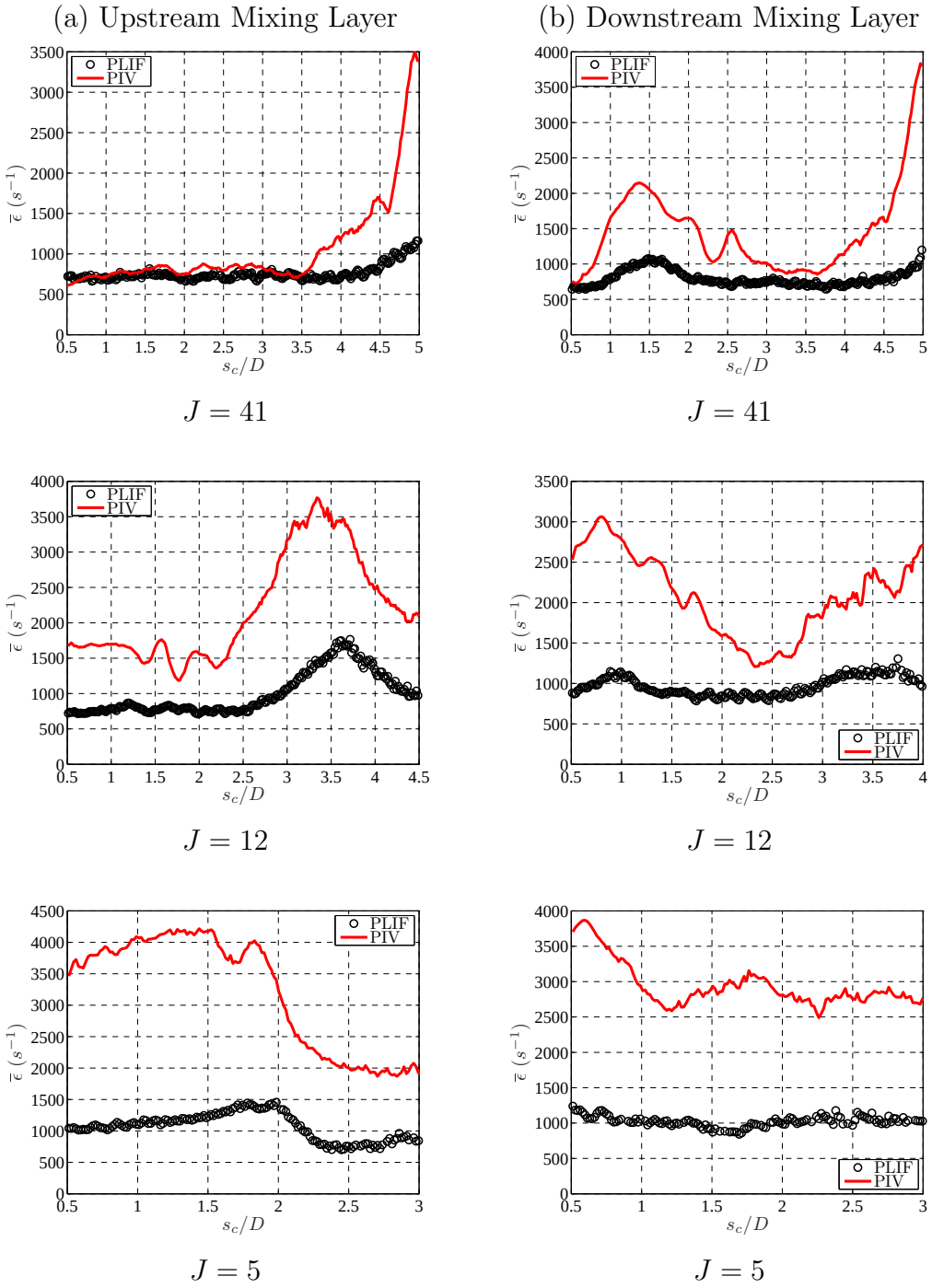


Figure 5.19: Average strain rate on the mixing layer calculated from scalar measurements using Equation 1.13, and average strain rate extracted from PIV in the direction normal to the scalar gradient direction, of $S = 1.00$, flush pipe-injected transverse jets with $J = 41$, $J = 12$, and $J = 5$ as indicated below each plot. Data shown for (a) upstream mixing layer, and (b) downstream mixing layer. Data points with extensive strain in the scalar gradient direction are removed from averaging process.

rate values are significantly different, however; the higher resolution scalar dissipation rates were larger. Some of the more subtle differences in values could be caused by slight day to day variation.

Since the resolution seems to be affecting the quantitative values of the scalar dissipation rate, the effect of the resolution on the strain rate calculated from the PLIF measurements was also studied. As summarized in Section 5.3.4, the strain rate was calculated from the PLIF measurements using an error function fit to the scalar profile around the mixing layer location. Figure 5.17 shows example fits used to determine the scalar boundary values C/C_o^+ and C/C_o^-, for PLIF data taken at lower and higher resolutions. The strain rates calculated from the error function fits of both PLIF data sets are shown in Figure 5.21 for flush nozzle-injected, $J = 41$ and $J = 5$ transverse jets. It can be seen from these plots that, similar to the scalar dissipation rates, although the general trends are not affected significantly by the resolution degradation associated with the PLIF portion of the simultaneous PLIF/PIV data, the values are affected significantly. It is once again noted that slight differences could be caused by day-to-day variation.

Assuming resolution degradation of measurements is not affecting the trends of the gradient quantities calculated here and only decreases actual gradient values, it is possible to correct for the effect of the PLIF measurement resolution on the strain rate calculation. The method for determining imaging system blur effects on the scalar gradients was outlined in the work of Wang and Clemens (2004). In short, a line-spread function (LSF) of the imaging system is determined using experimental data of a back-lit razor blade traversed through the PLIF camera field of view. Using the LSF, one can determine the degradation of the scalar dissipation rate caused by the finite resolution of the entire imaging system (camera lens, intensifier, and CCD array). Calculation of the LSF was done for the high resolution PLIF images, and the strain rates calculated from those images shown in Figure 5.21 were corrected for the effect of imaging blur. The results are shown in Figure 5.22. After this strain rate correction was applied, the difference between the maximum strain rate calculated from the PLIF measurement for the flush nozzle-injected, $J = 41$ case, and the strain rate extracted from the PIV measurements for the same case was reduced to 14%,

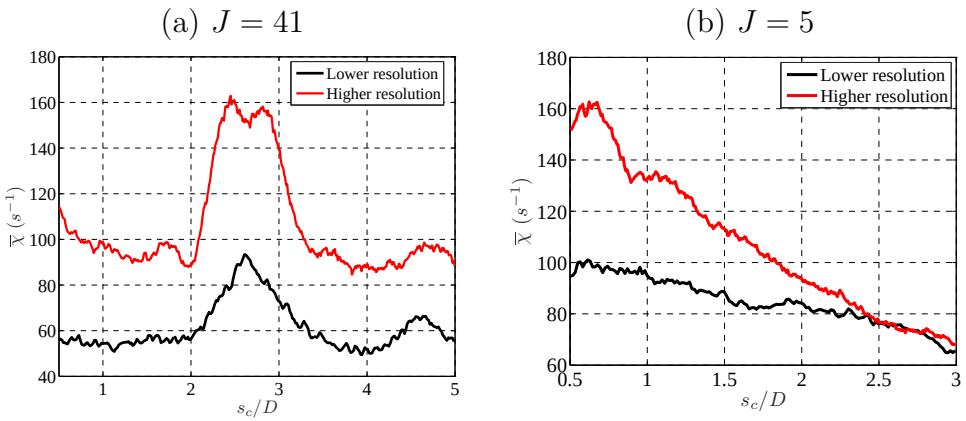


Figure 5.20: Average scalar dissipation rate comparison between high resolution PLIF imaging data, and PLIF portion of simultaneous PLIF/PIV measurements. Data shown for $S = 1.00$, flush nozzle-injected transverse jets with (a) $J = 41$, and (b) $J = 5$.

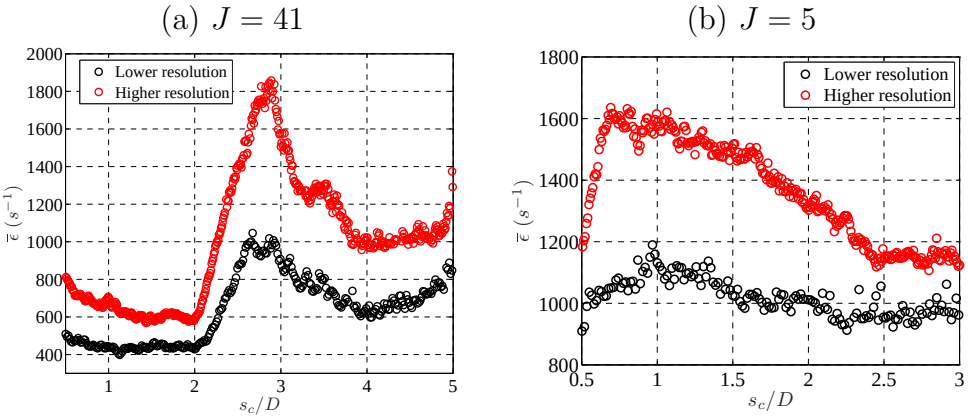


Figure 5.21: Average strain rate comparison between high resolution PLIF imaging data, and PLIF portion of simultaneous PLIF/PIV measurements. Data shown for $S = 1.00$, flush nozzle-injected transverse jets with (a) $J = 41$, and (b) $J = 5$.

which is a highly remarkable correspondence considering all the factors that could affect this comparison (e.g. measurement noise, day-to-day-variations, and PIV resolution and/or bias effects). However, comparing the resolution-corrected data for $J = 5$ in Figure 5.22b to the PIV-extracted strain rate data for the same case shown in the bottom row of Figure 5.18a, resolution correction does not account for all discrepancies between PLIF-calculated and PIV-extracted strain rates. As mentioned previously, additional differences could be caused by violations of the assumptions applied in the SDRL model formulation, such as finite response time of scalar dissipation structures to variations in strain rate and/or three-dimensional effects.

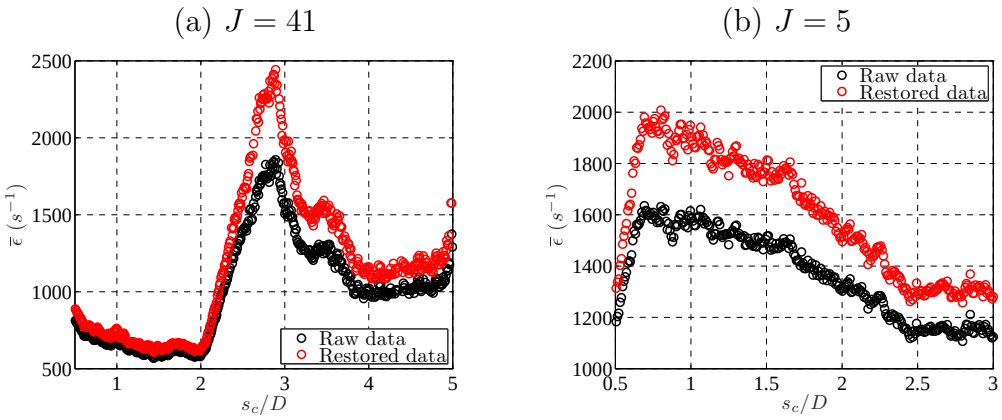


Figure 5.22: Resolution-corrected strain rates calculated from high-resolution PLIF measurements. Data shown for $S = 1.00$, flush nozzle-injected transverse jets with (a) $J = 41$, and (b) $J = 5$.

CHAPTER 6

Conclusions and Future Work

The experimental results shown here provide a systematic assessment of transverse jet stability and structural characteristics and their relationship to scalar transport, mixing, vorticity evolution, and fluid mechanical straining. The effect of variations in jet fluid injector type, jet-to-crossflow momentum flux ratio J, jet-to-crossflow density ratio S, and jet Reynolds number on scalar and velocity field stability and structure were studied using upstream shear layer hotwire measurements, jet centerplane PIV and PLIF measurements, and PLIF measurements of the cross-section of the jet. Hotwire, PIV, and acetone-PLIF measurements all suggest that for flush injection, lowering either the density ratio, or the momentum flux ratio, results in a transition to absolute instability in the upstream shear layer, which leads to generation of coherent vortices that dominate the near-field evolution of the jet. For elevated injection from the nozzle contour, lowering momentum flux ratio weakened the upstream shear layer in the momentum flux ratio range studied here, which was due to vertical co-flow effects outlined in the work of Megerian et al. (2007).

Definitive trends in shear layer stability characteristics and their effect on jet cross-sectional structure were observed. Stronger and more rapid upstream shear layer vortex rollup had a high correlation with the formation of a structurally symmetric, counter-rotating vortex pair (CVP) shape in the jet cross-sectional scalar field measurements, whereas jets with weak upstream shear layer instability typically did not form a clear, symmetric CVP. Moreover, highly asymmetric jet cross-sectional structures were observed for flush-injected, convectively unstable jets, with evidence of tertiary vortices drawing jet fluid from the main jet lobes and skewing the cross-sectional symmetry. The cross-sectional symmetry also seemed to have secondary dependence on jet Reynolds number, with large increases in Reynolds numbers resulting in a more structurally symmetric jet cross-section and CVP.

Systematic variation of jet Reynolds number, jet-to-crossflow momentum flux ratio, and crossflow speed suggested that the transverse jet is highly susceptible to any slight asymmetric perturbations and/or mean variations within certain flowfield regimes (i.e. relatively low Reynolds number, convectively unstable jets).

The effect of stability and structural variation on the scalar field mixing efficiency of the jet in crossflow was examined using both centerplane and cross-sectional PLIF measurements. Systematic assessments of the jet's cross-sectional and centerplane mixing efficiency variation with alterations in momentum flux ratio, density ratio, and injector type were accomplished by applying scalar field mixing metrics such as the cross-sectional spatial probability density function (PDF), the cross-sectional and centerplane spatial Unmixedness, and the centerplane concentration decay and non-reactive "flame" length. Trends in these metrics all corresponded well with each other, and comparisons among the centerplane and cross-sectional mixing trends suggested that the centerplane can be used effectively as a general measure of the mixing trends in the cross-section. There was, however, significant variation in the mixing trends when metrics were plotted against the downstream coordinate x/D as opposed to the jet trajectory coordinate s_c/D, which can affect determination of the "best" conditions for mixing in a given application. For research purposes, however, the jet trajectory coordinate was used as the coordinate system for comparisons among different jets, given that the exposure of the jet fluid to crossflow fluid occurs along the trajectory of the jet, and that mixing associated with this exposure may be compared more directly with that of the free jet.

In general, when comparing the mixing trends along the jet trajectory coordinate, all centerplane and cross-sectional mixing metrics suggested an overall increase in mixing when the jet transitions to absolute instability with either a reduction of density ratio S for high momentum flux ratio J, or a reduction of J for equidensity ($S = 1.00$) jets. Interestingly, for flush nozzle-injected, low J conditions, where the jet shear layer was absolutely unstable for any density ratio, lowering S from unity actually decreased overall mixing efficiency. This effect was determined to be caused by a reduction of crossflow fluid entrainment into the jet's shear layer vortices when density ratio was lowered. Comparing the mixing efficiency of

the three different injectors revealed that jets injected from the flush-mounted pipe injector generally mixed with the crossflow the best, whereas the jets injected from the elevated nozzle injector mixed the worst due to vertical co-flow stabilization of the elevated nozzle injector's upstream shear layer.

The relationship between the velocity and scalar fields, which provides the mechanism for mixing and transport processes in the JICF, was studied in more detail in order to gain insights into the evolution of this flowfield. Simultaneous PLIF/PIV measurements of the jet centerplane were used as a basis for comparing the evolution of the scalar and velocity fields. Direct comparisons of the two fields revealed excellent general correspondence between regions of high vorticity and high scalar dissipation rate. Comparisons between the maximum scalar dissipation rate and the minimum principal strain rate at the same location showed a lack of correspondence in trends along the jet trajectory. This was determined to be caused by variations in the angle of orientation between the scalar gradient vector and the minimum principal axis of strain along the shear layer. Comparisons between the maximum scalar dissipation rate, derived from PLIF data, and the strain rate in the scalar gradient direction, derived from stereo PIV data, resulted in improved correspondence as compared with use of the minimum principal strain rate. Yet trend correspondence between the two metrics decreased with a reduction in J. There was also typically less correspondence between scalar dissipation rate and strain rate on the lee-side of the jet as compared to the upstream side, possibly due to the strongly time-varying and three-dimensional velocity field in the wake of the jet.

The correspondence in scalar dissipation rate and layer-normal strain rate was studied in more detail using direct application of the Strained Dissipation and Reaction Layer (SDRL) model for calculation of the one-dimensional, quasi-steady strain rate predicted for a given scalar distribution profile. The results showed qualitative trend correspondence between the strain rate calculated from the scalar profile and the layer-normal strain rate extracted from PIV. Yet good quantitative correspondence between the strain rate calculated from the scalar field and the strain rate extracted from PIV was only seen in regions of relatively low strain rate and relatively little three-dimensional variation or time-varying effects (e.g.

in the windward side jet shear/mixing layer of the equidensity, flush pipe-injected, $J = 41$ jet). This lack of quantitative correspondence between the variations in the scalar field and the underlying strain field makes it difficult to predict where reactions in an equivalent reacting flow could be sustained. In general, however, regions of lower strain rate are more likely to facilitate combustion. This contention suggests that a stable flame is more likely to be present for the higher momentum flux ratio cases. For lower momentum flux ratios, ignition may be more likely on the lee-side of the jet rather than the windward side, which is consistent with what is often seen in reactive transverse jets (Sullivan et al., 2014; Cetegen, 2015). It should be kept in mind, however, that the jet Reynolds number is fixed in this study, and the crossflow is varied. In an application setting, the jet mass flow rate will most likely be the varied parameter, in which case variations in strain rate with variations in J will not necessarily equate with the trends seen in this study. The methods used to analyze the data, however, will still be applicable.

The methods established for systematic analysis of jet structure and mixing in this study provide a solid foundation for future interrogation of this flowfield. Some other potential transverse jet studies for which the methods outlined here could be useful are as follows:

- Cross-sectional PIV in order to visualize the entire flowfield's vorticity distribution. PIV on this measurement plane may reveal additional vortices that do not contain jet fluid but nevertheless may be contributing to the highly asymmetric structure of convectively unstable, flush-injected jets.

- Acoustic forcing intended to affect the symmetry/asymmetry of the jet. Low-level, sinusoidal forcing at frequencies close to the fundamental mode of convectively unstable jets may result in enhanced structural symmetry.

- Strategic sinusoidal and square-wave forcing of both convectively and absolutely unstable transverse jets for enhanced mixing. The systematic mixing metric application method highlighted in this work should prove useful in comparing levels of mixing. The POD analysis method, as well as the strain rate/scalar dissipation rate comparison method, will prove useful for analyzing the forced jet in crossflow as well.

APPENDIX A

Mean Cross-sectional (yz-plane) Scalar Field Data

The following results correspond to additional data sets for mean cross-sectional PLIF images of the transverse jets for various flow conditions. These are intended to supplement images shown in Chapter 3.

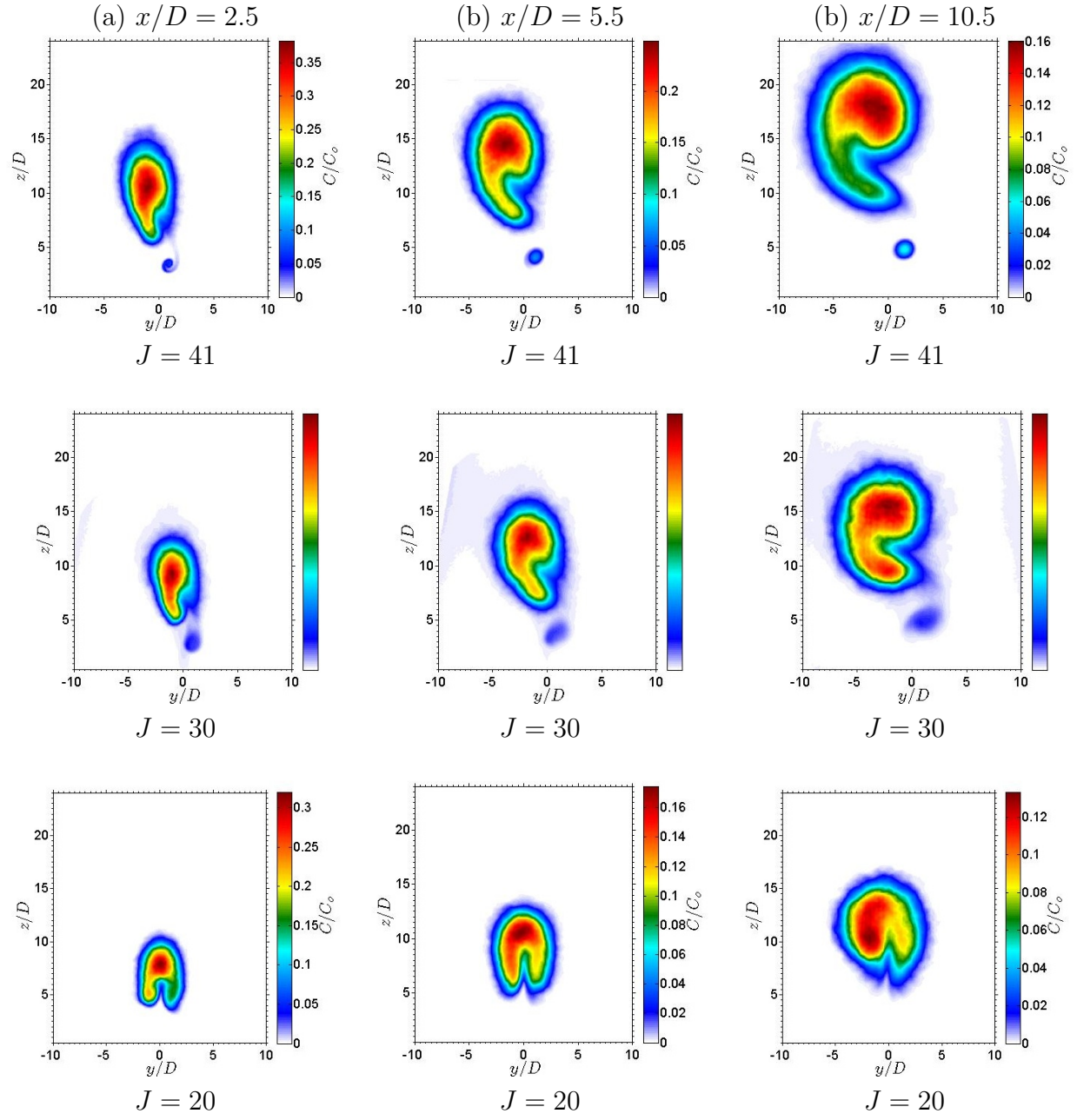


Figure A.1: Mean cross-sectional scalar field visualization at (a) $x/D = 2.5$, (b) $x/D = 5.5$, and (a) $x/D = 10.5$ for $S = 1.00$, flush nozzle-generated JICF with varying momentum flux ratios: $J = 41$ (top row), $J = 30$ (middle row), $J = 20$ (bottom row). Colormap linearly scaled to maximum value within FOV. Quantitative C/C_o values only given when fluorescence data was scalable to jet fluid concentration.

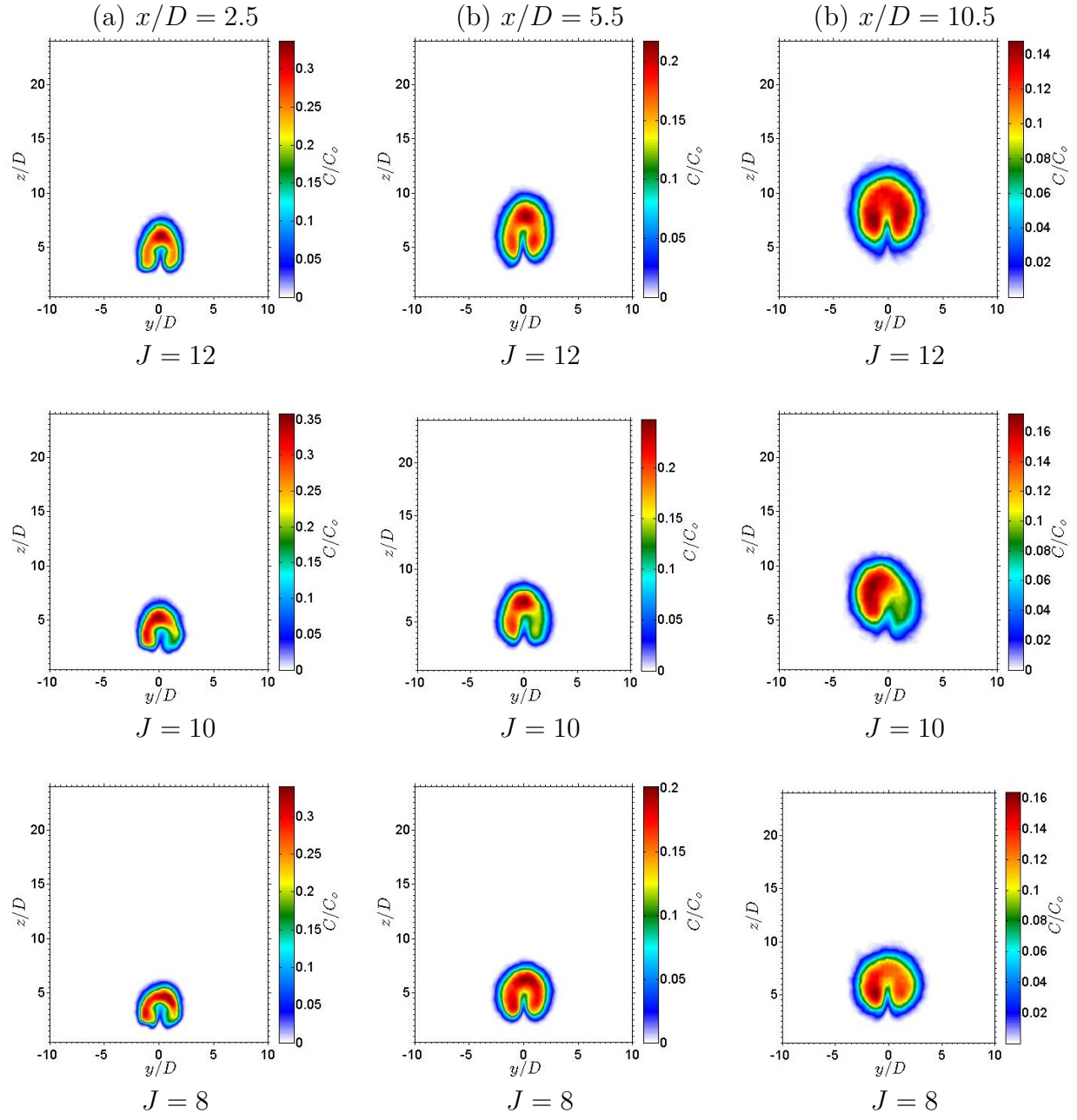


Figure A.2: Mean cross-sectional scalar field visualization at (a) $x/D = 2.5$, (b) $x/D = 5.5$, and (a) $x/D = 10.5$ for $S = 1.00$, flush nozzle-generated JICF with varying momentum flux ratios: $J = 12$ (top row), $J = 10$ (middle row), $J = 8$ (bottom row). Colormap linearly scaled to maximum value within FOV. Quantitative C/C_o values only given when fluorescence data was scalable to jet fluid concentration.

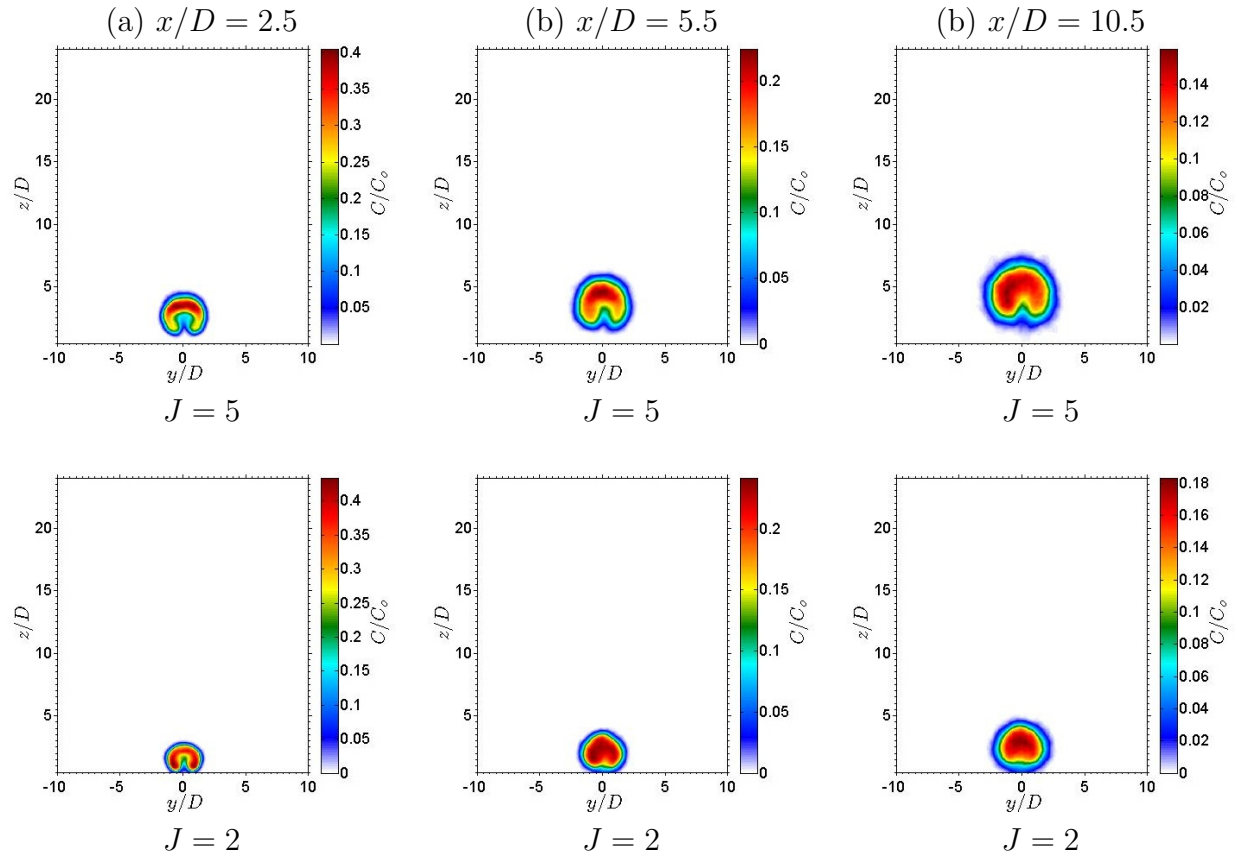


Figure A.3: Mean cross-sectional scalar field visualization at (a) $x/D = 2.5$, (b) $x/D = 5.5$, and (a) $x/D = 10.5$ for $S = 1.00$, flush nozzle-generated JICF with varying momentum flux ratios: $J = 5$ (top row), $J = 2$ (bottom row). Colormap linearly scaled to maximum value within FOV. Quantitative C/C_o values only given when fluorescence data was scalable to jet fluid concentration.

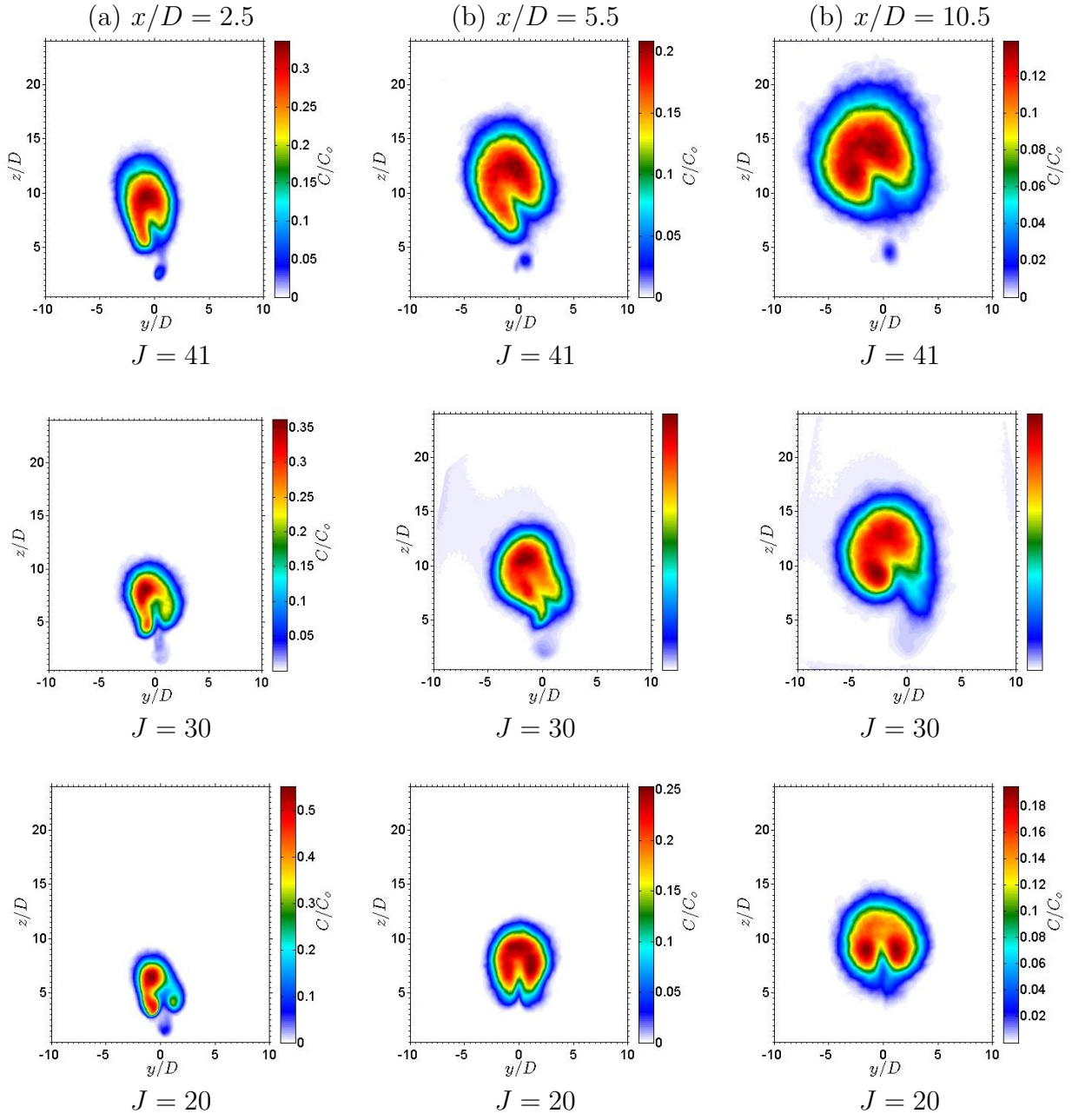


Figure A.4: Mean cross-sectional scalar field visualization at (a) $x/D = 2.5$, (b) $x/D = 5.5$, and (a) $x/D = 10.5$ for $S = 0.55$, flush nozzle-generated JICF with varying momentum flux ratios: $J = 41$ (top row), $J = 30$ (middle row), $J = 20$ (bottom row). Colormap linearly scaled to maximum value within FOV. Quantitative C/C_o values only given when fluorescence data was scalable to jet fluid concentration.

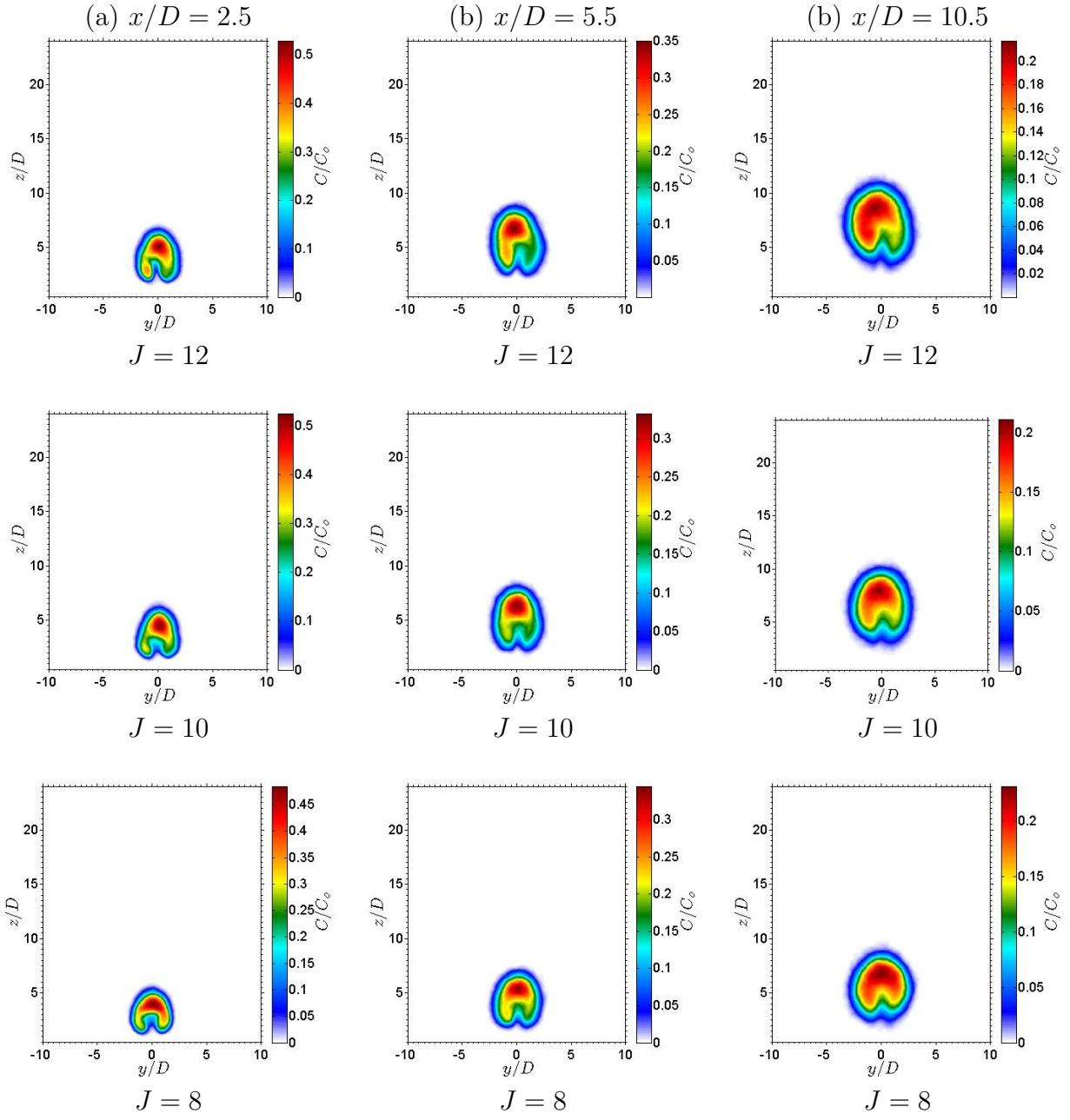


Figure A.5: Mean cross-sectional scalar field visualization at (a) $x/D = 2.5$, (b) $x/D = 5.5$, and (a) $x/D = 10.5$ for $S = 0.55$, flush nozzle-generated JICF with varying momentum flux ratios: $J = 12$ (top row), $J = 10$ (middle row), $J = 8$ (bottom row). Colormap linearly scaled to maximum value within FOV. Quantitative C/C_o values only given when fluorescence data was scalable to jet fluid concentration.

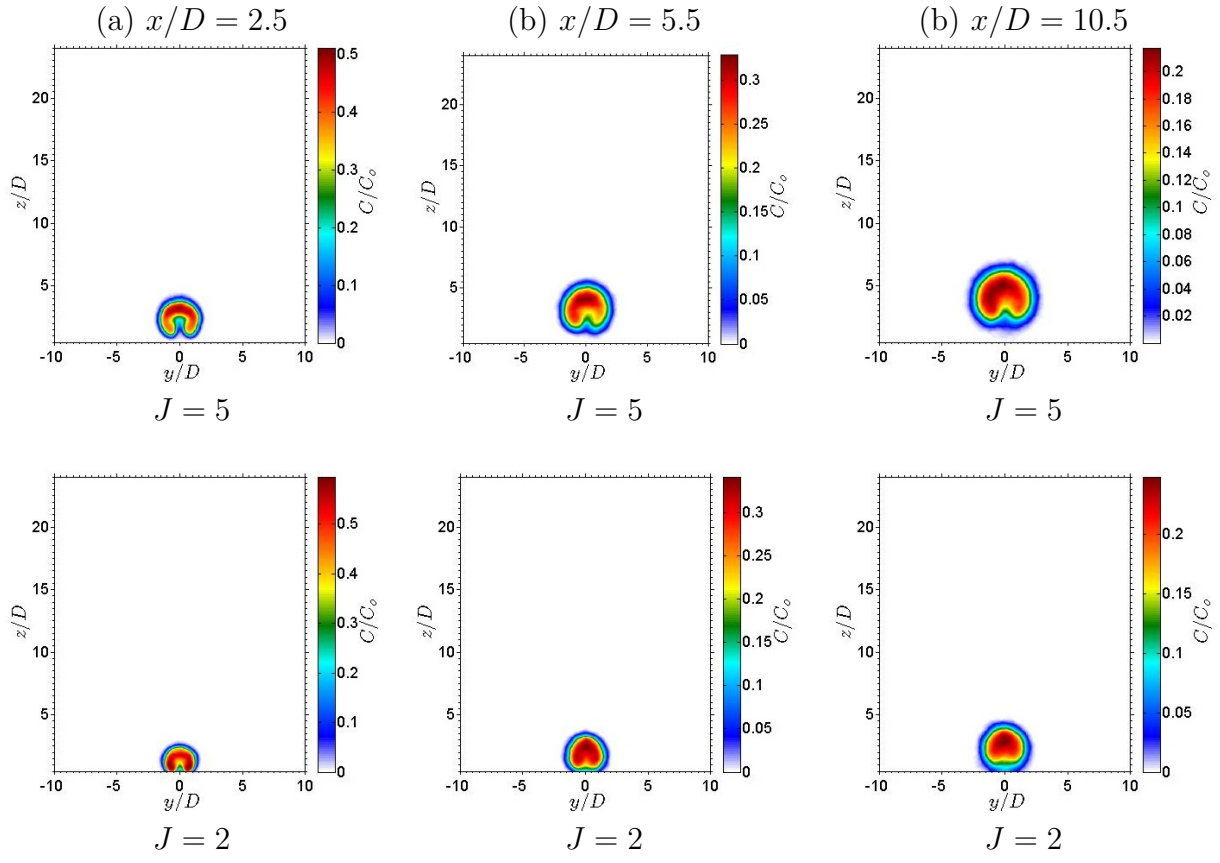


Figure A.6: Mean cross-sectional scalar field visualization at (a) $x/D = 2.5$, (b) $x/D = 5.5$, and (a) $x/D = 10.5$ for $S = 0.55$, flush nozzle-generated JICF with varying momentum flux ratios: $J = 5$ (top row), $J = 2$ (bottom row). Colormap linearly scaled to maximum value within FOV. Quantitative C/C_o values only given when fluorescence data was scalable to jet fluid concentration.

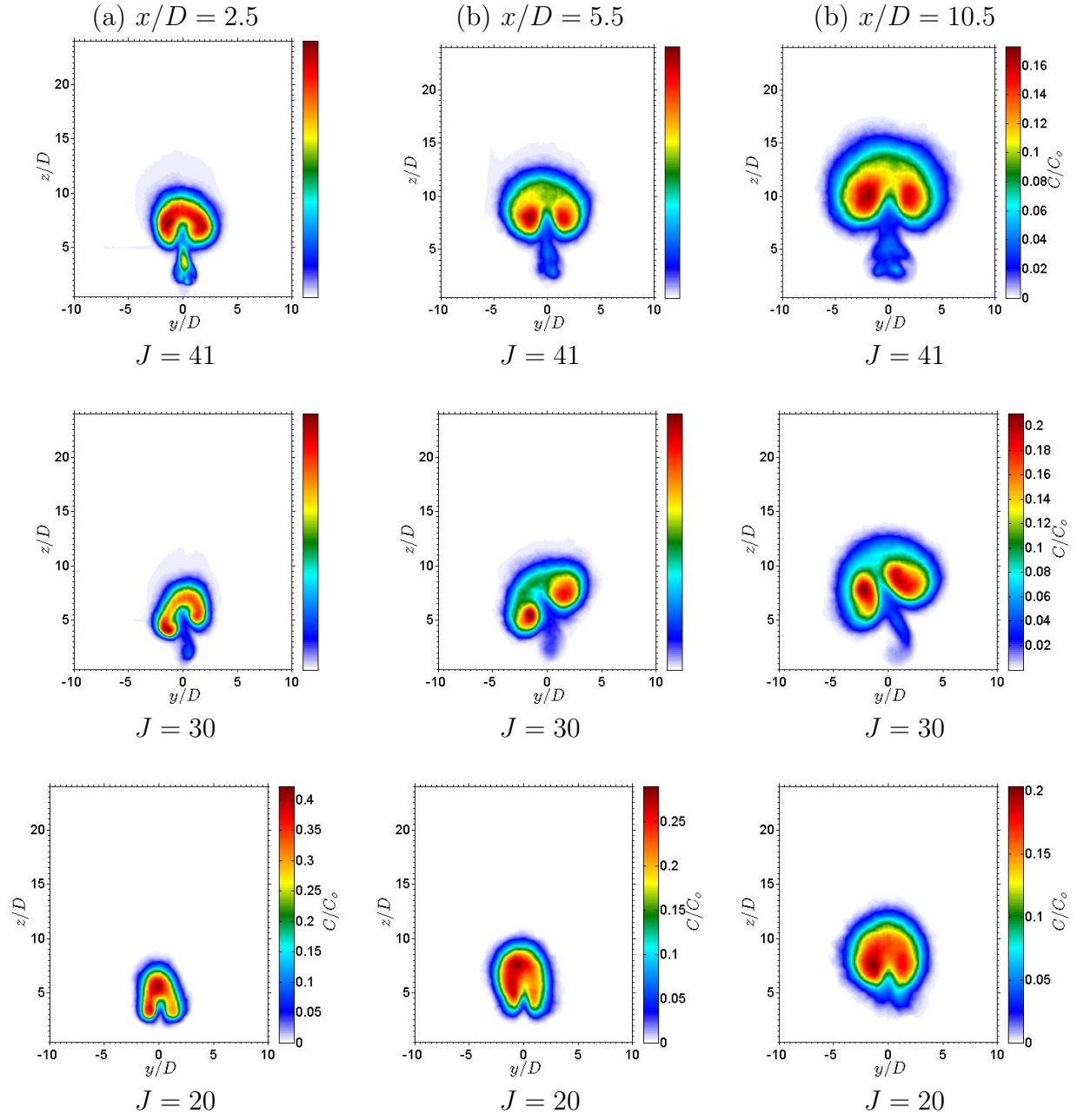


Figure A.7: Mean cross-sectional scalar field visualization at (a) $x/D = 2.5$, (b) $x/D = 5.5$, and (a) $x/D = 10.5$ for $S = 0.35$, flush nozzle-generated JICF with varying momentum flux ratios: $J = 41$ (top row), $J = 30$ (middle row), $J = 20$ (bottom row). Colormap linearly scaled to maximum value within FOV. Quantitative C/C_o values only given when fluorescence data was scalable to jet fluid concentration.

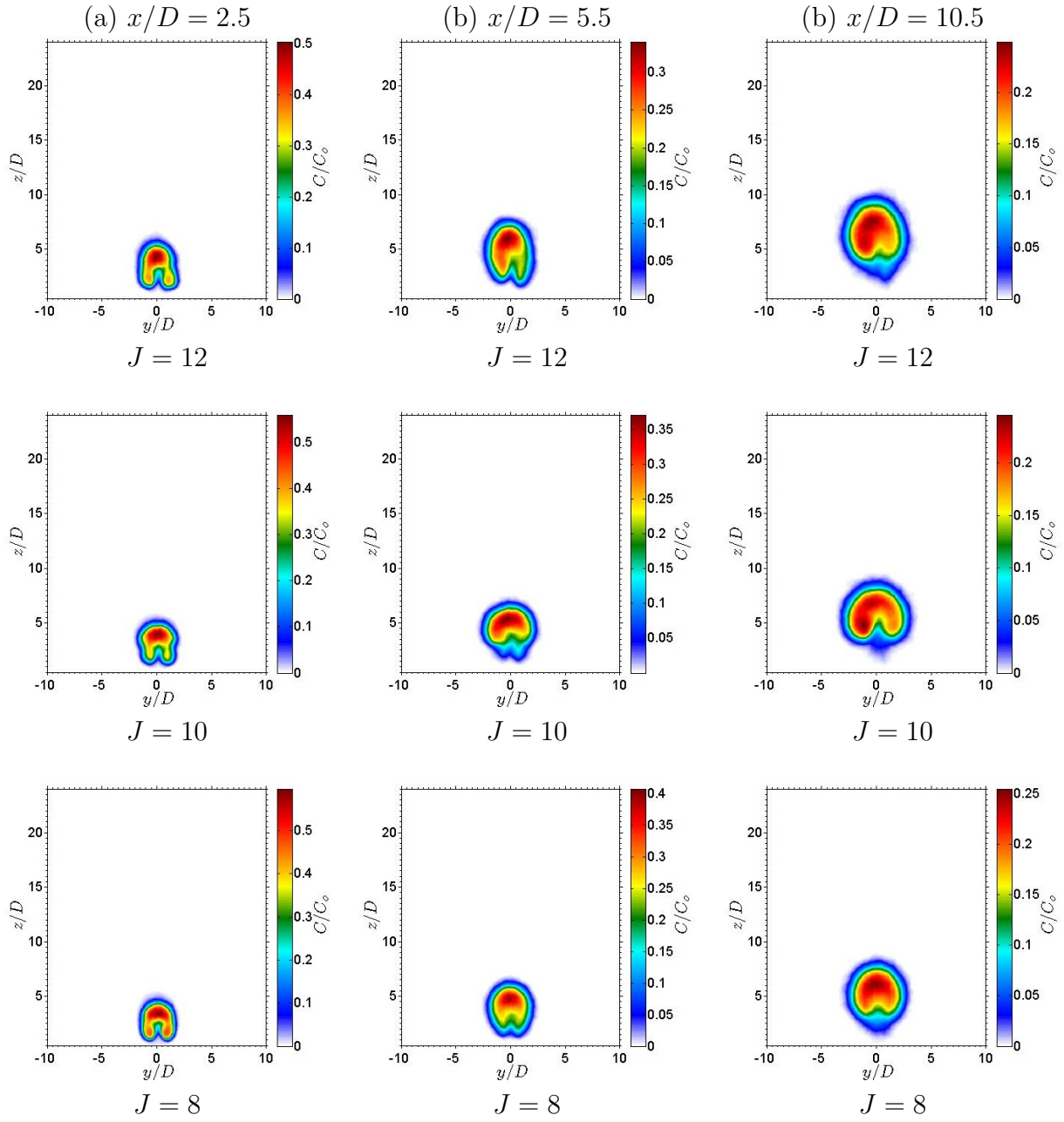


Figure A.8: Mean cross-sectional scalar field visualization at (a) $x/D = 2.5$, (b) $x/D = 5.5$, and (a) $x/D = 10.5$ for $S = 0.35$, flush nozzle-generated JICF with varying momentum flux ratios: $J = 12$ (top row), $J = 10$ (middle row), $J = 8$ (bottom row). Colormap linearly scaled to maximum value within FOV. Quantitative C/C_o values only given when fluorescence data was scalable to jet fluid concentration.

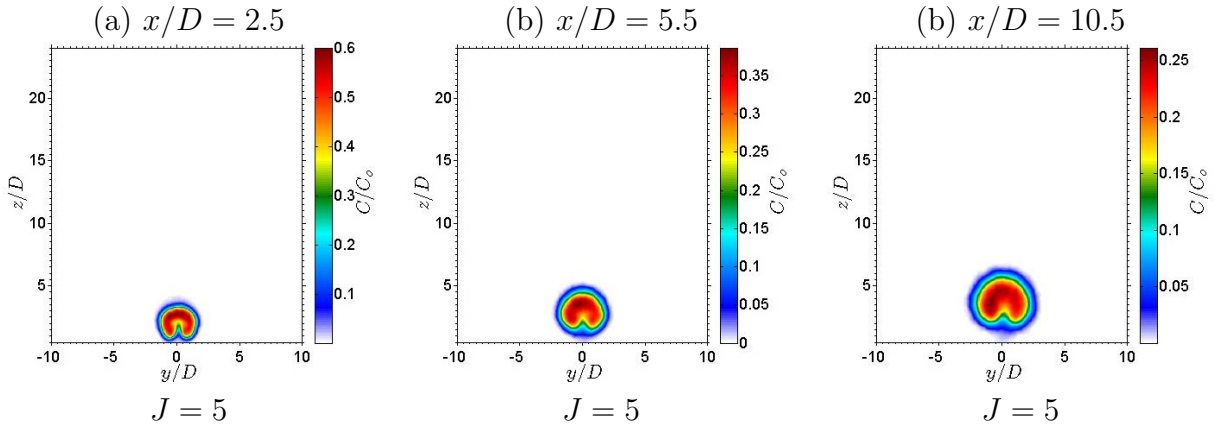


Figure A.9: Mean cross-sectional scalar field visualization at (a) $x/D = 2.5$, (b) $x/D = 5.5$, and (a) $x/D = 10.5$ for $S = 0.35$, flush nozzle-generated JICF with $J = 5$. Colormap linearly scaled to maximum value within FOV. Quantitative C/C_o values only given when fluorescence data was scalable to jet fluid concentration.

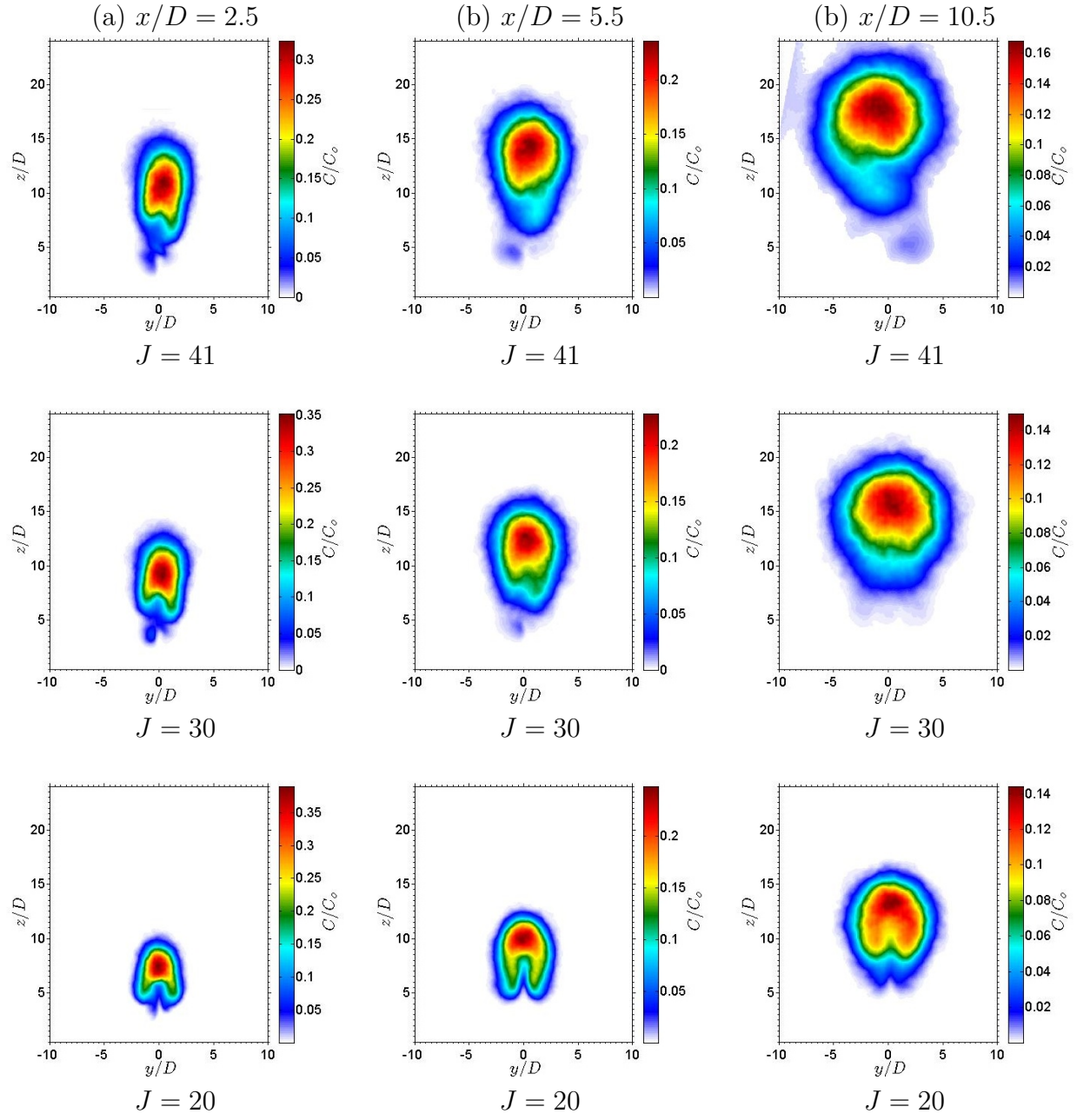


Figure A.10: Mean cross-sectional scalar field visualization at (a) $x/D = 2.5$, (b) $x/D = 5.5$, and (a) $x/D = 10.5$ for $S = 1.00$, elevated nozzle-generated JICF with varying momentum flux ratios: $J = 41$ (top row), $J = 30$ (middle row), $J = 20$ (bottom row). Colormap linearly scaled to maximum value within FOV. Quantitative C/C_o values only given when fluorescence data was scalable to jet fluid concentration.

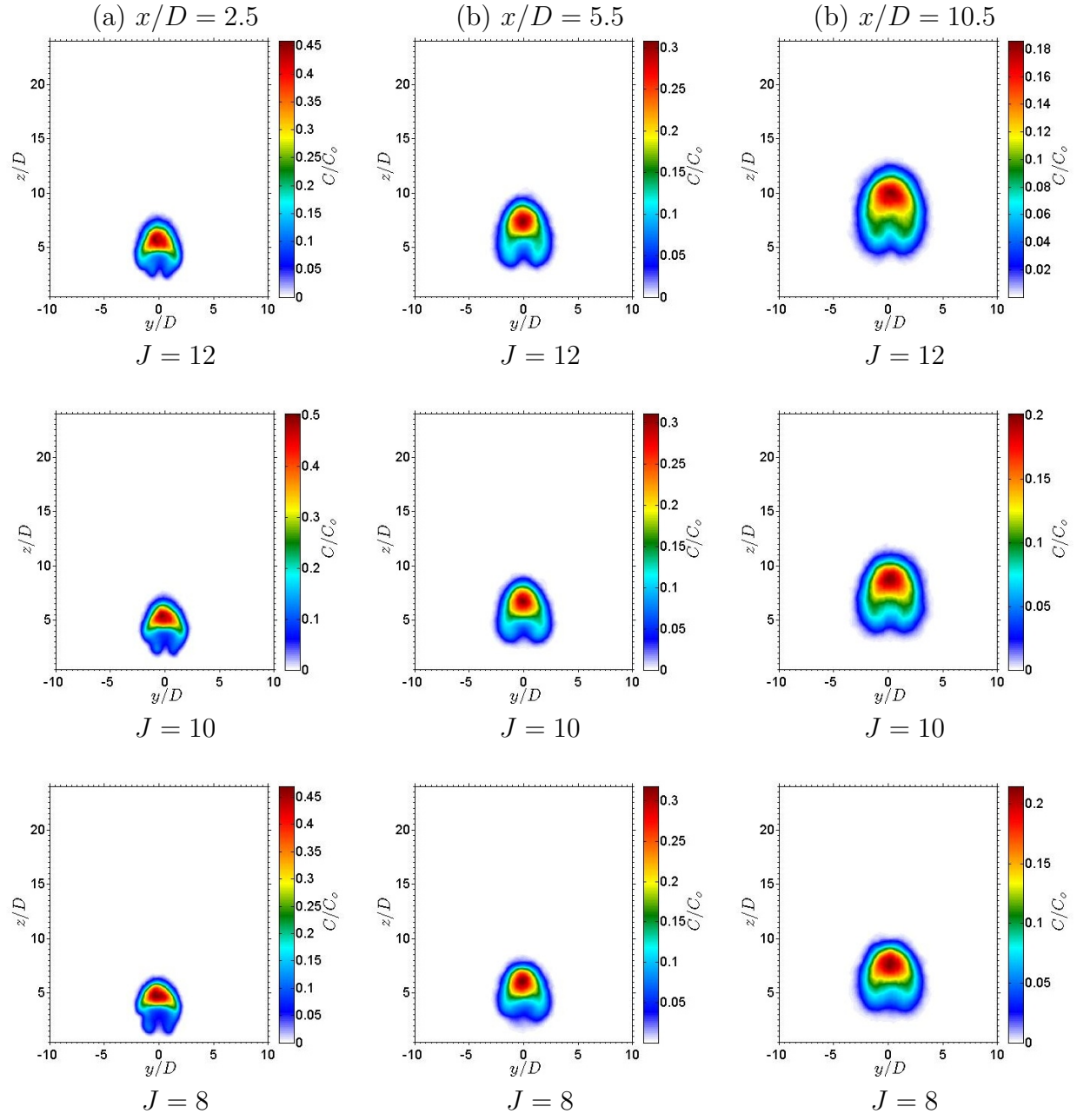


Figure A.11: Mean cross-sectional scalar field visualization at (a) $x/D = 2.5$, (b) $x/D = 5.5$, and (a) $x/D = 10.5$ for $S = 1.00$, elevated nozzle-generated JICF with varying momentum flux ratios: $J = 12$ (top row), $J = 10$ (middle row), $J = 8$ (bottom row). Colormap linearly scaled to maximum value within FOV. Quantitative C/C_o values only given when fluorescence data was scalable to jet fluid concentration.

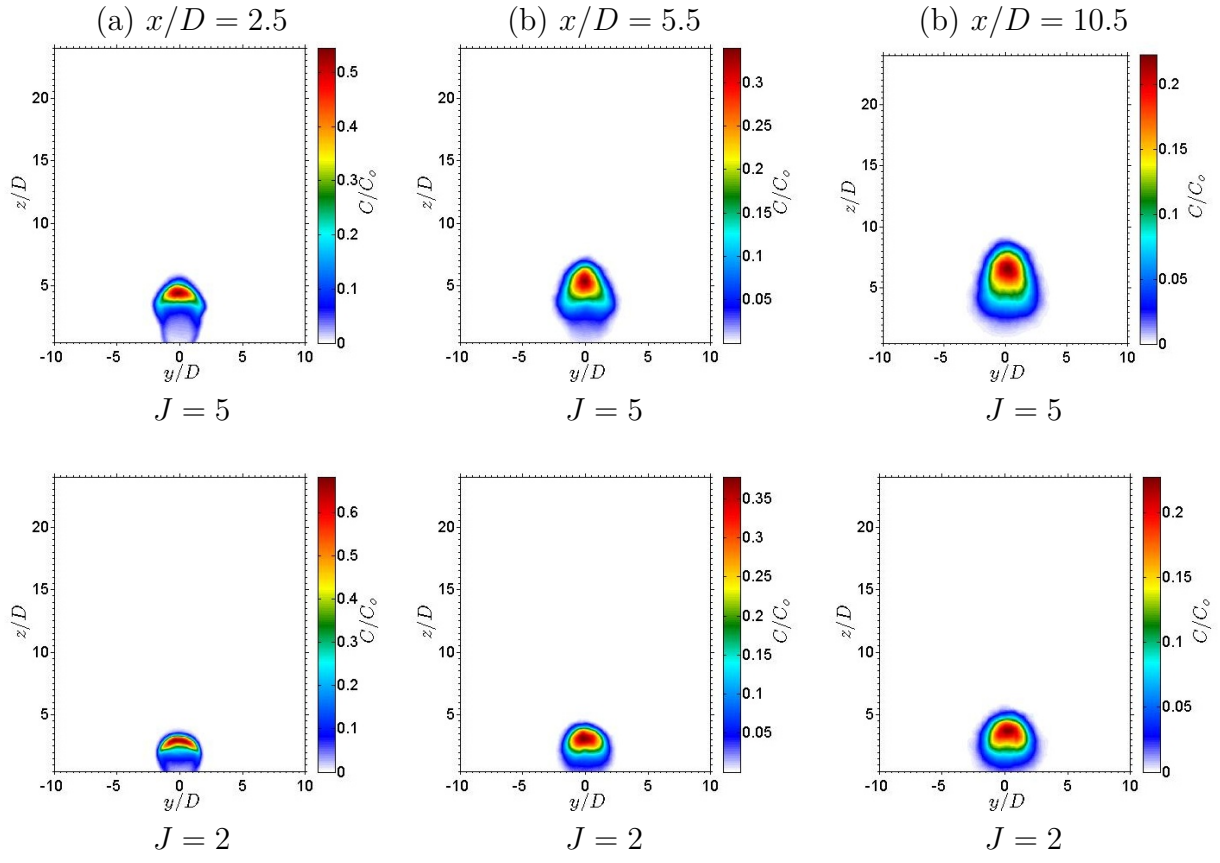


Figure A.12: Mean cross-sectional scalar field visualization at (a) $x/D = 2.5$, (b) $x/D = 5.5$, and (a) $x/D = 10.5$ for $S = 1.00$, elevated nozzle-generated JICF with varying momentum flux ratios: $J = 5$ (top row), $J = 2$ (bottom row). Colormap linearly scaled to maximum value within FOV. Quantitative C/C_o values only given when fluorescence data was scalable to jet fluid concentration.

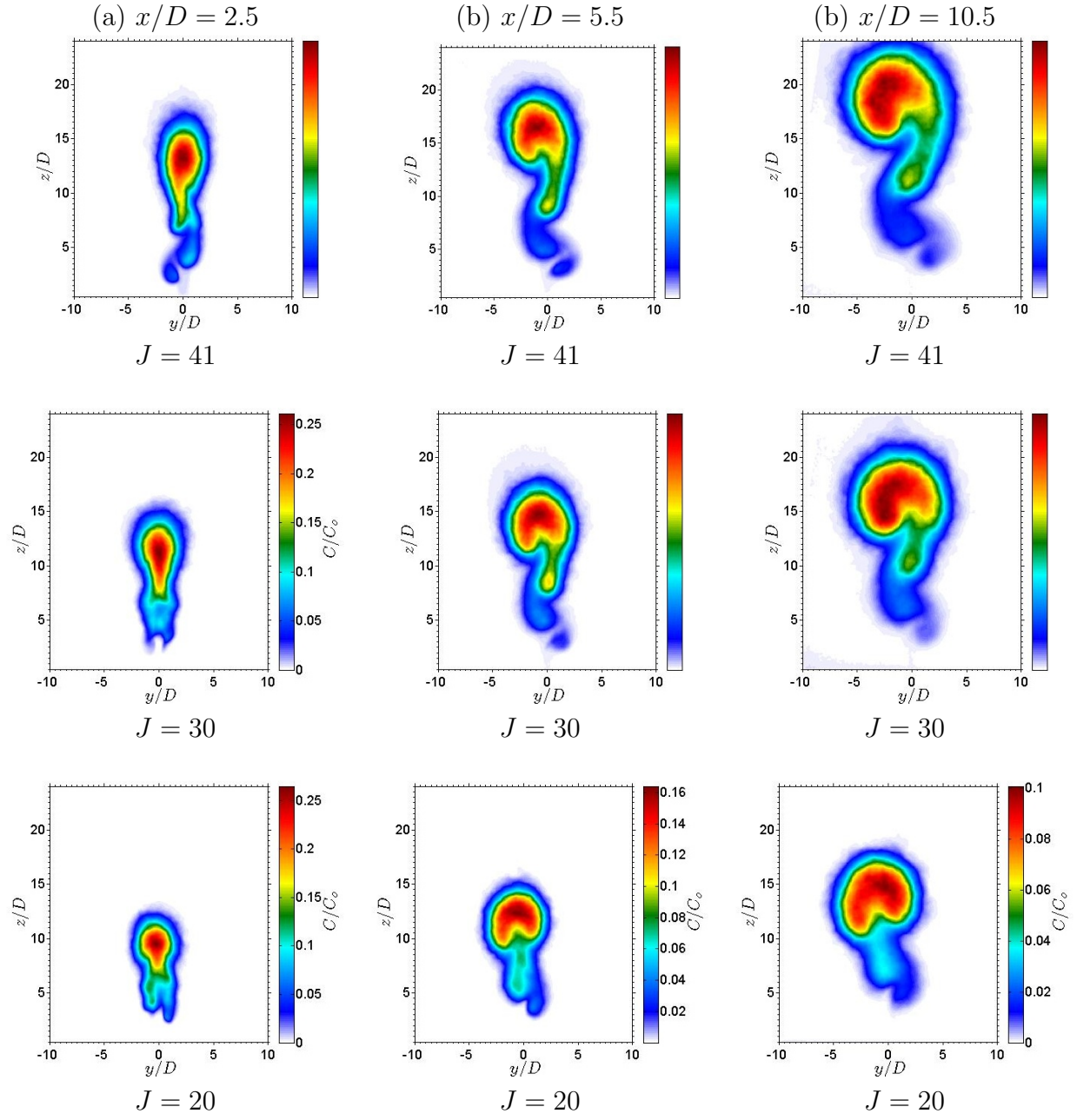


Figure A.13: Mean cross-sectional scalar field visualization at (a) $x/D = 2.5$, (b) $x/D = 5.5$, and (a) $x/D = 10.5$ for $S = 1.00$, flush pipe-generated JICF with varying momentum flux ratios: $J = 41$ (top row), $J = 30$ (middle row), $J = 20$ (bottom row). Colormap linearly scaled to maximum value within FOV. Quantitative C/C_o values only given when fluorescence data was scalable to jet fluid concentration.

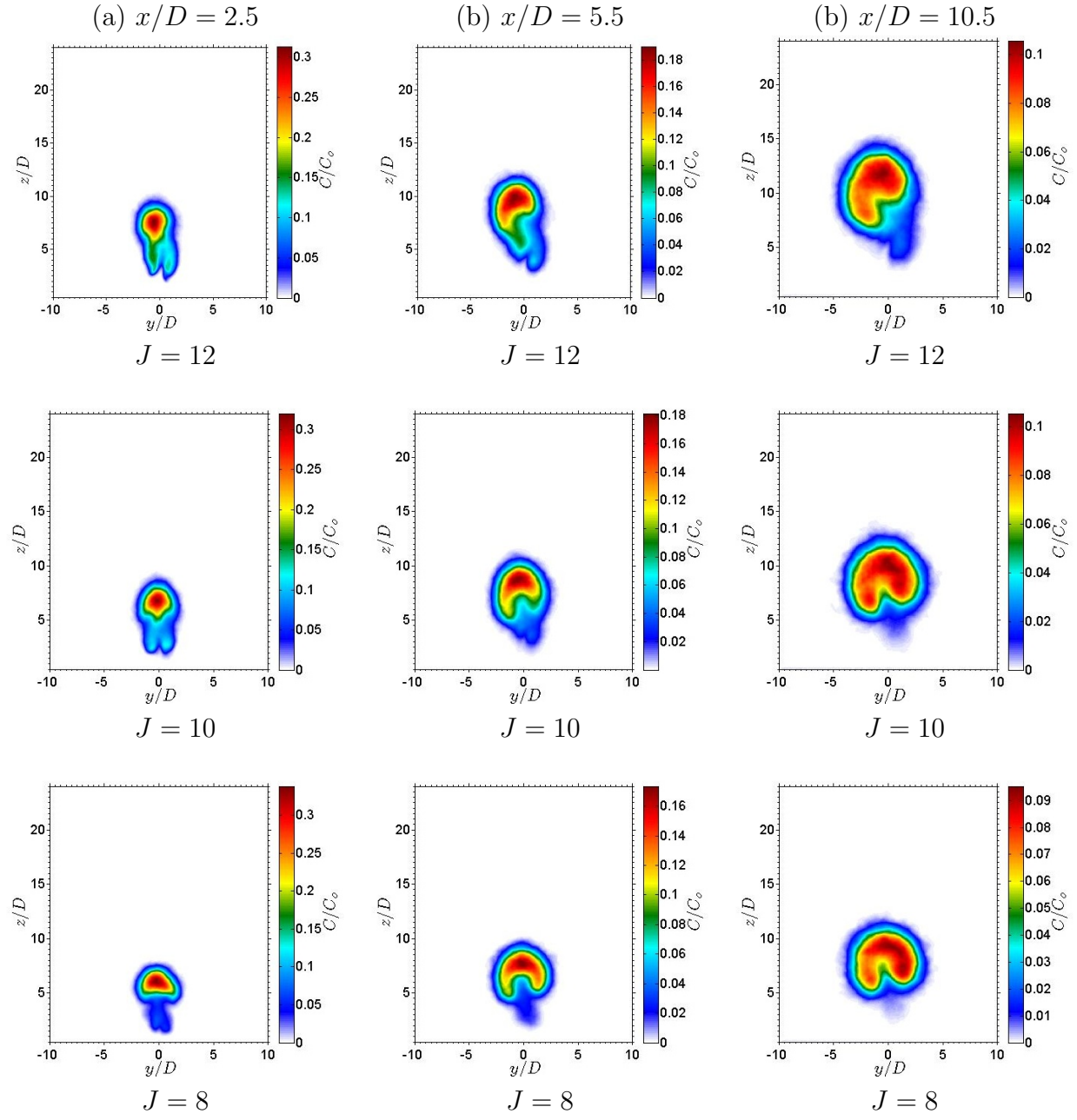


Figure A.14: Mean cross-sectional scalar field visualization at (a) $x/D = 2.5$, (b) $x/D = 5.5$, and (a) $x/D = 10.5$ for $S = 1.00$, flush pipe-generated JICF with varying momentum flux ratios: $J = 12$ (top row), $J = 10$ (middle row), $J = 8$ (bottom row). Colormap linearly scaled to maximum value within FOV. Quantitative C/C_o values only given when fluorescence data was scalable to jet fluid concentration.

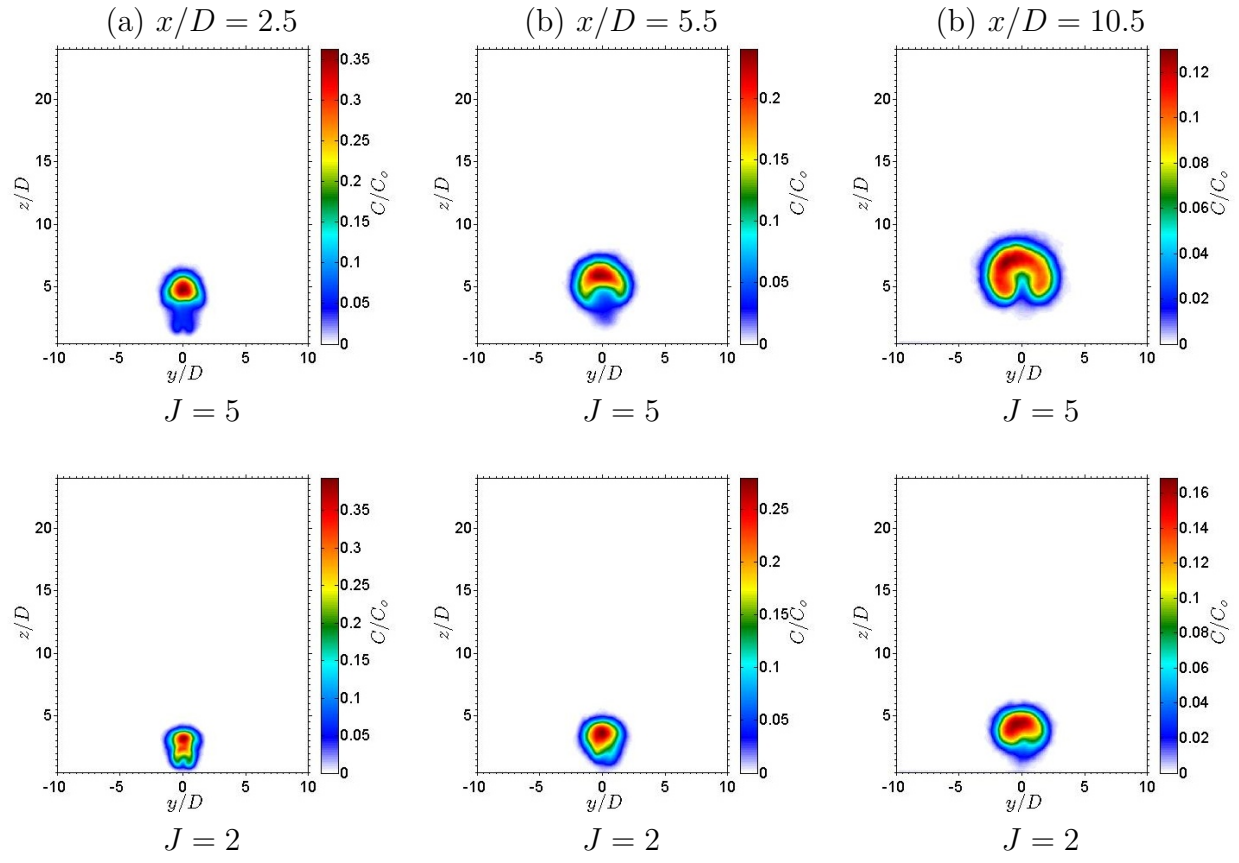


Figure A.15: Mean cross-sectional scalar field visualization at (a) $x/D = 2.5$, (b) $x/D = 5.5$, and (a) $x/D = 10.5$ for $S = 1.00$, flush pipe-generated JICF with varying momentum flux ratios: $J = 5$ (top row), $J = 2$ (bottom row). Colormap linearly scaled to maximum value within FOV. Quantitative C/C_o values only given when fluorescence data was scalable to jet fluid concentration.

APPENDIX B

Centerplane Mean and Instantaneous Data

The following results correspond to additional data sets for centerplane-based PLIF images of the transverse jet, both averaged and instantaneous. These are intended to supplement images shown in Chapter 4.

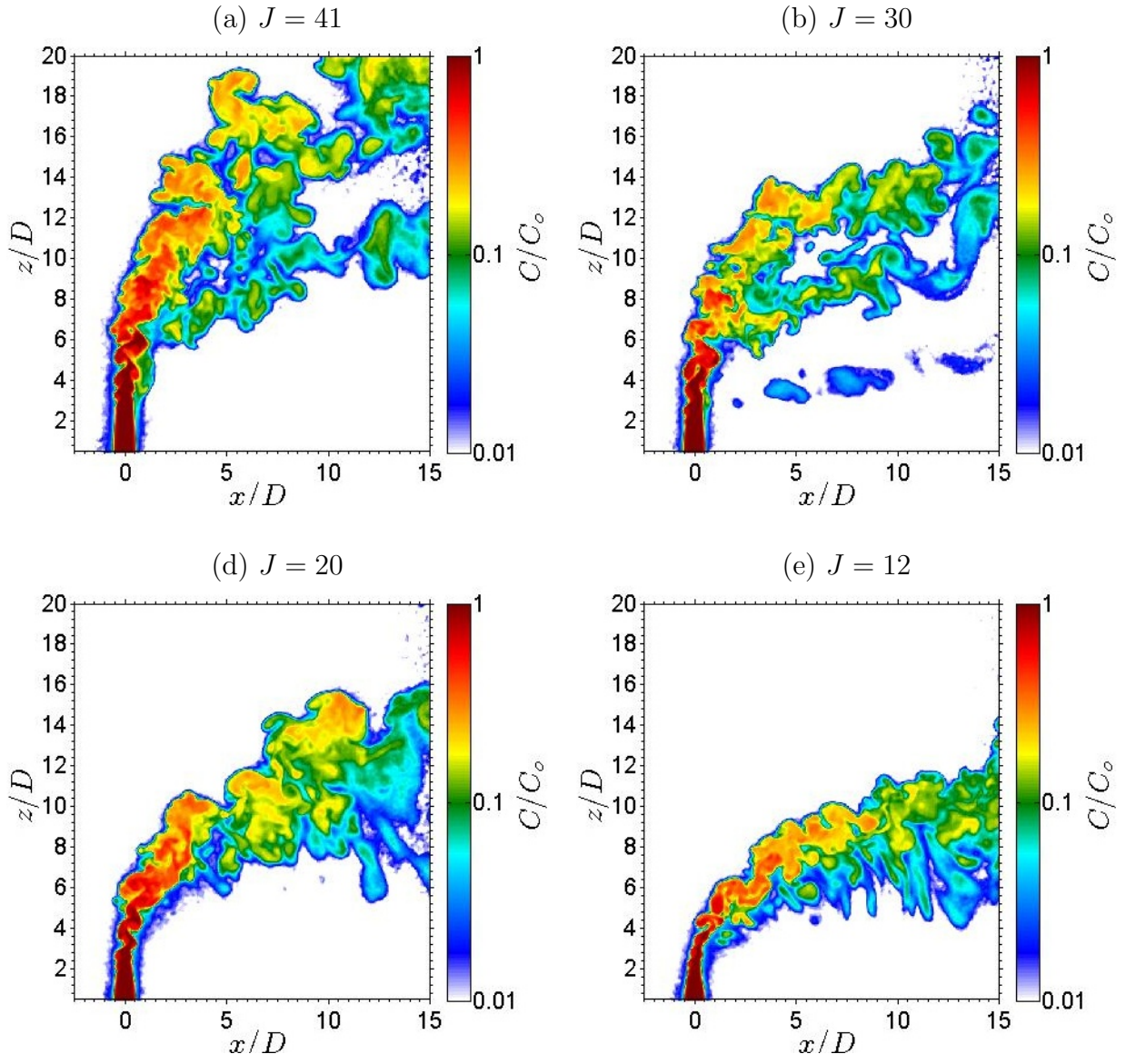


Figure B.1: Instantaneous centerplane (side view) acetone PLIF imaging of $S = 1.00$, flush nozzle-generated JICF with varying momentum flux ratios: (a) $J = 41$, (b) $J = 30$, (c) $J = 20$, (d) $J = 12$. Data shown in logarithmic scale.

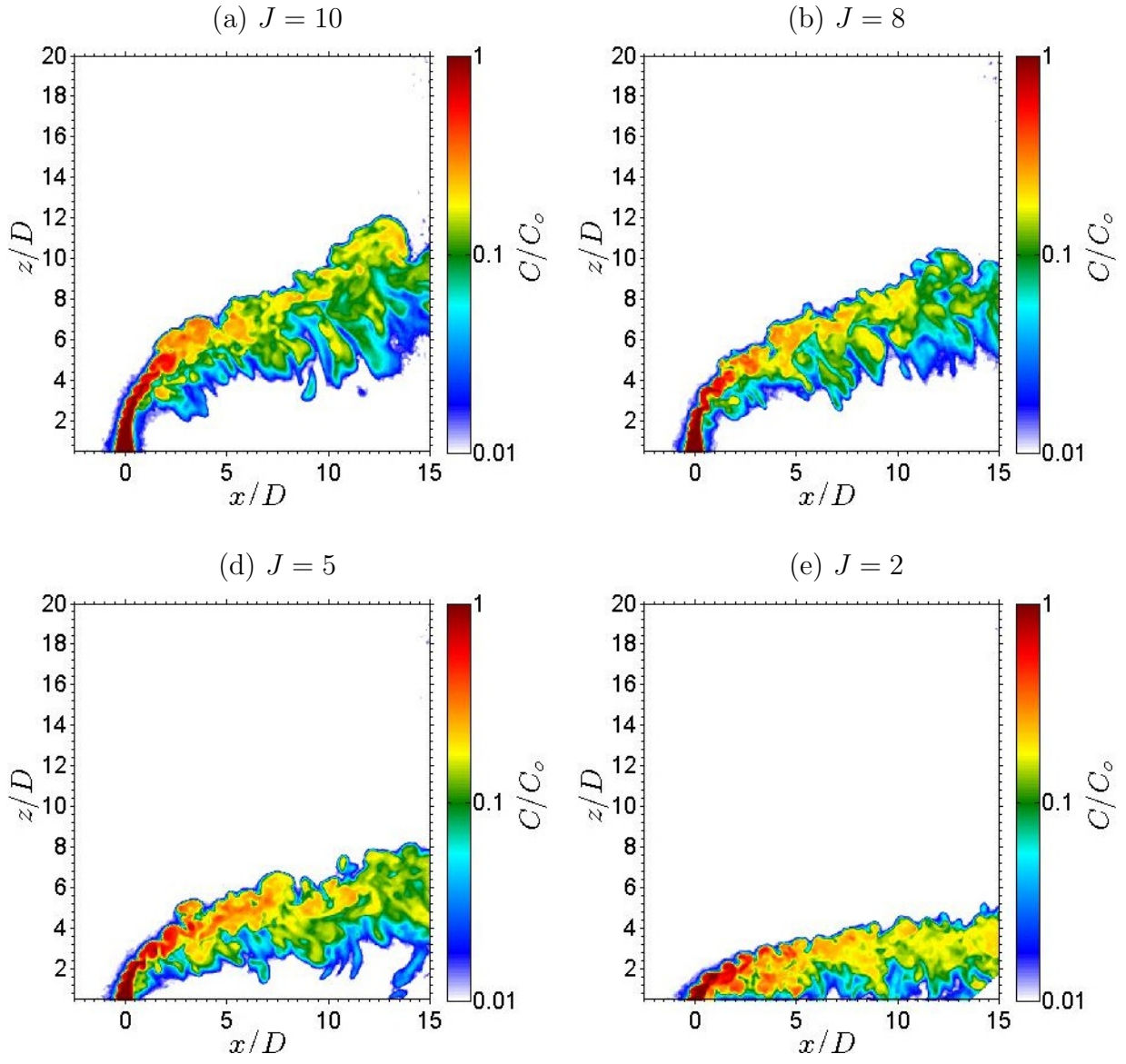


Figure B.2: Instantaneous centerplane (side view) acetone PLIF imaging of $S = 1.00$, flush nozzle-generated JICF with varying momentum flux ratios: (a) $J = 10$, (b) $J = 8$, (c) $J = 5$, (d) $J = 2$. Data shown in logarithmic scale.

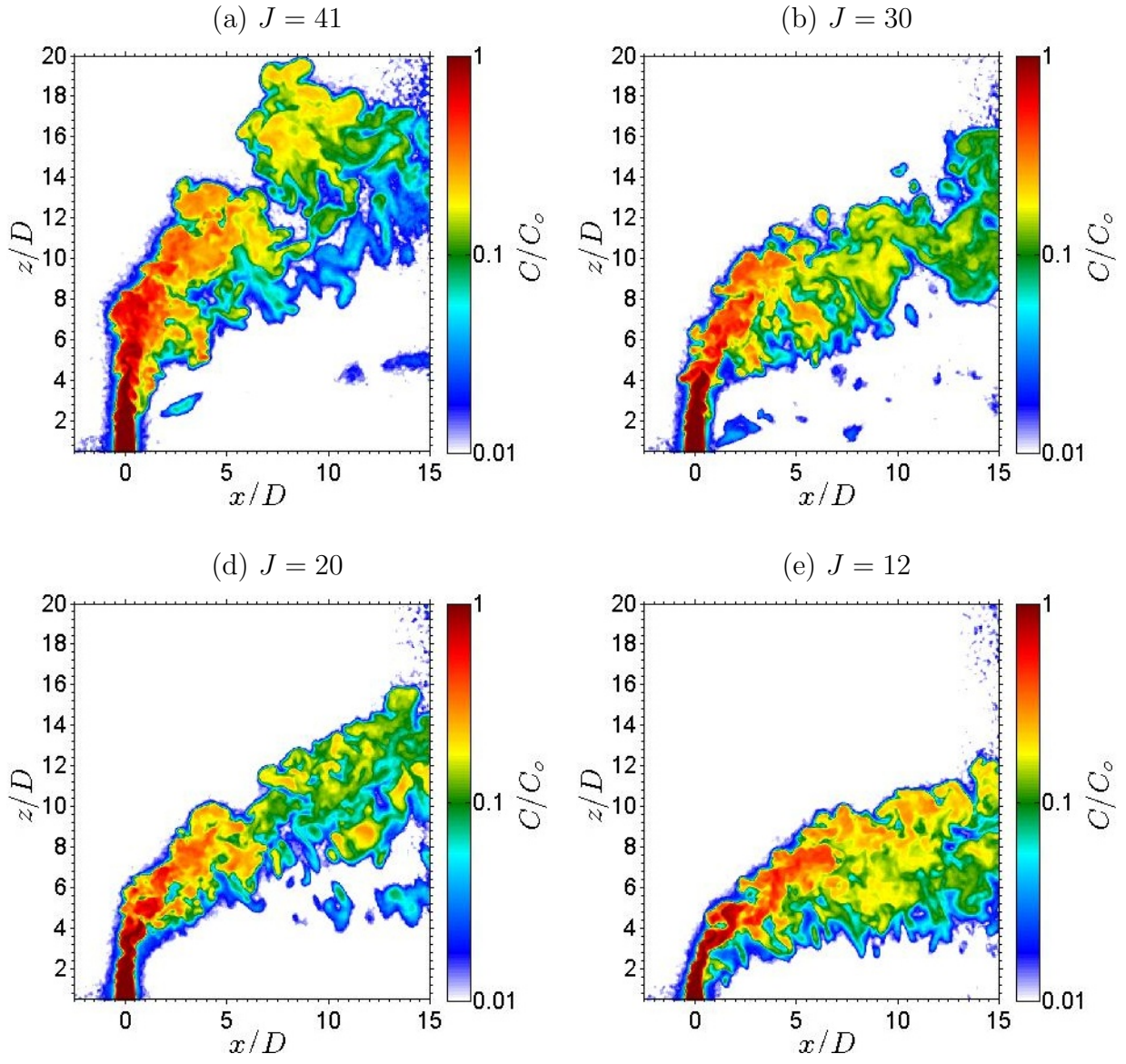


Figure B.3: Instantaneous centerplane (side view) acetone PLIF imaging of $S = 0.55$, flush nozzle-generated JICF with varying momentum flux ratios: (a) $J = 41$, (b) $J = 30$, (c) $J = 20$, (d) $J = 12$. Data shown in logarithmic scale.

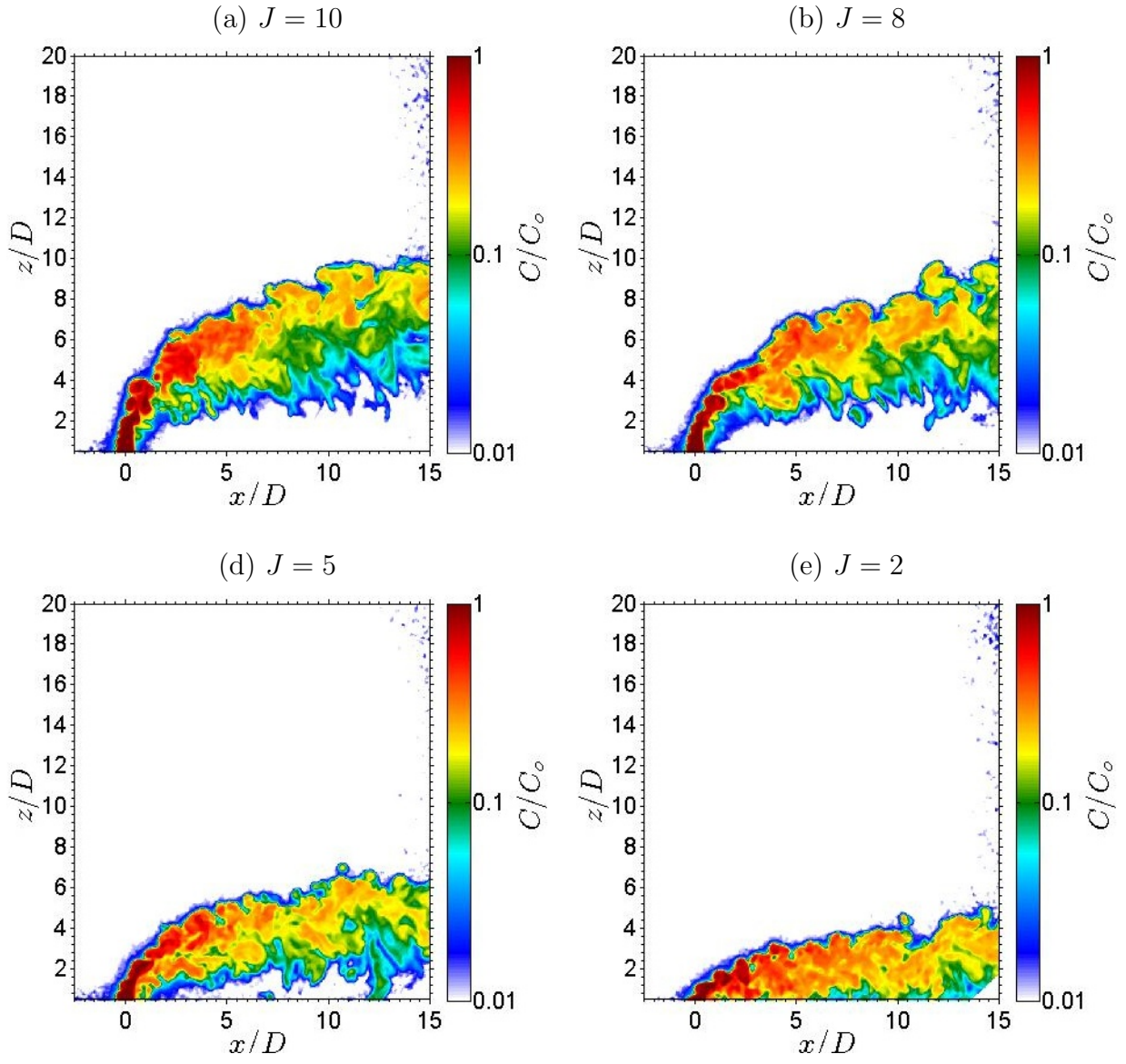


Figure B.4: Instantaneous centerplane (side view) acetone PLIF imaging of $S = 0.55$, flush nozzle-generated JICF with varying momentum flux ratios: (a) $J = 10$, (b) $J = 8$, (c) $J = 5$, (d) $J = 2$. Data shown in logarithmic scale.

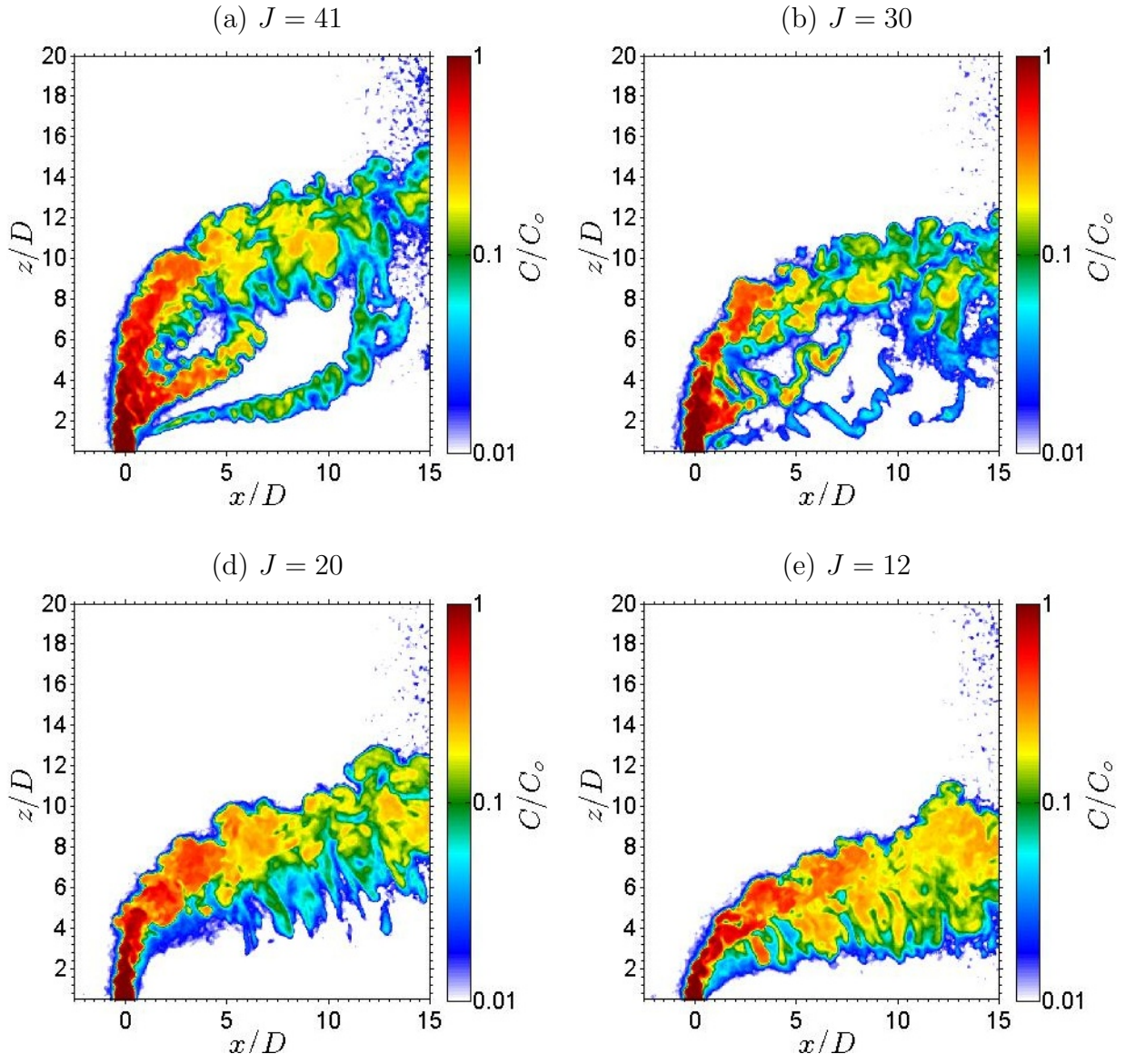


Figure B.5: Instantaneous centerplane (side view) acetone PLIF imaging of $S = 0.35$, flush nozzle-generated JICF with varying momentum flux ratios: (a) $J = 41$, (b) $J = 30$, (c) $J = 20$, (d) $J = 12$. Data shown in logarithmic scale.

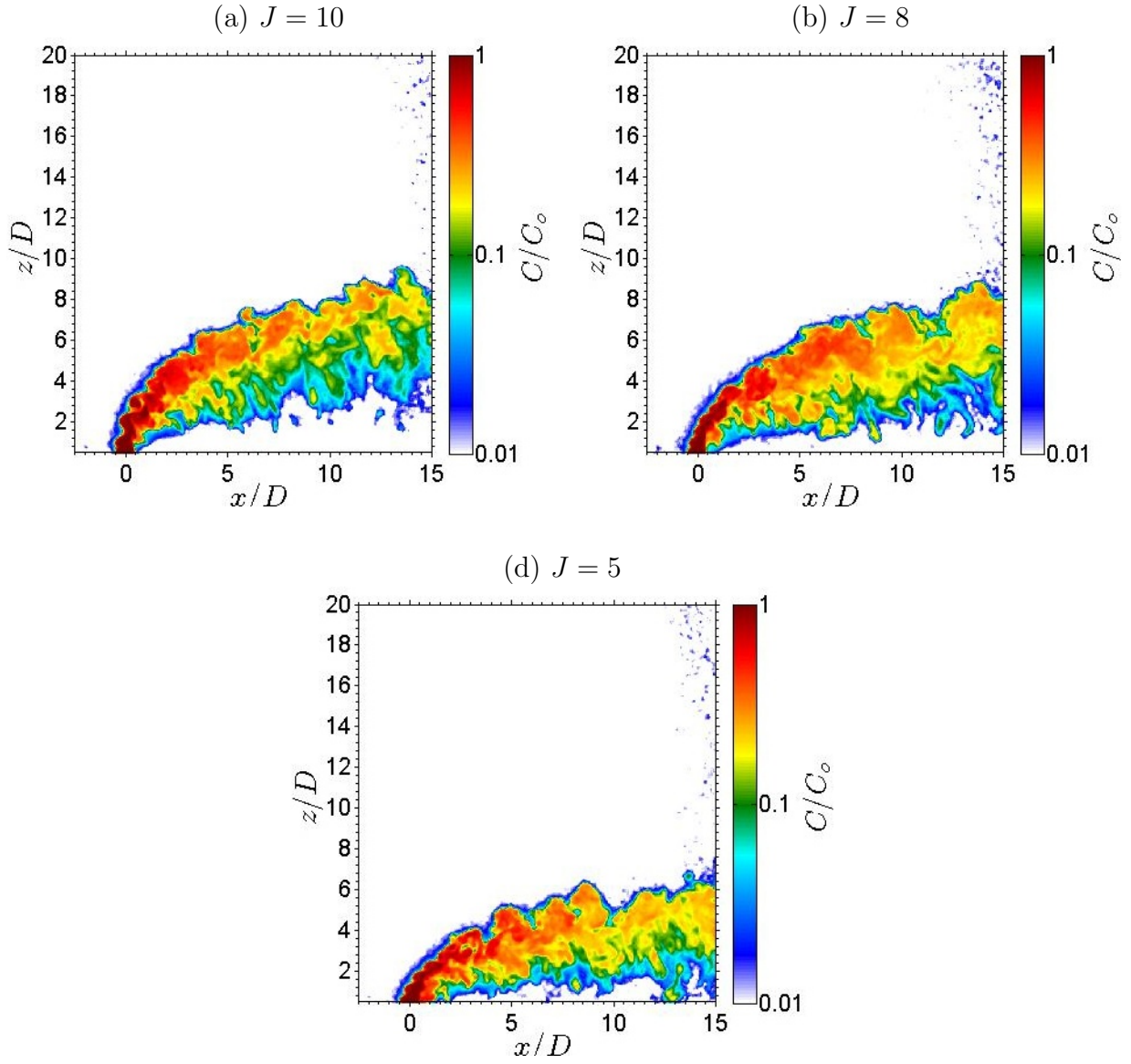


Figure B.6: Instantaneous centerplane (side view) acetone PLIF imaging of $S = 0.35$, flush nozzle-generated JICF with varying momentum flux ratios: (a) $J = 10$, (b) $J = 8$, (c) $J = 5$. Data shown in logarithmic scale.

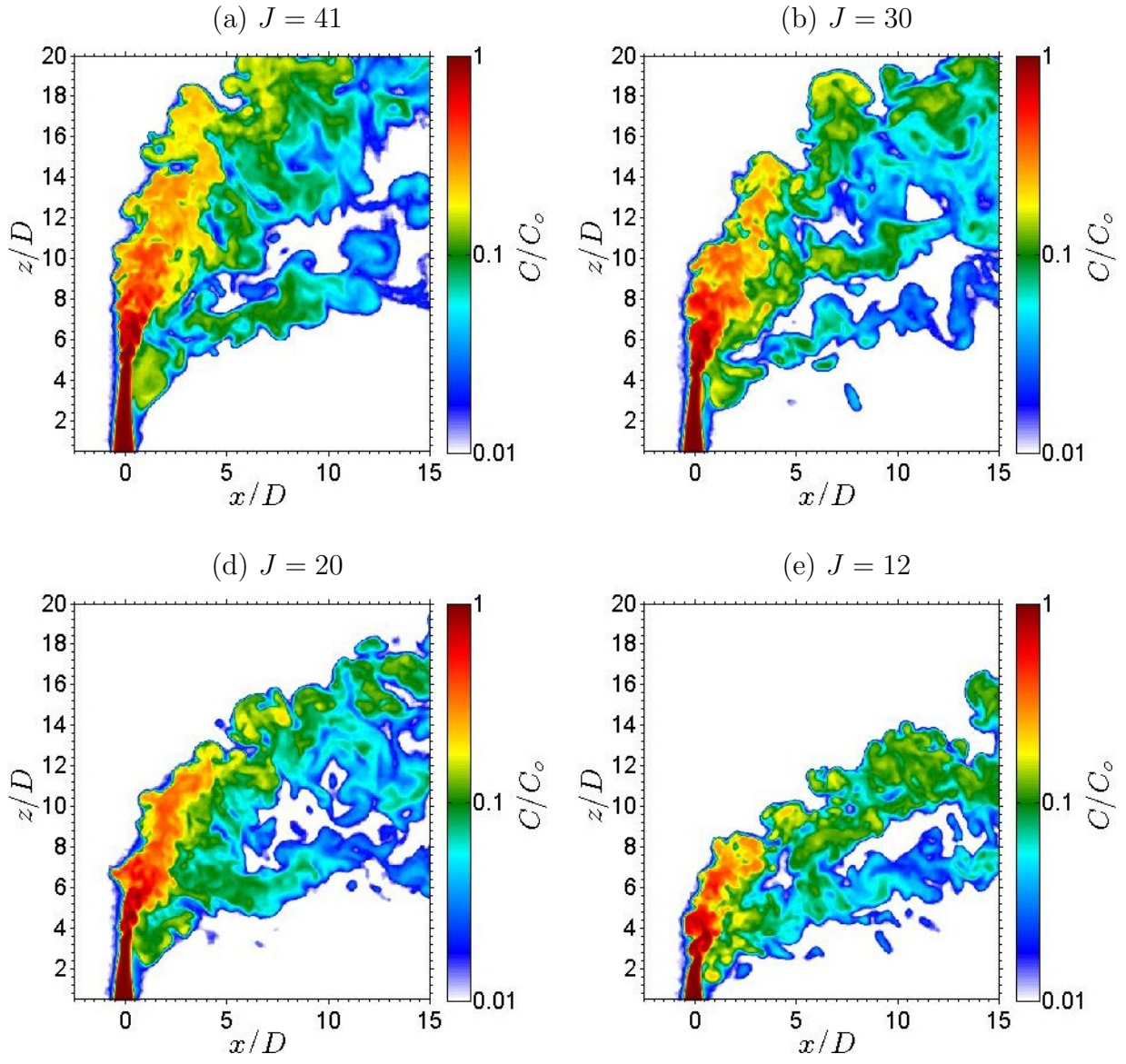


Figure B.7: Instantaneous centerplane (side view) acetone PLIF imaging of $S = 1.00$, flush pipe-generated JICF with varying momentum flux ratios: (a) $J = 41$, (b) $J = 30$, (c) $J = 20$, (d) $J = 12$. Data shown in logarithmic scale.

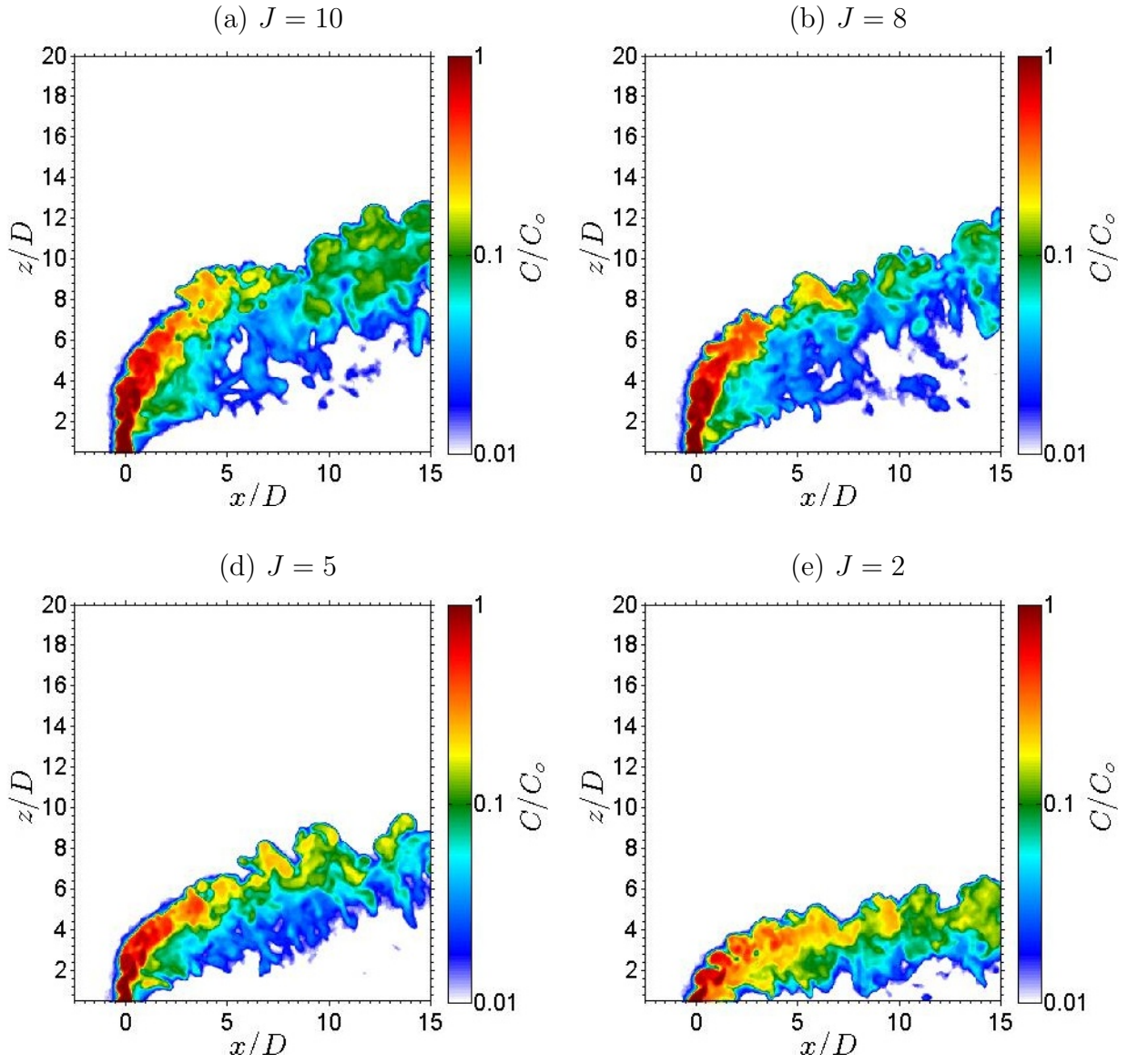


Figure B.8: Instantaneous centerplane (side view) acetone PLIF imaging of $S = 1.00$, flush pipe-generated JICF with varying momentum flux ratios: (a) $J = 10$, (b) $J = 8$, (c) $J = 5$, (d) $J = 2$. Data shown in logarithmic scale.

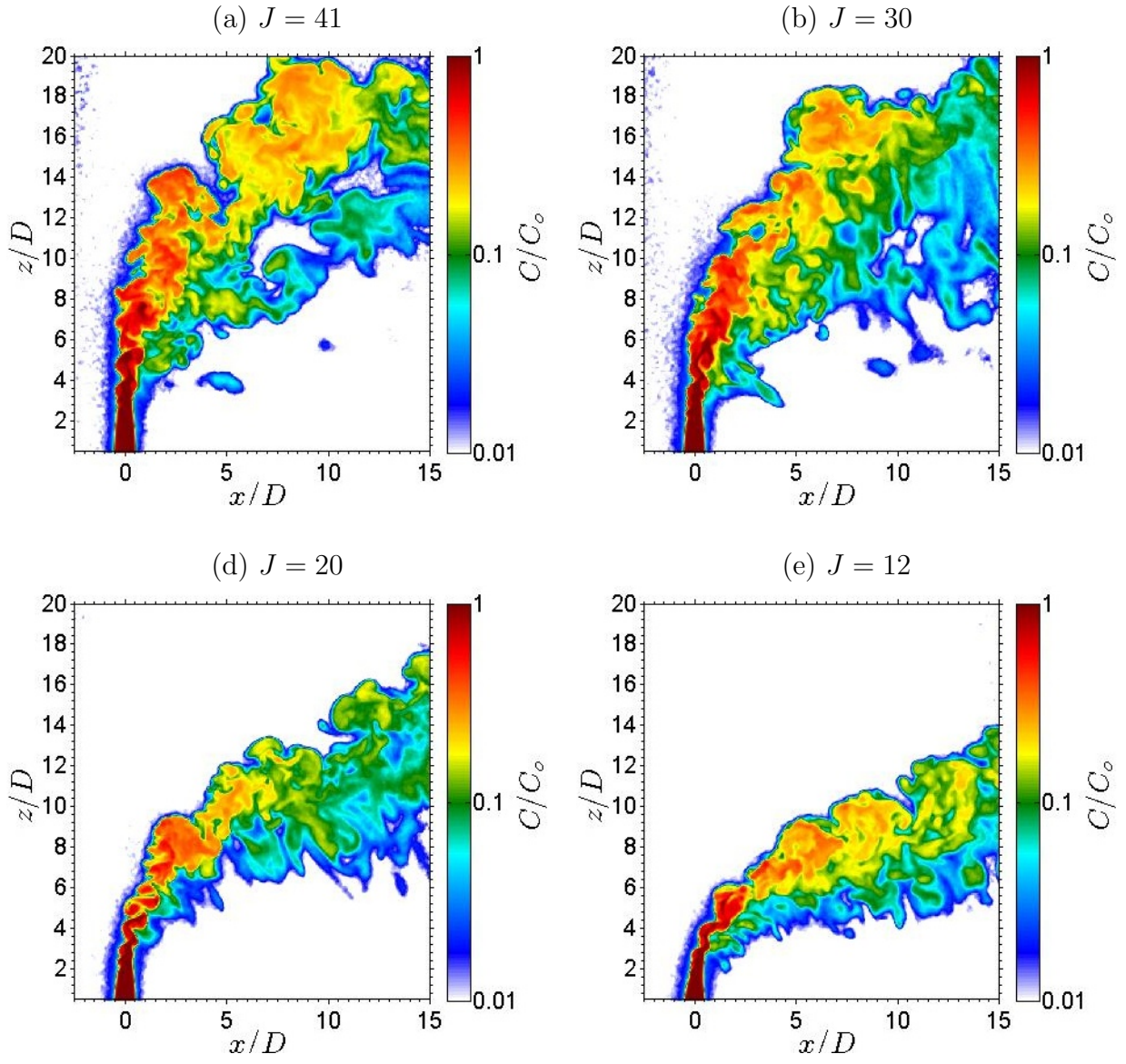


Figure B.9: Instantaneous centerplane (side view) acetone PLIF imaging of $S = 1.00$, elevated nozzle-generated JICF with varying momentum flux ratios: (a) $J = 41$, (b) $J = 30$, (c) $J = 20$, (d) $J = 12$. Data shown in logarithmic scale.

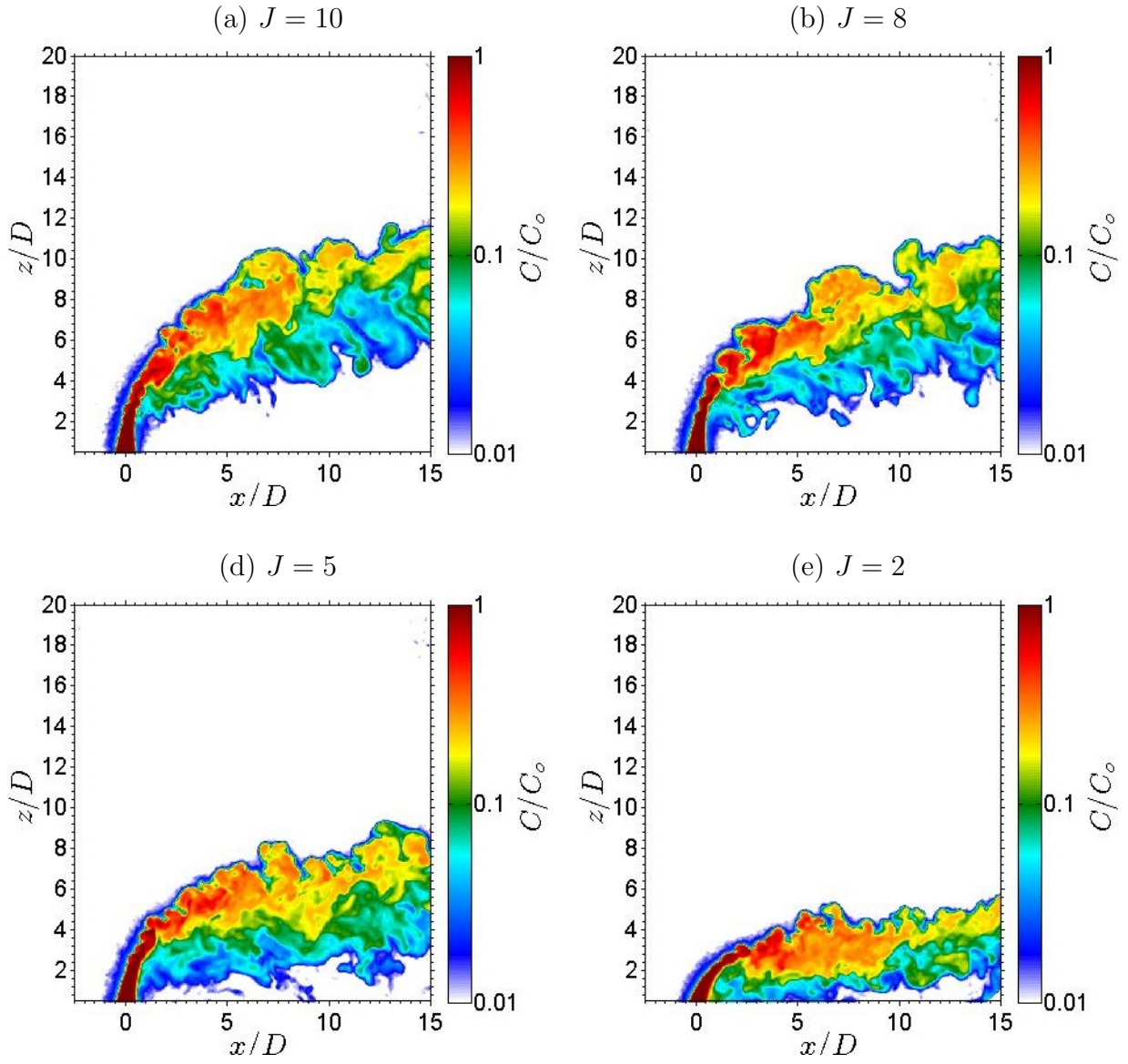


Figure B.10: Instantaneous centerplane (side view) acetone PLIF imaging of $S = 1.00$, elevated nozzle-generated JICF with varying momentum flux ratios: (a) $J = 10$, (b) $J = 8$, (c) $J = 5$, (d) $J = 2$. Data shown in logarithmic scale.

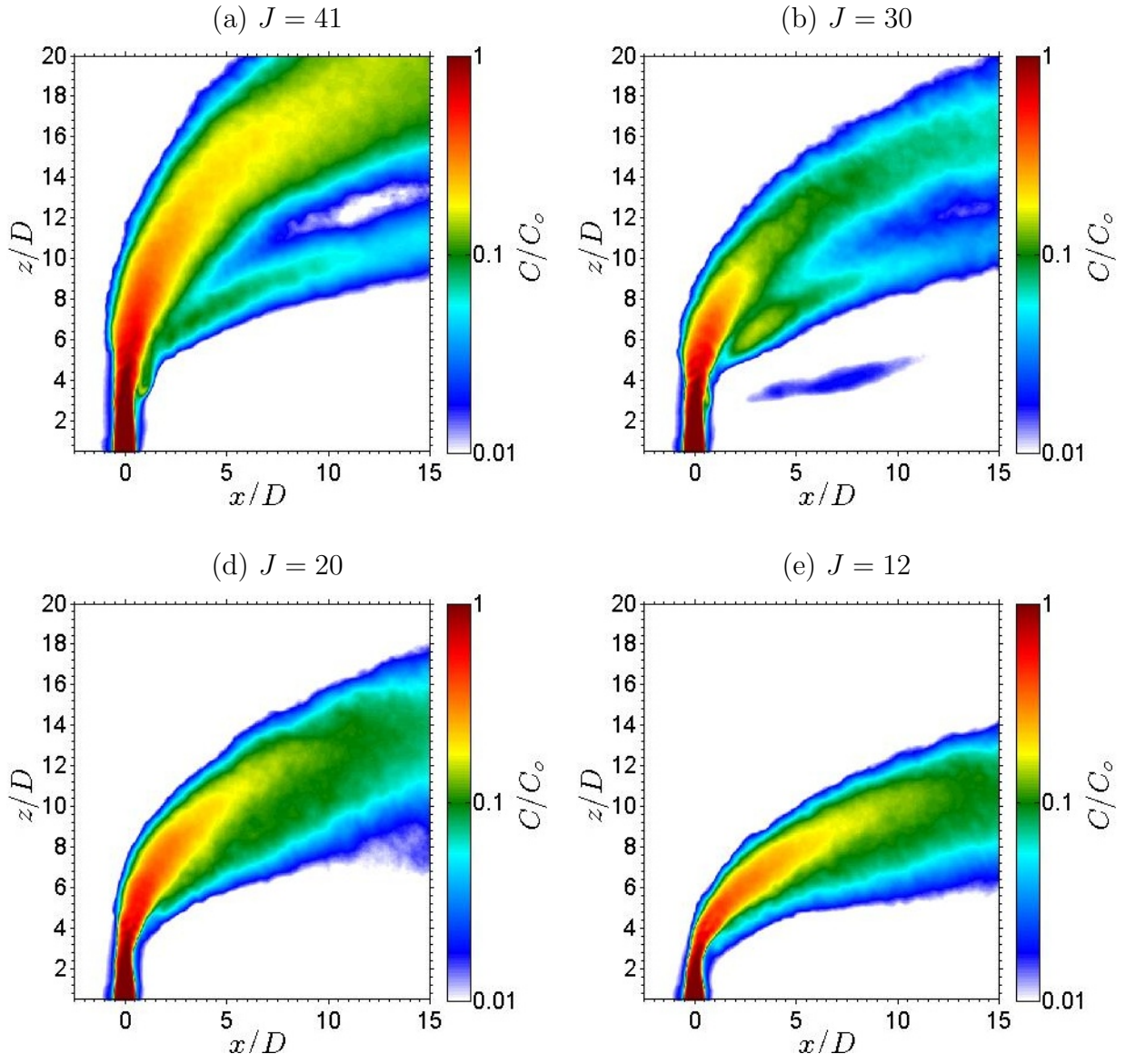


Figure B.11: Mean centerplane (side view) acetone PLIF imaging of $S = 1.00$, flush nozzle-generated JICF with varying momentum flux ratios: (a) $J = 41$, (b) $J = 30$, (c) $J = 20$, (d) $J = 12$. Data shown in logarithmic scale.

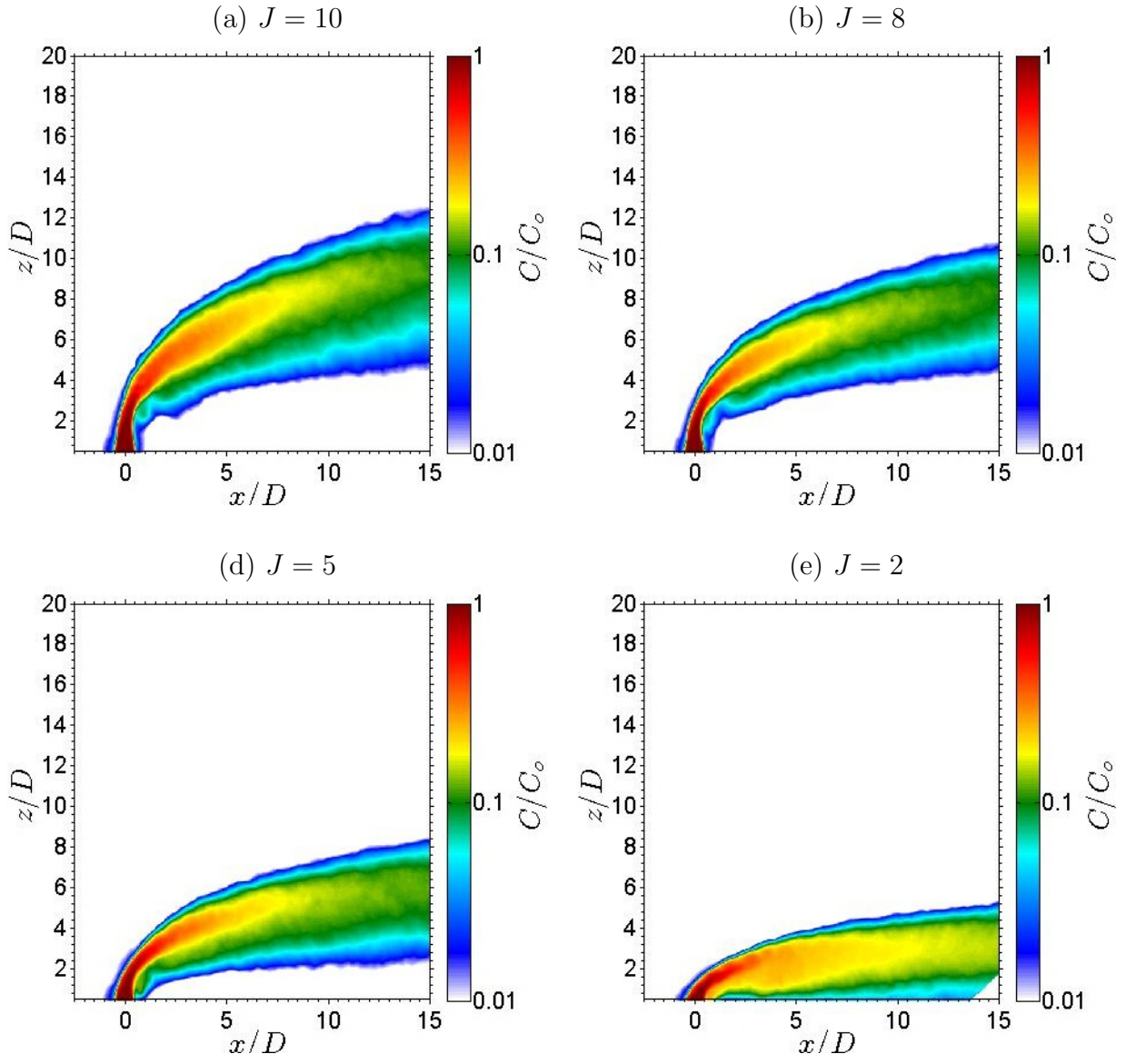


Figure B.12: Mean centerplane (side view) acetone PLIF imaging of $S = 1.00$, flush nozzle-generated JICF with varying momentum flux ratios: (a) $J = 10$, (b) $J = 8$, (c) $J = 5$, (d) $J = 2$. Data shown in logarithmic scale.

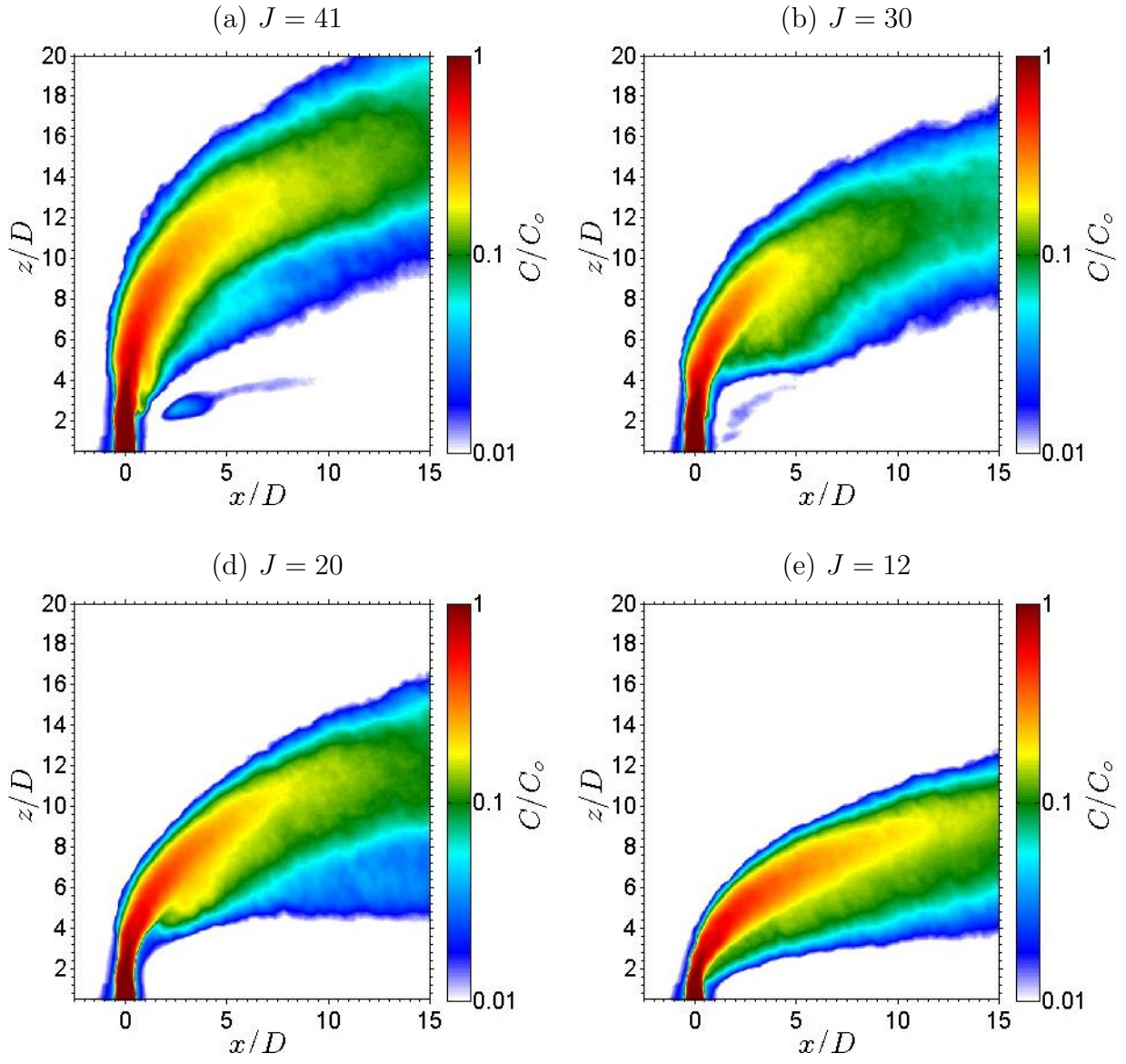


Figure B.13: Mean centerplane (side view) acetone PLIF imaging of $S = 0.55$, flush nozzle-generated JICF with varying momentum flux ratios: (a) $J = 41$, (b) $J = 30$, (c) $J = 20$, (d) $J = 12$. Data shown in logarithmic scale.

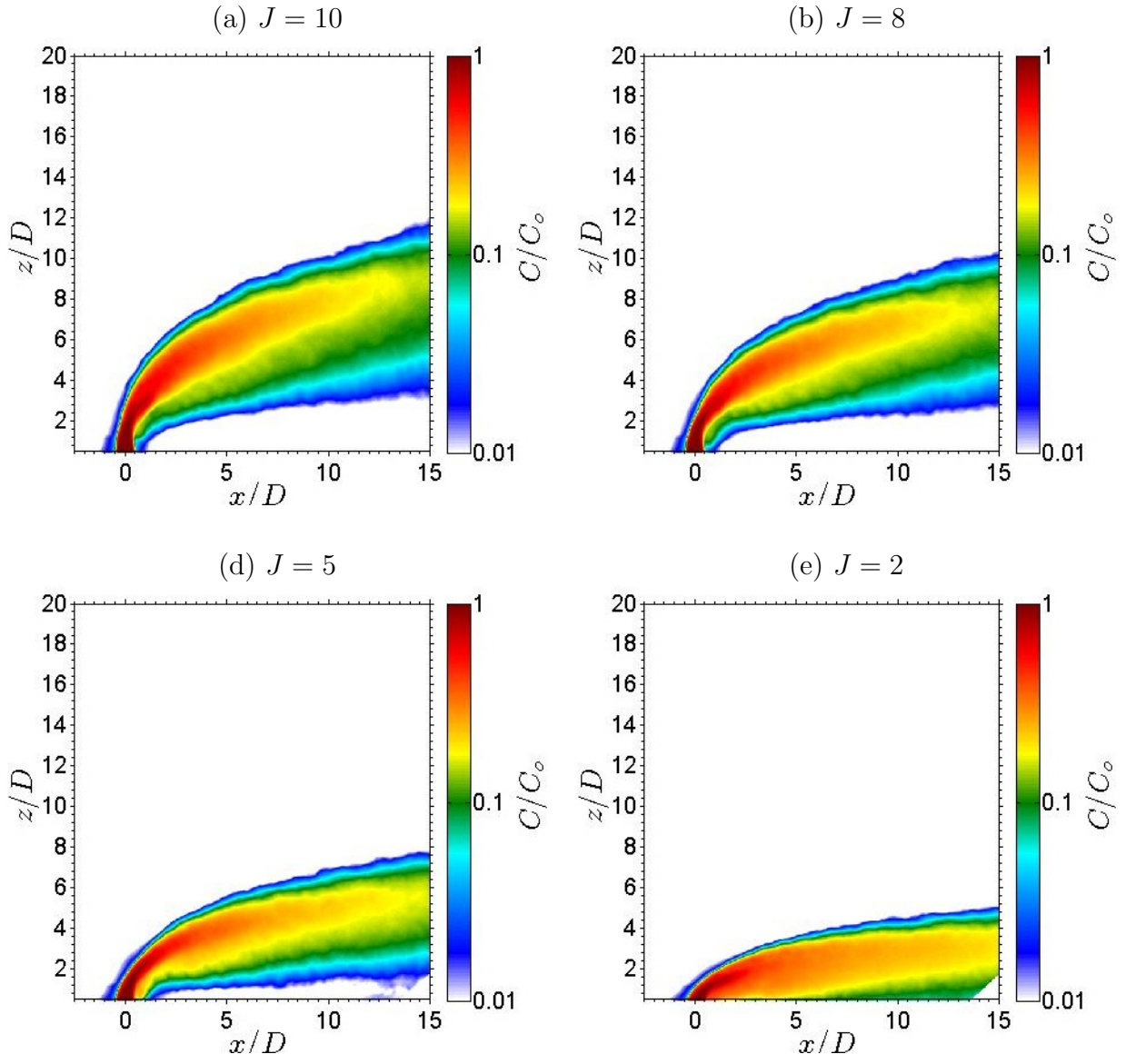


Figure B.14: Mean centerplane (side view) acetone PLIF imaging of $S = 0.55$, flush nozzle-generated JICF with varying momentum flux ratios: (a) $J = 10$, (b) $J = 8$, (c) $J = 5$, (d) $J = 2$. Data shown in logarithmic scale.

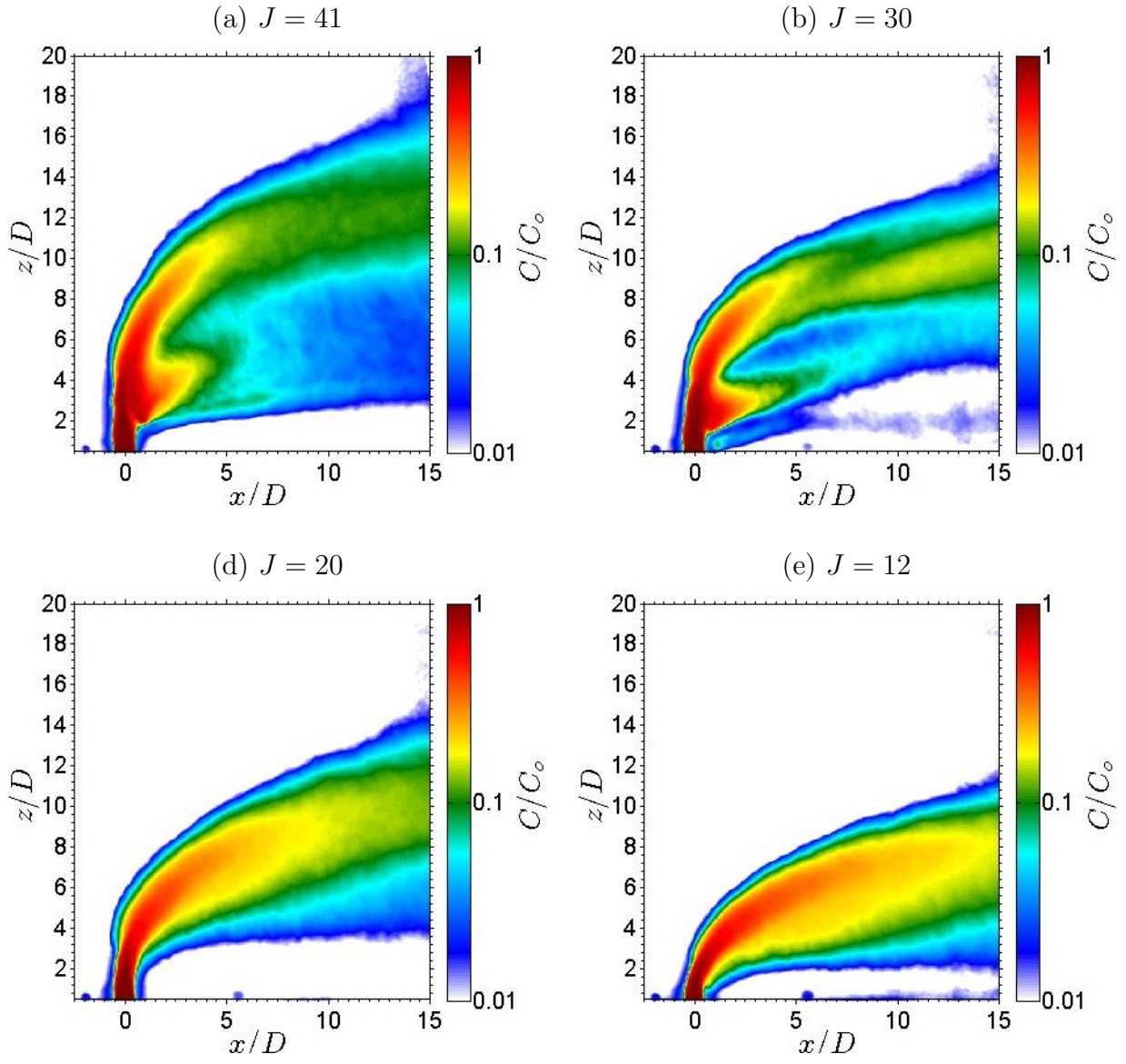


Figure B.15: Mean centerplane (side view) acetone PLIF imaging of $S = 0.35$, flush nozzle-generated JICF with varying momentum flux ratios: (a) $J = 41$, (b) $J = 30$, (c) $J = 20$, (d) $J = 12$. Data shown in logarithmic scale.

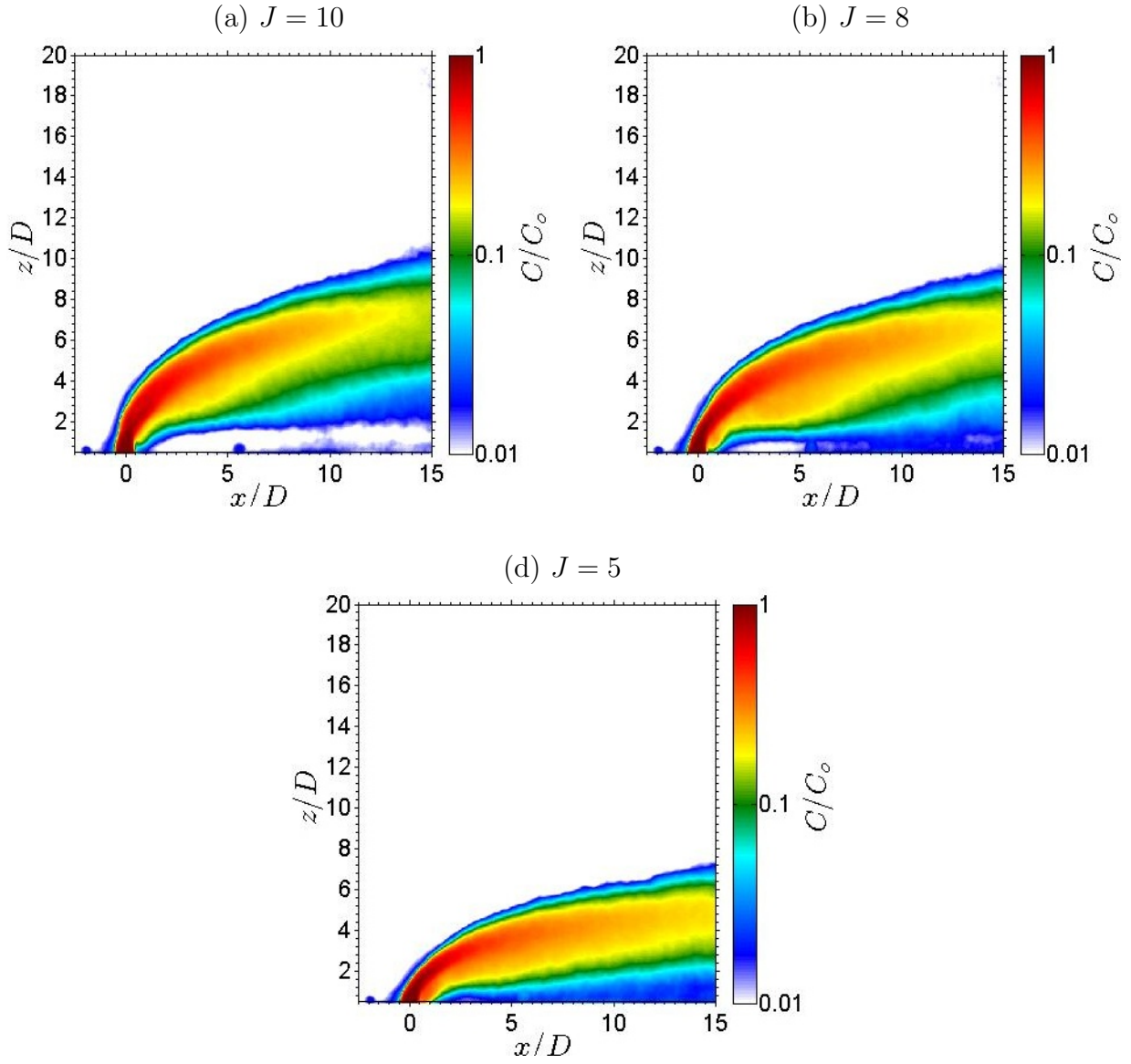


Figure B.16: Mean centerplane (side view) acetone PLIF imaging of $S = 0.35$, flush nozzle-generated JICF with varying momentum flux ratios: (a) $J = 10$, (b) $J = 8$, (c) $J = 5$. Data shown in logarithmic scale.

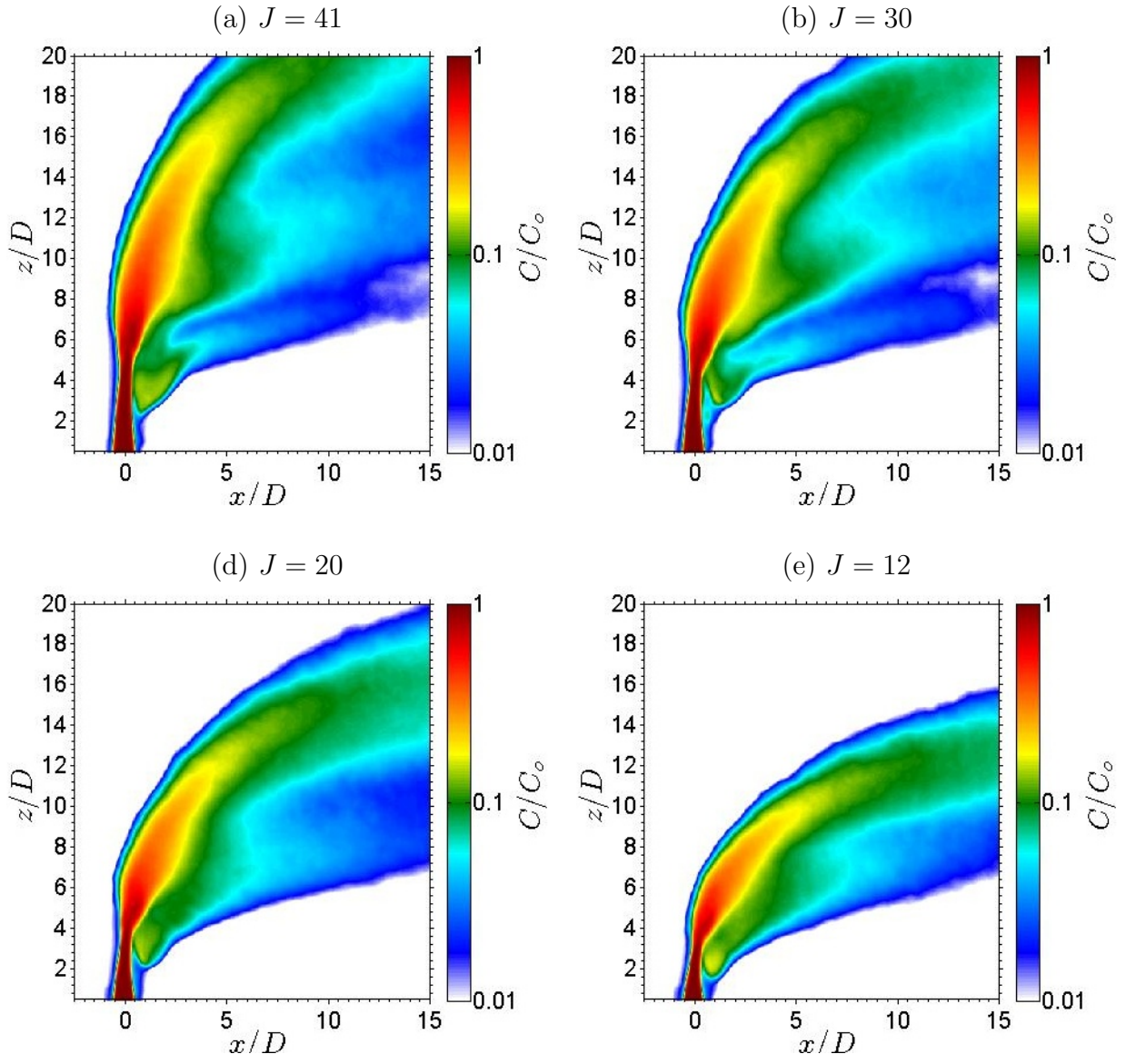


Figure B.17: Mean centerplane (side view) acetone PLIF imaging of $S = 1.00$, flush pipe-generated JICF with varying momentum flux ratios: (a) $J = 41$, (b) $J = 30$, (c) $J = 20$, (d) $J = 12$. Data shown in logarithmic scale.

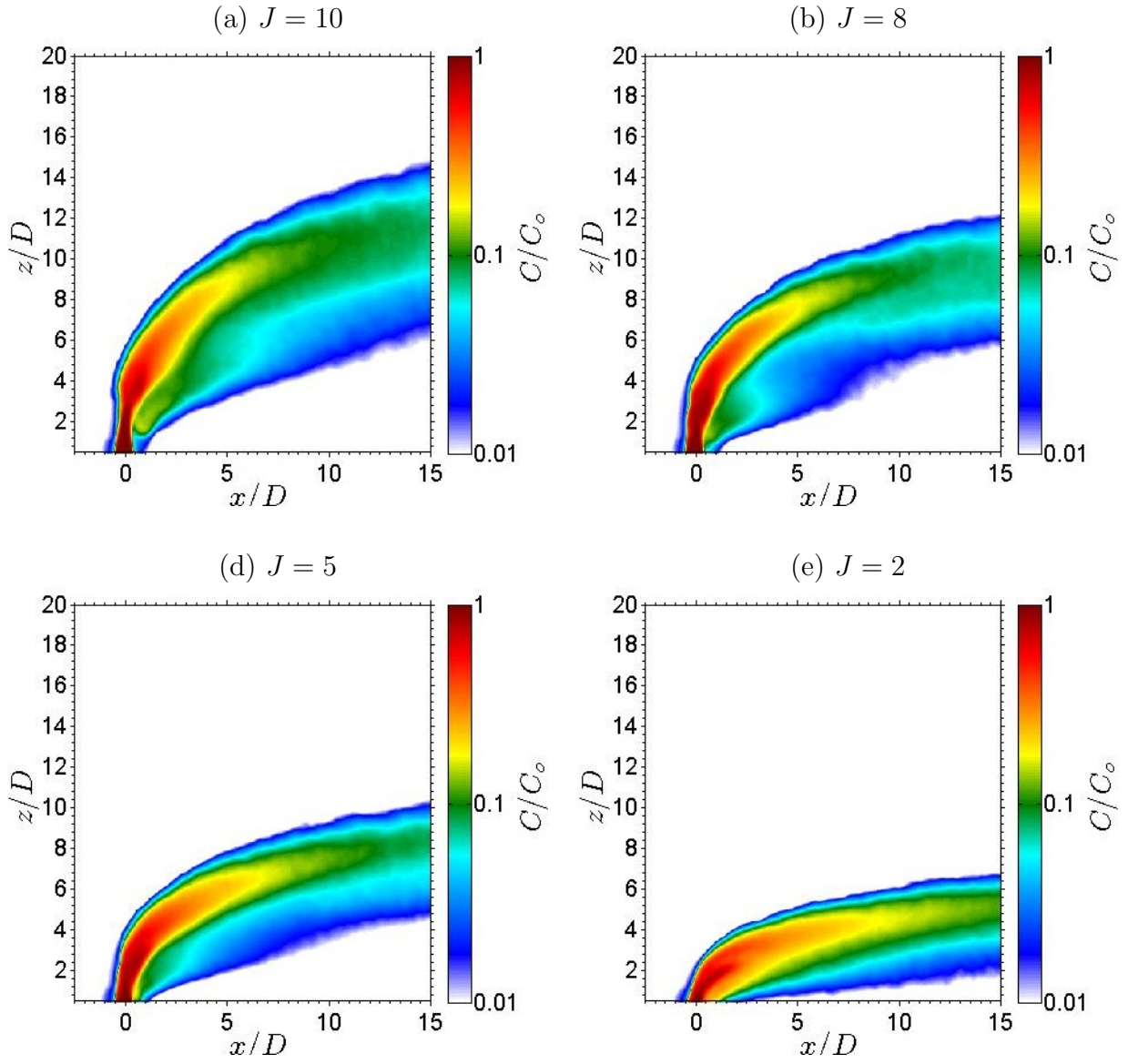


Figure B.18: Mean centerplane (side view) acetone PLIF imaging of $S = 1.00$, flush pipe-generated JICF with varying momentum flux ratios: (a) $J = 10$, (b) $J = 8$, (c) $J = 5$, (d) $J = 2$. Data shown in logarithmic scale.

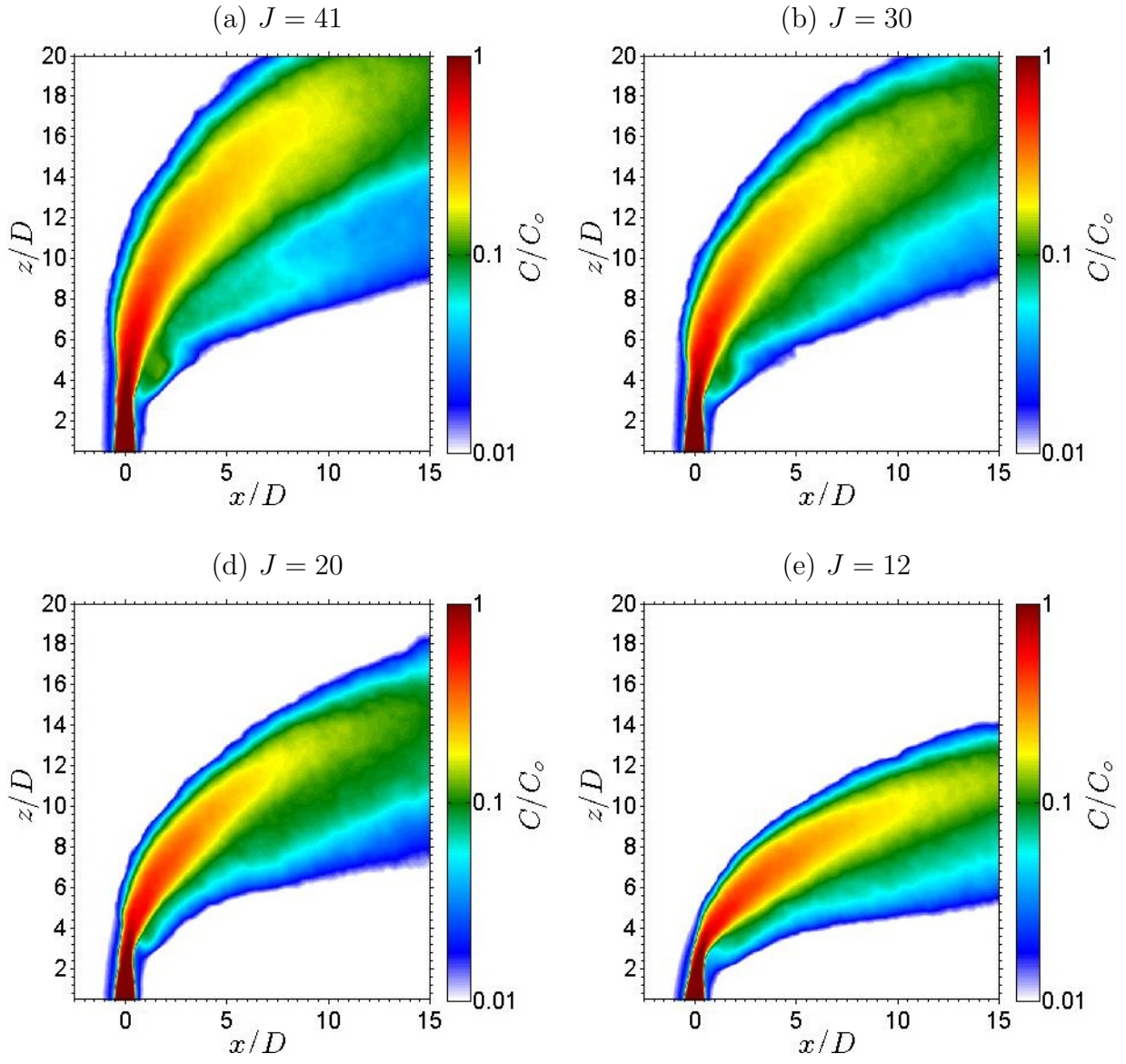


Figure B.19: Mean centerplane (side view) acetone PLIF imaging of $S = 1.00$, elevated nozzle-generated JICF with varying momentum flux ratios: (a) $J = 41$, (b) $J = 30$, (c) $J = 20$, (d) $J = 12$. Data shown in logarithmic scale.

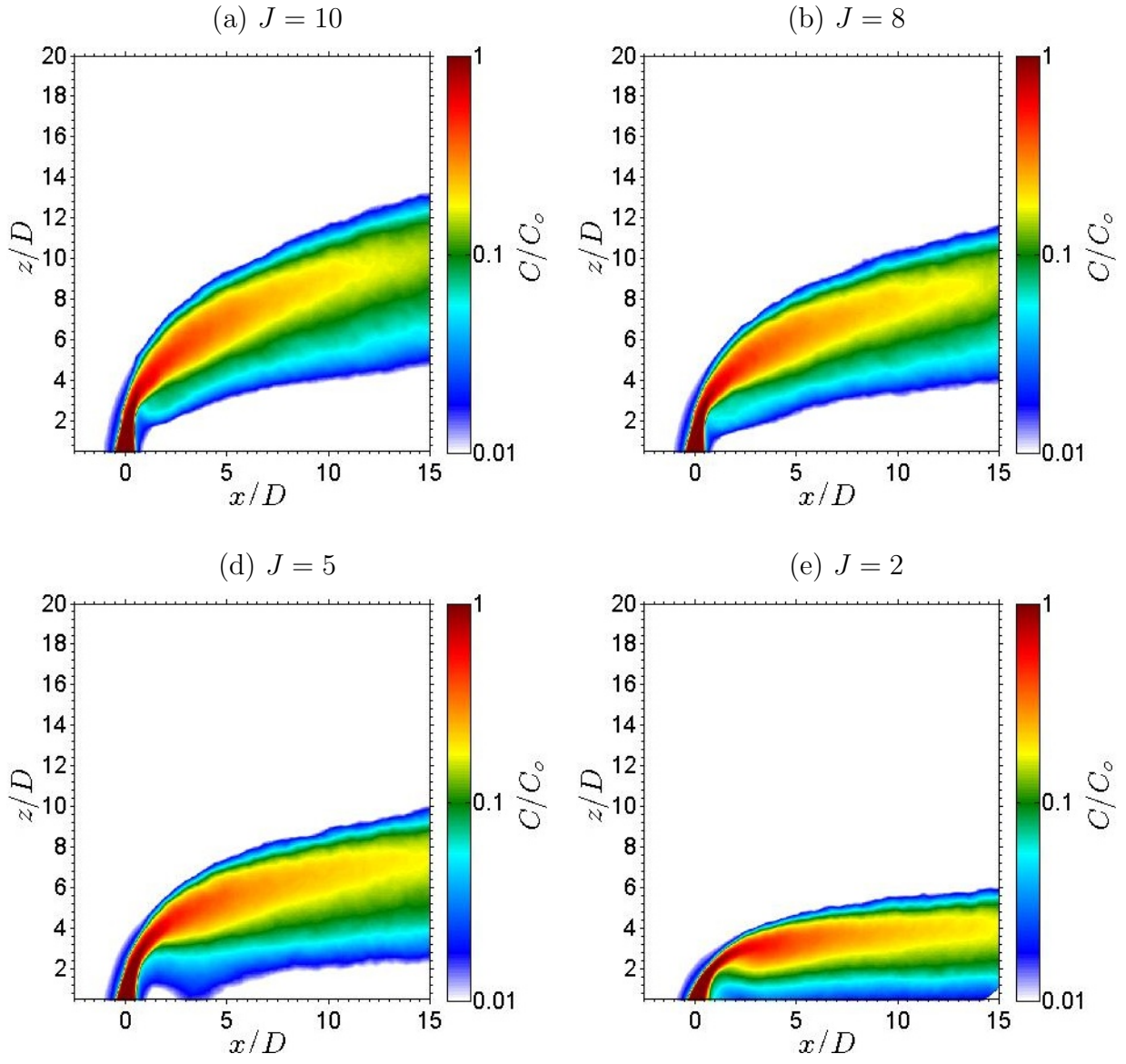


Figure B.20: Mean centerplane (side view) acetone PLIF imaging of $S = 1.00$, elevated nozzle-generated JICF with varying momentum flux ratios: (a) $J = 10$, (b) $J = 8$, (c) $J = 5$, (d) $J = 2$. Data shown in logarithmic scale.

APPENDIX C

Additional Instantaneous High Resolution Centerplane Scalar Field Data

The following results correspond to additional high resolution data sets for centerplane-based PLIF images of the transverse jet. These are intended to supplement images shown in Chapter 4.

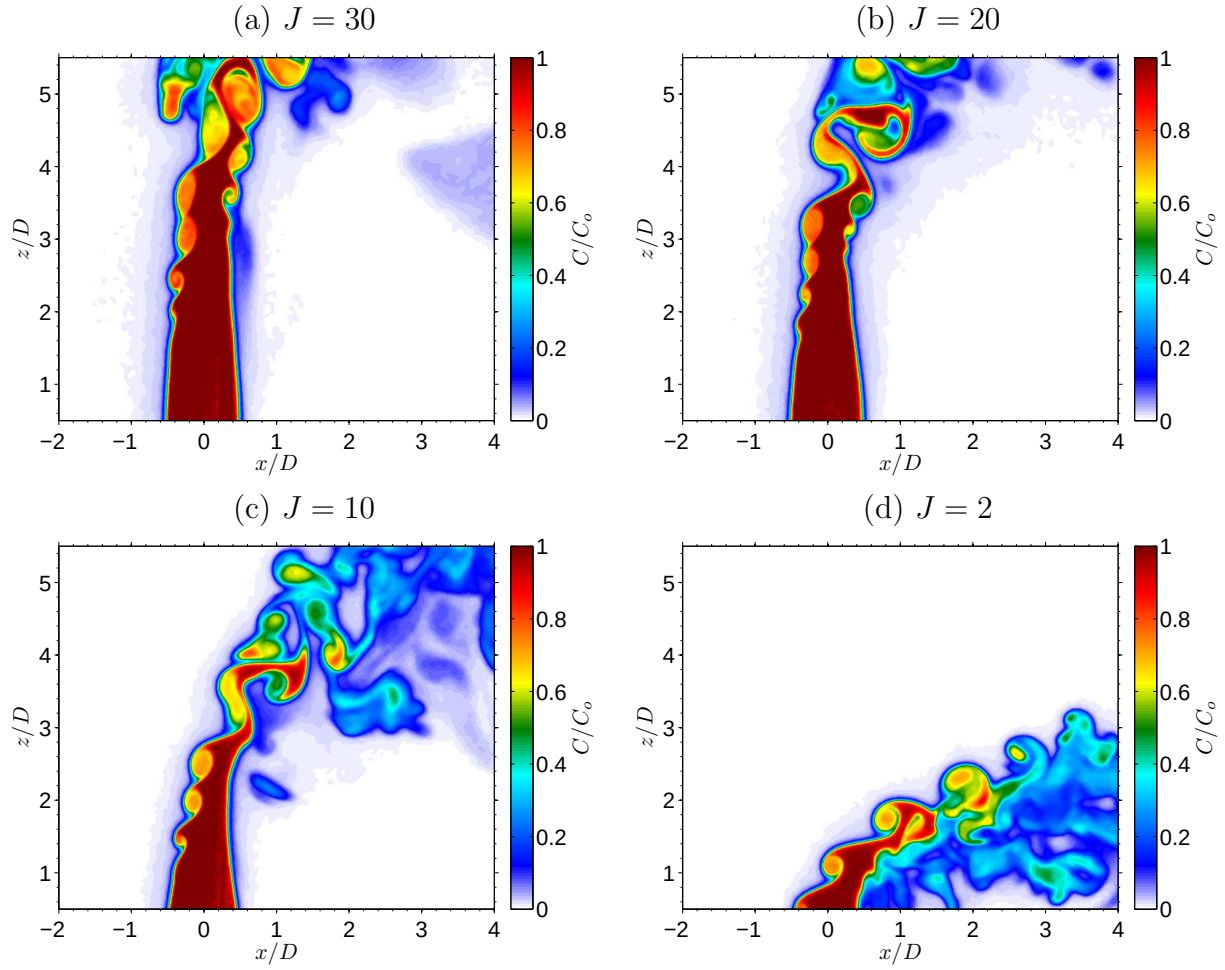


Figure C.1: Instantaneous high-resolution centerplane (side view) acetone PLIF imaging of $S = 1.00$, flush nozzle-generated JICF with (a) $J = 30$, (b) $J = 20$, (c) $J = 10$, (d) $J = 2$.

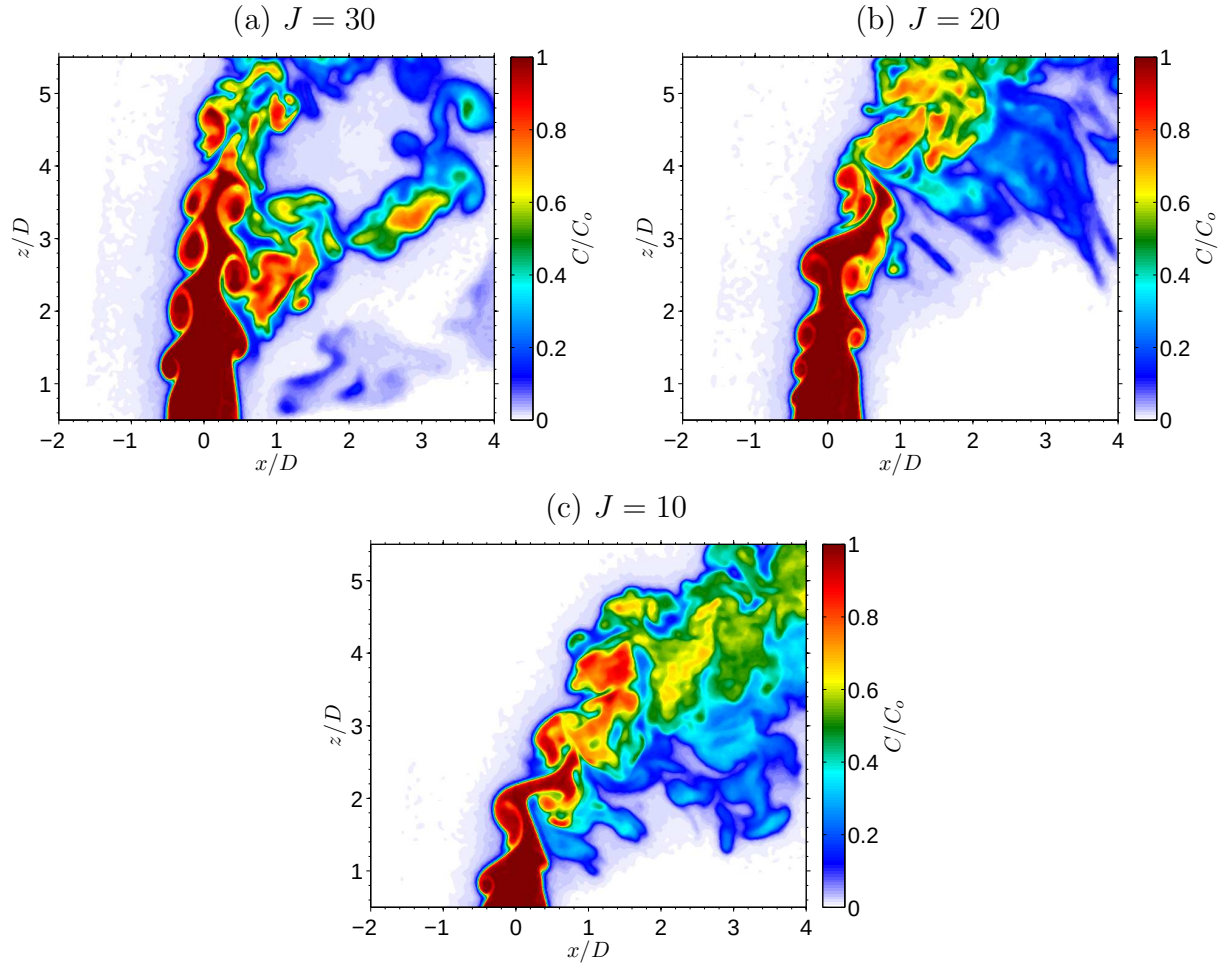


Figure C.2: Instantaneous high-resolution centerplane (side view) acetone PLIF imaging of $S = 0.35$, flush nozzle-generated JICF with (a) $J = 30$, (b) $J = 20$, (c) $J = 10$.

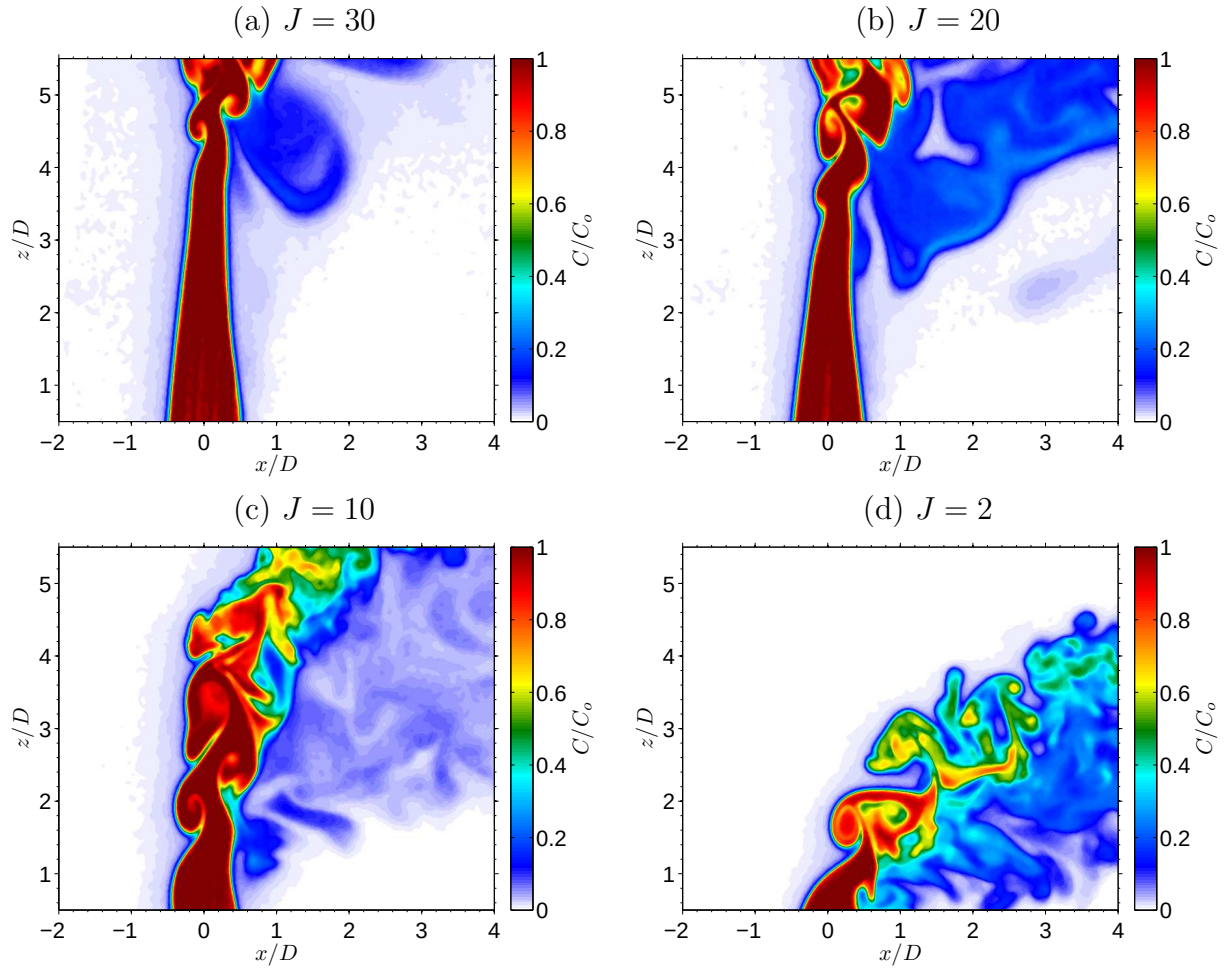


Figure C.3: Instantaneous high-resolution centerplane (side view) acetone PLIF imaging of $S = 1.00$, flush pipe-generated JICF with varying momentum flux ratios (a) $J = 30$, (b) $J = 20$, (c) $J = 10$, (d) $J = 2$.

APPENDIX D

Simultaneous PLIF/PIV Data

The following results correspond to additional data sets that are extracted from simultaneous PLIF/PIV measurements in the centerplane of the transverse jet. Vorticity and scalar gradient images, as well as velocity components in multiple dimensions, are shown. These are designed to supplement images shown in Chapter 5.

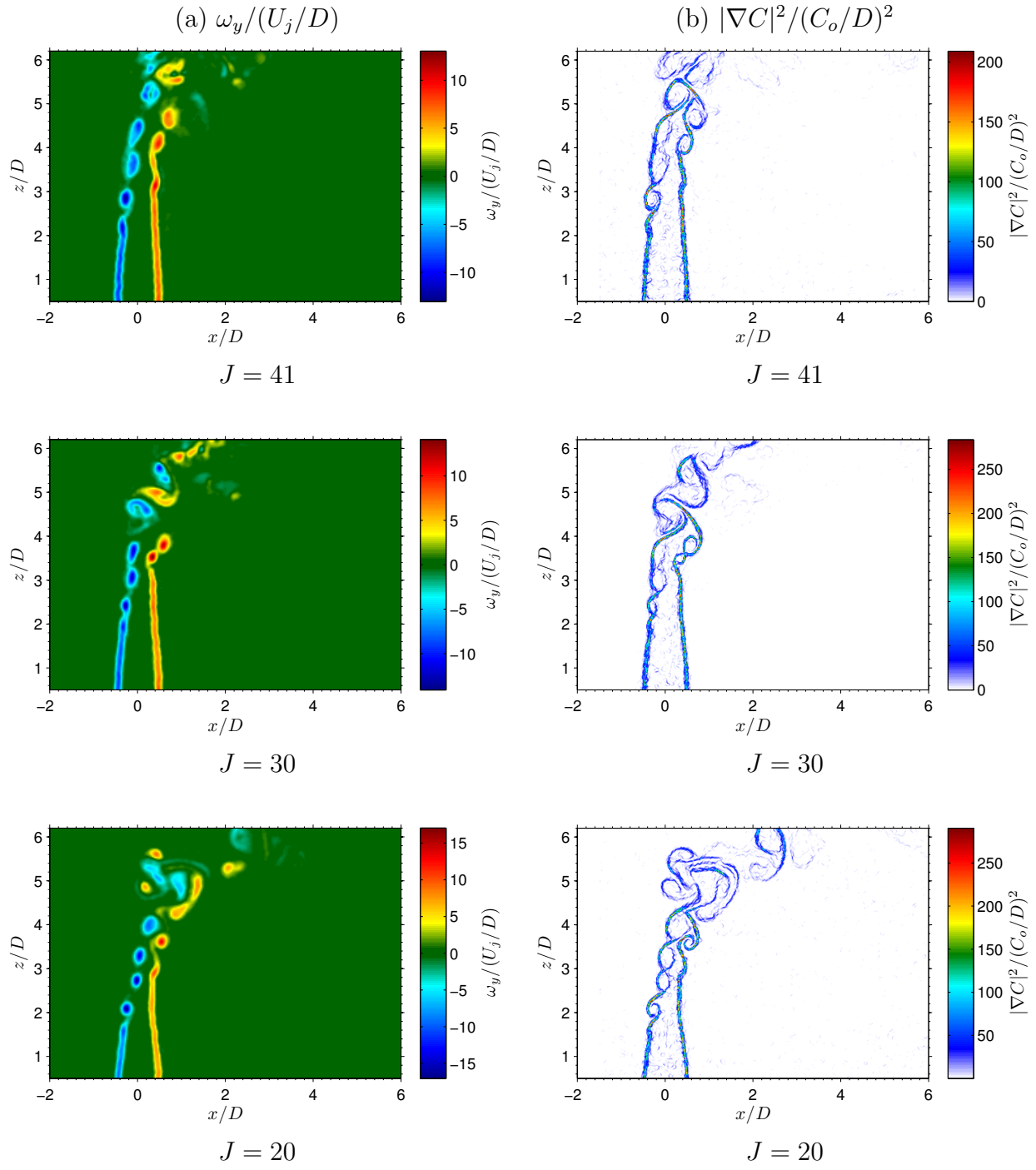


Figure D.1: Instantaneous centerplane (side view) simultaneous PLIF/PIV imaging of $S = 1.00$, flush nozzle-generated JICF with varying momentum flux ratios: $J = 41$ (top row), $J = 30$ (middle row), $J = 20$ (bottom row). Data shown for (a) scaled vorticity $\omega_y/(U_j/D)$ and (b) scaled jet fluid concentration gradient magnitude $|\nabla C|^2/(C_o/D)^2$.

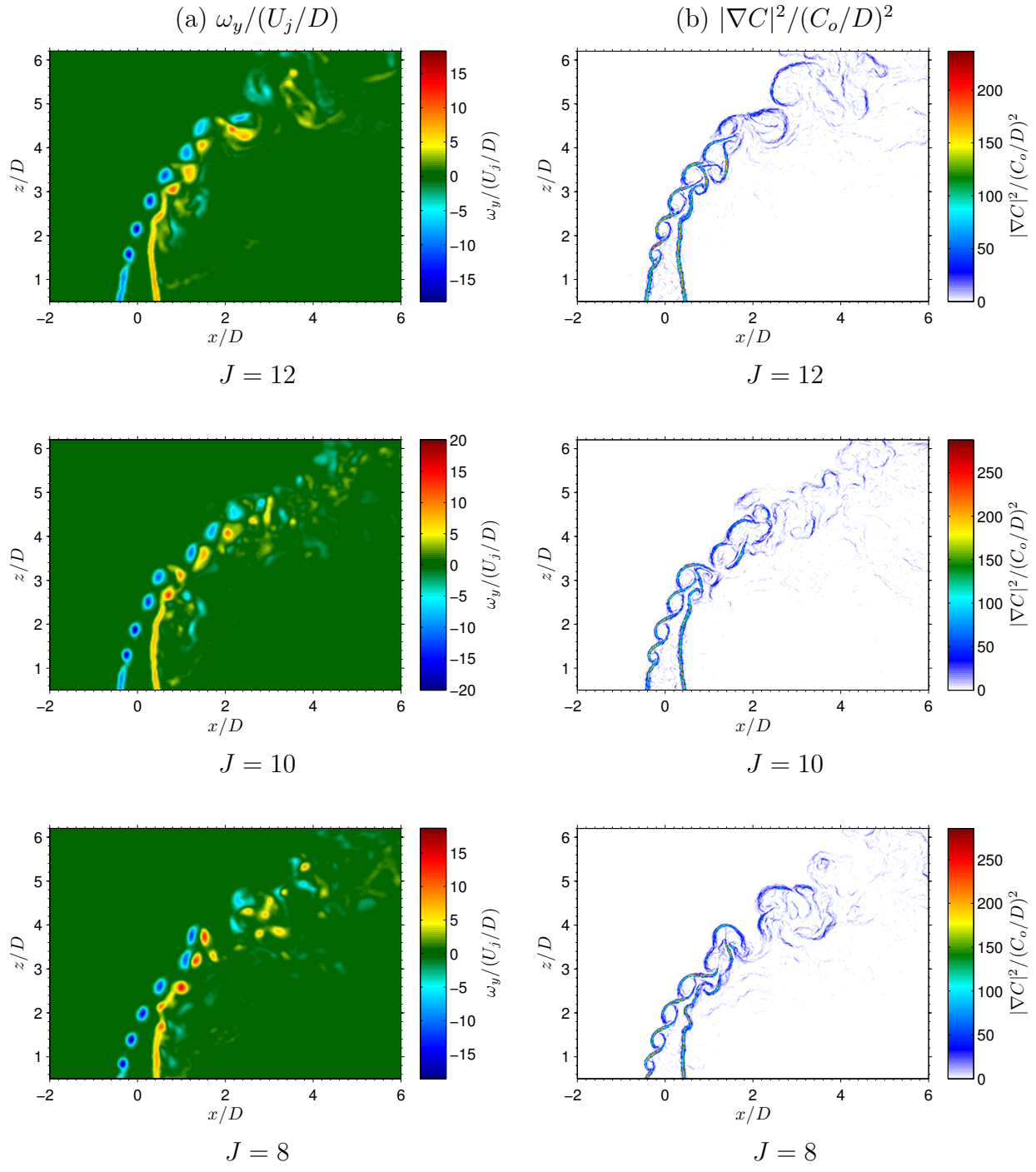


Figure D.2: Instantaneous centerplane (side view) simultaneous PLIF/PIV imaging of $S = 1.00$, flush nozzle-generated JICF with varying momentum flux ratios: $J = 12$ (top row), $J = 10$ (middle row), $J = 8$ (bottom row). Data shown for (a) scaled vorticity $\omega_y/(U_j/D)$ and (b) scaled jet fluid concentration gradient magnitude $|\nabla C|^2/(C_o/D)^2$.

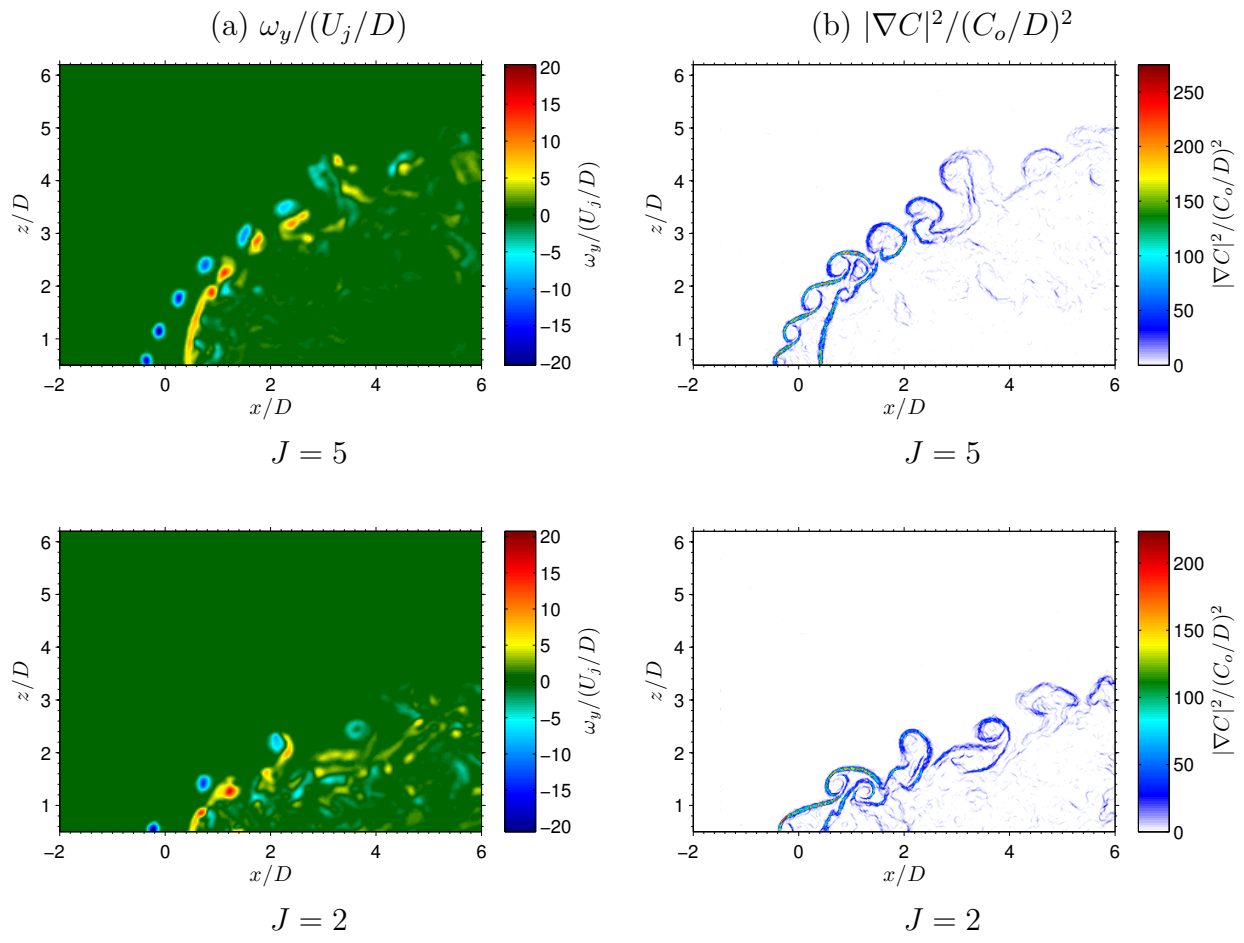


Figure D.3: Instantaneous centerplane (side view) simultaneous PLIF/PIV imaging of $S = 1.00$, flush nozzle-generated JICF with varying momentum flux ratios: $J = 5$ (top row), $J = 2$ (bottom row). Data shown for (a) scaled vorticity $\omega_y/(U_j/D)$ and (b) scaled jet fluid concentration gradient magnitude $|\nabla C|^2/(C_o/D)^2$.

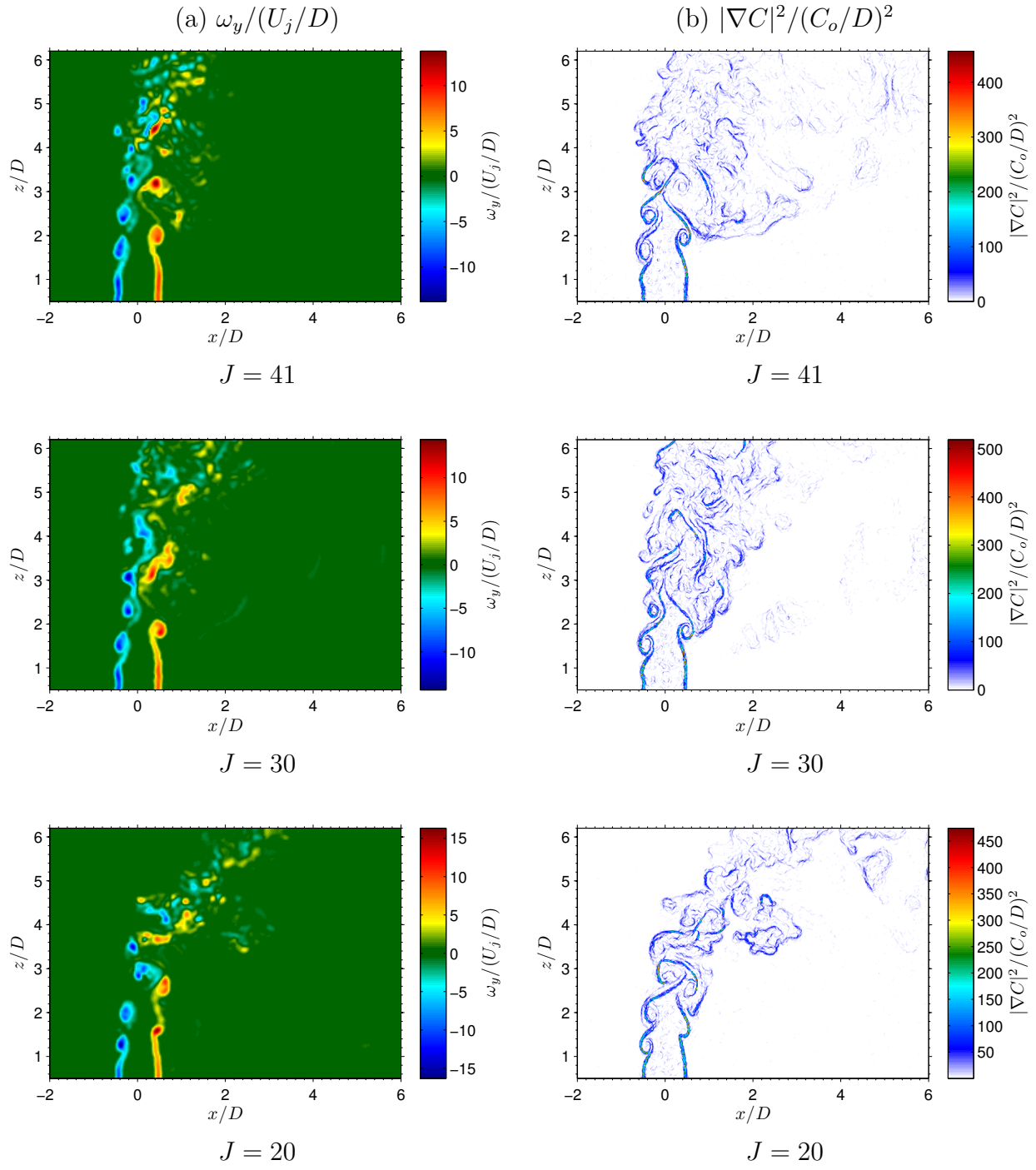


Figure D.4: Instantaneous centerplane (side view) simultaneous PLIF/PIV imaging of $S = 0.35$, flush nozzle-generated JICF with varying momentum flux ratios: $J = 41$ (top row), $J = 30$ (middle row), $J = 20$ (bottom row). Data shown for (a) scaled vorticity $\omega_y/(U_j/D)$ and (b) scaled jet fluid concentration gradient magnitude $|\nabla C|^2/(C_o/D)^2$.

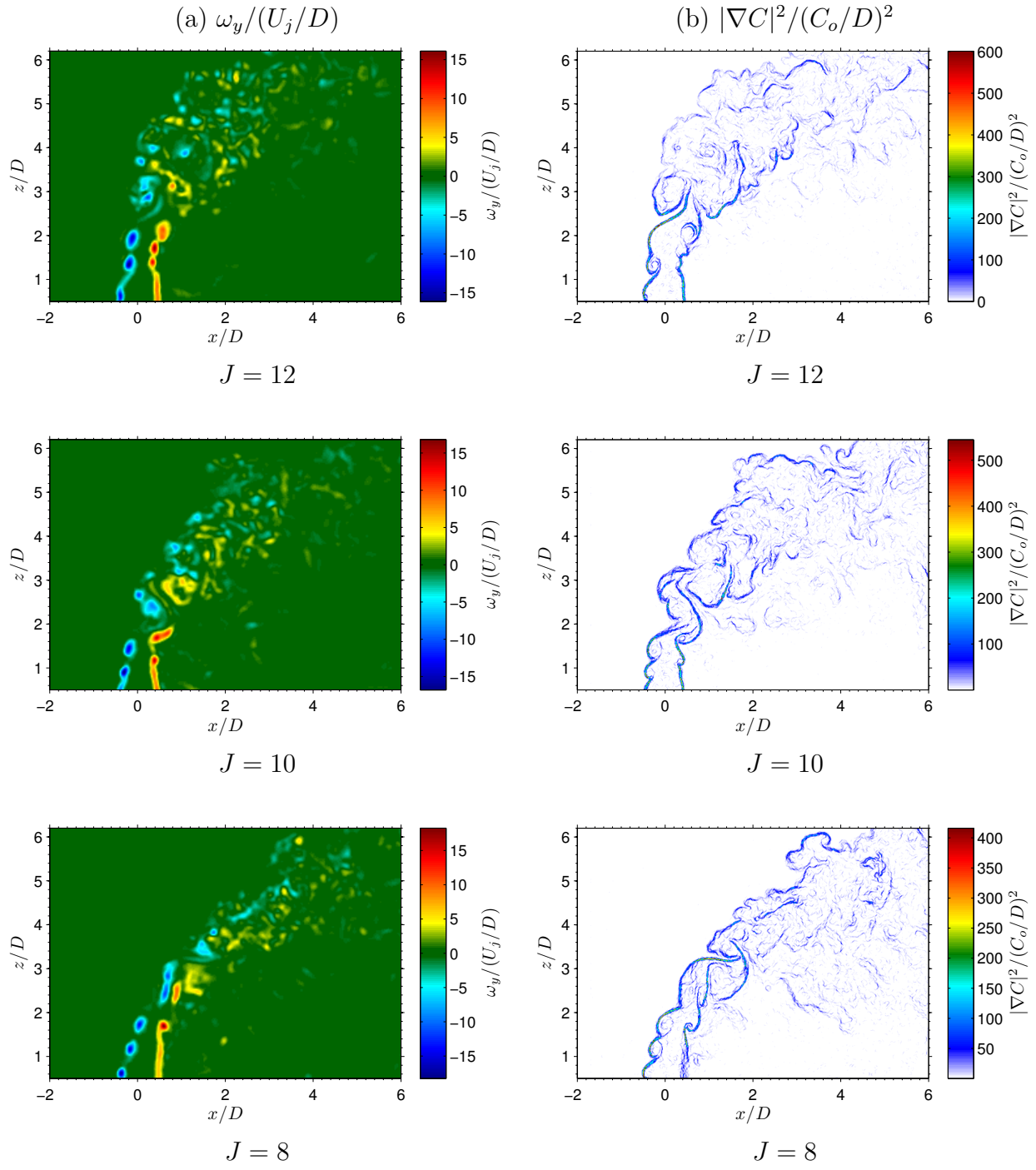


Figure D.5: Instantaneous centerplane (side view) simultaneous PLIF/PIV imaging of $S = 0.35$, flush nozzle-generated JICF with varying momentum flux ratios: $J = 12$ (top row), $J = 10$ (middle row), $J = 8$ (bottom row). Data shown for (a) scaled vorticity $\omega_y/(U_j/D)$ and (b) scaled jet fluid concentration gradient magnitude $|\nabla C|^2/(C_o/D)^2$.

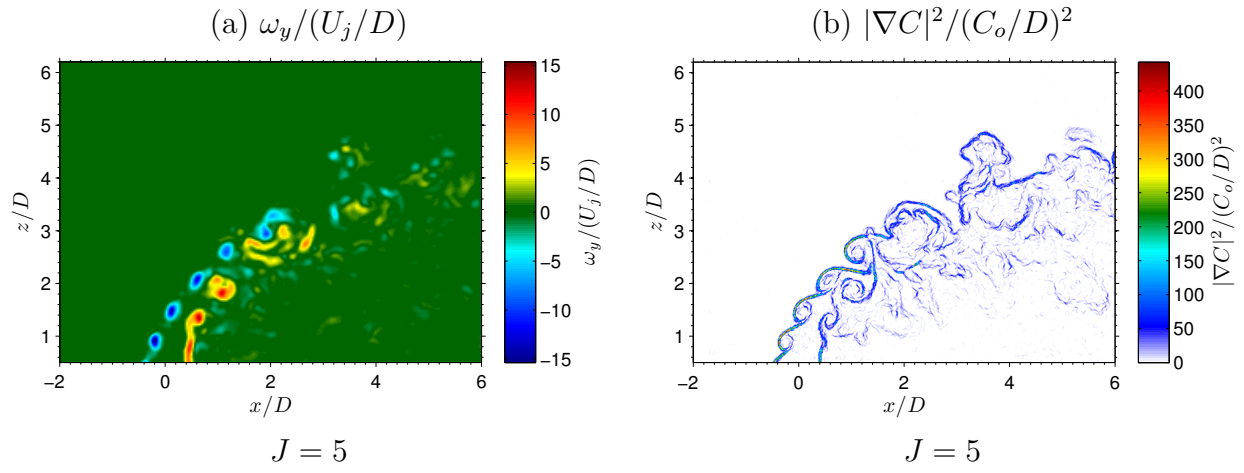


Figure D.6: Instantaneous centerplane (side view) simultaneous PLIF/PIV imaging of $S = 0.35$, flush nozzle-generated JICF with $J = 5$. Data shown for (a) scaled vorticity $\omega_y/(U_j/D)$ and (b) scaled jet fluid concentration gradient magnitude $|\nabla C|^2/(C_o/D)^2$.

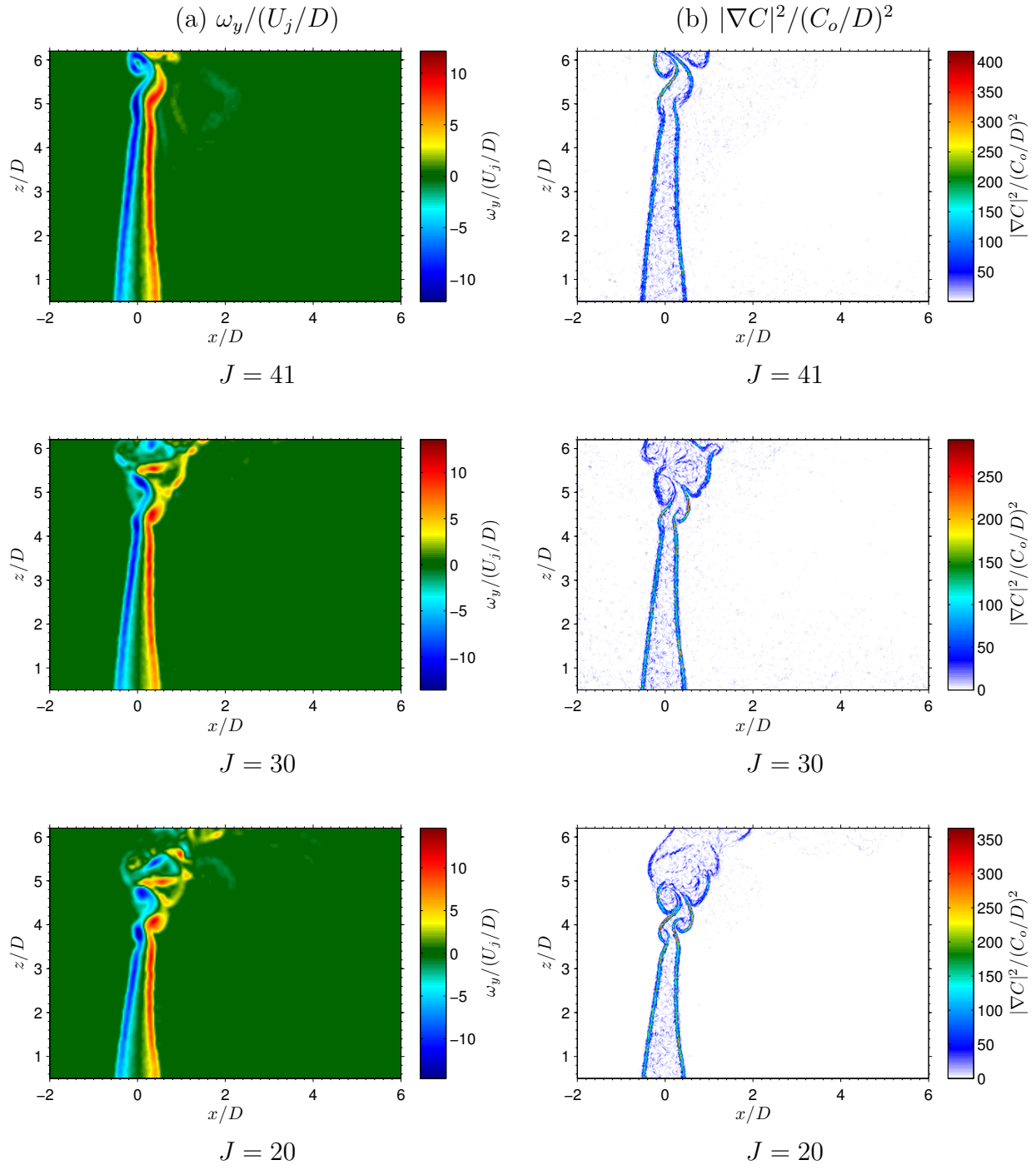


Figure D.7: Instantaneous centerplane (side view) simultaneous PLIF/PIV imaging of $S = 1.00$, flush pipe-generated JICF with varying momentum flux ratios: $J = 41$ (top row), $J = 30$ (middle row), $J = 20$ (bottom row). Data shown for (a) scaled vorticity $\omega_y/(U_j/D)$ and (b) scaled jet fluid concentration gradient magnitude $|\nabla C|^2/(C_o/D)^2$.

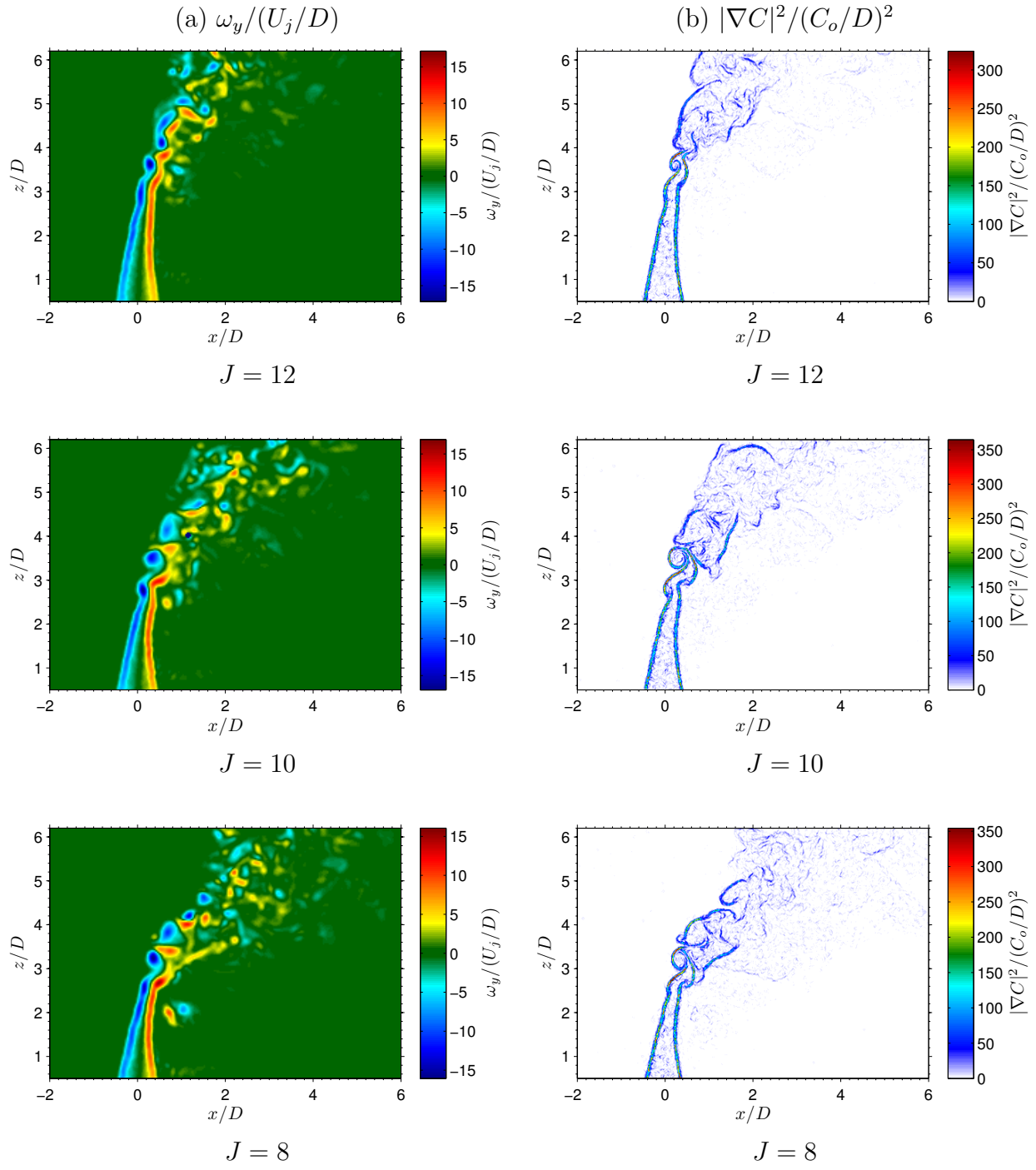


Figure D.8: Instantaneous centerplane (side view) simultaneous PLIF/PIV imaging of $S = 1.00$, flush pipe-generated JICF with varying momentum flux ratios: $J = 12$ (top row), $J = 10$ (middle row), $J = 8$ (bottom row). Data shown for (a) scaled vorticity $\omega_y/(U_j/D)$ and (b) scaled jet fluid concentration gradient magnitude $|\nabla C|^2/(C_o/D)^2$.

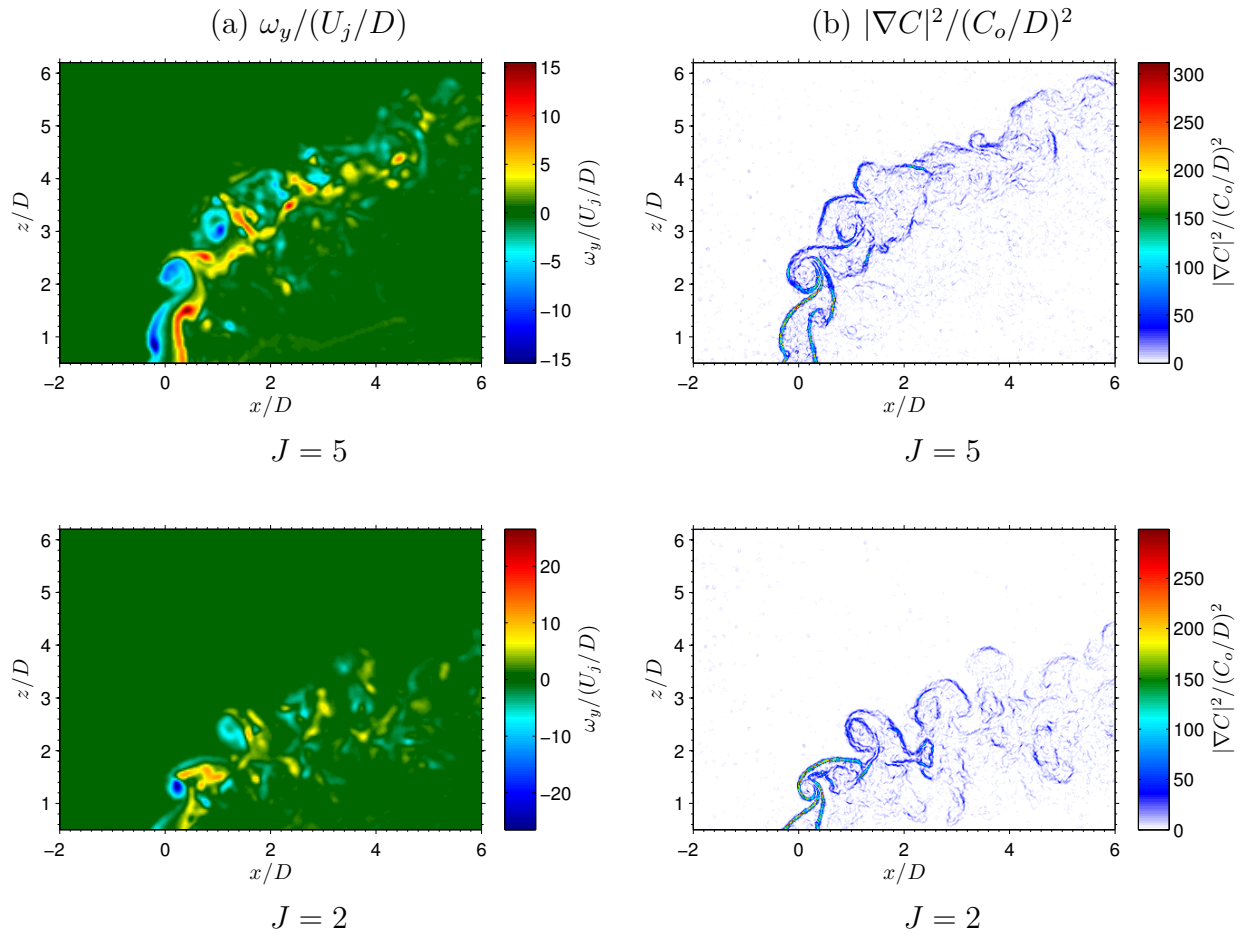


Figure D.9: Instantaneous centerplane (side view) simultaneous PLIF/PIV imaging of $S = 1.00$, flush pipe-generated JICF with varying momentum flux ratios: $J = 5$ (top row), $J = 2$ (bottom row). Data shown for (a) scaled vorticity $\omega_y/(U_j/D)$ and (b) scaled jet fluid concentration gradient magnitude $|\nabla C|^2/(C_o/D)^2$.

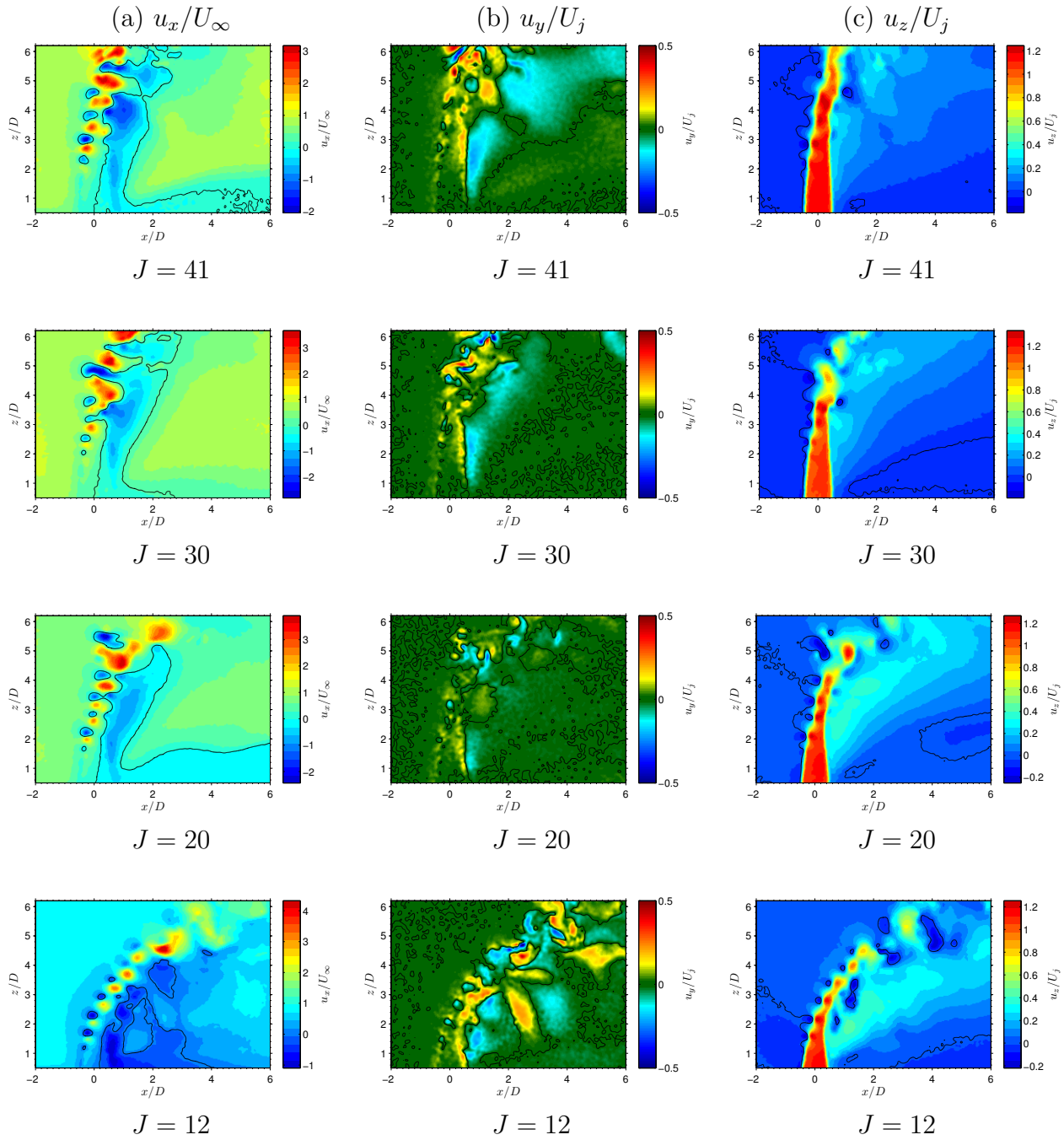


Figure D.10: Instantaneous centerplane velocity field visualization for $S = 1.00$, flush nozzle-generated JICF with varying momentum flux ratios in the range $41 \geq J \geq 12$ as indicated below each image. Data shown for (a) u_x/U_∞, (b) u_y/U_j, and (c) u_z/U_j. Black line corresponds to delineation between positive and negative values.

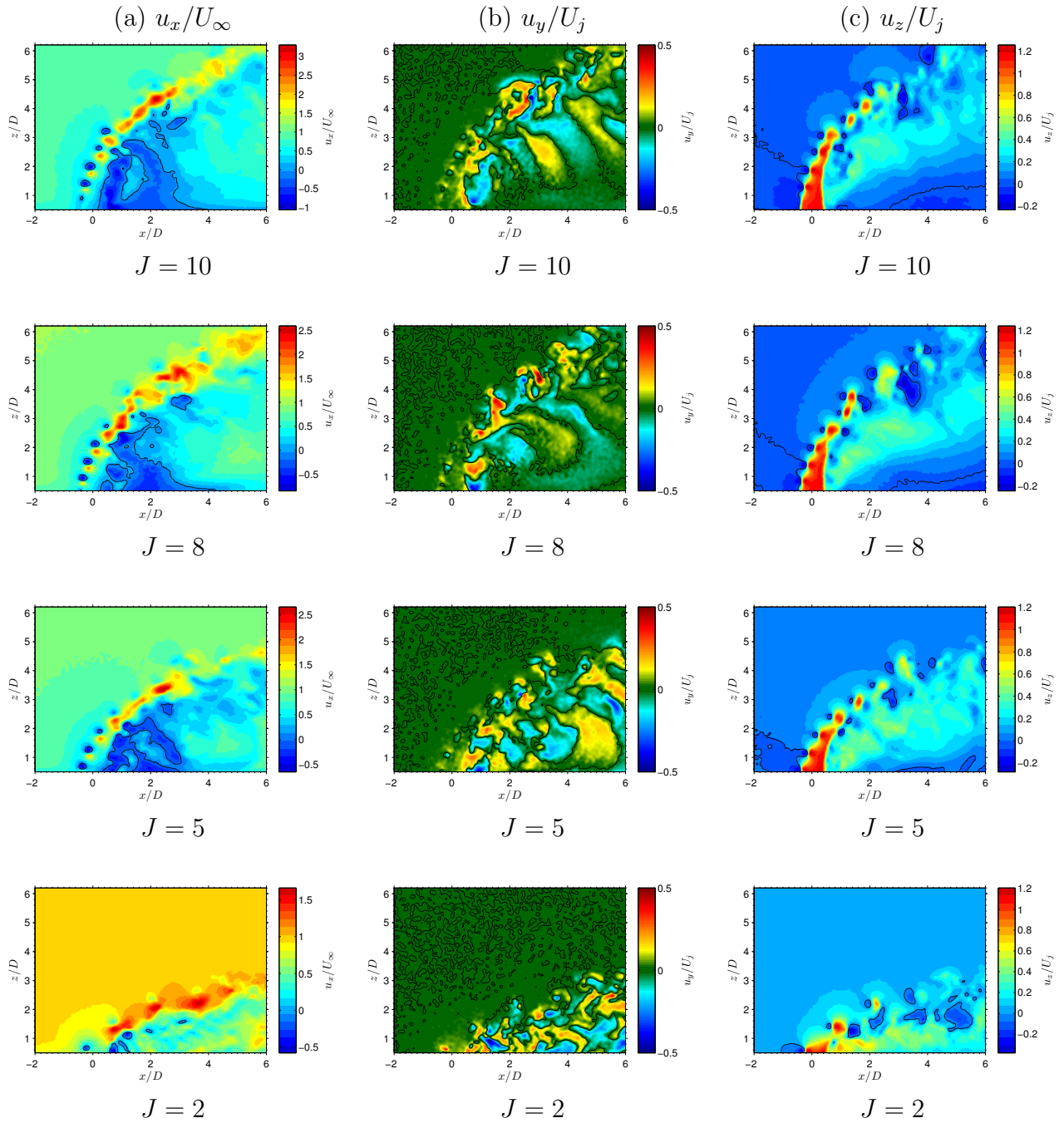


Figure D.11: Instantaneous centerplane velocity field visualization for $S = 1.00$, flush nozzle-generated JICF with varying momentum flux ratios in the range $10 \geq J \geq 2$ as indicated below each image. Data shown for (a) u_x/U_∞, (b) u_y/U_j, and (c) u_z/U_j. Black line corresponds to delineation between positive and negative values.

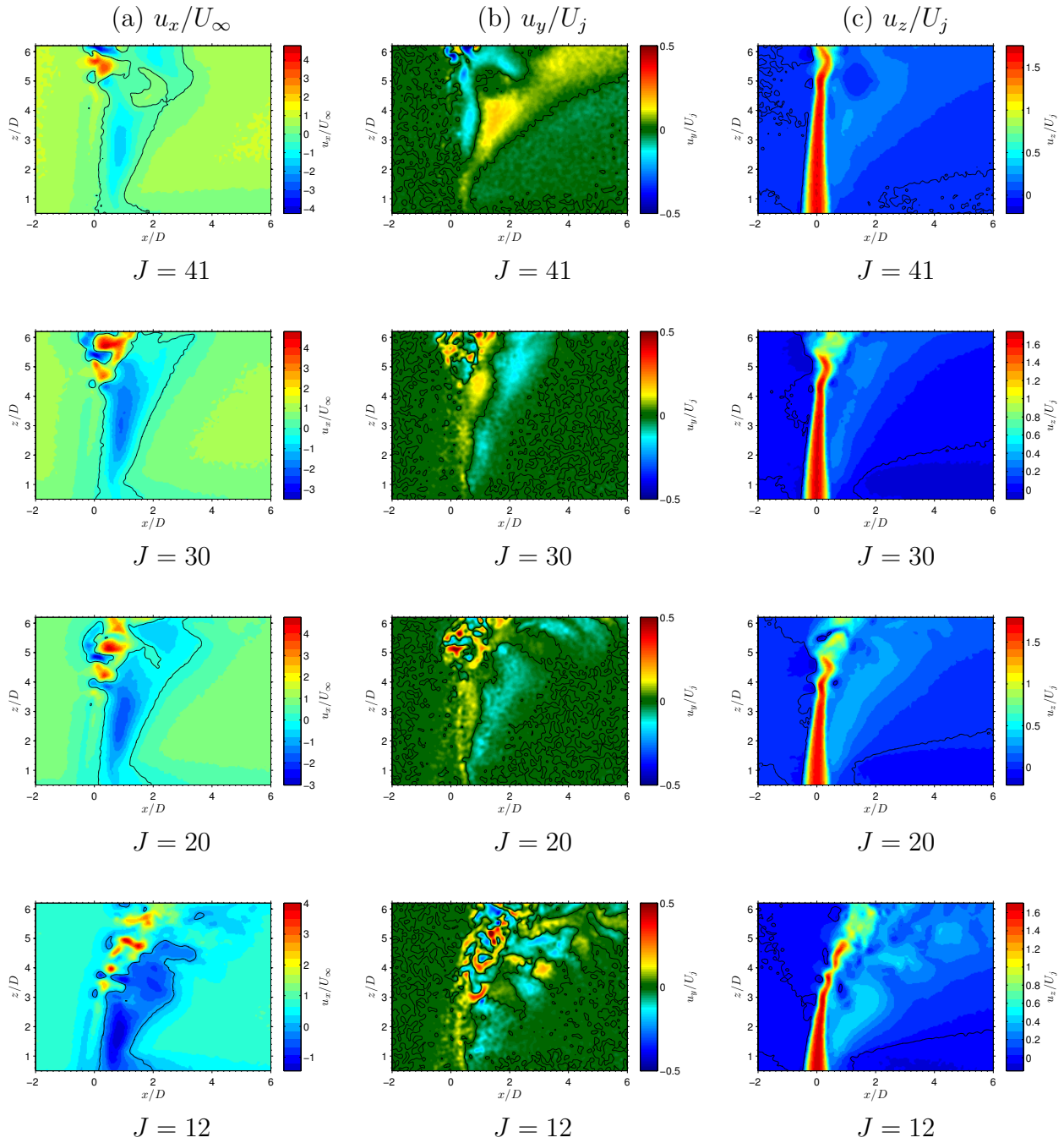


Figure D.12: Instantaneous centerplane velocity field visualization for $S = 1.00$, flush pipe-generated JICF with varying momentum flux ratios in the range $41 \geq J \geq 12$ as indicated below each image. Data shown for (a) u_x/U_∞, (b) u_y/U_j, and (c) u_z/U_j. Black line corresponds to delineation between positive and negative values.

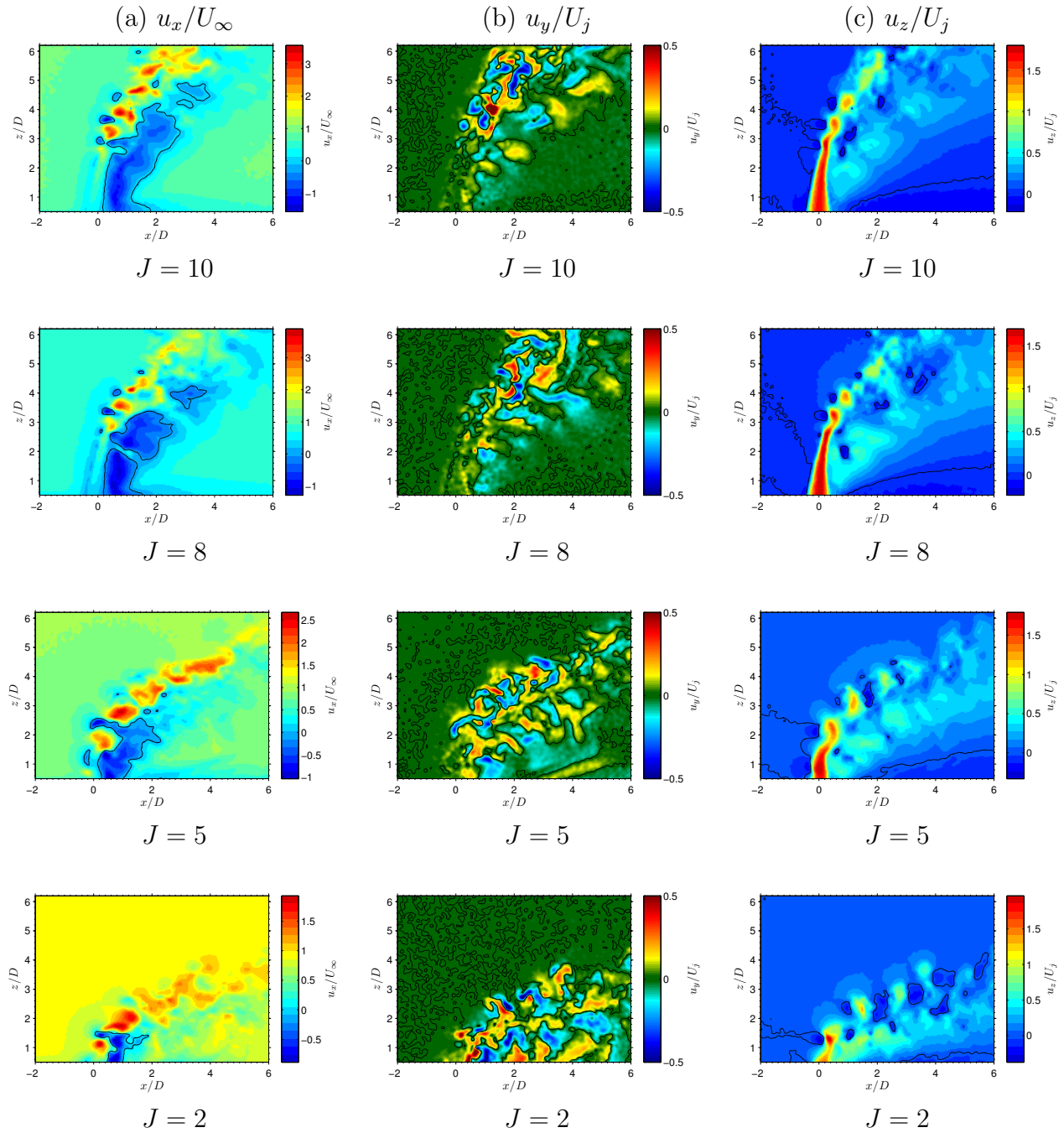


Figure D.13: Instantaneous centerplane velocity field visualization for $S = 1.00$, flush pipe-generated JICF with varying momentum flux ratios in the range $10 \geq J \geq 2$ as indicated below each image. Data shown for (a) u_x/U_∞, (b) u_y/U_j, and (c) u_z/U_j. Black line corresponds to delineation between positive and negative values.

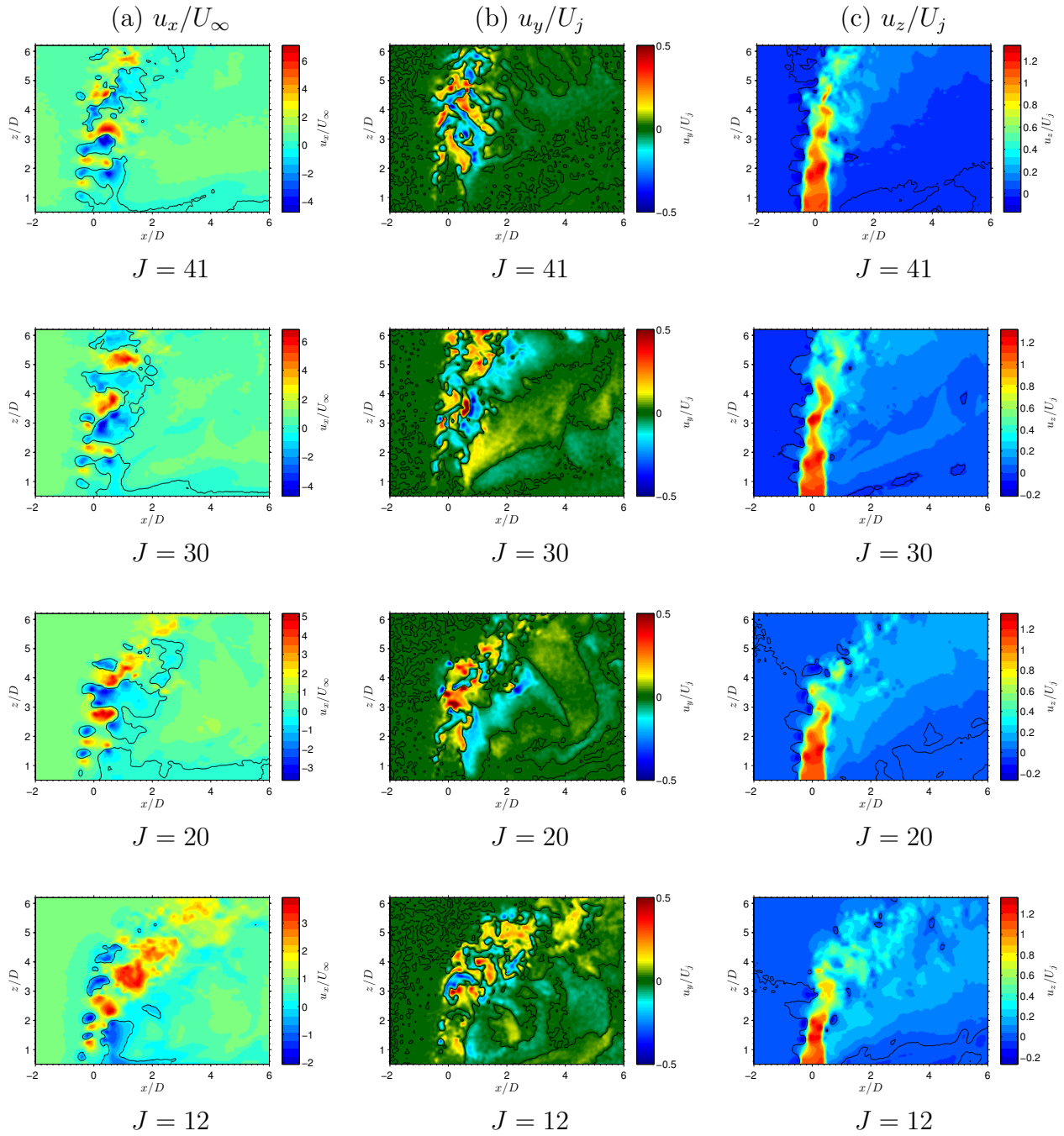


Figure D.14: Instantaneous centerplane velocity field visualization for $S = 0.35$, flush nozzle-generated JICF with varying momentum flux ratios in the range $41 \geq J \geq 12$ as indicated below each image. Data shown for (a) u_x/U_∞, (b) u_y/U_j, and (c) u_z/U_j. Black line corresponds to delineation between positive and negative values.

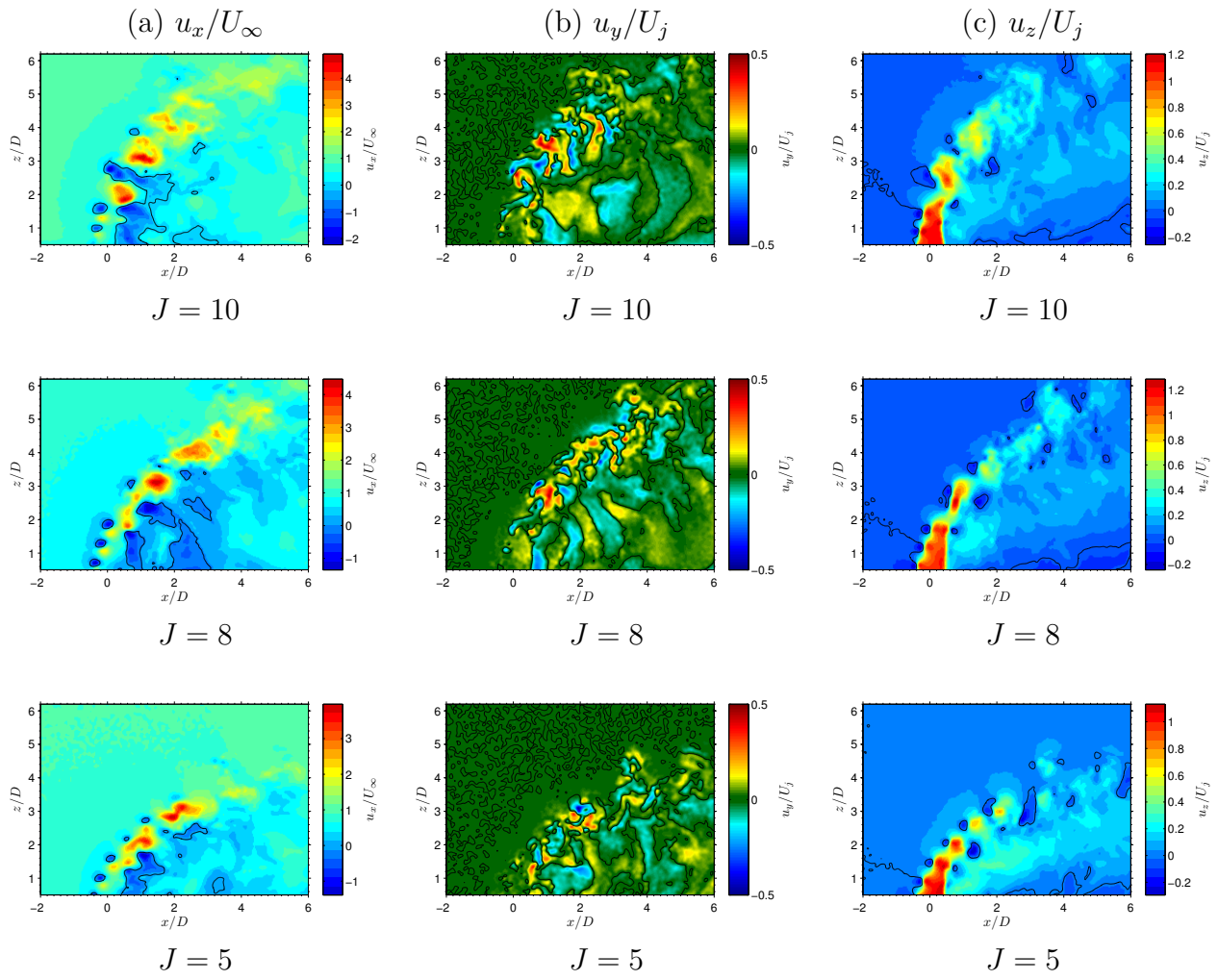


Figure D.15: Instantaneous centerplane velocity field visualization for $S = 0.35$, flush nozzle-generated JICF with varying momentum flux ratios in the range $10 \geq J \geq 5$ as indicated below each image. Data shown for (a) u_x/U_∞, (b) u_y/U_j, and (c) u_z/U_j. Black line corresponds to delineation between positive and negative values.

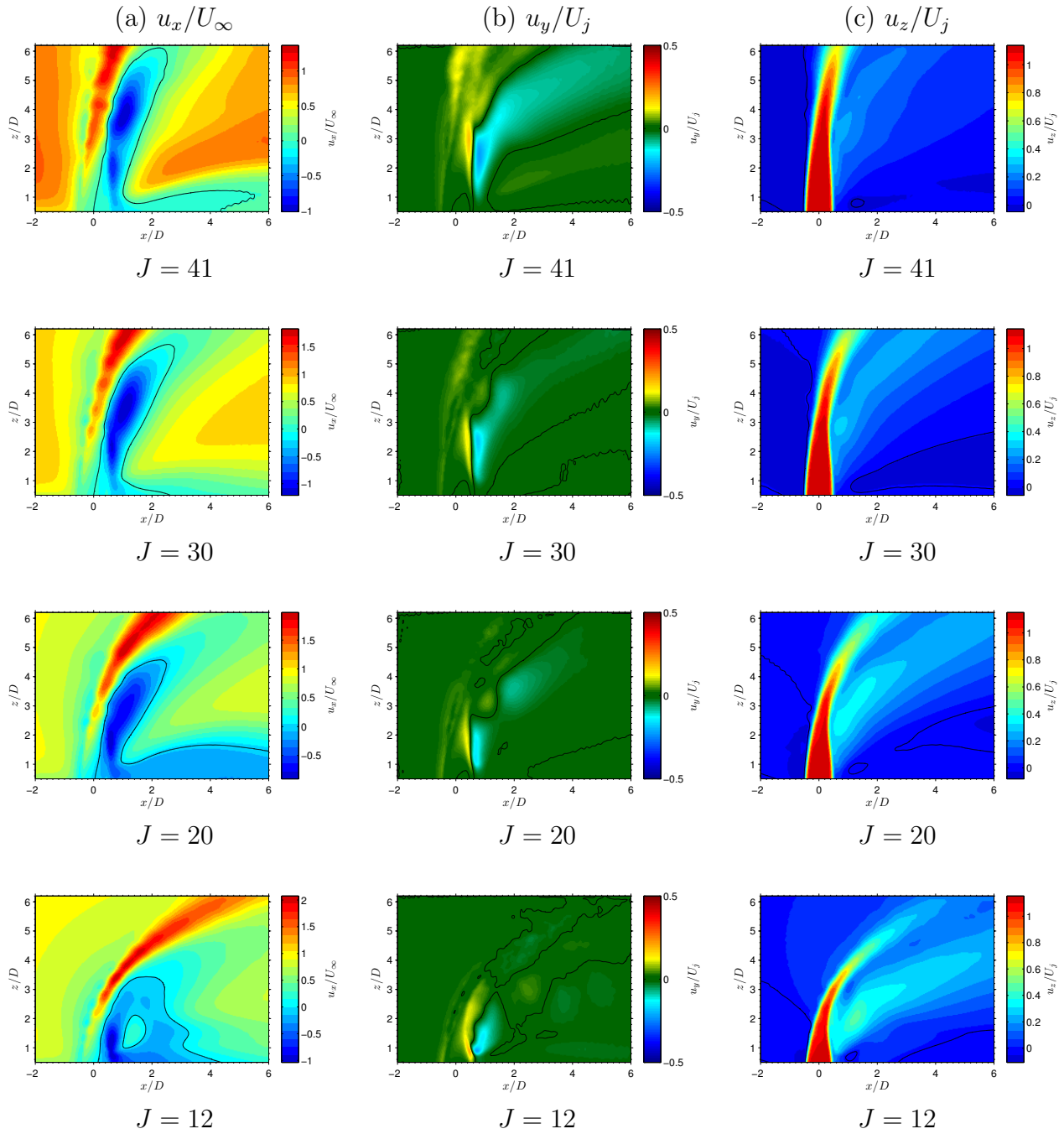


Figure D.16: Mean centerplane velocity field visualization for $S = 1.00$, flush nozzle-generated JICF with varying momentum flux ratios in the range $41 \geq J \geq 12$ as indicated below each image. Data shown for (a) u_x/U_∞, (b) u_y/U_j, and (c) u_z/U_j. Black line corresponds to delineation between positive and negative values.

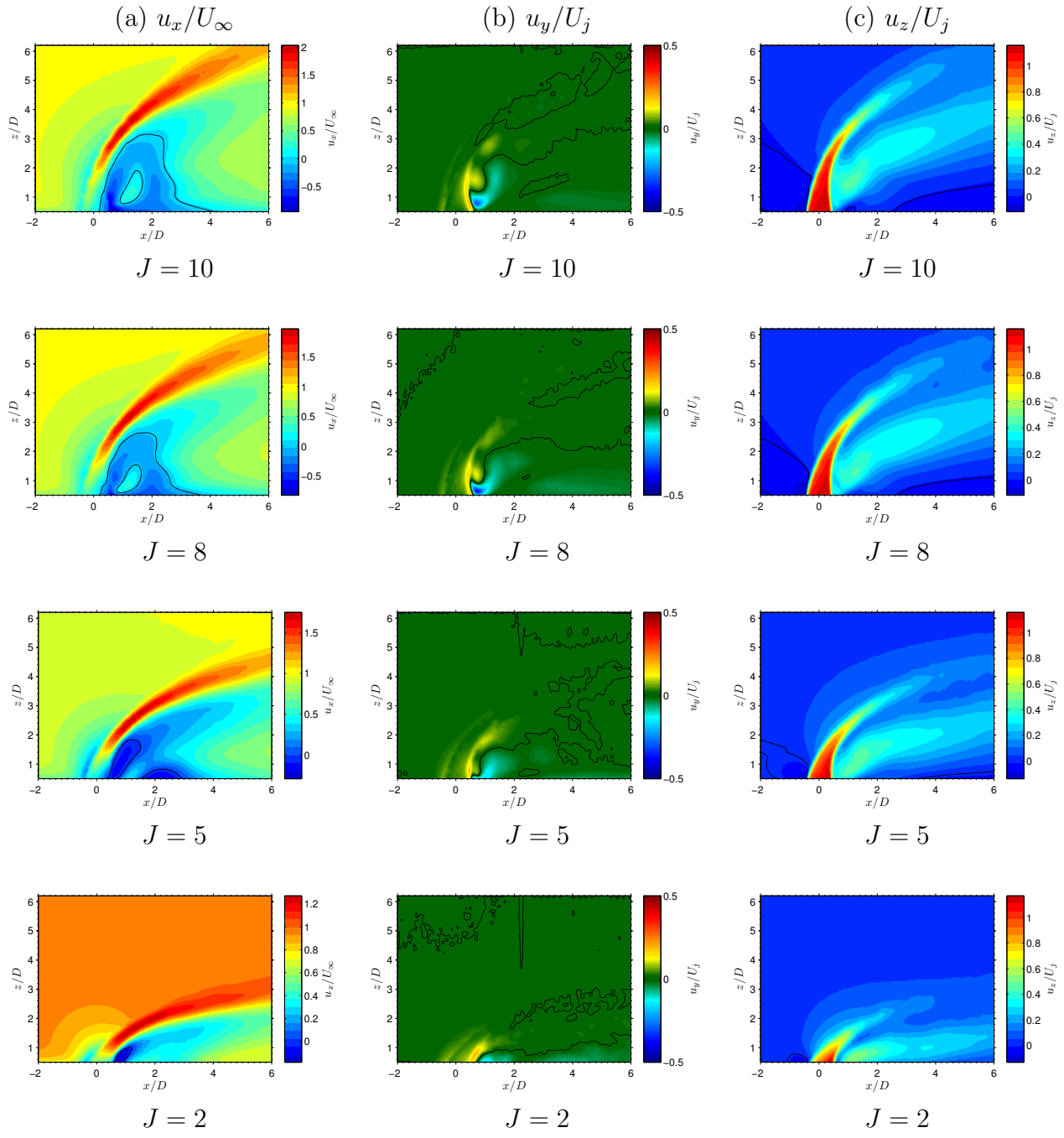


Figure D.17: Mean centerplane velocity field visualization for $S = 1.00$, flush nozzle-generated JICF with varying momentum flux ratios in the range $10 \geq J \geq 2$ as indicated below each image. Data shown for (a) u_x/U_∞, (b) u_y/U_j, and (c) u_z/U_j. Black line corresponds to delineation between positive and negative values.

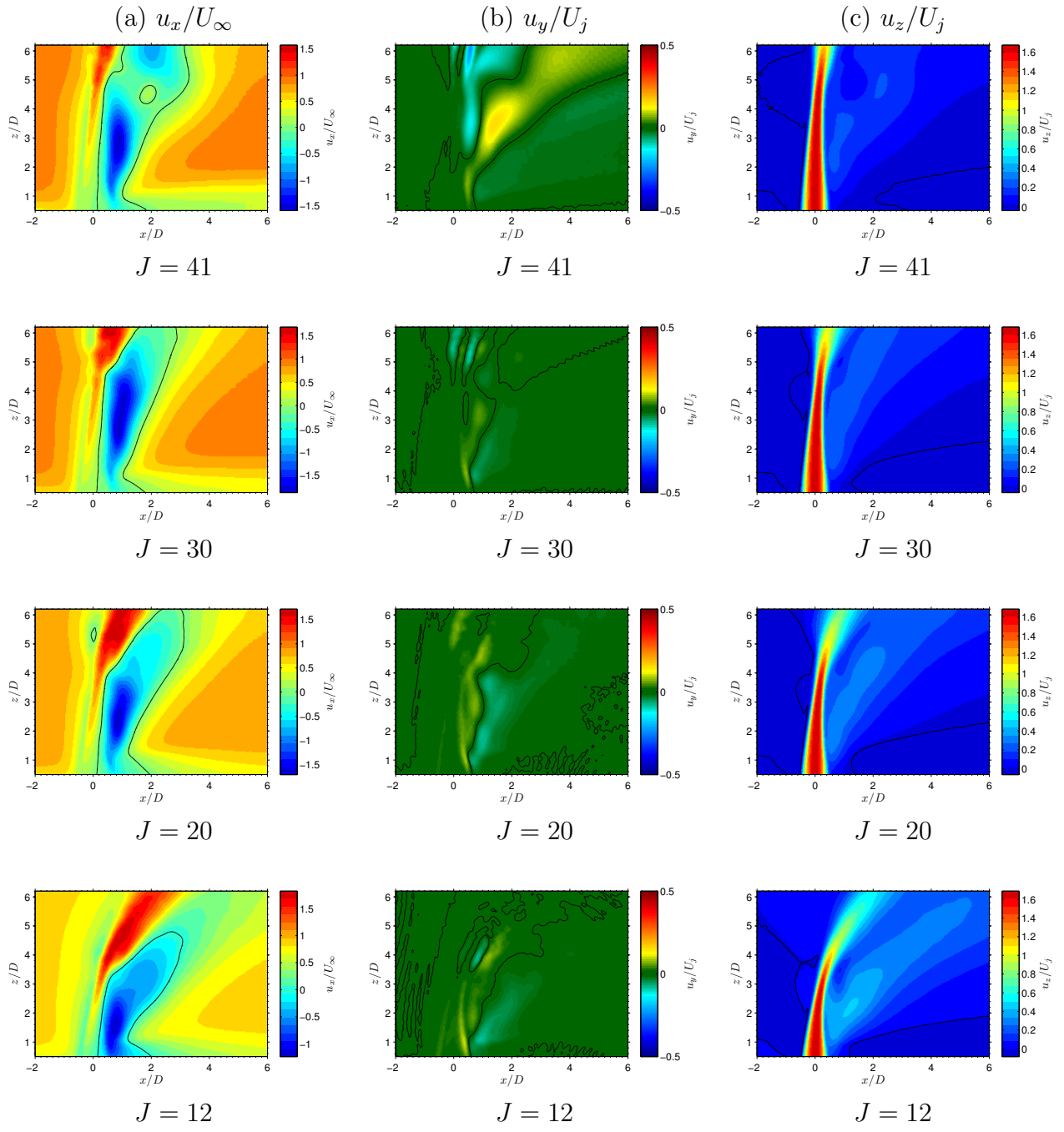


Figure D.18: Mean centerplane velocity field visualization for $S = 1.00$, flush pipe-generated JICF with varying momentum flux ratios in the range $41 \geq J \geq 12$ as indicated below each image. Data shown for (a) u_x/U_∞, (b) u_y/U_j, and (c) u_z/U_j. Black line corresponds to delineation between positive and negative values.

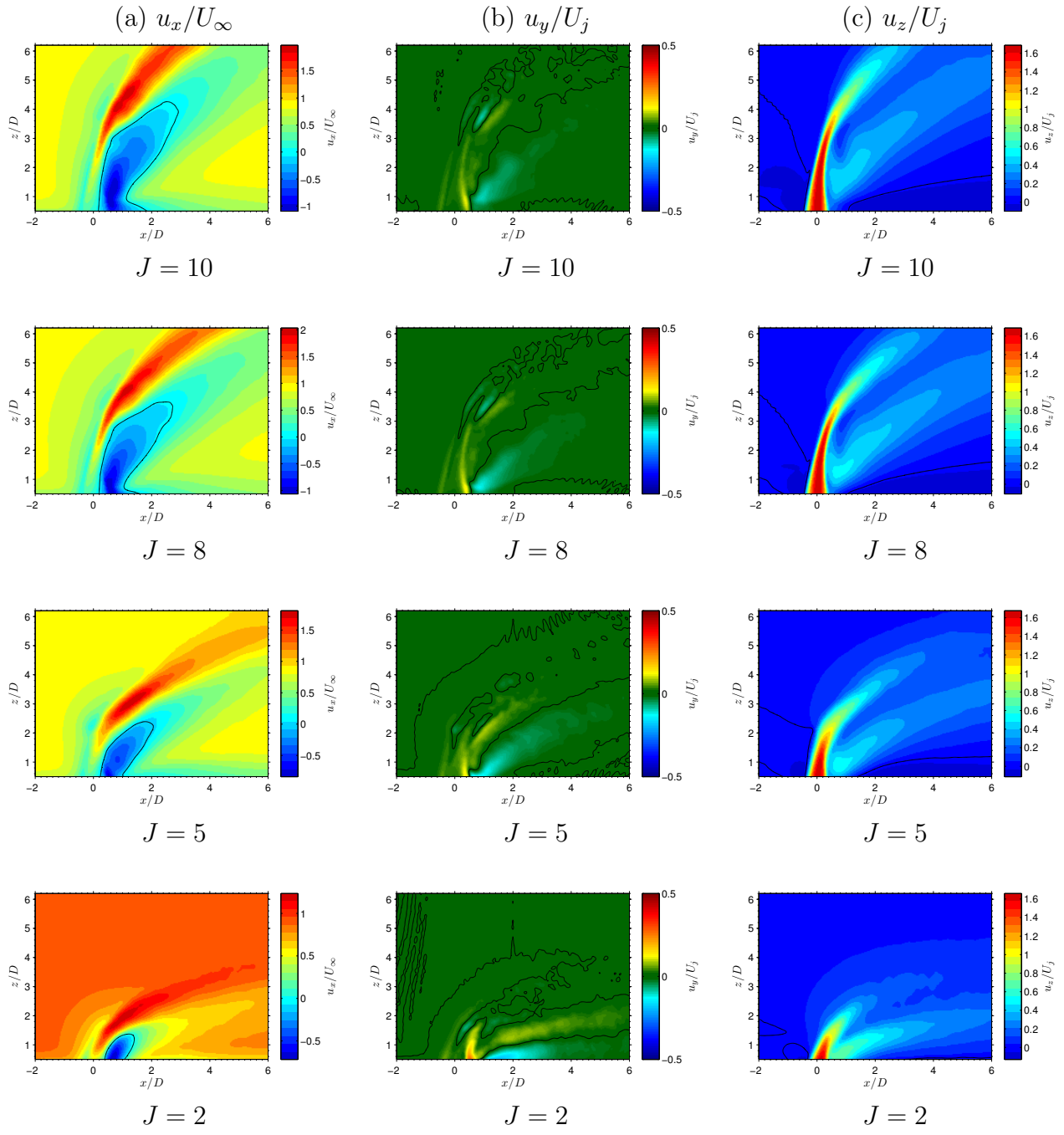


Figure D.19: Mean centerplane velocity field visualization for $S = 1.00$, flush pipe-generated JICF with varying momentum flux ratios in the range $10 \geq J \geq 2$ as indicated below each image. Data shown for (a) u_x/U_∞, (b) u_y/U_j, and (c) u_z/U_j. Black line corresponds to delineation between positive and negative values.

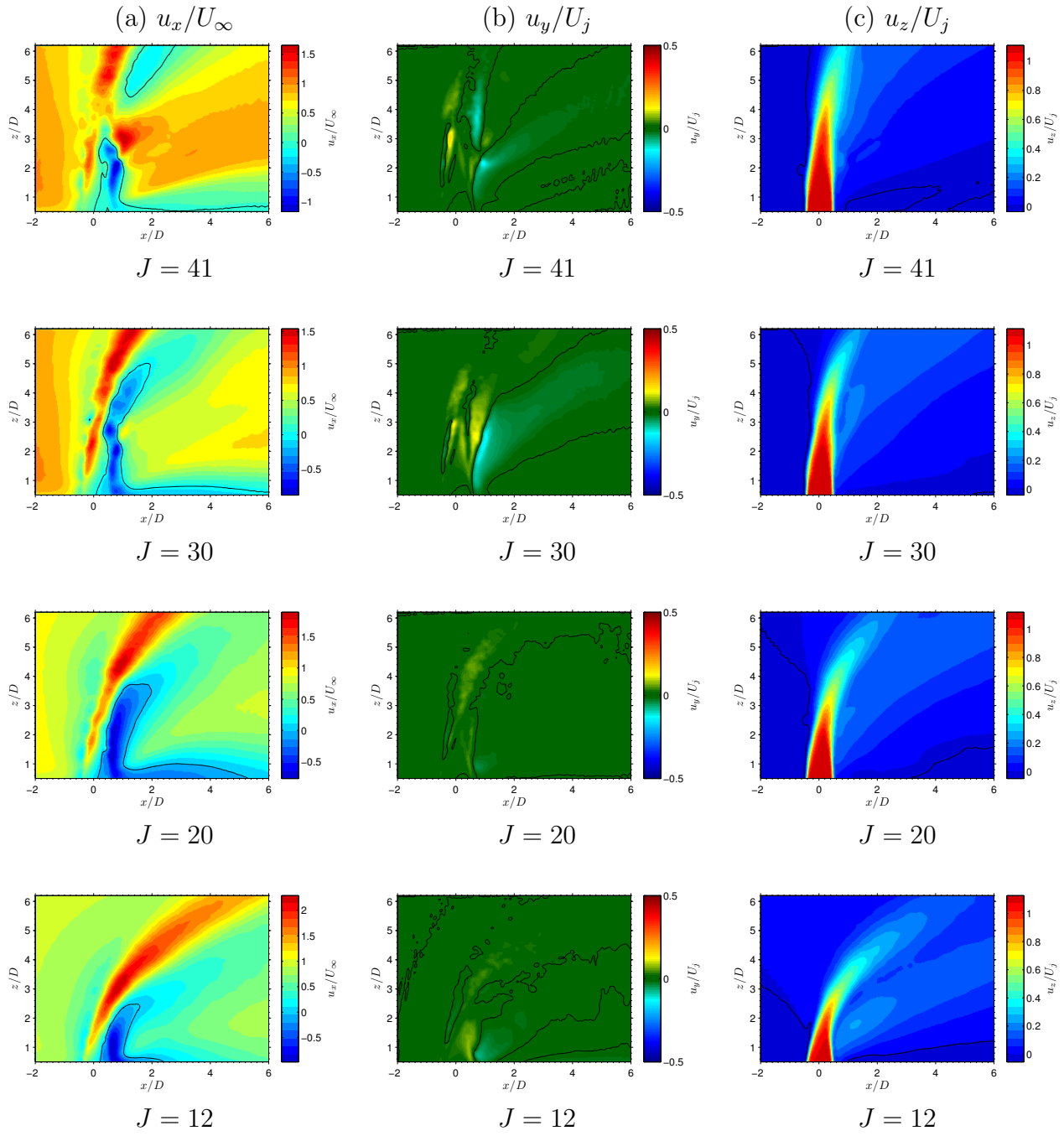


Figure D.20: Mean centerplane velocity field visualization for $S = 0.35$, flush nozzle-generated JICF with varying momentum flux ratios in the range $41 \geq J \geq 12$ as indicated below each image. Data shown for (a) u_x/U_∞, (b) u_y/U_j, and (c) u_z/U_j. Black line corresponds to delineation between positive and negative values.

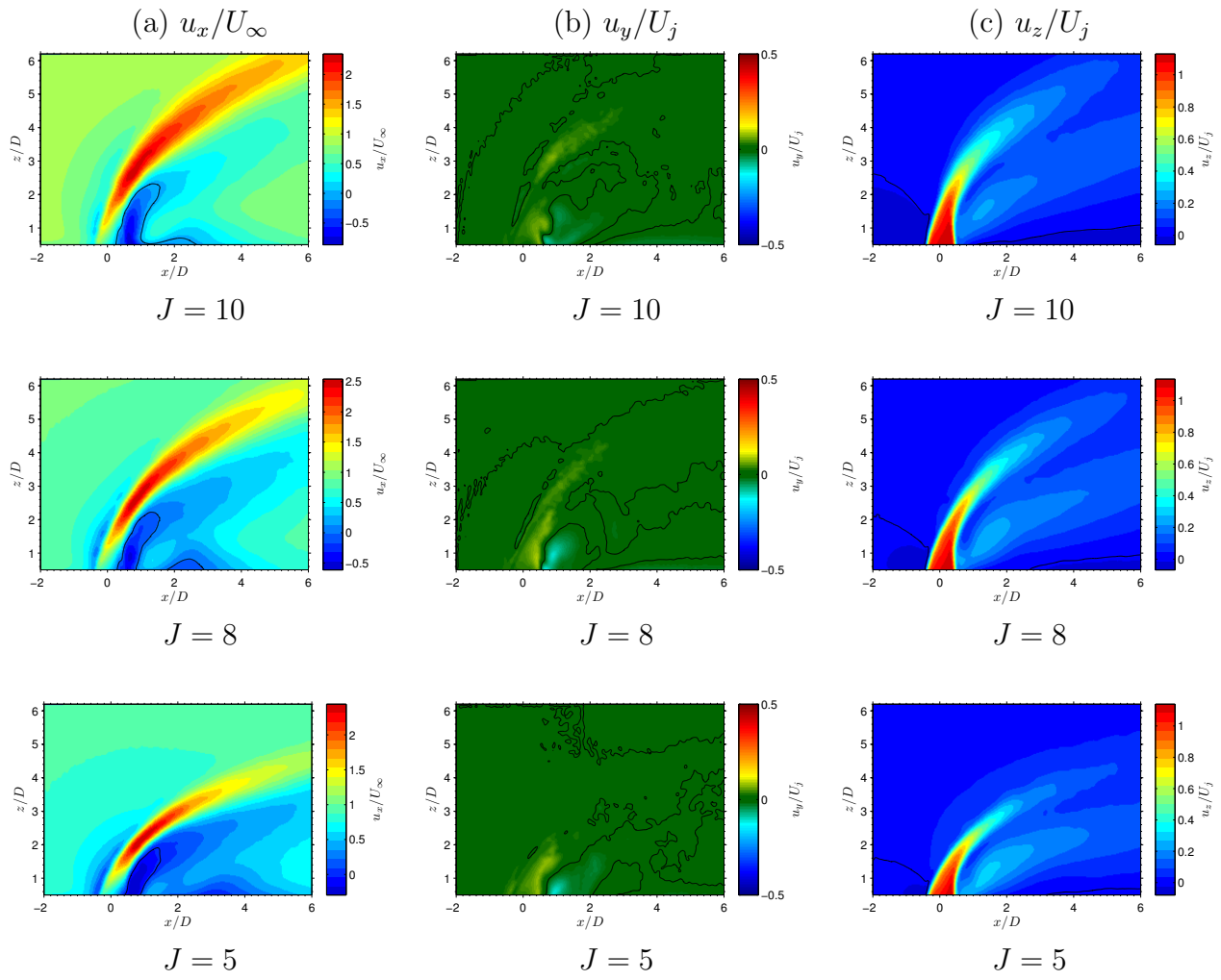


Figure D.21: Mean centerplane velocity field visualization for $S = 0.35$, flush nozzle-generated JICF with varying momentum flux ratios in the range $10 \geq J \geq 5$ as indicated below each image. Data shown for (a) u_x/U_∞, (b) u_y/U_j, and (c) u_z/U_j. Black line corresponds to delineation between positive and negative values.

Bibliography

R. J. Adrian and J. Westerweel. *Particle Image Velocimetry*. Cambridge University Press, New York, NY, 2011.

L. S. de B. Alves, R. E. Kelly, and A. R. Karagozian. Local stability analysis of an inviscid transverse jet. *Journal of Fluid Mechanics*, 581:401–418, 2007.

L. S. de B. Alves, R. E. Kelly, and A. R. Karagozian. Transverse-jet shear-layer instabilities. part 2. linear analysis for large jet-to-crossflow velocity ratio. *Journal of Fluid Mechanics*, 602:383–401, 2008.

J. Andreopoulos. On the structure of jets in a crossflow. *Journal of Fluid Mechanics*, 157: 163–197, 1985.

Wm. T. Ashurst, A. R. Kerstein, R. M. Kerr, and C. H. GIbson. Alignment of vorticity and scalar gradient with strain rate in simulated navierstokes turbulence. *Physics of Fluids*, 30:2343–2353, 1987.

S. Bagheri, P. Schlatter, P. J. Schmid, and D. S. Henningson. Global stability of a jet in crossflow. *Journal of Fluid Mechanics*, 624:33–44, 2009.

J.B. Barlow, W.H. Rae Jr., and A. Pope. *Low-Speed Wind Tunnel Testing*. Wiley-Interscience, 1999.

A. Ben-Yakar, M. R. Kamel, C. I. Morris, and R. K. Hanson. Hypersonic combustion and mixing studies using simultaneous oh-plif and schlieren imaging. In *36th AIAA Aerospace Sciences Meeting & Exhibit*, January 1998. AIAA Paper 98-0940.

G. Berkooz, P. Holmes, and J. L. Lumley. The proper orthogonal decomposition in the analysis of turbulent flows. *Annual review of fluid mechanics*, 25:539–575, 1993.

R. B. Bird, W. E. Stewart, and E. N. Lightfoot. *Transport Phenomena*. John Wiley & Sons, Inc., New York, 1960.

E. S. Bish and W. J. A. Dahm. Strained dissipation and reaction layer analyses of nonequilibrium chemistry in turbulent reacting flows. *Combustion and Flame*, 100:457–464, 1995.

J. N. Blanchard, Y. Brunet, and A. Merlen. Influence of a counter rotating vortex pair on the stability of a jet in crossflow: an experimental study by flow visualizations. *Experiments in Fluids*, 26:63–74, 1999.

H. Bockhorn, D. Mewes, W. Peukert, and H. Warnecke, editors. *Micro and Macro Mixing*. Springer, 2010.

D. Bothe. Evaluating the quality of a mixture: Degree of homogeneity and scale of segregation. In Henning Bockhorn, Dieter Mewes, Wolfgang Peukert, and Hans-Joachim Warnecke, editors, *Micro and Macro Mixing*, Heat and Mass Transfer, pages 17–35. Springer Berlin Heidelberg, 2010. ISBN 978-3-642-04549-3.

J. E. Broadwell and R. E. Breidenthal. Structure and mixing of a transverse jet in incompressible flow. *Journal of Fluid Mechanics*, 148:405–412, 1984.

J. E. Broadwell and M. G. Mungal. Large-scale structures and molecular mixing. *Physics of Fluids*, 3:1193–1206, 1991.

C. J. Brownell and L. K. Su. Planar laser imaging of differential molecular diffusion in gas-phase turbulent jets. *Physics of Fluids*, 20, 2008.

K. A. Buch and W. J. A. Dahm. Experimental study of the fine-scale structure of conserved scalar mixing in turbulent shear flows. part 1. sc ¿¿1. *Journal of Fluid Mechanics*, 317: 21–71, 1996.

K. A. Buch and W. J. A. Dahm. Experimental study of the fine-scale structure of conserved scalar mixing in turbulent shear flows. part 2. sc =1. *Journal of Fluid Mechanics*, 364: 1–29, 1998.

R. Camussi, G. Guj, and A. Stella. Experimental study of a jet in a crossflow at very low reynolds number. *Journal of Fluid Mechanics*, 454:113–144, 2002.

K. Canzonieri. Experimental studies on low density jets in crossflow. Master's thesis, University of California, Los Angeles, Department of Mechanical and Aerospace Engineering, 2009.

K. Canzonieri, D. Getsinger, C. Hendrickson, O. I. Smith, and A. R. Karagozian. Shear layer instabilities in low density jets in crossflow. In *Fall Technical Meeting of the Western States Section of the Combustion Institute*, October 2009. Paper 09F-17.

B. M. Cetegen. Private communication. 2015.

Y. K. Chang and A. D. Vakili. Dynamics of vortex rings in crossflow. *Physics of Fluids*, 7: 1583–1597, 1995.

J.-M. Chomaz. Global instabilities in spatially developing flows: Non-normality and nonlinearity. *Annual Review of Fluid Mechanics*, 37:357–392, 2005.

L. Cortelezzi and A. R. Karagozian. On the formation of the counter-rotating vortex pair in transverse jets. *Journal of Fluid Mechanics*, 446:347–373, 2001.

P.V. Danckwerts. The definition and measurement of some characteristics of mixtures. *Applied Science Research*, A3:279–296, 1952.

J. Davitian, D. Getsinger, C. Hendrickson, and A. R. Karagozian. Transition to global instability in transverse-jet shear layers. *Journal of Fluid Mechanics*, 661:294–315, 2010a.

J. Davitian, C. Hendrickson, D. Getsinger, R. T. M'Closkey, and A. R. Karagozian. Strategic control of transverse jet shear layer instabilities. *AIAA Journal*, 48(9):2145–2156, 2010b.

P. Dimotakis. The mixing transition in turbulent flows. *Journal of Fluid Mechanics*, 409: 69–98, 2000.

P. E. Dimotakis and P. L. Miller. Some consequences of the boundedness of scalar fluctuations. *Physics of Fluids A*, 2(11):1919–1920, 1990.

D. R. Dowling and P. E. Dimotakis. Similarity of the concentration field of gas-phase turbulent jets. *Journal of Fl*, 218:109–141, 1990.

F. Durst and E. S. Zanoun. Experimental investigation of near-wall effects on hot-wire measurements. *Experiments in Fluids*, 33:210–218, 2002.

C. Eckart. An analysis of the stirring and mixing processes in incompressible fluids. *Journal of Marine Research*, 7:265–275, 1948.

S. V. Ekkad, S. Ou, and R. B. Rivir. Effect of jet pulsation and duty cycle on film cooling from a single jet on a leading edge model. *Journal of Turbomachinery*, 128(3):564–571, 2006.

A. Eroglu and R. E. Breidenthal. Structure, penetration, and mixing of pulsed jets in crossflow. *AIAA Journal*, 39(3):417–423, 2001.

R. Fearn and R. Weston. Vorticity associated with a jet in a crossflow. *AIAA J*, 12:1666–1671, 1974.

D. J. Forliti, D. V. Salazar, and A. J. Bishop. Physics-based scaling laws for confined and unconfined transverse jets. *Experiments in Fluids*, 56(36), 2015.

T. F. Fric and A. Roshko. Views of the transverse jet near field. *Physics of Fluids*, 31(9): 2390, 1988.

T. F. Fric and A. Roshko. Vortical structure in the wake of a transverse jet. *Journal of Fluid Mechanics*, 279:1–47, 1994.

D. Getsinger, L. Gevorkyan, O. I. Smith, and A. R. Karagozian. Structural and stability characteristics of jets in crossflow. *Journal of Fluid Mechanics*, 760:342–367, 2014.

D. R. Getsinger, C. Hendrickson, and A. R. Karagozian. Shear layer instabilities in low-density transverse jets. *Experiments in Fluids*, 53:783–801, 2012.

D.R. Getsinger. *Shear Layer Instabilities and Mixing in Variable Density Transverse Jet Flows*. PhD thesis, UCLA, 2012.

J. B. Ghandhi. Spatial resolution and noise considerations in determining scalar dissipation rate from passive scalar image data. *Experiments in Fluids*, 40:577–588, 2006.

M. Gharib, E. Rambod, and K. Shariff. A universal time scale for vortex ring formation. *Journal of Fluid Mechanics*, 360:121–141, 1998.

M. Gruber, J. Donbar, C. Carter, and K-Y Hsu. Mixing and combustion studies using cavity-based flameholders in a supersonic flow. *Journal of Propulsion and Power*, 20:769–778, 2004.

O. Gubanov and L. Cortelezzi. Towards the design of an optimal mixer. *Journal of Fluid Mechanics*, 651:27–53, 2010.

M. P. Hallberg and P. J. Strykowski. On the universality of global modes in low-density axisymmetric jets. *Journal of Fluid Mechanics*, 569:493–507, 2006.

R. K. Hanson, J. M. Seitzman, and P. H. Paul. Planar laser-fluorescence imaging of combustion gases. *Applied Physics B*, 50:441–454, 1990.

E. F. Hasselbrink. *Transverse Jets and Jet Flames: Structure, Scaling, and Effects of Heat Release*. PhD thesis, Stanford University, Department of Mechanical Engineering, 1999.

E. F. Hasselbrink and M. G. Mungal. Transverse jets and jet flames. part 1. scaling laws for strong transverse jets. *Journal of Fluid Mechanics*, 443:1–25, 2001.

C. Hendrickson and R. M'Closkey. Phase compensation strategies for modulated-demodulated control with application to pulsed jet injection. *ASME Journal of Dynamic Systems, Measurement, and Control*, 134(011024), 2012. accepted for publication.

P. Huerre and P. A. Monkewitz. Local and global instabilities in spatially developing flows. *Annual Review of Fluid Mechanics*, 22:473–537, 1990.

M. Ilak, P. Schlatter, S. Bagheri, and D.S. Henningson. Bifurcation and stability analysis of a jet in crossflow: onset of global instability at a low velocity ratio. *Journal of Fluid Mechanics*, 696:94–121, 2012.

S. Jendoubi and P. J. Strykowski. Absolute and convective instability of axisymmetric jets with external flow. *Physics of Fluids*, 6:3000–3009, 1994.

H. Johari, M. Pacheco-Tougas, and J. C. Hermanson. Penetration and mixing of fully modulated turbulent jets in crossflow. *AIAA Journal*, 37(7):842–850, 1999.

Y. Kamotani and I. Greber. Experiments on a turbulent jet in a cross flow. *AIAA Journal*, 10(11):1425–1429, 1972.

A. R. Karagozian. An analytical model for the vorticity associated with a transverse jet. *AIAA Journal*, 24:429–436, 1986.

A. R. Karagozian. Transverse jets and their control. *Progress in Energy and Combustion Science*, 36:531–553, 2010.

A. R. Karagozian, K. C. Wang, A.-T. Le, and O. I. Smith. Transverse gas jet injection behind a rearward-facing step. *Journal of Propulsion and Power*, 12(6):1129–1136, 1996.

J. F. Keffer and W. D. Baines. The round turbulent jet in a cross-wind. *Journal of Fluid Mechanics*, 15(4):481–496, 1963.

R. M. Kelso and A. J. Smits. Horseshoe vortex systems resulting from the interaction between a laminar boundary layer and a transverse jet. *Phys. Fluids*, 7:153–158, 1995.

R. M. Kelso, T. T. Lim, and A. E. Perry. An experimental study of round jets in cross-flow. *Journal of Fluid Mechanics*, 306:111–144, 1996.

R. M. Kerr. Higher-order derivative correlations and the alignment of small scale structures in isotropic numerical turbulence. *Journal of Fluid Mechanics*, 153:31–58, 1985.

M.M. Koochesfahani and P.E. Dimotakis. Mixing and chemical reactions in a turbulent liquid mixing layer. *Journal of Fluid Mechanics*, 170:83–112, 1986.

P.S. Kothnur and N. T. Clemens. Effects of unsteady strain rate on scalar dissipation structures in turbulent planar jets. *Physics of Fluids*, 17, 2005.

A. Krothapalli, L. Lourenco, and J. M. Buchlin. Separated flow upstream of a jet in a crossflow. *AIAA Journal*, 28(3):414–420, 1990.

A. Kukukova, J. Aubin, and S. M. Kresta. A new definition of mixing and segregation: Three dimensions of a key process variable. *Chemical Engineering Res*, 87:633–647, 2009.

D. M. Kuzo. *An Experimental Study of the Turbulent Transverse Jet*. PhD thesis, California Institute of Technology, 1995.

D. M. Kyle and K. R. Sreenivasan. The instability and breakdown of a round variable-density jet. *Journal of Fluid Mechanics*, 249:619–664, 1993.

A. Linan, M. Vera, and A. L. Sanchez. Ignition, liftoff, and extinction of gaseous diffusion flames. *Annual Review of Fluid Mechanics*, 47:293–314, 2015.

A. Lozano. *Laser-Excited Luminescent Tracers for Planar Concentration Measurements in Gaseous Jets*. PhD thesis, Stanford University, Department of Mechanical Engineering, 1992.

A. Lozano, B. Yip, and R. K. Hanson. Acetone: a tracer for concentration measurements in gaseous flows by planar laser-induced fluorescence. *Experiments in Fluids*, 13:369–376, 1992.

K. Mahesh and P. Iyer. Numerical study of shear layer instability in transverse jets. In *Bulletin of the American Physical Society*, volume 58, 2013.

F.E. Marble and J. E. Broadwell. The coherent flame model for turbulent chemical reactions. Technical report, Project Squid Technical Report TRW-9-PU, 1977.

R. J. Margason. Fifty years of jet in cross flow research. *AGARD-CP-534*, 1:1–141, 1993.

G Mathew, I Mezic, and L Petzold. A multiscale measure of mixing. *Physica D: Nonlinear Phenomena*, 211(1):23–46, 2005.

R. T. M'Closkey, J. King, L. Cortelezzi, and A. R. Karagozian. The actively controlled jet in crossflow. *Journal of Fluid Mechanics*, 452:325–335, 2002.

S. Megerian, J. Davitian, L. S. de B. Alves, and A. R. Karagozian. Transverse-jet shear-layer instabilities. part 1. experimental studies. *Journal of Fluid Mechanics*, 593:93–129, 2007.

K.E. Meyer, J.M. Pedersen, and O. Özcan. A turbulent jet in crossflow analysed with proper orthogonal decomposition. *Journal of Fluid Mechanics*, 583:199–227, 2007.

T. R. Meyer, G. F. King, G. C. Martin, R. P. Lucht, F. R. Schauer, and J. C. Dutton. Accuracy and resolution issues in no/acetone plif measurements of gas-phase molecular mixing. *Experiments in Fluids*, 32:603–611, 2002.

D. N. Miller, P. J. Yagle, and J. W. Hamstra. Fluidic throat skewing for thrust vectoring in fixed-geometry nozzles. *AIAA P. 99-0365*, 1999.

P. A. Monkewitz, D. W. Bechert, B. Barsikow, and B. Lehmann. Self-excited oscillations and mixing in a heated round jet. *Journal of Fluid Mechanics*, 213:611–639, 1990.

Z. M. Moussa, J. W. Trischka, and S. Eskinazi. The nearfield in the mixing of a round jet with a cross-stream. *J. Fluid Mech.*, 80:49–80, 1977.

F. Muldoon and S. Acharya. Direct numerical simulation of pulsed jets in crossflow. *Computers & Fluids*, 39:1745–1773, 2010.

S. Muppidi and K. Mahesh. Study of trajectories of jets in crossflow using direct numerical simulations. *Journal of Fluid Mechanics*, 530:81–100, 2005.

S. Muppidi and K. Mahesh. Direct numerical simulation of round turbulent jets in crossflow. *Journal of Fluid Mechanics*, 574:59–84, 2007.

S. Narayanan, P. Barooah, and J. M. Cohen. Dynamics and control of an isolated jet in crossflow. *AIAA Journal*, 41(12):2316–2330, 2003.

T. H. New, T. T. Lim, and S. C. Luo. Effects of jet velocity profiles on a round jet in cross-flow. *Experiments in Fluids*, 40:859–875, 2006.

C.E. Niederhaus, F.H. Champagne, and J.W. Jacobs. Scalar transport in a swirling transverse jet. *AIAA Journal*, 35(11):1697–1704, 1997.

T. S. Oh and J. A. Schetz. Finite element simulation of complex jets in a crossflow for v/stol applications. *Journal of Aircraft*, 27:389–399, 1990.

N. Peters. Laminar flamelet concepts in turbulent combustion. In *Twenty-first Symposium (International) on Combustion*, page 1231, 1986.

S. D. Peterson and M. W. Plesniak. Evolution of jets emanating from short holes into crossflow. *Journal of Fluid Mechanics*, 503:57–91, 2004.

B. E. Poling, J. M. Prausnitz, and J. P. O'Connell. *The Properties of Gases and Liquids*. McGraw-Hill, New York, 5^{th} edition, 2001.

M. Provansal, C. Mathis, and L. Boyer. Benard-von karman instability: transient and forced regimes. *Journal of Fluid Mechanics*, 182:1–22, 1987.

J. E. Rehm and N. T. Clemens. The association of scalar dissipation rate layers and oh zones with strain, vorticity, and 2-d dilatation fields in turbulent non-premixed jets and jet flames. In *37th Aerospace Sciences Conference*, 1999.

R. C. Reid, J. M. Prausnitz, and T. K. Sherwood. *The Properties of Gases and Liquids*. McGraw-Hill, 1977.

P. Schlatter, S. Bagheri, and D.S. Henningson. Self-sustained global oscillations in a jet in crossflow. *Theoretical and Computational Fluid Dynamics*, 25:29–146, 2011.

F. Schlegel, D. Wee, Y. Marzouk, and A. Ghoniem. Contributions of the wall boundary layer to the formation of the counter-rotating vortex pair in transverse jets. *Journal of Fluid Mechanics*, 676:461–490, 2011.

J. Shan and P. Dimotakis. Reynolds-number effects and anisotropy in transverse-jet mixing. *Journal of Fluid Mechanics*, 566:47–96, 2006.

S. Shapiro, J. King, R. T. M'Closkey, and A. R. Karagozian. Optimization of controlled jets in crossflow. *AIAA Journal*, 44:1292–1298, 2006.

L Sirovich. Turbulence and the dynamics of coherent structures. *Quarterly of Applied Mathematics*, 45:561–590, 1987.

L. L. Smith, A. J. Majamaki, I. T. Lam, O. Delabroy, A. R. Karagozian, F. E. Marble, and O. I. Smith. Mixing enhancement in a lobed injector. *Physics of Fluids*, 9(3):667–678, March 1997.

S. H. Smith and M. G. Mungal. Mixing, structure and scaling of the jet in crossflow. *Journal of Fluid Mechanics*, 357:83–122, 1998.

A.M. Steinberg, R. Sadanandan, C. Dem, and P. Kutne. Structure and stabilization of hydrogen jet flames in crossflow. *Proceedings of the Combustion Institute*, 34:1499–1507, 2013.

P. J. Strykowski. *The control of absolutely and convectively unstable shear flows.* PhD thesis, Yale University, 1986.

L. K. Su and N. T. Clemens. Planar measurements of the full three-dimensional scalar dissipation rate in gas-phase turbulent flows. *Experiments in Fluids*, 27:507–521, 1999.

L. K. Su and W. J. A. Dahm. Scalar imaging velocimetry measurements of the velocity gradient tensor field in turbulent flows. ii. experimental results. *Physics of Fluids*, 8, 1996.

L. K. Su and M. G. Mungal. Simultaneous measurements of scalar and velocity field evolution in turbulent crossflowing jets. *Journal of Fluid Mechanics*, 513:1–45, 2004.

R. Sullivan, B. WIlde, D. R. Noble, J. M. Seitzman., and T. C. Lieuwen. Time-averaged characteristics of a reacting fuel jet in vitiated cross-low. *Combustion and Flame*, 161: 1792–1803, 2014.

I. van Cruyningen. *Quantitative Imaging of Turbulent Gaseous Jets Using Planar Laser-Induced Fluorescence.* PhD thesis, Stanford University, Department of Mechanical Engineering, September 1990.

P. Vedula, P. K. Yeung, and R. O. Fox. Dynamics of scalar dissipation in isotropic turbulence: a numerical and modelling study. *Journal of Fluid Mechanics*, 433:2960, 2001.

P. J. Vermeulen, P. Grabinski, and V. Ramesh. Mixing of an acoustically excited air jet with a confined hot crossflow. *J. Engr. for Gas Turbines and Power, ASME Transactions*, 114: 46–54, 1992.

R. Vernet, L. Thomas, and L. David. Analysis and reconstruction of a pulsed jet in crossflow by multi-plane snapshot pod. *Experiments in Fluids*, 47:707–720, 2009.

G. H. Wang and N. T. Clemens. Effects of imaging system blur on measurements of flow scalars and scalar gradients. *Experiments in Fluids*, 37:194–205, 2004.

B. Wieneke. Stereo-piv using self-calibration on particle images. *Experiments in Fluids*, 39: 267–280, 2005.

C. R. Wilke. A viscosity equation for gas mixtures. *Journal of Chemical Physics*, 18(4): 517–519, 1950.

P. J. Yagle, D. N. Miller, K. B. Ginn, and J. W. Hamstra. Demonstration of fluidic throat skewing for thrust vectoring in structurally fixed nozzles. *ASME Journal of Engineering for Gas Turbines and Power*, 123(3):502–507, 2001.

L. L. Yuan, R. L. Street, and J. H. Ferziger. Large-eddy simulations of a round jet in crossflow. *Journal of Fluid Mechanics*, 379:71–104, 1999.